AN ABSTRACT OF THE THESIS OF

David J. Gaskell for the degree of Doctor of Philosophy in Physics presented on March 22,2001.

Title: Longitudinal Electroproduction of Charged Pions from Hydrogen, Deuterium, and Helium-3.

Abstract approved: ______________________________

T. Patrick Welch Harold E. Jackson

Conventional pictures of nuclear interactions, in which the pion mediates the long/medium range part of the nuclear force, predict an enhancement of the virtual pion cloud in nuclei relative to that in the free nucleon. Jefferson Lab Experiment E91003 measured charged pion electroproduction from Hydrogen, Deuterium, and Helium-3. The longitudinal cross section, which in the limit of pole dominance can be viewed as the quasifree knockout of a virtual pion, was extracted via a Rosenbluth separation. The longitudinal cross sections from Deuterium and Helium-3 were compared to Hydrogen to look for signatures of the nuclear pions.

Longitudinal Electroproduction of Charged Pions from Hydrogen, Deuterium, and Helium-3

by

David J. Gaskell

A THESIS

submitted to

Oregon State University

in partial fulfillment of
the requirements for the
degree of

Doctor of Philosophy

Completed March 22,2001
Commencement June 2001

Doctor of Philosophy thesis of David J. Gaskell presented on March 22,2001

APPROVED:

Co-Major Professor, representing Physics

Co-Major Professor, representing Physics

Chair of the Department of Physics

Dean of Graduate School

I understand that my thesis will become part of the permanent collection of Oregon State University libraries. My signature below authorizes release of my thesis to any reader upon request.

David J. Gaskell, Author

ACKNOWLEDGMENTS

There is, of course, no way I can thank everyone who has made it possible for me to finally reach this milestone. Nonetheless, I will attempt to uphold the grand Hall C tradition of mentioning everyone that I can.

First, I have to thank the Physics Department at Oregon State University for giving me the chance to come to Corvallis in the middle of my first year of graduate school. I am confident that had I stayed at my previous school, I would not have had such a great experience.

Of course I must thank my advisor Pat Welch for getting me started and, even after moving on to other things, keeping an eye on me and performing his "advisorly duties".

During my two years at Jefferson Lab, I met many fantastic people who helped me in innumerable ways. I must thank the polarized target group, especially Charlie Sinclair and Matt Poelker for allowing me to take up valuable lab space while working on building a high gain laser cavity. Tom Chyba from Hampton University taught me everything I know about lasers while helping me on that particular project (and allowing me to sit in on his laser physics class). In Hall C, I got the chance to work with many great scientists. These people taught me how to run experiments, analyze data, and endure those endless night shifts. Among them were (in no particular order) Cynthia Keppel, Dave Mack, Steve Wood, Ketevi Assamagan, Allison Lung, Paul Gueye, Bill Vulcan, Joe Mitchell, Jim Dunne, Heinz Anklin, Hamlet Mkrtchyan, Vardan Tadevosyan, Beni Zihlmann (king of the owl shift!) and my hero, Rolf Ent. I also have to thank all the hardworking graduate students at Jefferson Lab. Many helped get Hall C going while others were there to help out during the running of E91003. These folks include Derek van Westrum, Dipangkar Dutta, Rick Mohring, Dave Meekins, Kenneth Gustafson, Pawel Abrozewicz, Valera Frolov, Chris Armstrong, Chris Bochna, Bart Terburg, Doug Koltenuk, the Niculescus (Gaby and Ioana), Wendy Hinton, Jinseok Cha, Mark Harvey, and Dave McKee. In particular I must thank Steven Avery, my fellow nucpi-er and Jochen Volmer, whose hard work on Fpi made my life oh, so much easier. I can honestly say that I learned something from every one of these people, whether they meant to teach me anything or not. I would be remiss if I failed to mention all the other people at Jefferson Lab who made our experiment work. In particular the target group - Mikell Seeley and Chris Keith put in many long hours to give us cold targets. And of course I can't forget those who lent us their technical expertise - Paul Hood, Paul Brindza, Steve Lassiter, Mike Fowler, Joe Beaufait, and Mark Hoegerl.

Some of the most interesting time I've spent in grad school came at Argonne, for which I must primarily thank Hal Jackson who gave me the opportunity to work on his experiment and then invited me out to Argonne. I have to thank Don Geesaman, Tom O'Neill, Dirk DeScheper, Paul Reimer, Joerg Reinhold, David Potterveld, Ben Zeidman, Roy Holt, Frank Dohrmann, and Ralph Segel, who all had to sit through those long and lively nucpi meetings at one time or another. Kevin Bailey and Tom O'Connor also probably know more about pion electroproduction than they ever wanted to. Harry Lee and Kawtar Hafidi also deserve kudos for their theoretical efforts. Finally I have to thank Bryon Mueller, who is the only person I've known who makes me feel downright optimistic, and John Arrington, who may well be the only person to have read this work cover-to-cover (more than once!). Those two deserve medals for enduring my endless questions and cries for help.

Through this long process, I enjoyed the support of friends and family, but no one contributed more to my happiness and sanity than Karen Bean. Through all the moves to strange and exotic locales, she has always kept a positive attitude. And despite my apparent desire to do nothing but work, she has forced me to occasionally step back and have fun. If not for her, I am sure I would have forgotten that there is more to life than physics.

I would like to thank Professor Lothar Tiator for providing the Fortran code for the MAID pion electroproduction model, which played an integral role in the analysis of the E91003 data. This work is supported by the U.S. Department of Energy and the National Science Foundation.

TABLE OF CONTENTS

TABLE OF CONTENTS (Continued)

Page

TABLE OF CONTENTS (Continued)

Page

TABLE OF CONTENTS (Continued)

LIST OF FIGURES

LIST OF FIGURES (Continued)

Figure | Page

LIST OF FIGURES (Continued)

Figure | Page

LIST OF FIGURES (Continued)

Figure | Page

LIST OF APPENDIX FIGURES

LIST OF TABLES

LIST OF TABLES (Continued)

Table Page

LIST OF APPENDIX TABLES

LONGITUDINAL ELECTROPRODUCTION OF CHARGED PIONS FROM HYDROGEN, DEUTERIUM, AND HELIUM-3

1. INTRODUCTION

1.1. Where are the Nuclear Pions?

In "Where are the Nuclear Pions?", Bertsch *et al.* [1] summarize a series of experiments that raise questions about the conventional picture of the pion as the mediator of the nuclear force. While models employing pion exchange have enjoyed remarkable success in describing nuclear forces, probes that in theory should be sensitive to these pion fields yield null results. If the anticipated effects of the nuclear pion cloud are lacking, then a re-evaluation of the pion as mediator of the nuclear force may be in order.

Using standard nuclear models, one can calculate a pion-excess distribution that maps out the pion field of a nucleus relative to that of the free nucleon as a function of the virtual pion momentum. Here, one can construct a pion number operator, either in terms of a realistic nucleon-nucleon potential or nuclear response functions derived from a mean-field theory. Figure 1.1 shows an example of one such calculation where the excess pion density for a few sample nuclei is plotted as a function of the virtual pion momentum, k_π [2]. The suppression at low virtual

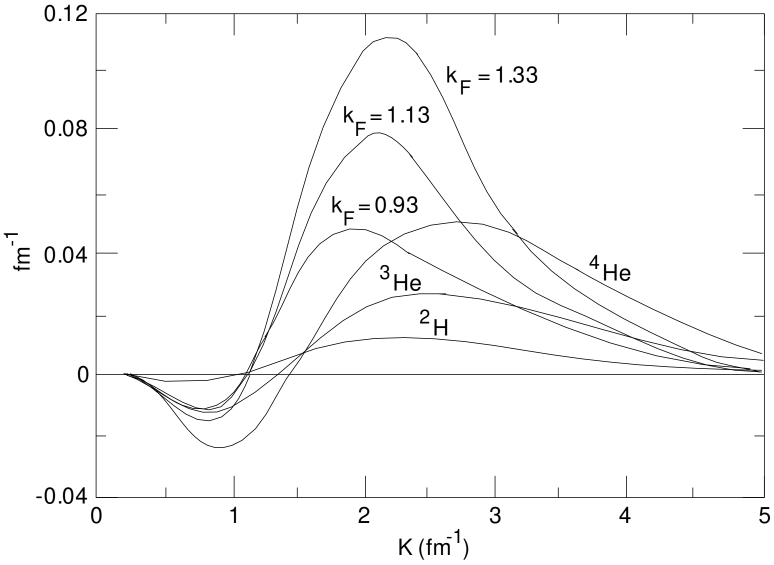

FIGURE 1.1. Pion excess distribution as calculated by Friman *et al.* The quantity plotted is $k_\pi^2\langle\delta n^\pi(k_\pi)\rangle/2\pi^2 A$ where $\langle\delta n^\pi\rangle = \langle n^\pi\rangle_A - A\langle n^\pi\rangle_N$. Distributions for ^{2}H, ^{3}He, ^{4}He, as well as nuclear matter with Fermi momentum k_F, of $k_F = 0.93$, 1.13, and 1.33 fm^{-1} are shown [2].

pion momenta comes from Pauli blocking of the nuclear final state. [1] Of particular interest here is the enhancement around $k_\pi \approx 2-3$ fm^{-1} (400-600 MeV/c). When integrated over k_π this leads to a net enhancement of the pion field in nuclei relative to the free nucleon (the pion excess). Table 1.1 shows the resulting number of excess pions per nucleon for several nuclei. The failure to detect such an enhancement raises questions as to the role of pions in nuclei.

---

[1]The nucleons, being spin-1/2 particles, must obey Fermi statistics so that two nucleons cannot be in the same quantum state. The emission of a positively charged pion, for example, requires that the emitting proton become a neutron. However, if there is already a neutron with identical quantum numbers to the proton, this transition will be blocked by the Pauli Exclusion Principle. Pauli blocking is less significant at higher virtual pion momentum because the transformed nucleon is more likely to be in an excited state.

Nucleus	$\langle \delta n_\pi \rangle / A$
^{2}H	0.024
^{3}He	0.05
^{4}He	0.09
^{27}Al	0.11
^{56}Fe	0.12
^{208}Pb	0.14
Nuclear Matter, $k_F = 0.93$	0.08
Nuclear Matter, $k_F = 1.13$	0.12
Nuclear Matter, $k_F = 1.33$	0.18

TABLE 1.1. Pion excess per nucleon for various nuclei from Friman *et al.* These numbers are the curves from Figure 1.1 integrated over k_π [2].

1.1.1. The EMC Effect and Nuclear Pions

Deep Inelastic Scattering (DIS) by either electrons or muons has provided much insight into the quark structure of hadrons. To first order, DIS is viewed in terms of the exchange of a single virtual photon with the target nucleon or nucleus (see Figure 1.2). In the limit of large Q^2 ($-q^2$, where q^2 is the invariant mass of the exchanged photon) and large ω (the energy of the virtual photon), DIS can be viewed as scattering from the quarks within the hadronic system. The cross section can be written in terms of two structure functions, F_1 and F_2,

$$\frac{d\sigma}{dxdQ^2} = \frac{4\pi\alpha^2 E'^2}{xQ^4}\frac{E'}{E}\left(F_2\cos^2\frac{\theta}{2} + 2\frac{\omega}{M}F_1\sin^2\frac{\theta}{2}\right) . \tag{1.1}$$

These structure functions are in turn related to quark distributions in the target nucleon or nucleus.

In 1983, the European Muon Collaboration found that the ratio of the nuclear structure function (F_2) per nucleon in iron differed significantly from that in deuterium [3]. Figure 1.3 shows the original data as a function of

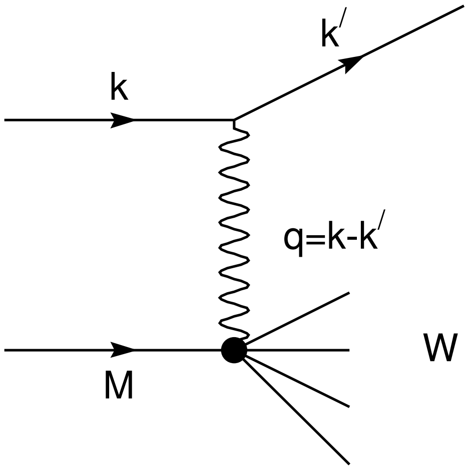

FIGURE 1.2. Feynman diagram of Deep Inelastic Scattering (DIS). k and k' represent the 4-momentum of the initial and scattered lepton (electron or muon), q the 4-momentum of the exchanged photon, and W the invariant mass of the final hadronic state.

Bjorken x ($= Q^2/2m_p\omega$). In DIS, x is interpreted as the fraction of the total nucleon momentum carried by the struck quark (in the nucleon infinite momentum frame). Of particular interest here is the apparent enhancement at $x < 0.2$. This was quickly attributed to contributions from scattering from the virtual pion field of the nucleus. Since a heavy nucleus is a bound system, it stands to reason that there is an enhanced pion cloud due to the nuclear interactions. An electron (or muon) then, can just as easily scatter from a quark in one of these pions as from a quark in a nucleon.

Ericson and Thomas [4] were able to calculate the observed enhancement using the Sullivan formula [5] and the spin-isospin nuclear response function. The incremental change in the structure function F_2 due to the excess nuclear pion

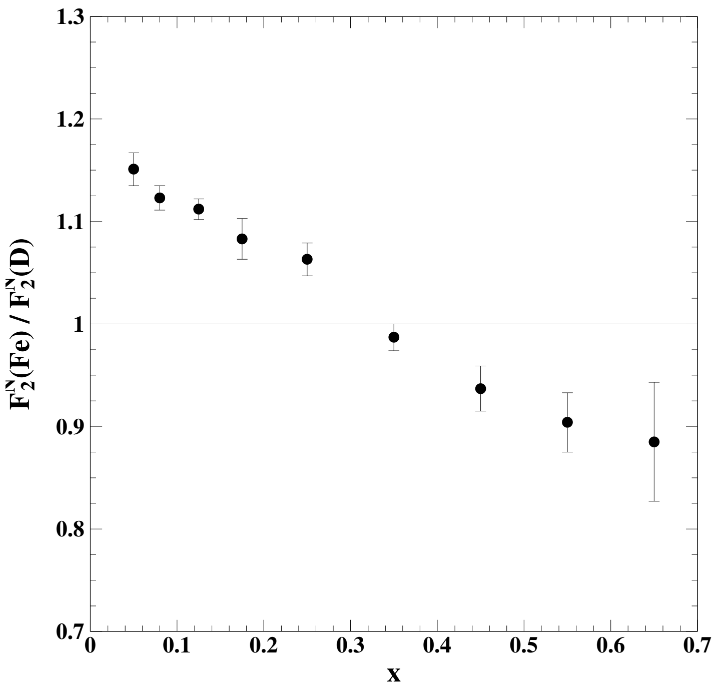

FIGURE 1.3. Ratio of the F_2 structure function per nucleon in iron to F_2 per nucleon in deuterium as a function of $x = Q^2/2m_p\omega$. Data are from Ref. [3]. There is an additional 7% overall systematic uncertainty not shown on the plot.

field can be expressed as a convolution of the pion structure function with the distribution of "extra" pions in the nucleus,

$$\delta^\pi F_2^A(x) = \int_x^1 dy[f_\pi^A(y) - f_\pi^N(y)]F_2^\pi(x/y)\,, \tag{1.2}$$

where F_2^π is the free pion structure function and $f_\pi^N(y)$ represents the probability that the pion carries a fraction y of the free nucleon momentum in the infinite momentum frame. Using the Sullivan formula, f_π^N can be written [6],

$$f_\pi^N(y) = \frac{3g^2}{16\pi^2}y\int_{M_N^2y^2/(1-y)}^\infty dt\frac{t|G_{\pi NN}(t)|^2}{(t+m_\pi^2)^2}\,, \tag{1.3}$$

where $G_{\pi NN}$ is the πNN vertex form factor (calculated in the Cloudy Bag Model) with g the coupling constant and $-t$ is the 4-momentum squared of the virtual pion, $-t = \omega^2 - q^2$. Note that in this context, ω and q represent the energy and 3-momentum of the virtual pion and should not be confused with ω and q as defined above - the energy and 4-momentum of the exchanged virtual photon in DIS.[2] The corresponding pion distribution in the nucleus, f_π^A, can be expressed,

$$f_\pi^A(y) = \frac{3g^2}{16\pi^2} y \int_{M_N^2 y^2}^{\infty} dq^2 \int_0^{q - M_N y} d\omega \frac{q^2 |G_{\pi NN}(q^2)|^2}{(t + m_\pi^2)^2} R_L(q, \omega) \, . \tag{1.4}$$

This expression differs from the expression for the nucleon pion distribution function by the addition of $R_L(q, \omega)$, the isovector nuclear spin-isospin (longitudinal) response function. The nuclear longitudinal response is derived from pion exchange and is normalized such that $f_\pi^A = f_\pi^N$ in a dilute (non-interacting) nuclear system. $R_L(q, \omega)$ can be calculated using a Fermi gas model in the random phase approximation (RPA), the strength of the response function controlled by the Landau-Migdal parameter, g'. Using reasonable values of g', Ericson and Thomas were able to fit the EMC enhancement well (see Figure 1.4).

The original EMC data along with the Ericson and Thomas calculation support the concept of nuclear pions and a pion excess, however later data from SLAC found a reduced enhancement in the $0.1 < x < 0.2$ region and a suppression (due to shadowing) at $x < 0.1$ [9, 10]. This apparent lack of enhancement was later confirmed by the EMC collaboration [11, 7] (see Figure 1.5). While g' is certainly not a fixed parameter and can be adjusted to improve agreement with

[2]We use these variables despite the potential for confusion to be consistent with the conventions commonly used in the literature. One should keep in mind that, in this context, q can be identified with k_π as defined in the previous section.

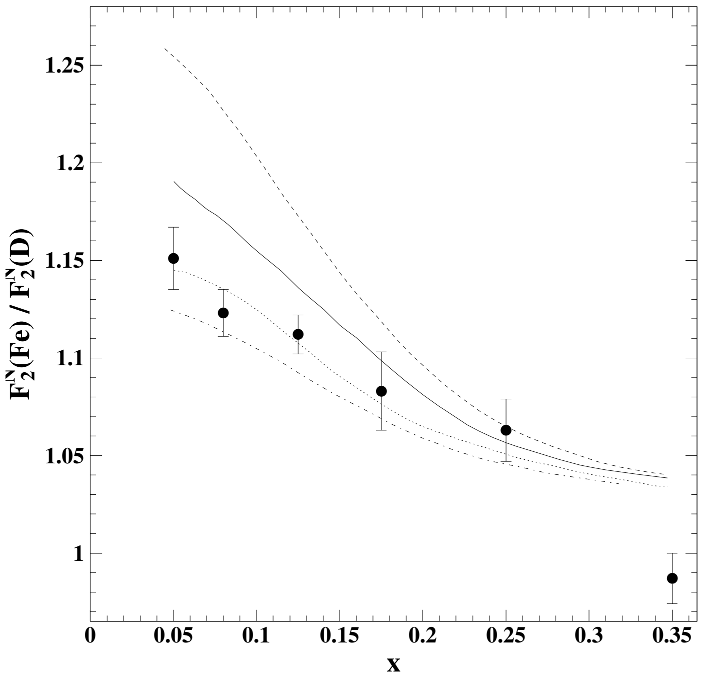

FIGURE 1.4. $F_2(Fe)/F_2(D)$ ratio as calculated by Ericson and Thomas. Points are the original EMC data and the solid curve is their calculation with the nominal input parameters (g'=0.7, $k_F = 1.30$ fm^{-1}, and a cloudy bag radius R of 0.7 fm). The dashed, dotted, and dashed-dotted lines show the calculation when altering g' (0.6), k_F (1.1 fm^{-1}), and R (0.8 fm), respectively [4].

the newer structure function results, this reduces the pion excess and hence raises some uncertainty as to the role of pions in nuclei.

1.1.2. Spin Transfer Experiments

Since the expected effect of an enhanced nuclear pion field shows up in the spin-isospin nuclear response, a more direct way to look for evidence of the pion excess is to directly measure $R_L(q,\omega)$ in the region where one expects some

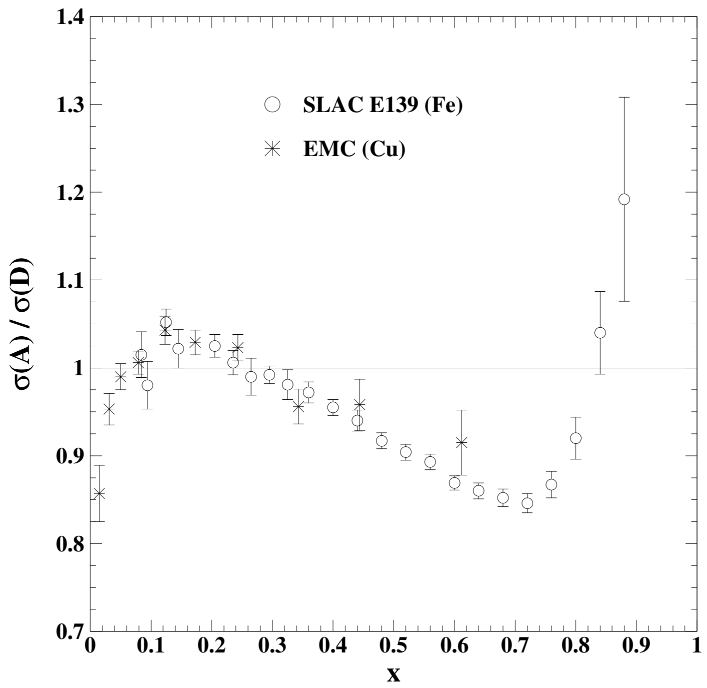

FIGURE 1.5. Ratio of cross section per nucleon in nuclear targets to deuterium as a function of $x = Q^2/2m_p\omega$. The EMC data [7] were taken on copper while the SLAC data [8] were taken on iron. Not shown on the SLAC data is an extra 1% systematic error between targets as well as an overall 1% systematic error.

enhancement ($q \approx 400$ MeV/c). To isolate the spin-isospin longitudinal nuclear response, one can perform $(\vec{p}, \vec{p}\ ')$ and $(\vec{p}, \vec{n})$ experiments in which a polarized proton beam scatters from a nuclear target and the emergent nucleon polarization is also measured.

The first such experiment [12, 13] was carried out at LAMPF and scattered polarized protons from lead and calcium. Spin flip probabilities from these targets were compared to those from deuterium to extract the response functions at $q \approx 350$ MeV/c. It should be noted that in this experiment, the ratio

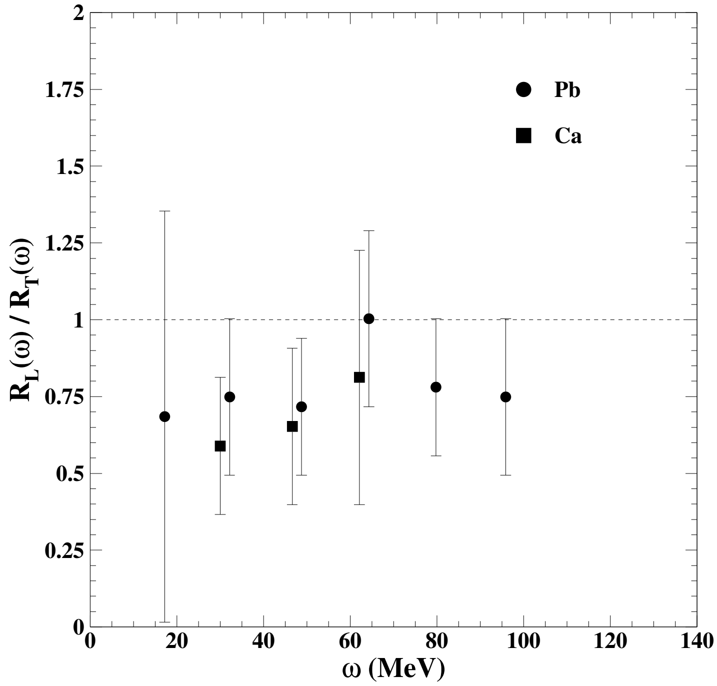

FIGURE 1.6. Ratio of spin longitudinal and spin transverse responses from the $(\vec{p}, \vec{p}\ ')$ reaction on lead and calcium. Data are from Ref. [13], taken at $q \approx 350$ MeV/c. Note that each response function is really a linear combination of the isovector and isoscalar response. Standard RPA calculations consistent with a pion excess would predict a significant enhancement of the isovector longitudinal response at low ω.

of longitudinal to transverse response (R_L/R_T), and not the isolated longitudinal response was extracted. It was generally assumed that there should be no enhancement in the transverse response so that measurement of the longitudinal to transverse ratio would be sensitive to enhancements in the longitudinal channel. The results are shown in Figure 1.6. It was concluded that there was no evidence for enhancement of the longitudinal response.

One drawback of using the $(\vec{p},\vec{p}\ ')$ process to examine the longitudinal nuclear response is that it includes isoscalar components as well as isovector. Since any enhancement due to pion exchange should be in the purely isovector channel (since the pion is isospin 1) this makes $(\vec{p},\vec{p}\ ')$ experiments difficult to interpret. On the other hand, the $(\vec{p},\vec{n})$ reaction is pure isovector so is a more promising (though more difficult experimentally) candidate for detecting the enhancements in the longitudinal response. Such an experiment was carried out on carbon and calcium targets (as well as the baseline deuterium) at $q = 340$ MeV/c [14, 15]. The results are shown in Figure 1.7. As in the $(\vec{p},\vec{p}\ ')$ experiment, the ratio of longitudinal to transverse response shows no evidence for an enhancement of the longitudinal response.

One problem with both of the above kinds of experiments is that, since the nucleus interacts strongly with hadronic probes, such reactions tend to be localized near the nuclear surface. This may potentially dilute the collective effects leading to enhancements of the spin-isospin longitudinal response. Furthermore, there is some evidence that the assumption that the transverse response should see no enhancement in nuclei may be wrong [16]. Unfortunately, the uncertainty involved in extracting the isolated response functions is much greater than that involved in the response function ratio. So while standard RPA calculations (that lead to a pion enhancement) are consistent with the data in Ref. [16], the uncertainties are too large to make a definitive statement.

1.1.3. The Drell-Yan Process

Like Deep Inelastic Scattering, the Drell-Yan process provides another means to investigate the quark structure of nuclei compared the free nucleon.

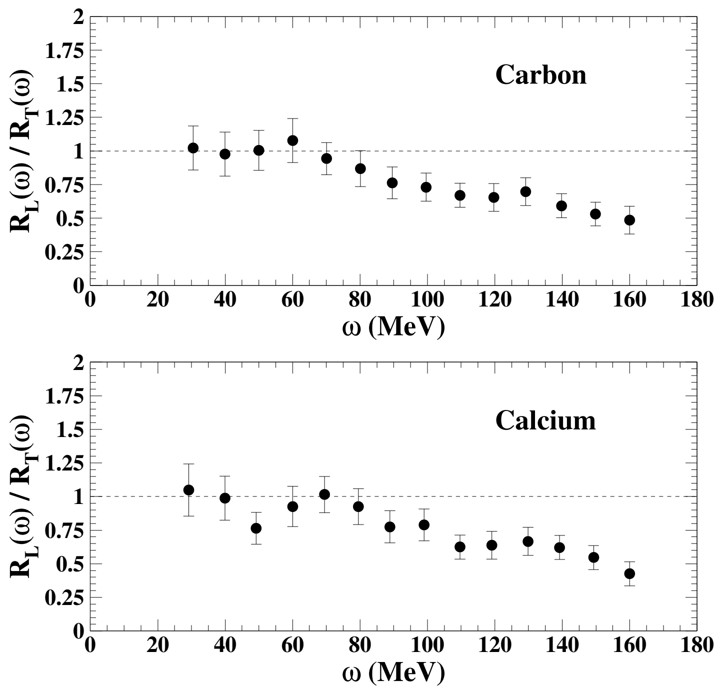

FIGURE 1.7. Ratio of spin longitudinal and spin transverse responses from the $(\vec{p}, \vec{n})$ reaction on carbon and calcium. Data are from Ref. [14], taken at $q \approx 340$ MeV/c. In this case, the response functions are pure isovector with no isoscalar components. RPA calculations predict significant enhancements at low ω.

In this case, a quark from a proton beam annihilates on an antiquark from the target resulting in a lepton pair. With the appropriate choice of kinematics, the Drell-Yan cross section is sensitive to the antiquark content of the target, while DIS is sensitive to both quarks and antiquarks. Since the valence structure of the pion is a quark-antiquark pair while the valence structure of the nucleon involves only quarks, one might expect that Drell-Yan would provide maximal sensitivity to the presence (or absence) of nuclear pions.

Experiment E772 at Fermi National Accelerator Laboratory measured muon pairs from proton collisions with deuterium, carbon, calcium, iron, and tungsten [17]. The ratio of the Drell-Yan yield from the heavy targets to deuterium as a function of x is shown in Figure 1.8. Clearly, there is no evidence for any enhancement at small x. Calculations that include pion excess effects are inconsistent with the data.

1.1.4. Discussion

While the evidence for a pion excess seems lacking in light of the above experiments, it is not clear that it can be ruled out. In particular, it is possible that the pion enhancement contributions to the quark distributions in nuclei are masked by shadowing in Drell-Yan and DIS.

There have been several attempts to explain the null results described above while maintaining the strong role of the pion in mediating the nuclear force. One hypothesis is that in the nuclear medium, the masses of hadrons decrease with density [18]. This "Brown-Rho" rescaling leads to altered couplings and calculations including these effects yield results consistent with the Drell-Yan and DIS data as well providing some explanation for the null spin transfer results.

On the other hand, nuclear models based on realistic nucleon-nucleon potentials (rather than mean field models like the RPA) predict that the longitudinal response will only be enhanced at high energy transfers, i.e. away from the quasielastic peak [19]. This is in marked contrast to standard RPA calculations, which predict the enhancement to manifest at the quasifree peak. Although it is difficult to calculate the response functions ($R(q, \omega)$) themselves using these realistic potentials, one can calculate the energy integral of the response as well as

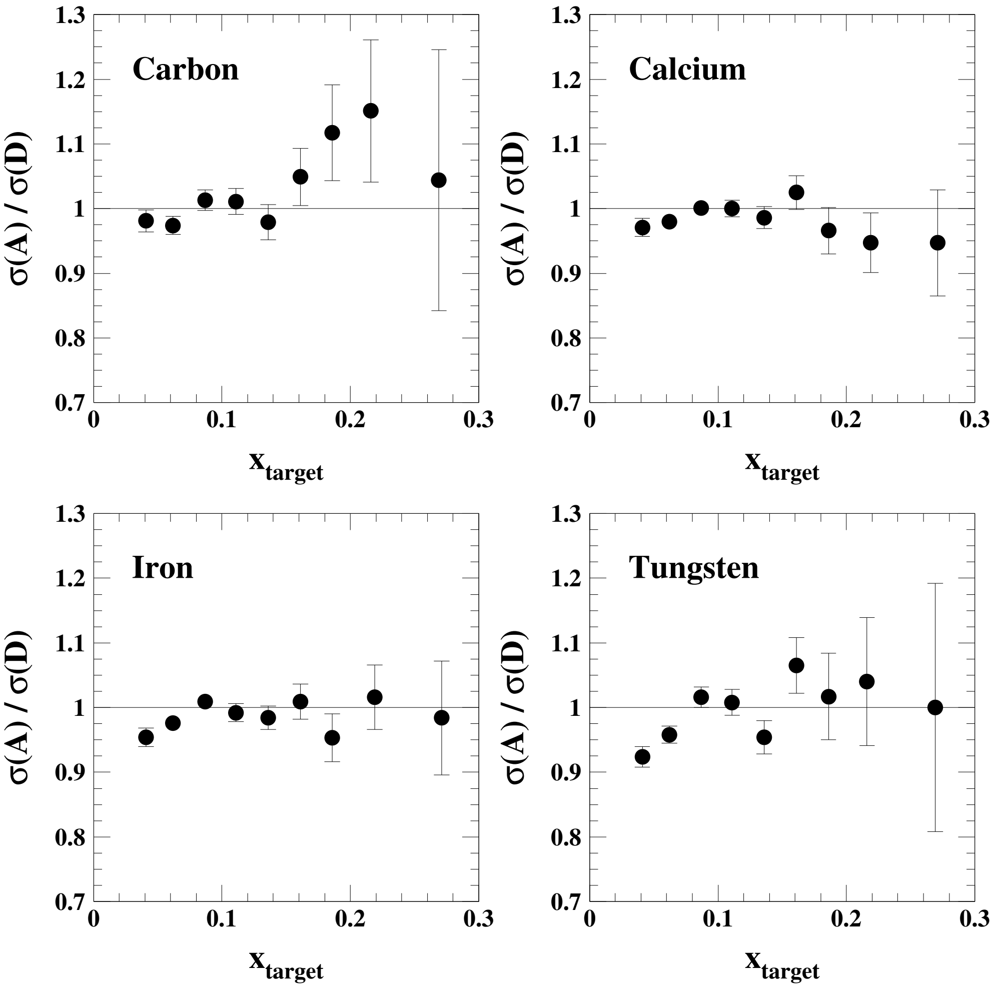

FIGURE 1.8. Ratios of Drell-Yan cross sections per nucleon from nuclear targets to deuterium. Data are from Ref. [17]. There is no evidence for any enhancement at small x_{target}.

the energy (ω) weighted integral of the response. These calculations indicate that the effects of the pion excess appear at higher ω than indicated by RPA calculations. Furthermore, one can make estimates as to the effect of this shifting of the extra strength on the DIS and spin-transfer experiments [20]. One consequence is that the region of energy transfer sampled by the spin transfer experiments may not have been adequate to see the enhanced responses. Furthermore, kinematic constraints in the pion distribution function in nuclei (the upper limit of the ω integration in Equation 1.4) may prevent one from seeing the effects of the pion excess in DIS (or Drell-Yan) experiments.

Clearly, additional probes to shed light on the presence or absence of the expected pion excess would be extremely useful. With the advent of high duty factor electron accelerators like the one at Thomas Jefferson National Accelerator Facility (Jefferson Lab), direct pion electroproduction from nuclei is a practical alternative. To the extent that the pole process dominates, pion electroproduction can be viewed as the knockout of a virtual pion by a virtual photon. This then would give one more direct access to the virtual pion field of the nucleus with hopefully less theoretical ambiguity as to the meaning of the result.

This was the goal of Jefferson Lab experiment E91003. The longitudinal charged pion electroproduction cross section was measured on hydrogen, deuterium, and helium-3 to look for effects from the virtual pion cloud of these light nuclei. Two values of the struck virtual pion momentum k_π were sampled: one corresponding to the region where the pion excess is predicted to be negative ($k_\pi \approx 200$ MeV/c) and one where the excess is predicted to be positive ($k_\pi \approx 470$ MeV/c).

1.2. Pion Electroproduction

1.2.1. Kinematics

The reaction studied in E91003 was,

$$e + A \rightarrow e' + \pi^{\pm} + X \ , \tag{1.5}$$

where A denotes the hydrogen, deuterium, or helium-3 target. $\pi^{\pm}$ indicates that data was taken for both positively and negatively charged pions. X is the final hadronic state which was either a free continuum state of one, two, or three nucleons or a bound nuclear state. The data was constrained such that none of the final nucleons were in an excited state. A diagram of the reaction is shown in Figure 1.9.

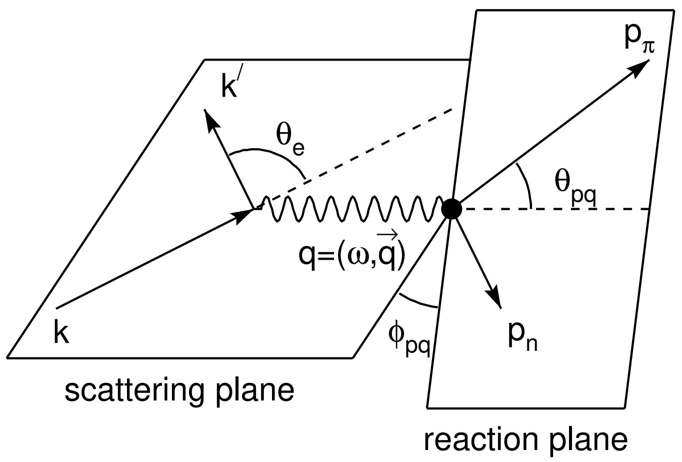

FIGURE 1.9. Diagram of the pion electroproduction reaction. The initial and final electron define the scattering plane, while the pion and recoiling nucleon(s) define the reaction plane.

The kinematics are defined as follows. The incoming electron (4-momentum k) and outgoing electron (k') which scatters at some angle θ_e define the scattering plane. A virtual photon with 4-momentum $q = (\omega, \mathbf{q}) = (k - k')$ is exchanged with the target. The square of the virtual photon 4-momentum, $q^2 = \omega^2 - |\mathbf{q}|^\mathbf{2}$ is negative in electron scattering, hence the common definition of $Q^2 \equiv -q^2$. The pion emerges at an angle θ_{pq} relative to the virtual photon direction. The outgoing pion and recoiling nucleon(s) define the reaction plane which is inclined at an angle ϕ_{pq} relative to the scattering plane.

If one detects the scattered electron and pion (and assuming one has knowledge of the incident electron), one can calculate the missing energy and missing momentum of the recoiling nucleon(s),

$$E_m = E_e - E_{e'} + M - E_\pi \,, \tag{1.6}$$

$$\mathbf{P_m} = \mathbf{q} - \mathbf{p}_\pi \,. \tag{1.7}$$

The missing mass is then $M_x = \sqrt{E_m^2 - |\mathbf{P_m}|^\mathbf{2}}$. In the case of pion electroproduction from hydrogen the missing mass is $M_x = m_n$, the mass of the neutron. In the case of quasifree pion electroproduction from deuterium or helium-3, the missing mass is not fixed due to the extra degree of freedom of the relative momentum between the recoiling nucleons.

Pion electroproduction is typically described in terms of Q^2, W, and t. Q^2 we have defined above and describes the invariant mass of the exchanged virtual photon. $W^2 = (q + P_{target})^2$ is the total energy in the virtual photon - target center of mass system, and can be expressed in terms of lab quantities,

$$W = \sqrt{M^2 + 2M\omega - Q^2}\,, \tag{1.8}$$

where M is target mass. Commonly, M is taken to be the proton mass even in the case of nuclear targets since one is often interested in comparing with electroproduction from the proton. $t = (q - p_\pi)^2$ is the 4-momentum squared of the momentum transferred to the nucleon(s) and is given by,

$$t = (\omega - E_\pi)^2 - |\mathbf{q}|^2 - |\mathbf{p}_\pi|^2 + 2|\mathbf{q}||\mathbf{p}_\pi| \cos\theta_{pq} \,. \tag{1.9}$$

Note that the three momentum of t is simply given by $\mathbf{P_m}$ and is equivalent to k_π, the momentum of the virtual struck pion in our quasifree knockout picture.

1.2.2. Cross Section

The pion electroproduction cross section can be written in terms of a virtual photon flux factor, Γ, multiplied by a virtual photon cross section. In the case of pion electroproduction from hydrogen, the five-fold lab cross section can be written in terms of the scattered electron lab energy (E'_e) and solid angle (Ω_e) as well as the pion solid angle (Ω_π),

$$\frac{d^5\sigma}{d\Omega_e dE'_e d\Omega_\pi} = \Gamma \left(\frac{d\sigma}{d\Omega_\pi} \right) \,. \tag{1.10}$$

The virtual photon flux is given by,

$$\Gamma = \frac{\alpha}{2\pi^2} \frac{E'_e}{E_e} \frac{1}{Q^2} \frac{1}{1-\epsilon} K_{eq} \,, \tag{1.11}$$

where ϵ describes the longitudinal polarization of the virtual photon and is,

$$\epsilon = \frac{1}{1 + 2\frac{|\mathbf{q}|^2}{Q^2} \tan^2(\theta_e/2)} \,. \tag{1.12}$$

K_{eq} is the equivalent photon energy, i.e. the energy a real photon would need to excite a target of mass M to an excited state of mass W and is given in the Hand convention by,

$$K_{eq} = \frac{W^2 - M^2}{2M} \,. \tag{1.13}$$

It should be noted that a common convention is to boost the virtual photon cross section ($d\sigma/d\Omega_\pi$) in Equation 1.10 to the virtual photon - target center of mass frame. This is more convenient when one wishes to extract resonance multipoles etc. However, since in the end we wish to compare cross sections from different targets, it is less convenient in that each boost would be to a different frame of reference. Hence, in this work we will usually describe the virtual photon cross section in the lab frame.

The virtual photon cross section can be decomposed into contributions from longitudinal (L) and transverse (T) photons as well as longitudinal-transverse (LT) and transverse-transverse (TT) interference terms,

$$\frac{d\sigma}{d\Omega_\pi} = \frac{d\sigma_T}{d\Omega_\pi} + \epsilon\frac{d\sigma_L}{d\Omega_\pi} + \sqrt{2\epsilon(1+\epsilon)}\frac{d\sigma_{LT}}{d\Omega_\pi}\cos\phi_{pq} + \epsilon\frac{d\sigma_{TT}}{d\Omega_\pi}\cos 2\phi_{pq}\,. \tag{1.14}$$

Note that in real photoproduction only the transverse terms can be sampled - the fact that the virtual photon has $Q^2 \neq 0$ allows us to sample the longitudinal pieces. Along the virtual photon direction, the interference terms (LT and TT) go to zero. Furthermore, if one integrates over ϕ_{pq} for θ_{pq} greater than zero, these terms also disappear. Then one is left with,

$$\frac{d\sigma}{d\Omega_\pi} = \frac{d\sigma_T}{d\Omega_\pi} + \epsilon\frac{d\sigma_L}{d\Omega_\pi}\,. \tag{1.15}$$

The longitudinal and transverse terms can be separated via the Rosenbluth technique, i.e. by measuring the virtual photon cross section at two (or more) values of ϵ and fitting a straight line. The longitudinal cross section is given by the slope and the transverse by the y-intercept.

In the case of pion electroproduction from deuterium and helium-3 there is an extra kinematic degree of freedom and the 5-fold cross section becomes a 6-fold cross section,

$$\frac{d^6\sigma}{d\Omega_e dE_e d\Omega_\pi dP_\pi} = \Gamma \left(\frac{d\sigma}{d\Omega_\pi dP_\pi} \right) . \tag{1.16}$$

In this case, the final pion momentum, P_π, is not fixed by the electron kinematics and the pion direction. Equivalently, one could say that the final nuclear state is no longer fixed but can have relative momentum between the outgoing nucleons. Note however that the lab cross section can be broken down as before into a virtual photon flux times the virtual photon cross section. The virtual photon cross section can also be broken down into longitudinal and transverse pieces just as in the hydrogen case. Hence,

$$\frac{d\sigma}{d\Omega_\pi dP_\pi} = \frac{d\sigma_T}{d\Omega_\pi dP_\pi} + \epsilon \frac{d\sigma_L}{d\Omega_\pi dP_\pi} . \tag{1.17}$$

In order to compare the nuclear virtual photon cross sections to those from hydrogen, one can integrate over all final states (i.e. over P_π). Note that the integral of the virtual photon cross section can be written,

$$\int \frac{d\sigma}{d\Omega_\pi dP_\pi} dP_\pi = \int \frac{d\sigma_T}{d\Omega_\pi dP_\pi} dP_\pi + \epsilon \int \frac{d\sigma_L}{d\Omega_\pi dP_\pi} dP_\pi . \tag{1.18}$$

This means that one can extract the *integrated* longitudinal and transverse cross sections by measuring the *integrated* virtual photon cross section at two or more values of ϵ.

Experiment E91003 measured the virtual photon cross sections for charged pion electroproduction for each target (hydrogen, deuterium, and helium-3) at two values of ϵ. The measurement was made in parallel kinematics ($\theta_{pq} \approx 0$) and the cross sections integrated over ϕ_{pq} to eliminate the interference terms. Finally, a Rosenbluth separation was performed for the purpose of extracting and comparing the longitudinal cross sections from each target.

1.2.3. Contributing Processes

The Born level, or first order, processes that contribute to pion electroproduction are shown in Figure 1.10. The first (a) is the pole process in which pion electroproduction can be viewed as the knockout of a virtual pion by a virtual photon. The next two (b and c) are the nucleon pole and crossed nucleon pole terms and finally, the last (d) is known as the seagull term. This diagram is necessary to preserve gauge invariance when using pseudovector coupling of the virtual photon. Higher order processes involve resonances (the $\Delta(1232)$ for example), multiple pion exchange, or the exchange of heavier mesons (ρ, ω). While the transverse pion electroproduction cross section can couple strongly to these higher order processes as well as the other Born terms, it is believed that in certain kinematic regions, the longitudinal cross section is dominated by the pole term (a).

The pole process can roughly be described as the probability to have a virtual photon interact with a virtual pion of a given momentum multiplied by the probability to find a virtual pion with that momentum. The former is governed by the charged pion form factor $F_\pi(Q^2)$ while the latter is described by the πNN form factor, $g_{\pi NN}(t)$. In this simple picture, the longitudinal cross section is (assuming pole dominance),

$$\sigma_L \approx \frac{-tQ^2}{(t-m_\pi^2)^2} g_{\pi NN}^2(t) F_\pi^2(Q^2) \ . \tag{1.19}$$

In pion electroproduction from nuclei, the presence of excess pions would be perceived as a modification of $g_{\pi NN}(t)$ and hence an enhancement of the longitudinal cross section.

One can test that the extracted longitudinal cross section is truly dominated by the pole term by looking at the longitudinal π^-/π^+ ratio in deuterium. The virtual photon can be viewed as a linear combination of two isospin states; $I = 0$,

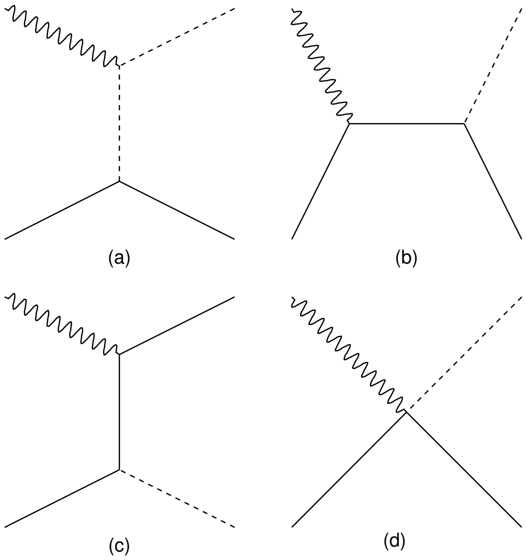

FIGURE 1.10. Born diagrams for pion electroproduction. Wavy lines indicate the virtual photon, dashed lines the pion, and solid lines the nucleon. (a) is the pion pole process (t-channel process), (b) the nucleon pole (s-channel), (c) the crossed nucleon pole (u-channel), and (d) the seagull term necessary to preserve gauge invariance.

the isoscalar photon and $I = 1$, the isovector photon. The longitudinal π^-/π^+ ratio is then given in terms of isoscalar and isovector amplitudes (A_s and A_v),

$$\frac{\sigma(\gamma^* n \to \pi^- p)}{\sigma(\gamma^* p \to \pi^+ n)} = \frac{|A_v - A_s|^2}{|A_v + A_s|^2} \,. \tag{1.20}$$

Since the pole term is pure isovector (by G parity conservation) while the other born terms contain both isoscalar and isovector pieces, any deviation of the longitudinal π^-/π^+ ratio from 1 is an indication of the presence of isoscalar backgrounds. A deviation from 1, although a sign of isoscalar backgrounds, can also be consistent with the pole term being the single largest contributing term to the cross section. So while the longitudinal π^-/π^+ ratio is a useful check, a ratio different from unity does not alone imply that one is not sensitive to the pole process when measuring the longitudinal cross section.

1.3. Overview of the Experiment

The goal of experiment E91003 ("NucPi") was to measure the longitudinal (and transverse) cross sections of pion electroproduction from H, ^{2}H, and ^{3}He. The experiment was carried out in the experimental Hall C at Jefferson Lab from February to April 1998. Scattered electrons were detected in the High Momentum Spectrometer (HMS), while the charged pions were detected in the Short Orbit Spectrometer (SOS).

All data were taken at $Q^2 = 0.4$ (GeV/c)^2. One of the aims of the experiment was to sample the longitudinal cross section at different values of the nucleon recoil momentum (i.e. the struck virtual pion momentum, k_π). Since Q^2, k_π, and W (the total energy in the center of mass) are correlated, varying k_π meant that it was necessary to vary W simultaneously. For the low k_π point, data were taken at $W = 1.6$ GeV, while the high k_π data were taken at $W = 1.15$ GeV. At each k_π, Q^2, and W data were taken for two values of the virtual photon polarization, ϵ (see Table 1.2). The charged pions were detected along the direction of the momentum transfer, $\mathbf{q}$.

In general, the hydrogen and deuterium data were taken at the same period in time (without any changes made to the spectrometers or beam energy), thus reducing the systematic error in comparisons between the two targets. However, since the helium-3 target is cooled by a different cryogen (4 K helium gas as opposed to 15 K for the Z$\leq$2 targets) it could not be cooled on the target ladder at the same

E_{beam} (GeV)	ϵ	W (GeV)	Q^2 $(\mathrm{GeV}/c)^2$	k_π (GeV/c)
0.845	0.437	1.15	0.4	0.47
1.645	0.861	1.15	0.4	0.47
1.645	0.490	1.60	0.4	0.20
3.245	0.894	1.60	0.4	0.20

TABLE 1.2. E91003 kinematics.

time as the hydrogen and deuterium targets. The systematic uncertainty, then, in comparing the helium data to either of the other two targets is correspondingly larger.

In the both the HMS and SOS (when at negative polarity), threshold gas Čerenkov detectors were used to separate pions and electrons. Lead-glass calorimeters were also available in both detectors, but their efficiencies suffered when run at low momentum (and were not necessary to achieve good particle identification) so were not used in analysis of the data other than for tests and calibration. The Čerenkov detectors in both spectrometers were sufficiently efficient such that this did not cause any problems. In the SOS, positively charged pions were separated from protons using the velocity (β_{tof}) as measured by the four layers of scintillators in the detector stack.

2. EXPERIMENTAL APPARATUS

2.1. Accelerator

Experiment E91003 made use of the Continuous Electron Beam Accelerator (CEBA) at Jefferson Lab. At the time of experiment E91003 running, the accelerator was able to deliver 0.845 GeV to 4.045 GeV unpolarized electrons at $\approx$100μA. The accelerator was, at that time, beginning to deliver polarized electrons for experimental use, but at lower currents. Experiment E91003 typically ran at currents of 10 to 50 μA, and beam energies of 0.845, 1.645, and 3.245 GeV. The great majority of runs were taken with unpolarized electrons. Those runs taken when polarized electrons were in the accelerator were later discarded because the available current was too low (below the region where the Hall C current monitoring devices are considered accurate).

The electrons are accelerated by means of superconducting radio-frequency cavities in pulses of $\approx$ 1.7 ps at 1497 MHz. The beam delivered to each of the three experimental halls is then 499 MHz. Note that this rate of beam delivery is, for all intents and purposes, continuous. This was particularly important at the $W = 1.15$ GeV kinematics where the random coincidence rate was rather high (reals/randoms $\approx$ 1). Since the random rate is inversely proportional to the beam duty factor, the accidental coincidence rate would have been unacceptably large at a typical pulsed beam accelerator (duty factor = 10^{-4} to 10^{-2}).

Electrons from the injector are sent to the first linac at 45 MeV. They are then accelerated an additional 400 MeV in the north linac, bent through the east arc and accelerated another 400 MeV in the south linac. At this point, the beam can either be extracted and sent to one of the experimental halls, or sent on another circuit, or pass, through the machine (see Figure 2.1). In its standard tune at the

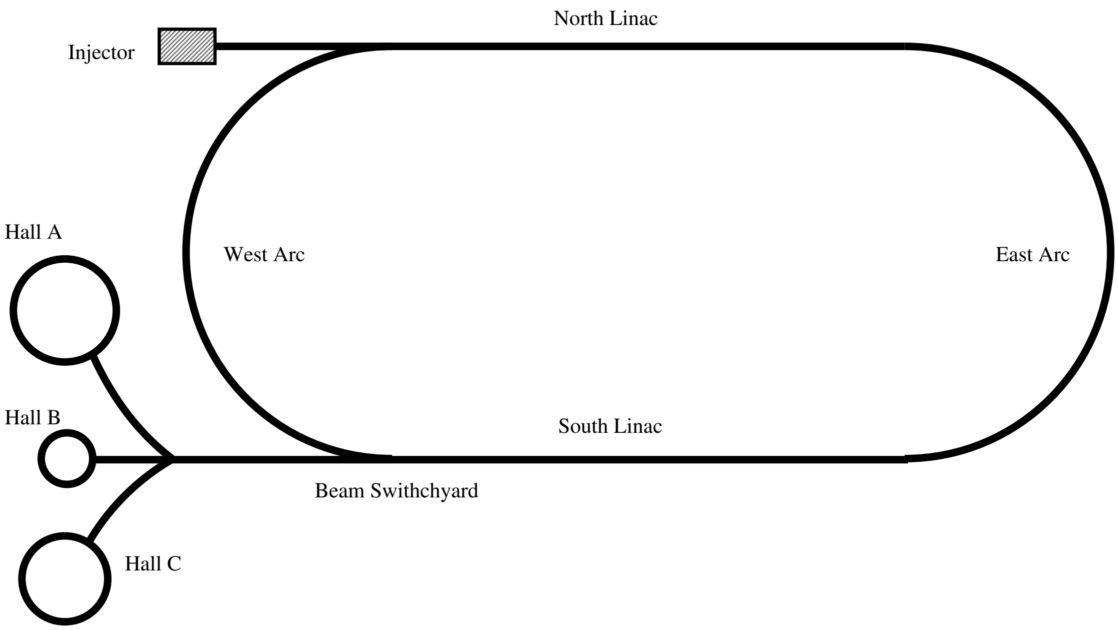

FIGURE 2.1. Schematic of the Continuous Electron Beam Accelerator at Jefferson Lab.

time of the experiment, CEBA imparts 800 MeV of energy for each pass (+45 MeV from the injector), up to 5 passes resulting in a maximum energy of 4.045 GeV. In the linacs, beams of different energies share the same pipe, but at the arcs, they must be split off to achieve the proper bend for each electron energy. Thus, there are five beamlines in the east arc and four in the west arc.

At the time of this experiment, preparations were being made to run the accelerator at 5 GeV. This meant each linac would have to provide more than the standard 400 MeV through each leg. It turns out that this is well within the capabilities of the superconducting RF cavities. During experiment E91003, a few cavities in each linac were turned off so that the accelerator operators could get experience with running the cavities at higher field gradients. Unfortunately, since this was a relatively new procedure, the end result was diminished reliability of the accelerator, the net effect of which was periodic, short "beam trips" in which an RF cavity tripped off interrupting delivery of the beam to the hall. While this was not a large problem, it was an issue that had to be addressed since the Hall C current monitoring devices have some zero current counting rate.[1]

2.2. Beamline

2.2.1. Beam Position Monitors

The path of the beam in the Hall C arc and beamline are monitored using five Beam Position Monitors (BPMs) (see Figure 2.2). These monitors are essentially resonating cavities with fundamental frequencies such that both the 1497 MHz beam pulse frequency in the accelerator and the 499 MHz pulse frequency in Hall C are harmonics of that fundamental frequency. Four antennae (rotated at 45^o with respect to the x-y axes to minimize synchrotron damage) pick up the relevant harmonic frequency. The beam displacement with respect to each antenna can then be directly related to the amplitude of the signal from each. The BPMs are described in more detail in Ref. [21].

During experiment E91003, the BPMs were mostly used by the machine operators to steer the beam. However, the two BPMs nearest the Hall C target (H00A and H00B) were closely monitored by Hall C shift crews to ensure that the beam was impinging on the target at a consistent point. The nominal beam

---

[1]The obvious solution would have been to immediately end a run whenever the beam tripped off. However, the beam trips were of such frequency that this would have been extremely tedious. Rather, the effect of the current monitor zero counting rate was removed in software.

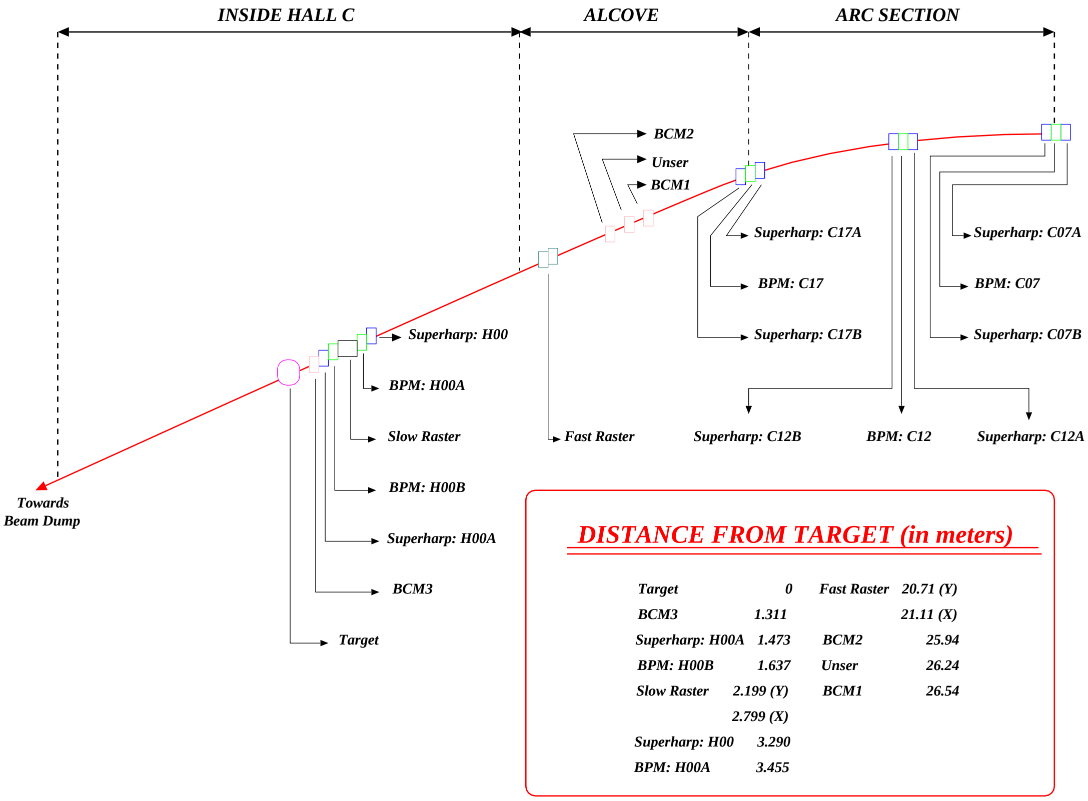

FIGURE 2.2. Hall C beamline.

position was set according to H00B ($x = -1.0$ mm and $y = -2.0$ mm). These coordinates were not believed to necessarily reflect the absolute position[2] of the beam and were chosen such that one achieved mid-plane symmetry in both spectrometers simultaneously. Using H00A in combination with H00B, we can project the beam position to the actual target (since the closest BPM H00B is 1.63 m upstream) and see that the position at the target typically varied by less than 0.5 mm.

[2]A survey of the BPM positions after the experiment, however, indicated that the values used online were accurate to about 0.5 mm.

2.2.2. Beam Energy Measurement

The energy of the electron beam sent to Hall C is measured using the magnets in the Hall C arc as a spectrometer [22]. During the energy measurement, all focusing elements in the arc are turned off and degaussed. The position and direction at the beginning and end of the 34.3° bend are carefully measured using high resolution wire sensors (superharps). The beam is then steered so that it follows the nominal central path and the beam energy can be determined using,

$$p = \frac{e}{\theta_{bend}} \int B dl, \tag{2.1}$$

where e is the electron charge, θ_{bend} is the arc bend angle and B is the magnetic field in the dispersive elements. The key to this measurement, of course, is a precise knowledge of the magnetic field in the dipoles. To this end, one of the dipoles in the Hall C arc has been extensively field-mapped as a function of the current applied. This knowledge of the field integral then allows one to measure the beam energy to a precision of $\delta p/p \approx 1 \times 10^{-3}$.

2.2.3. Beam Current Monitors

The Beam Current Monitors (BCMs) are used to measure the current of the electron beam as it passes through the beamline on its way to the target. The standard BCMs (BCM1 and BCM2) are resonating cavities in which the TEM_{010} mode is excited by the electron beam pulse train frequency. The TEM_{010} mode is desirable because its magnitude changes very slowly with respect to the position of the beam within the cavity. BCM1 and BCM2 are geometrically identical, differing only in their readout electronics. BCM1 uses a power meter to measure directly the power coupled to the cavity, while BCM2 uses a downconverter in combination with a high precision RMS to DC converter. A switchable gain precedes the RMS-DC converter, keeping the input signal within nominal operating parameters for the converter. The result is a high degree of linearity over a wide dynamic range. For this reason, BCM2 is typically used to extract the accumulated charge for data analysis. A more detailed explanation of the cavities and readout electronics can be found in Refs. [23, 24].

Since the cavities can expand and contract with changes in temperature, thus changing the resonant frequency and the power measured from the cavity, it was important to maintain the cavities at constant temperature over the course of the experiment. The cavity temperature was checked at least once an 8 hour shift, and deviations from the nominal temperature were less than 0.2 degrees C. The temperature of the readout electronics can also affect the current measurement, but the electronics room was maintained at constant temperature minimizing these effects.

BCM1 and BCM2 have reasonable gain stability over time, but need to be calibrated to an absolute standard periodically. This is done using an Unser current monitoring device. The Unser monitor is a parametric DC current transformer. The Unser monitor has an extremely stable gain, but large drifts in offset. For this reason, it was not used to measure the beam current on a run to run basis. The resonating cavity BCMs were calibrated by taking runs with periods of no beam (to set the Unser zero) interspersed with periods of beam at various currents (during E91003 these currents typically ranged from 10 μA to 50 μA in steps of 10 μA). The gain of BCM1 and BCM2 was then determined by comparing to the Unser monitor. Calibrations were typically taken on a daily basis, but the BCMs were stable enough that the calibrations were implemented for only five different periods of time. Comparison of the current as measured by BCM1 and BCM2 indicate that uncertainties due to the calibration procedure are less than 0.5%, and the absolute uncertainty for the charge measurement is taken to be 1%.

2.3. Targets

In order to achieve reasonable rates of data-taking, it is desirable to use dense targets to maximize the experimental luminosity. To that end, experiment E91003 made use of the existing liquid hydrogen and liquid deuterium cryogenic target systems in Hall C. Furthermore, a new cryogenic, high density helium-3 target was constructed and commissioned for this experiment.

Three cryogenic target cells are mounted on the cryotarget ladder[3] as well as a combination optics and dummy target sled. The latter consists of a series of slabs of carbon and aluminum at different z positions ($z = 0$ cm, $z = \pm 2$ cm, $z = \pm 4$ cm, and $z = \pm 6$ cm) along the beam direction. The two aluminum slabs at $z = \pm 2$ cm are used to subtract the aluminum can contribution to the cryotarget yields. The so-called dummy target is about seven times the nominal thickness of the cryotarget cell walls, allowing us to measure the cell wall contribution rapidly. The dummy target, in combination with the carbon targets on the optics sled, is used to take calibration data to check the reconstruction matrix elements of the spectrometers.

---

[3]In addition to the cryotarget ladder, there is also a separate ladder for solid targets. This ladder was not used during E91003.

2.3.1. Hydrogen and Deuterium Targets

The liquid hydrogen and deuterium targets are very similar to the targets used in previous Hall C experiments, although the geometry is somewhat different. The E91003 vertical-flow target cells are a round "pudding can" design, while previous experiments had used horizontal flow "beer can" cells. The old design had allowed for two target cells (one 15 cm and one 4 cm cell) per target loop. However, the new design only allows for one 4 cm cell per loop.

Since the hydrogen and deuterium targets use the same coolant supply, they can be cooled on the cryotarget ladder simultaneously. 15 K helium is provided by the End Station Refrigerator (ESR) and coolant flow to the loops is controlled by the target operator using Joule Thompson (JT) valves. The 15 K helium is sent to a heat exchanger where the target material is cooled. The target fluid moves continuously through the heat exchanger, to the target cell and back. A high and low power heater regulates the temperature of the target material, mimicking the power deposition of the electron beam during low current or beam-off periods. A single target cell is shown in Figure 2.3. The target cell itself is about 4 cm long in the beam direction with ≈ 0.0127 cm aluminum walls. Note that although the geometry of the vertical-flow target cells is new for E91003, most of the details of the cooling and regulation of the targets are unchanged. More details concerning the mechanical aspects of the cryotargets can be found in Ref. [25].

The nominal operating temperature of the hydrogen loop is typically 19 K, however, due to technical problems with the target it was necessary to run at 18 K for three out of four of the kinematic settings. There is a small density difference, which is taken into account in the analysis, along with target stability (temperature and pressure) and boiling effects. The deuterium target was run at a constant 22 K for all kinematics.

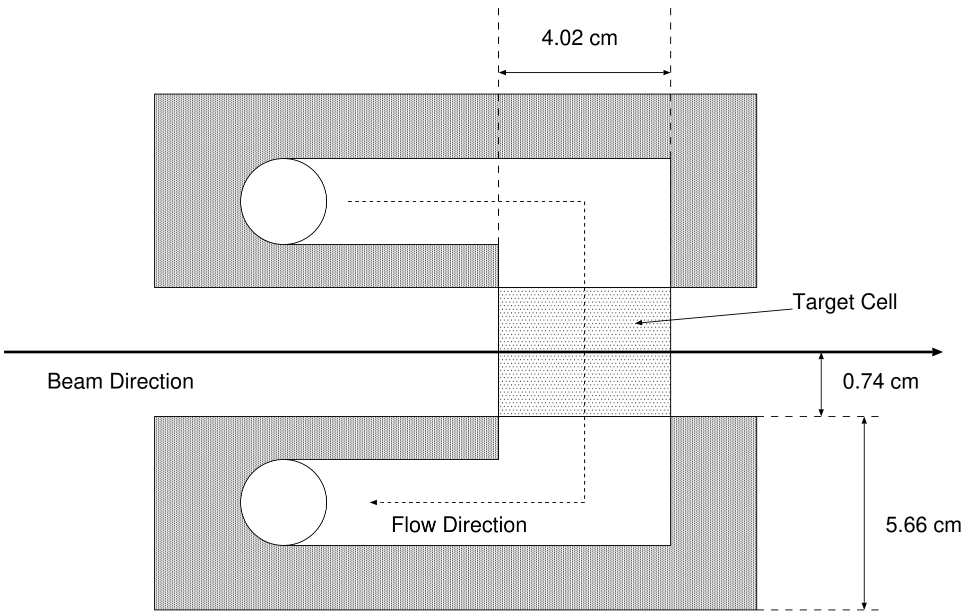

FIGURE 2.3. Side view of one cryotarget loop.

2.3.2. Helium-3 Target

The cryogenic helium-3 target, while not a liquid target, was run at low temperature (5.5 K) and high pressure (about 130 PSI) such that the target material existed in a "fluid-like" state. The fact that the targets were run at such high pressures necessitated the new "pudding can", vertical flow design. The high pressure targets also require that the aluminum walls of the target cells be thicker than previous cells (about 0.0127 cm as opposed to 0.0076 cm), thus increasing the experimental background from the target cell.

The operation of the helium-3 target is very similar to the operation of the hydrogen and deuterium targets. In this case, the coolant is 4 K (instead of 15 K) helium and the target is operated using the same system of JT valves and heaters described above.

2.3.3. *Target Thickness and Associated Uncertainties*

Tables 2.1 and 2.2 summarize the cryogenic target thicknesses and associated uncertainties. The total target thickness is determined using knowledge of the target cell geometry combined with close monitoring of the target density (temperature and pressure). For all three cryogenic targets, the temperature was kept constant throughout the experiment and was known absolutely to 0.1 K, contributing negligible uncertainty to the target density. The largest uncertainty in the cryotarget density comes from the equation of state, leading to a 0.5% uncertainty for the hydrogen and deuterium targets and a 1% uncertainty for the helium-3 target. The outer diameter of the target cell (warm) is determined to within 0.7%, while the correction due to contraction of cells at low temperature is estimated to be $\approx (0.4 \pm 0.2)\%$. In addition, the thickness of the cell wall itself is known to 0.0003 cm.

Target	Thickness (g/cm^2)
18K H2	0.2923
19K H2	0.2876
D2	0.6675
^{3}He	0.3068

TABLE 2.1. Nominal (cold) cryogenic target thicknesses. These values are not corrected for beam offset effects and target impurities.

Target	18K H2	19K H2	D2	^{3}He
Cell diameter	0.7%	0.4%	0.6%	0.7%
Cold length correction	0.2%	0.2%	0.2%	0.2%
Beam position at target	0.1%	0.1%	0.1%	0.1%
Equation of State	0.5%	0.5%	0.5%	1.0%
Target Purity	<0.1%	<0.1%	0.2%	<0.1%
Total	0.89%	0.68%	0.83%	1.24%

TABLE 2.2. Cryotarget thickness uncertainties.

Samples of the target gases were analyzed after the experiment to check for target purity. The hydrogen target was found to be $>$ 99.9% hydrogen with the only detectable impurity coming from nitrogen (14 ppm). No correction is assigned for this target. The deuterium gas was found to be 99.69% pure with the main source of impurity coming from 3000 ppm HD [26]. We assume that half the HD contributes to the experimental deuterium yields so that the target is effectively 99.85% deuterium. We assign an uncertainty of 0.15% to the effective deuterium target thickness due to the estimated HD contribution. The only measurable source of contamination of the helium-3 target was tritium, and measurements by the Radiation Control Group at Jefferson Lab indicate that this was less 0.1%.

Since the target cans are cylindrical, beam offsets can also affect the effective target length. In particular, one finds that the effect from the 0.15 cm radius raster reduces the effective target length (as seen by the beam) by $\approx$ 0.1%. Optics data and information from the Beam Position Monitors indicate that the beam was offset by 1.5 mm (beam left facing downstream) relative to an "ideal" beamline. However, post run surveys show that the target cells were on average also about 1.3 mm offset in the same direction. Hence, it is assumed that in the worst case the

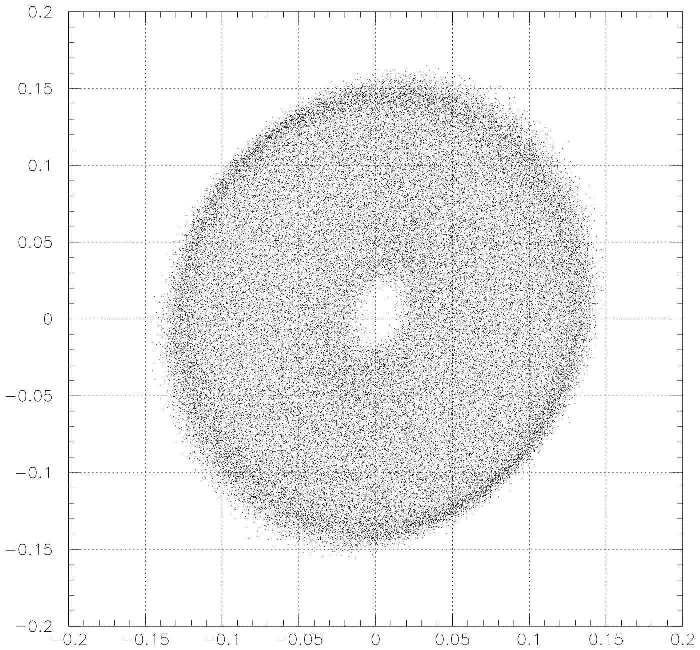

FIGURE 2.4. Electron beam raster pattern.

beam deviated from the center of the target can by 1 mm so that the net reduction of the effective target length is 0.15±0.1%.

In addition to the "static" uncertainties associated with the cryogenic targets, there ware also dynamic, target heating effects due to the energy deposited by the electron beam in the target material. The beam is rastered in a pancake type pattern (see Figure 2.4) to reduce these heating effects, however, they could not be eliminated entirely. The change in luminosity due to target heating was measured as a function of incident beam current and corrected on a run-to-run basis. For more details concerning the target heating correction, see Appendix A.

2.4. Spectrometers

One of the most critical pieces in an experiment of this nature is the detection of the particles of interest. Experiment E91003 made use of the two standard Hall C magnetic spectrometers. The Short Orbit Spectrometer (SOS) was designed and built to detect short-lived particles such as pions and kaons. This is accomplished by making the distance to the focal plane relatively short (about 10 m) in order to reduce decay losses. On the other hand, the High Momentum Spectrometer (HMS) has a greater distance to the focal plane ($\approx$ 25 m) making it more suitable for detection of electrons. (Of course, the HMS can and has been used for hadron detection - though in these cases the hadrons were at very high momentum such that it was not possible to use the SOS. Also, at higher momentum, decay losses are not such a large factor.)

2.4.1. High Momentum Spectrometer (HMS)

The HMS is a long focal length, 25^0 bend focusing spectrometer. It consists of three focusing quadrupoles and one momentum analyzing dipole (all magnets in the HMS are superconducting) with the focus perpendicular to the dispersive direction. The HMS was designed to have a large solid angle ($\approx$ 6-7 msr) with moderate momentum acceptance ($\approx \pm 10\%$). The maximum central momentum of the HMS is 7.4 GeV. Detectors are housed in a concrete shielding hut, about 25 meters from the pivot. The magnets and detector frame rest on a common carriage ensuring the detectors are stationary with respect to the optical axis. The HMS is shown in Figure 2.5.

The HMS dipole is set by field using an NMR probe inserted in the magnet, while the quadrupoles are set by current. Since the quadrupoles are

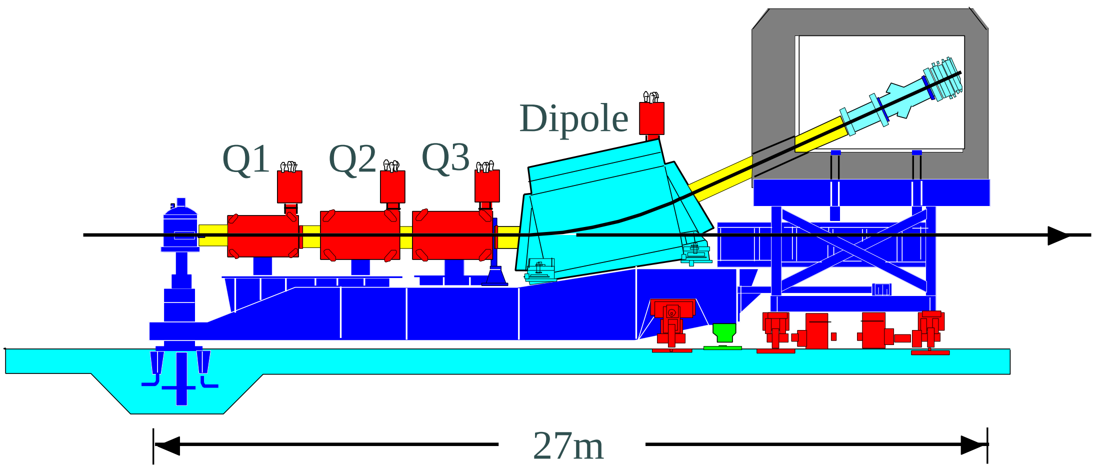

FIGURE 2.5. Side view of the HMS.

superconducting, hysteresis effects should be small (and in fact are found to be at the 10^{-3} level). These effects can be further minimized by cycling the quadrupoles such that the magnet is always on the same part of the hysteresis curve. For E91003, this cycling procedure consisted of ramping the magnets to 500 amps above the desired set current, and then ramping them down to the appropriate value. This cycling method results in fields reproducible to the 10^{-4} level. The fields in the quadrupoles are also monitored using Hall Probes, although these values are mostly used to check the relative field at the same set current (the Hall Probes were modified halfway through the run to correct a manufacturing defect so that they could not be reliably used as a monitor of the absolute field). After the completion of the experiment, it was noticed that there was a significant offset (up to a few tenths of a percent) in the third quadrupole (Q3) set current. A correction for this effect is applied in the analysis (see Section 3.1). However, to better model the acceptance effects, it is also simulated in the Monte Carlo of the experiment (and the same correction as used in the data reconstruction subsequently applied, as described in Section 4.3).

The HMS angular acceptance is set by an octagonal collimator mounted on the front of the first quadrupole. Three collimators were available (large, small, and HMS100[4]) in addition to a sieve slit collimator used for optics calibration. Experiment E91003 used the HMS100 collimator exclusively during production running. These collimators are made of 2.5 inch thick HEAVYMET (machinable Tungsten with 10% CuNi), flared along the inside edge to match the envelope of particles coming from the pivot. The collimator effectively stops all electrons that strike it, aside from those that may hit the inside flared edge and created a shower of particles. Such events are easily removed by tracking cuts.

Unfortunately, it was found after the completion of the experiment that the HMS100 collimator had a larger vertical acceptance than the sieve slit used for calibration. This means that events beyond a certain angle tend to reconstruct at the maximum sieve slit angle. This tends to somewhat distort the reconstructed distributions, but as long as one does not employ a strict cut near this region, the total number of events accepted should remain well understood. One could argue that this could also be accomplished by cutting in a region significantly smaller than the maximum sieve slit vertical acceptance, but even that would seem to be biased. The reconstructed events appear to cluster at the maximal sieve slit angle, but of course there may also be events that reconstruct to very small angle. It is difficult to predict how fitted reconstruction elements will behave outside the

[4]HMS100 refers to the fact that a new magnet configuration had been implemented just prior the E91003 sister experiment, E93021. To enable the HMS to reach more forward angles, the HMS quadrupoles were moved 40 cm further from the pivot. This necessitated the design and installation of a new collimator to maintain approximately the same solid angle as the old, HMS1 tune.

region of the fit. By allowing the collimator to determine the acceptance, we avoid errors coming from incorrect reconstruction.

More details of the optical properties of the HMS spectrometer and the HMS100 tune can be found in Ref. [27].

2.4.2. Short Orbit Spectrometer (SOS)

The Short Orbit Spectrometer consists of three resistive magnets in a QDD configuration. Like the HMS, the focus is transverse to the dispersive direction. The SOS was designed to have a large solid angle ($\approx$ 7 msr) in combination with a very large momentum bite ($\pm$20%). As its name implies, the distance to the detector hut is short, $\approx$ 10 meters. The SOS is designed with the ability to be raised up 20° out of plane, although this has never been done. In fact, the optical axis lies 0.15° below horizontal, the effect of which must be accounted for in the data analysis. The SOS is shown in Figure 2.6.

As the SOS magnets are resistive, care must be taken to always be on the same part of the hysteresis curve. The philosophy in this case is to fully degauss the magnets (for a given polarity) by; 1) cycling them to their maximum values at the chosen polarity, 2) setting the magnets to zero, 3) ramping the magnets to some empirically determined set value at the opposite polarity and then, 4) setting the magnets back to zero. From there, the field is set to the desired value. Subsequently, if the field is increased, the SOS need not be cycled, but a field decrease necessitates another degaussing cycle.

An additional complication arising from the resistive magnets is saturation at high fields (momentum). Analysis of elastic scattering from hydrogen indicates that the true central momentum of the spectrometer begins to deviate from the

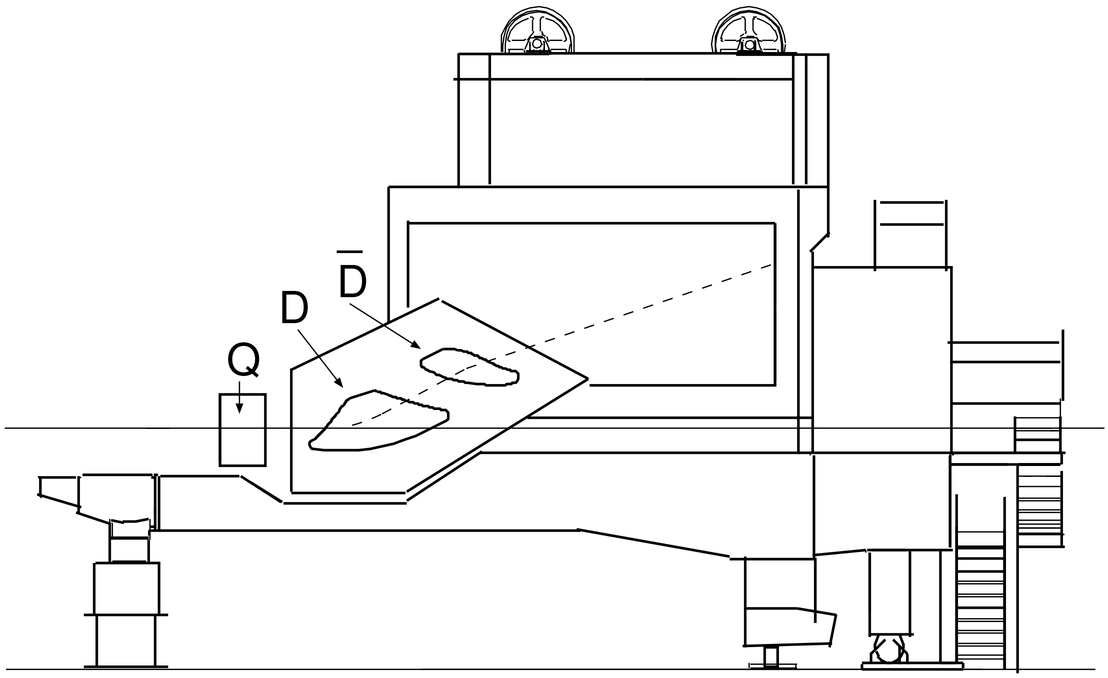

FIGURE 2.6. Side view of the SOS.

set value at about P=1.0 GeV/c and is on the order of 0.6% low at the maximum momentum of 1.6 GeV/c (see Figure 2.7). For E91003 kinematics, the true SOS central momentum is about 0.45% higher than the nominal set-point. This deviation is taken into account in the data analysis.

As with the HMS, the SOS angular acceptance is set by a HEAVYMET (2.5 inch thick) octagonal collimator. Experiment 91003 used the larger of the two available collimators, in addition to the sieve slit (similar to that in the HMS) for calibration. An additional complication arises from the fact that a significant fraction of the pions impinging on the collimator can pass through after undergoing only Coulomb multiple scattering, thus preventing the collimator from truly setting the SOS acceptance. This effect is accounted for and will be described in Section 4.6.

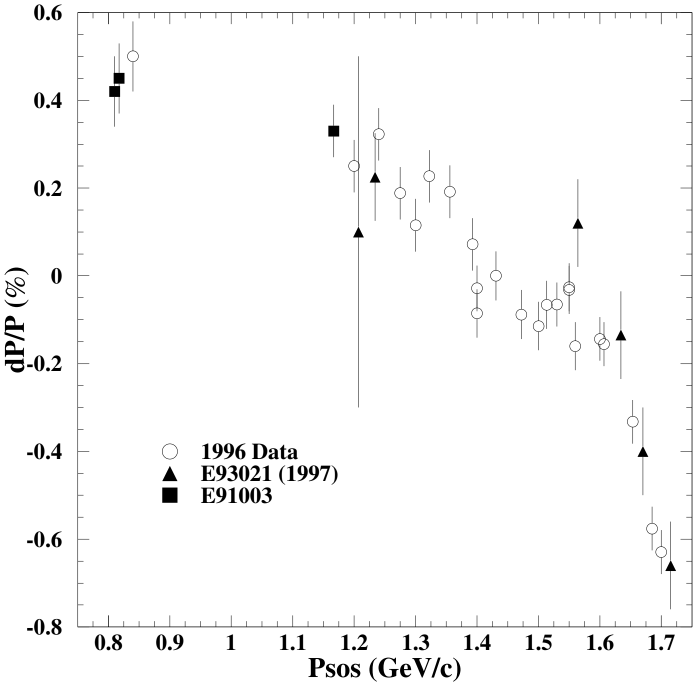

FIGURE 2.7. SOS central momentum saturation correction. Uncertainties on the 1996 and E91003 points are from errors in peak fitting only. Errors on the E93021 points include additional systematic effects.

2.5. Detector Package

The HMS and SOS detector packages are very similar, consisting essentially of a pair of drift chambers for tracking, four planes of scintillating hodoscopes for triggering and time-of-flight measurements, and threshold gas Čerenkov detectors and lead-glass calorimeters for particle identification. The SOS also has been outfitted with Aerogel and Lucite detectors when used for kaon detection - these were not present during E91003. The general layouts of the detector packages inside the spectrometer huts are also quite similar (see Figures 2.8 and 2.9). The drift chambers are positioned immediately after the analyzing magnets at the front of the hut followed by a layer of x and y oriented scintillator planes. The gas Čerenkov is positioned between the two pairs of x-y scintillators, while the lead glass calorimeter is positioned at the back of the hut. In the SOS, the y scintillators precede the x scintillators, while in the HMS the order is reversed.

What follows is a brief discussion of each of the detector components for the purposes of making the explanation of the data analysis (in Chapter 3) more clear. For more complete descriptions of the detector package including the detailed geometry and performance, see Ref. [28].

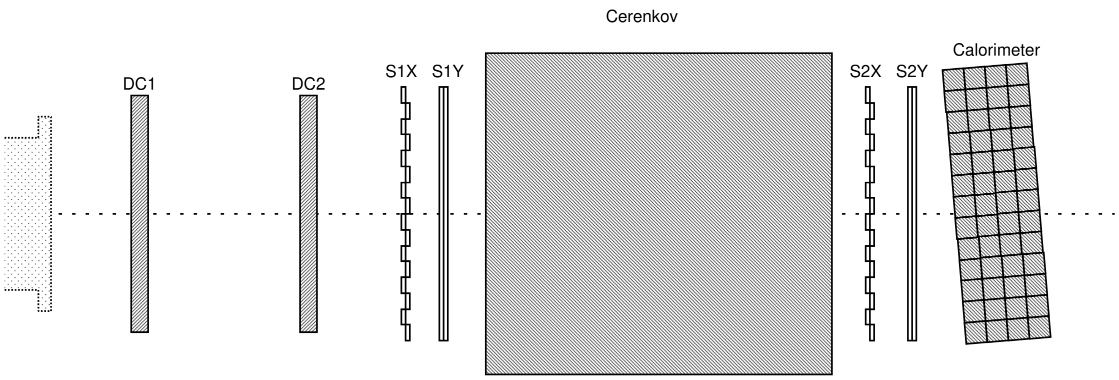

FIGURE 2.8. Detector layout in the HMS.

2.5.1. Drift Chambers

The principle of operation of particle tracking drift chambers is as follows. A chamber is filled with some gas mixture, while some number of layers of field and sense wires are also positioned inside the chamber. When a charged particle

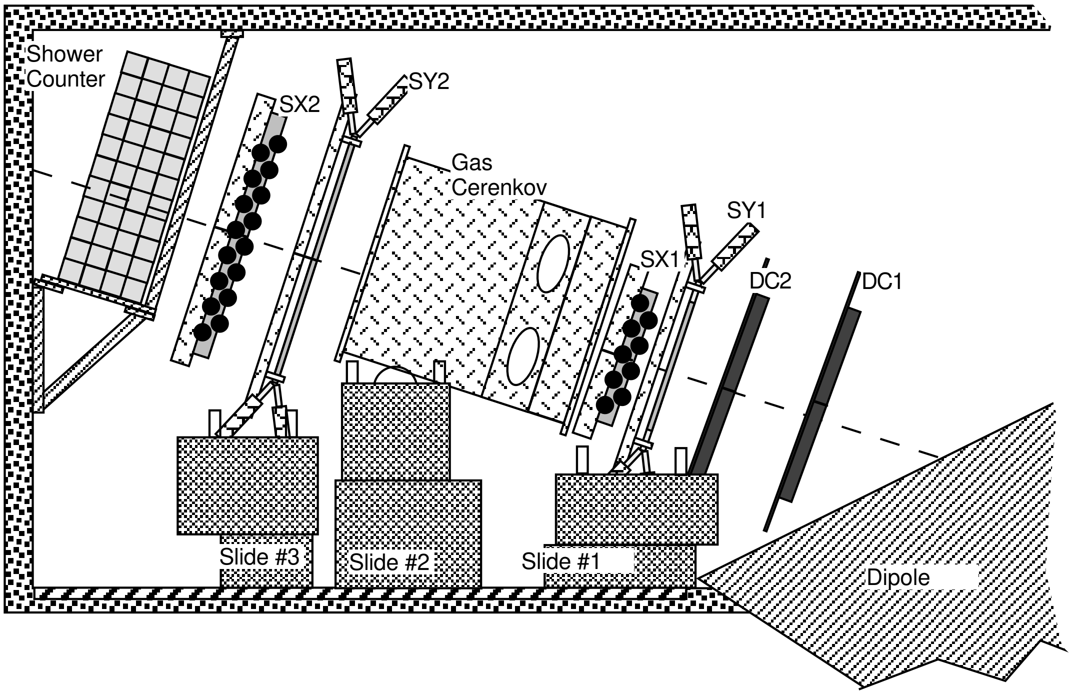

FIGURE 2.9. SOS detector hut.

traverses the chamber, the gas (or gas mixture) is ionized. The ionized electrons are then accelerated due to some (negative) potential difference between the sense and field wires - these electrons are then detected at the sense wires and read out as a current over some period of time. While the wire spacing itself gives some information regarding the trajectory of the track, the large wire spacing limits the precision. However, timing information (with respect to the trigger) can be used to increase the precision. If one measures the time that it took for the ionized electrons to reach the sense wires, one can then convert this to a distance and determine how far the track of a charged particle was from a given wire.

The two HMS drift chambers consist of six planes each. Two planes measure the dispersive direction (the x and x' planes), while two measured the non-dispersive direction (y and y'). The last two planes are rotated $\pm$ 15° with respect to the x and x' planes - these are called the u and v planes. Each plane consists of a set of alternating field and sense wires (each sense wire separated from the next by about 1 cm), with the field wires maintained at some large negative high voltage ($\approx$ 2000 V). In addition, guard wires are used to create a roughly equipotential surface about each sense wire, its voltage dependent on its distance from the nearest sense wire. The ionizing gas used in the HMS chambers is an equal parts Argon-Methane mixture controlled by a gas mixing system located above the experimental hall.

The track for a given particle is constructed using the hits from each plane in addition to the distance of the particle passed from each wire (the so-called drift distance). Using the hits in all six planes allows one to determine on which side of the sense wire the particle passed. For matched planes (x and x', y and y'), a small angle approximation is used, and for planes that measure the same position but for different (but adjacent) wires, the track is assumed to have passed between the two wires. Where the determination is ambiguous (i.e. for the u and v planes which are unmatched or when one of the matched planes does not have a hit) the track with the smallest χ^2 is taken.

The SOS drift chambers are in principle very similar to the HMS drift chambers, but differ in the details of their construction. Each SOS chamber also consists of six planes of wires. Like the HMS, two measure the dispersive direction (x and x'). The u and u' planes are rotated 60° clockwise to the x planes and the v and v' planes are rotated 60° counterclockwise to the x planes. The SOS chambers use the same gas mixture as the HMS. In this case, since all the planes are matched, the track determination does not suffer from the same problems as the HMS.

2.5.2. Hodoscopes

The HMS and SOS both contain four planes of hodoscopes arranged in two x-y planes. Each plane consists of a number of elements - each element being a long narrow strip of BC404 scintillator. A charged particle traversing the scintillating material will ionize electrons, these electrons in turn exciting the scintillating material to higher molecular energy states, the material consequently emitting light upon spontaneous de-excitation. The light then propagates down the material - any light emitted at an angle greater than the critical angle will be internally reflected. Each element is read out on both ends with a photomultiplier tube attached to a piece of lucite light guide. Each element is made light tight by wrapping it in some kind of reflecting material (aluminum foil in the HMS and aluminized mylar in the SOS) followed by one or two layers of (black) Tedlar. The scintillator paddles themselves are 1.0 cm thick and 8.0 cm (4.5 to 7.5 cm in the SOS) wide (the length depending on spectrometer and location within the hut). The elements are arranged such that there is a 0.5 cm overlap between neighboring scintillators.

The SOS hodoscopes are arranged in two pairs of planes - the front two planes separated from the back two by about 1.8 m. Each pair consists of a vertically oriented y-plane and a horizontally oriented x-plane. In the HMS, the arrangement is similar, except that the ordering within each pair is horizontal-vertical (x-y) with a separation of 2.2 m. The SOS timing resolution per plane is slightly better than the HMS due to reduced attenuation in the shorter scintillator elements, however the overall timing resolution is similar due to the smaller separation between the front and back pairs in the SOS.

In the counting house, hodoscope signals are sent to Analog to Digital Converters (ADCs), as well as discriminators and on to Time to Digital Converters (TDCs), scalers and (trigger) logic modules.

Timing information from the scintillators must be corrected for pulse height and timing offsets in each element. For example, a minimum ionizing pion will deposit less energy than a slow proton. Since the electronics use constant threshold discriminators, the proton timing information will be biased to lower time values. These effects are corrected for using an offline calibration routine developed for SLAC experiment NE18, and modified for use with the Hall C spectrometers. More details regarding time of flight fitting can be found in Ref. [29].

2.5.3. Čerenkov Detectors

The HMS and SOS each contain a threshold gas Čerenkov typically used for electron/pion identification and separation. Each detector monitors the radiation emitted when a charged particle traverses the medium (with index of refraction n) in the detector with velocity (β) which is faster than the speed of light in that medium (c/n). The light will be emitted with an angle $cos\theta_c = 1/n\beta$, which for fast particles and n close to one is a very small angle. This light is then reflected from focusing mirrors to photomultiplier tubes.

In each detector, the medium was chosen so as to allow electron detection and discrimination from pions over the momentum range of interest (a few hundred MeV/c to several GeV/c). It is still possible for a pion to be misidentified as an electron if it produces a knock-on δ ray that subsequently fires the Čerenkov detector. As will be shown later (in Chapter 3), this was not a significant effect for this experiment.

The SOS Čerenkov detector is filled with one atmosphere of Freon-12. Freon-12 has an index of refraction of 1.00108 giving an electron threshold of 11 MeV/c and a pion threshold of 3 GeV/c (greater than the SOS maximum central momentum of 1.7 GeV/c). The gas pressure is maintained by a solenoid valve that releases freon in the case of overpressure and will let freon into the detector in the case of underpressure.

The HMS Čerenkov is similar to the SOS detector, except that it was designed with the capability to run with the gas in the tank above or below atmospheric pressure (of course it could run at atmospheric pressure as well). This means that in addition to being used for π/e separation at atmospheric pressure, it could be used to separate pions from protons using Freon-12 at two to three atmospheres. During experiment E91003, the HMS Čerenkov used C_4F_{10} at 0.42 atmosphere. The index of refraction at this pressure is 1.0006 giving an electron threshold of 15 MeV/c and a pion threshold of 4 GeV/c.

2.5.4. Lead Glass Calorimeter

The lead glass calorimeter was not used for the actual analysis of E91003 data, however, it played an important role in testing Čerenkov efficiencies and searching for μ that resulted from π decays.

The SOS and HMS each has a lead glass calorimeter positioned at the back of the respective detector huts. Each lead glass calorimeter consists of four layers of 10 cm $\times$ 10 cm $\times$ 70 cm blocks stacked 13 (11) high in the HMS (SOS).

Photomultiplier tubes are attached to each block at one end and each block is wrapped in aluminized mylar and Tedlar to make them light tight.

Electrons entering the calorimeter undergo Bremsstrahlung radiating photons. These photons in turn form positron-electron pairs that radiate additional photons. Eventually a shower of particles is formed and the light radiated by the charged particles is detected by photomultiplier tubes on one end of the calorimeter. Electrons and positrons will deposit all of their energy in the calorimeter while pions and muons will deposit (approximately) a constant amount of energy per layer. Looking at the normalized energy deposited in all layers, one can separate electrons from other particles. One caveat, though, is that pions can also undergo nuclear interactions in the lead glass. This can lead to a shower similar to those created by electrons or positrons. The pion signal at low normalized energy deposition then, has a long tail that extends under the electron peak. For that reason, the lead glass calorimeter is typically not used alone, but in conjunction with the Čerenkov detector. Furthermore, the calorimeter becomes inefficient at low momentum ($\approx 95\%$ at $P_{central} \approx 500$ MeV/c) [30]. Since much of the E91003 data was taken at low momentum in both the HMS and SOS, and the Čerenkov detectors were determined to provide adequate particle identification, the calorimeter was not used during the analysis phase.

2.6. Trigger

A key element in an electroproduction experiment of this nature is the event trigger. The net rate of particles entering the spectrometers can be quite large and one needs to discriminate real events from events that are partially accepted (i.e. give signals in one or more detectors but not enough to be a good event). A good trigger balances discrimination with high efficiency. In Hall C, the HMS and SOS each have their own event selection criteria. Once passed, a so-called singles pretrigger is formed. In coincidence mode, pretriggers from the HMS and SOS that arrive within a certain timing window are accepted and the event read out (modulo computer dead time effects).

2.6.1. HMS (Electron) Pretrigger

Various hardware signals from the HMS detector stack are used to form the HMS pretrigger. These signals are converted to NIM pulses and sent to various logic units to test for a valid event. The logic of the HMS pretrigger is shown in Figure 2.10.

The scintillators form the main part of the HMS pretrigger. A pretrigger can proceed along two paths, ELHI and ELLO, both of which include the SCIN signal. SCIN is satisfied when three out of the four layers of scintillator planes gives a signal (within a timing window of about 100 ns). While requiring four out of four layers would give a cleaner signal, it increases the likelihood that problems in one particular hodoscope paddle could affect the overall trigger efficiency. Since a normally functioning paddle is quite efficient, the probability of three out of four planes firing is quite large, even if one paddle is totally dead (this is not to say that dead paddles are not promptly repaired). The "3/4" signal also allows online monitoring and offline calculation of hodoscope efficiencies.

An ELHI signal is formed when one has all three of the following: 1) the SCIN signal described above, 2) the PRHI signal, or 3) the SHLO signal. The PRHI signal is formed when the signal from the first layer of the calorimeter is

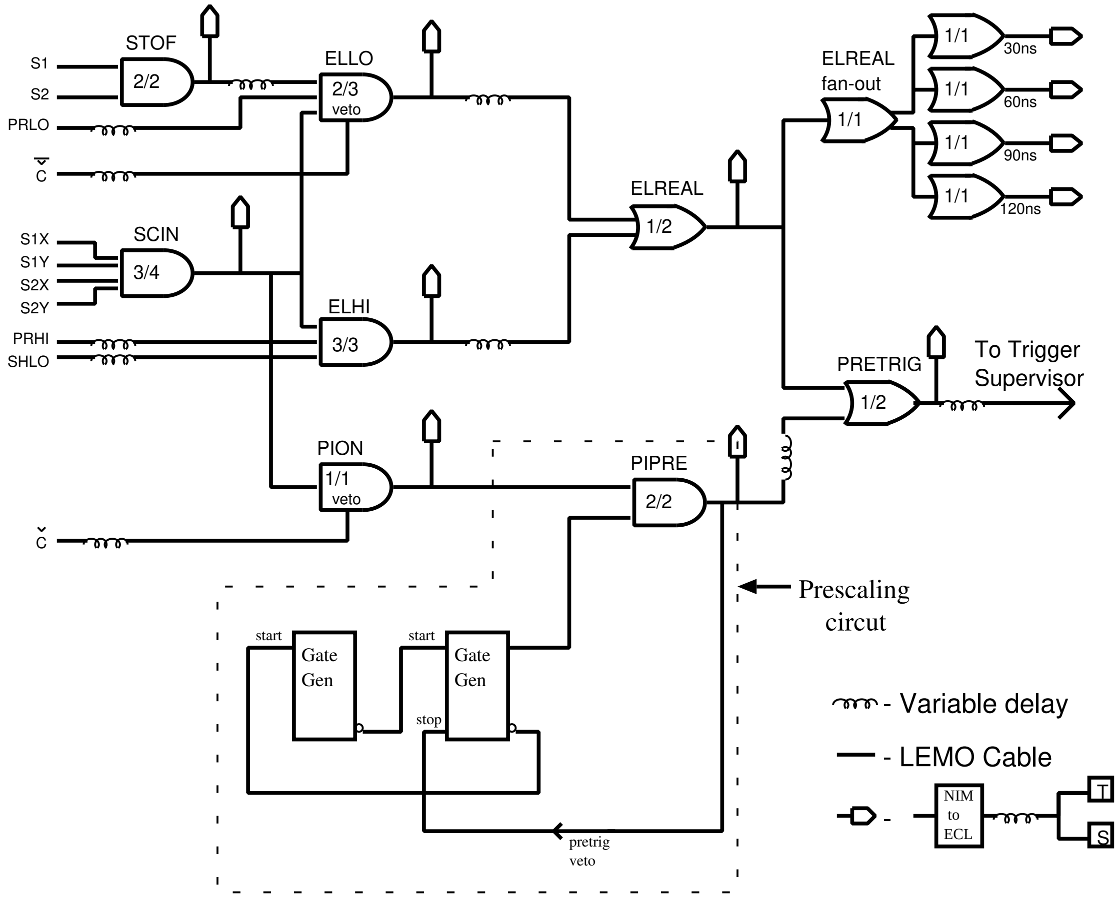

FIGURE 2.10. HMS pretrigger logic diagram. The signal marked HMS PRETRIG is sent to the trigger supervisor to check for coincidence with the SOS. Signals marked EL30, EL60, EL90, and EL120 are used to measure the electronic dead time.

above a certain (high) threshold, and the SHLO signal is formed when the total energy deposited in all four layers of the calorimeter is above some threshold.

An ELLO signal is formed from two of three of: 1) SCIN, 2) the PRLO signal, and 3) the STOF signal. The PRLO signal is formed when the energy deposited in the first layer of the calorimeter is above a certain (low) threshold. STOF is satisfied when there is at least one scintillator plane hit in both the front and back pairs on hodoscopes. This is the minimum number required to fit the time of flight of the particle (hence its name). Note that STOF only requires two planes to be hit, but there must be one in front and one in back. The ELLO also requires a Čerenkov signal to be present; if it is not, the event is vetoed.

The OR of ELHI and ELLO is taken to form ELREAL. The ELREAL signal is then sent to the PRETRIG module where it is ORed with a signal called PIPRE. The purpose of the PIPRE signal is to ensure that some small sample of pions is accepted for the purposes of testing the particle identification efficiencies of the Čerenkov detector and the calorimeter. The PIPRE signal was disabled during E91003. The ELREAL signal is also sent to four signals (EL30, EL60, EL90, EL120) which are used to measure electronic dead time.

During E91003, one of the kinematic settings was taken at quite low momentum (0.4 GeV/c) in the HMS. Since the efficiency of the calorimeter suffers at such low energies, the HMS pretrigger was altered by removing the requirement of a Čerenkov signal in ELLO. This meant that if there was some hardware problem in the Čerenkov detector and PRLO failed to fire (which was likely at such a low momentum), one could still get a valid ELLO signal. Some sample of runs was taken with and without the Čerenkov requirement at 0.4 GeV/c and no discernible difference was found.

2.6.2. SOS (Pion) Pretrigger

The E91003 SOS pretrigger configuration is much simpler than in the HMS. In essence, the SOS pretrigger consists of just the SCIN signal (three out of four scintillator planes) described above. The SOS pretrigger is shown in Figure 2.11.

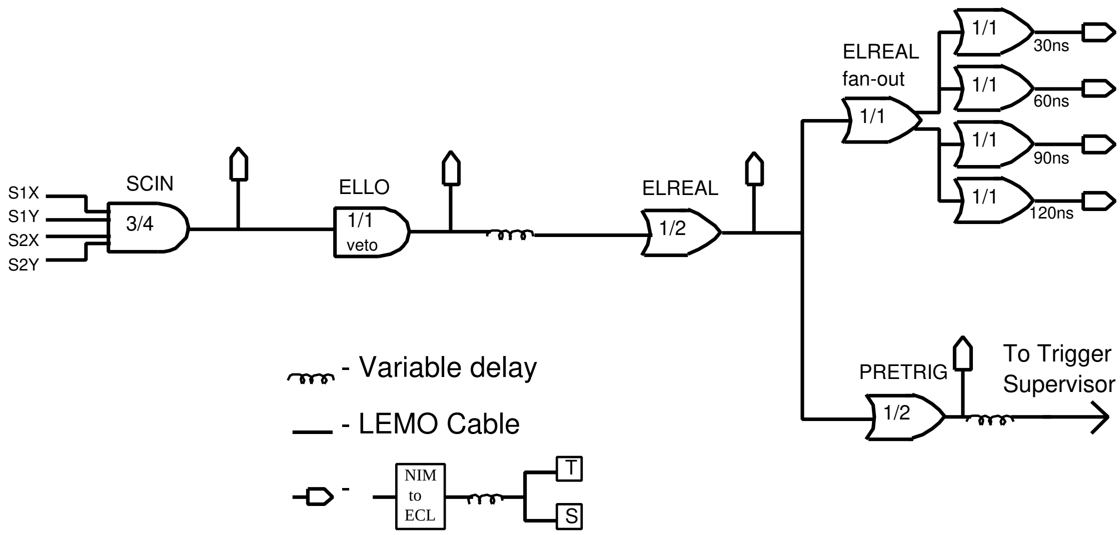

FIGURE 2.11. SOS pretrigger logic diagram. The signal marked SOS PRETRIG is sent to the trigger supervisor to check for coincidence with the HMS. Signals marked EL30, EL60, EL90, and EL120 are used to measure the electronic dead time.

Since the SOS was used to detect pions, the electron particle identification signals (like the shower counter and Čerenkov) used in the HMS (electron) pretrigger were not used. In theory, a Čerenkov veto could have been used to reduce positron or electron contamination, but these backgrounds were small enough at E91003 kinematics that they contributed little to the computer dead time. Protons, on the other hand, were a significant background, but no efficient method for cutting out protons at the trigger level existed.[5]

[5] At the low pion momentum setting, background protons were so slow that only a small fraction of them were able to form a valid SCIN (3/4) signal due to the 100 ns window. So there was actually an unplanned time-of-flight cut implemented at the trigger level.

The SOS pretrigger uses the same basic logic setup as in the HMS, but various tests are disabled to form a much looser trigger. As in the HMS, the SCIN (3/4) signal is sent to the ELLO module. However, in this case, all other inputs to ELLO are disabled and the coincidence level is set to one. The ELLO signal is then sent to ELREAL, which is split and sent to the SOS PRETRIG and EL30, EL60, EL90, and EL120 for electronic dead time measurements.

2.6.3. Coincidence Trigger

Once a valid pretrigger from the HMS and/or SOS is formed, it is sent to an 8LM LeCroy programmable logic unit. The 8LM has six inputs and is used to classify the event type before sending the signal on to the Trigger Supervisor. The Trigger Supervisor then controls the actual readout of the ADCs and TDCs from the event. A diagram of the 8LM and Trigger Supervisor signals is shown in Figure 2.12.

In addition to the HMS and SOS pretriggers, the 8LM also receives input from the PED PRETRIG signal. This signal is read out for the first 1000 events of each run to determine the pedestals for the ADCs. The Trigger Supervisor sends three signals back to the 8LM to indicate its status. The first, TS GO, is active anytime a run is in progress while the second, TS EN1, is active after the pedestal events have been taken; this indicates normal data taking. The third Trigger Supervisor signal, TS BUSY, is active when the Trigger Supervisor is busy processing an event and cannot take another.

The programming of the 8LM is shown in Figure 2.12. There are eight outputs determined from various combinations of the six inputs. The HMS PRE and SOS PRE signals are always present during normal data taking. The HMS TRIG

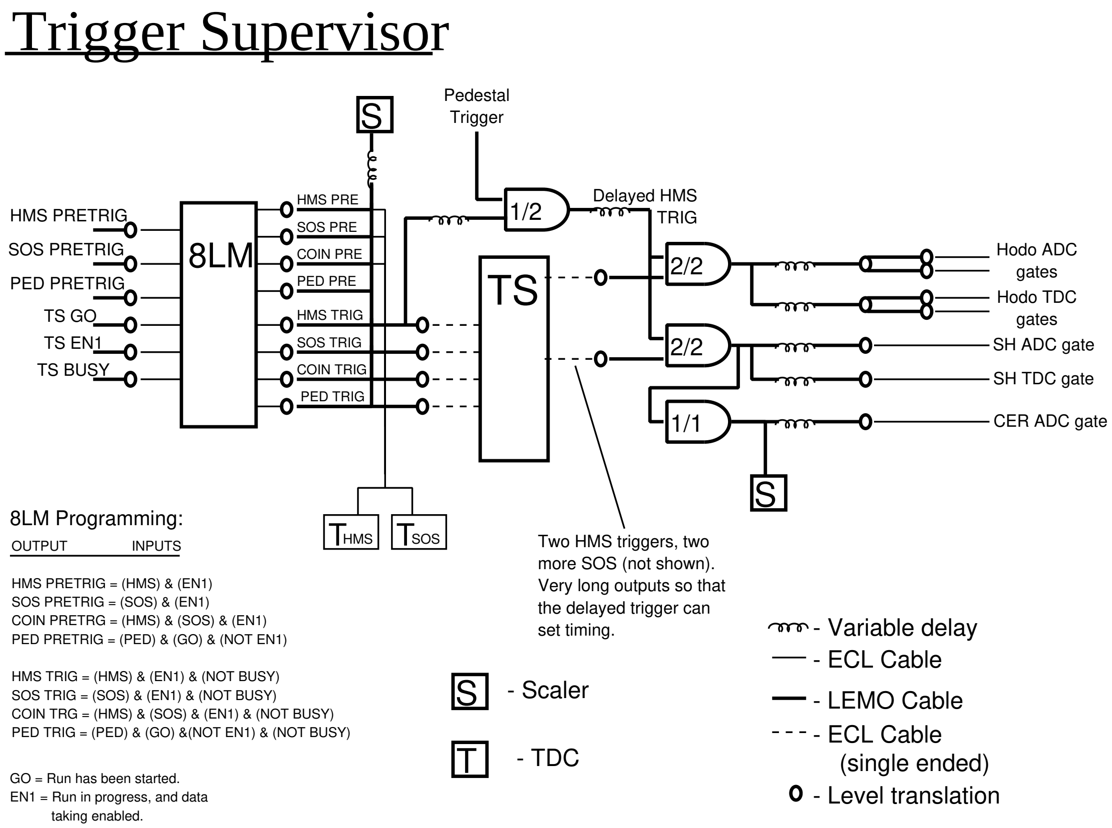

FIGURE 2.12. 8LM, Trigger Supervisor, and associated coincidence trigger signals.

and SOS TRIG signals are present during normal data taking only if the Trigger Supervisor is not busy. A coincidence pretrigger (COIN PRE) is formed when the HMS PRETRIG and SOS PRETRIG inputs overlap. During E91003, the HMS PRETRIG width was ≈40 ns while the SOS PRETRIG width was 20 ns creating an effective coincidence window of ≈60 ns. The COIN TRIG (like the HMS and SOS TRIG) is active when the Trigger Supervisor is not busy. Note that the PRE signals are read out to scalers even when the Trigger Supervisor is busy so that one can keep track of the computer dead time.

The TRIG signals are then sent to the Trigger Supervisor. It is possible at this point to reject (or prescale) singles events that have only HMS or SOS TRIG signals with no COIN TRIG signal. This is useful for reducing computer dead time (although in many cases the dead time was low enough that there was no reason to prescale away all the singles). When the Trigger Supervisor receives a COIN TRIG (either HMS or SOS), it puts out two long (100 μs or until the event is finished, whichever comes first) pulses for the HMS and SOS. These pulses are ANDed with the (HMS or SOS) TRIG signal that was split off after the 8LM and the resulting signal sent to enable the ADC readouts and begin the TDC starts. This "retiming" step is neccesary to ensure that the timing of the individual spectrometer readouts is set by that spectrometer, and not by the other (which can be the case if the coincidence trigger is used to enable the readouts). Two measurements of the coincidence are also made at this point. The first is started by the HMS (the HMS retimed trigger and the long trigger supervisor output) and stopped by the SOS TRIG, while the second is started by the SOS and stopped by the HMS.

2.7. Data Acquisition

The data acquisition (the recording of data as well as the user interface) was handled by the CODA (CEBAF Online Data Acquisition) software package [31] run on a Hewlett-Packard 9000 workstation. Data for each run was written directly to disk and consisted of three types of events: 1) detector information handled by the ADCs and TDCs, 2) scaler information, and 3) information from the EPICS database.

The ADCs and TDCs (as well as the scalers) were located in FASTBUS and VME crates. These crates had their own ROC (Read Out Controller) CPUs that were read out over an FDDI (fiber optic) network. The ADCs and TDCs were read out for each event while the scalers were read every two seconds. The EPICS database contained information such as magnet settings, beam position, and target temperature and pressure. These slowly varying quantities were read out every thirty seconds.

FASTBUS data was acquired in spasified mode, ie., only non-zero data was read. The ADCs are sparsified by setting a programmable threshold about fifteen channels above zero. For each run, a thousand zero (or pedestal) events were acquired. These events can be used to set the programmable zero via the data acquisition software and check that the zero is not drifting run by run. TDCs are more simply sparsified by not recording events that had no stops.

3. DATA ANALYSIS

Once the raw signals from the data acquisition have been recorded, the task of interpreting those signals and transforming them into tracking and particle identification information remains. For experiment 91003, this is accomplished in two stages. The first step entails the use of the standard Hall C analysis code, the replay ENGINE. The replay ENGINE takes care of converting the raw detector signals to detector summary quantities for each event. These include particle identification signals such as photoelectron numbers from the Čerenkov detectors and time-of-flight information as well as tracking information. Further, the ENGINE keeps track of various scaler quantities (i.e. quantities not necessarily associated with a particular track) like charge and tracking efficiency. E91003 uses the Hall C ENGINE to create a set of files that consists of mostly detector quantities as well as track quantities (trajectory and position at the focal plane of the spectrometer). A second, stand-alone program is then used to further process the tracks and calculate reconstructed quantities (like scattering angle at the target) and physics quantities (missing mass, Q^2, etc.). This separation of the analysis into two stages has the advantage of allowing one to modify cuts, reconstruction coefficients, and kinematic offsets without having to do a complete replay (which can be quite time consuming).

3.1. Tracking and Reconstruction

The determination of a particle's trajectory and momentum at the target can be broken into two major steps - finding the trajectory in the detector hut and then transforming that trajectory back to the target. The first part is done using the two drift chambers in each spectrometer. Each chamber has six planes of wires and the tracking algorithm requires that at least five planes in each chamber have a "hit". Intersections of hit wires determine "space points", and the space points in each chamber are used to form "stubs", or small tracks. The tracking algorithm performs a χ^2 minimization to fit a straight line through both chambers with the requirement that the resulting track is consistent with the stubs in each chamber. In the case where multiple tracks are found, the one with the smallest χ^2 is chosen. The fit track is then projected to the detector focal plane (halfway between the two drift chambers - hereafter simply the focal plane) and the position (x_{fp} and y_{fp}) and trajectory (x'_{fp} and y'_{fp}) are determined.

Given the four spectrometer coordinates, a matrix transformation is then used to determine the relevant target coordinates. The transformation is of the form,

$$x^i_{tar} = \sum_{j,k,l,m} M^i_{jklm}(x_{fp})^j(x'_{fp})^k(y_{fp})^l(y'_{fp})^m \, . \tag{3.1}$$

The sum over j, k, l, m is constrained such that

$$j + k + l + m \leq N \, , \tag{3.2}$$

where N is the order of the transformation. For the HMS, N=5 and for the SOS N=6. The reconstructed target quantities are as follows. x^1_{tar} is x'_{tar}, the out of plane scattering angle[1] at the target. x^2_{tar} is y_{tar}, the in-plane position of the event as seen by the spectrometer. x^3_{tar} is y'_{tar}, the in plane scattering angle relative to the spectrometer central angle. Finally, x^4_{tar} is δ, the fractional momentum deviation from the spectrometer central momentum. Note that the reconstruction matrix

[1]Actually, the primed quantities are really slopes, i.e. $x'_{tar} = \frac{dx}{dz} = \tan\phi_{spec}$. However, the spectrometer acceptance is small enough (generally less than 100 mrad) such that the difference between the slope and angle is at most 0.33%. Hence, common usage is to call the primed coordinates angles.

elements give no information about the out of plane position of the event at the target, x_{tar}. This is generally taken to be zero, or the deviation from zero to be given by the fast raster information.

The reconstruction matrix is fit using an iterative process in which one starts with a COSY INFINITY model [32] of the spectrometer optics. The matrix is then optimized using data taken especially for that purpose. For example, one uses data taken with a point target in combination with the sieve slits described in Section 2.4 to fit x'_{tar} and y'_{tar}. The starting model is used to determine which hole in the sieve slit an event passed through and the optimization routine [33] modifies the matrix such that the events reconstruct to that hole position. y_{tar} is fit using the optics target described in Section 2.3 and δ is fit using so-called δ scans of elastic electron scattering from carbon. Of course the optimization procedure often takes many cycles, optimizing x'_{tar} and y'_{tar} for each value of y_{tar}, etc.

The details of the HMS matrix element fitting can be found in Chapter 4 of Ref. [27]. These matrix elements were fit using optics data taken during experiment E93021 (the experiment immediately prior to E91003), the first experiment to use the new HMS100 tune. For the SOS, matrix elements fit from optics data taken in 1996 are used. More recent SOS optics data had been taken during E93021, however, these data were taken at $P_{SOS} \approx 1.4$ GeV/c, well into the SOS saturation region (see Section 2.4.2). This resulted in aberrant behavior of the matrix elements away from the momentum at which the elements were fit. On the other hand, the 1996 optics data were taken at $P_{SOS} \approx 0.9$ GeV/c. Since the saturation effects are fairly flat up to $P_{SOS} \approx 1.0$ GeV/c and all E91003 data points are at or below that momentum, the 1996 elements are more appropriate for this analysis. This is born out in the absence of the aberrant behavior seen in the newer matrix elements. It should be noted that there is no reason to expect the SOS optics to have changed

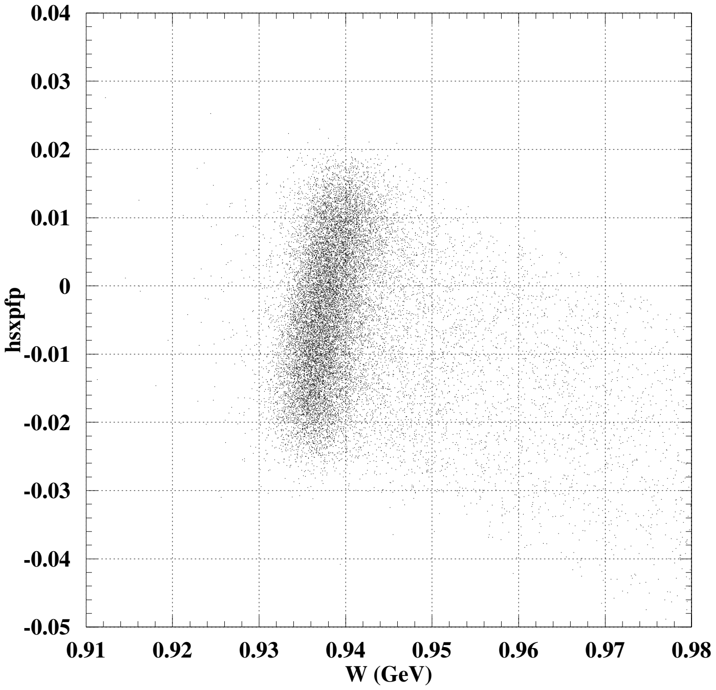

FIGURE 3.1. Reconstructed invariant mass, W, from elastic (e, e') plotted vs. HMS x'_{fp} $(hsxpfp)$ at $P_{HMS} = 0.5379$ GeV/c. W should reconstruct to the proton mass independent of target and focal plane variables, however, the centroid of the elastic peak varies by about 5 MeV over the range of x'_{fp} accepted.

between the taking of the 1996 data and E91003 so long as one accounts for any drift chamber position shifts that may have occurred in the interim.

A useful way to check the fitted matrix elements is to use elastic electron singles to look for correlations between reconstructed invariant mass and focal plane or target variables. It was found that just such a correlation exists in HMS x'_{fp} (see Figure 3.1) and that the correlation changes with the HMS central momentum. The effect is corrected by fitting an ad-hoc correction of the form

$$\delta_{corrected} = \delta + C_\delta \times hsxpfp\,. \tag{3.3}$$

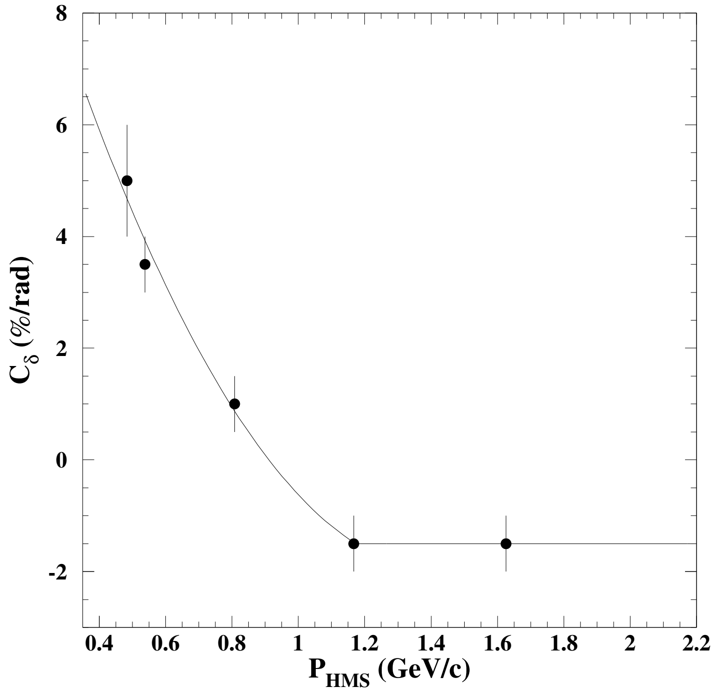

FIGURE 3.2. HMS $(\delta, hsxpfp)$ correction (C_δ) as a function of HMS central momentum.

The correction factor, C_δ, is fit for a number of values of P_{HMS} and a continuous function is then fit to parameterize the momentum dependence of the correction (see Figure 3.2). This correction is applied to the reconstruction of all data analyzed in this experiment. While the ad-hoc correction eliminates most of the correlations, there still remain some higher order effects, especially at lower HMS central momentum. It was discovered that the likely cause of these effects is an offset in the field of the third HMS quadrupole (Q3). This discovery enables the modeling of the effect in the Hall C Monte Carlo - hence any residual higher order correlations can be accounted for in the comparison of the data to the simulation. Further details of the simulation of this effect can be found in Section 4.3.

3.2. Time of Flight

Time of flight information is critical in the analysis of E91003 data in order to separate positively charged pions from protons. The time of flight, or conversely the particle velocity, is determined using the four layers of scintillating hodoscopes in the detector stack. The raw time that a given hodoscope paddle is hit is recorded relative to a common start. This raw time is then corrected for pulse height and shape, propagation of the scintillation light through the hodoscope paddle to the PMT, and timing offsets due to cable length differences etc.

These pulse height and propagation time corrections are fit as follows. A "pure" sample of events is analyzed in which only information concerning the particle of interest (in this case pions) is retained. In this case, a sample of negatively charged pions is used since electrons can easily be removed from the sample using the gas Čerenkov. Given that the particle sample is all pions, the particle velocity can be calculated using the reconstructed momentum of the particle,

$$\beta_p = \frac{|\mathbf{p}|}{E} = \frac{|\mathbf{p}|}{\sqrt{|\mathbf{p}|^2 + \mathbf{m}_\pi^2}}. \tag{3.4}$$

Since the distance between hit paddles is known, the timing coefficients and offsets can be adjusted so that the resulting velocity as calculated from the time of flight information, β_{tof}, is optimized to agree with the velocity as calculated from the momentum information, β_p. A sample β_{tof} spectrum is shown in Figure 3.3.

After completion of the running of the experiment, it was found that two of the PMTs in the SOS hodoscope array were erratic. These PMTs gave no signal for some subset of runs, resulting in a faulty calculation of the time of flight. One bad PMT was found prior to analysis of the data and one after. The first erratic PMT (in the SOS 2Y plane) was removed from the time of flight calculation in software. Since the time of flight calculation uses, but does not require, signals

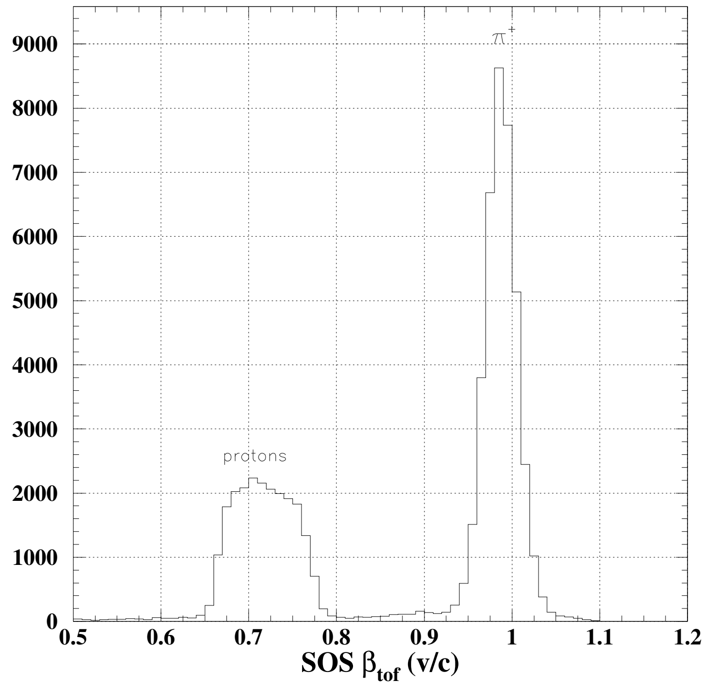

FIGURE 3.3. Sample SOS β_{tof} spectrum at $P_{SOS} = 1.0$ GeV/c.

from the PMTs on both ends of the paddle, time of flight information is still available for that paddle. The second bad PMT (in the SOS 2X plane), since it affected a smaller subset of runs than the first and had a less dramatic effect on the calculated velocity, was not found until after the data had been run through a full "replay". In order to truly remove the effect of this second PMT on the β_{tof} calculation, another time consuming replay would have been necessary. On the other hand, since the effect manifests as a nearly constant offset in β_{tof}, it is possible to partially correct for the effect in the secondary "recon" analysis. In this case, one need merely project the tracks to the location of the paddle with the bad PMT, and adjust the mean β_{tof} by hand (see Figure 3.4). While some

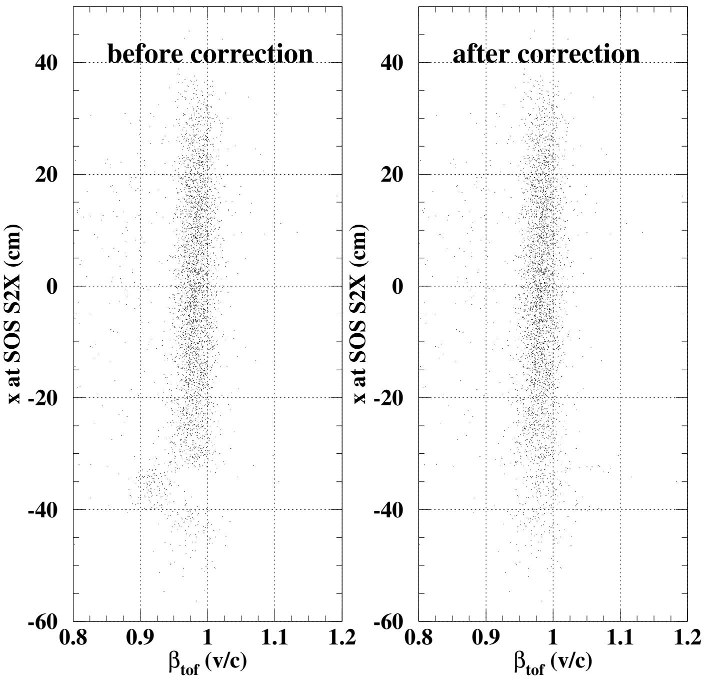

FIGURE 3.4. Position at the 2X hodoscope plane of the SOS vs. β_{tof}. The x position vs. β_{tof} is plotted both before, and after the "by-hand" correction described in the text. The paddle with the bad PMT is evident in the before picture at $x \approx -35$ cm. Note that the correction moves some of the events in the paddle overlap region to high β_{tof}. However, since there are no upper limits on the β_{tof} cut used in the analysis, no good events are lost.

of the events in the hodoscope paddle overlap region will be corrected to much higher values of the velocity, one need only to make sure to place a larger upper bound on the time of flight cut[2] (or none at all since the purpose of the cut is to eliminate protons, which only requires a lower limit). Since the cut efficiency with

[2]The time of flight cut used in the analysis was not on β_{tof} directly but on $\beta_{tof} - \beta_p$, but the idea is the same.

the "by-hand" correction is found to be comparable to that in other parts of the acceptance, and since the pion distributions are not peaked in the region of the acceptance with the bad PMT, it was decided that the "by-hand" correction is sufficient. Due to the good agreement between the cut efficiency in the vicinity of the bad paddle and the overall cut efficiency, no extra uncertainty is assigned for the "by-hand" correction.

3.3. Particle Identification and Event Selection

3.3.1. Electron Identification

Identification of electrons in the HMS is straightforward and is done entirely with the HMS gas Čerenkov. The HMS Čerenkov has been studied previously and has been found to be highly efficient. In particular, Ref. [30] found the HMS Čerenkov electron efficiency to be better than 99.4% for a photoelectron cut of $N_{photoelectrons} > 3$ and for $P_{HMS} = 0.84 - 4.045$ GeV/c. In that analysis, a pure electron sample was selected from elastic H(e, e') data using tight W and calorimeter cuts. A similar study of E91003 elastic and quasielastic data yields an efficiency of at least 99.72% for a photoelectron cut of 2 (see Table 3.1).[3] In the analysis, the efficiency is taken to be 99.86±0.14% for all runs.

The pion rejection of the HMS Čerenkov is also very good (≈500:1) [28]. Since the $\pi : e$ ratio is not very large for the E91003 kinematics and any remaining pions that pass the particle identification cuts are removed by the subtraction of

[3]Note that since the HMS gas Čerenkov is used in one leg of the HMS trigger (ELLO), it is necessary to use only events for which the other leg (ELHI), which uses only scintillator and calorimeter information, fired. Only in this way can an unbiased (at least from the point of view of the gas Čerenkov) sample be obtained.

P_{HMS} (GeV/c)	HMS Čerenkov electron efficiency (%)
0.484	99.72 $\pm$ 0.02
1.167	99.90 $\pm$ 0.01
3.149	99.96 $\pm$ 0.01

TABLE 3.1. HMS Čerenkov electron cut efficiency. The electron cut in this case is $N_{photoelectrons} > 2$. The efficiency shows a very slight momentum dependence.

random coincidences, no detailed study of the pion rejection was made, except to check that the gas Čerenkov gave results consistent with the shower counter.

In addition to the electron selection efficiency at the analysis level, one must also account for the electron detection efficiency at the trigger level since the trigger includes signals from both the gas Čerenkov and calorimeter. However, since these signals are used in combination with signals from the scintillators to form the trigger, they are best discussed in terms of the overall trigger efficiency which will be addressed in Section 3.4.1.

3.3.2. Pion Identification

Pions in the SOS are identified using a combination of particle velocity and the SOS gas Čerenkov. While it is sufficient to use only a particle velocity cut to separate pions from protons at positive polarity, and the Čerenkov detector alone is necessary to separate pions from electrons at negative polarity, both cuts are used at both polarities. This reduces the uncertainty in comparing π^+ results to π^- results in that the uncertainty that comes about from the (in)efficiency of the pion identification cuts will be largely common to both data sets, and will cancel in any extracted ratios.

The threshold gas Čerenkov is highly efficient in separating pions from electrons and positrons. However, while traversing the Čerenkov detector, there is some probability that the pions will produce knock-on electrons, which in turn will then give some number of photoelectrons greater than zero. These pions may then be rejected by the same cut used to eliminate electrons. To account for this, the pion efficiency of the SOS Čerenkov can be determined using π^+ production from hydrogen. A tight cut on the reconstructed neutron mass (M_x) in combination with a conservative cut on the SOS calorimeter effectively removes all positrons. Then the ratio of counts with and without the Čerenkov cut gives the efficiency. At $P_{SOS} = 0.29$ GeV/c the pion efficiency is 99.93$\pm$0.02% for a cut of $N_{photoelectrons} < 2$ while at $P_{SOS} = 1.0$ GeV/c the efficiency is 99.54 ± 0.05%.

To separate pions from protons, a cut on the difference between the velocity as measured by time of flight and the velocity as calculated from the momentum is used. Sample $\beta_{tof} - \beta_p$ distributions are shown in Figure 3.5. Note that in the $\beta_{tof} - \beta_p$ spectra there is a tail below the prominent pion peak. This feature results from pions hadronically interacting in the scintillator paddles, possibly knocking out a slower hadron, resulting in a larger time of flight measurement. Because the pion passes the drift chambers before hitting the scintillators, the tracking information is likely still valid. Looking at the missing mass distributions for these events, it is clear that they are still "good" events and we must correct for any good tracks that are lost due to the time of flight cut.

Not shown in Figure 3.5 are the events for which the analyzer fails to find any β_{tof} at all. These events are assigned a value of $\beta_{tof} = 0$ and would appear at $\beta_{tof} - \beta_p \approx -1$. The analyzer fails to find a value of β_{tof} when the track projected

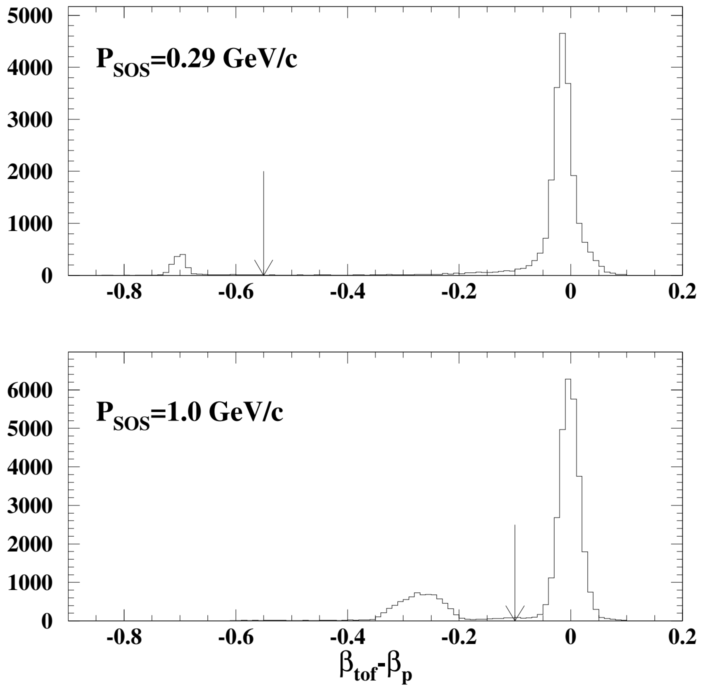

FIGURE 3.5. $\beta_{tof} - \beta_p$ spectra for $P_{SOS} = 0.29$ and 1.0 GeV/c. The pions are peaked at 0.0 while protons are at $\beta_{tof} - \beta_p < 0.0$. The arrows indicate the cuts used in the analysis.

to the relevant scintillator plane is a distance from the hit scintillator larger than a certain slop value. These events can also arise from pions undergoing nuclear interactions in the hodoscopes, and like the "tail" events, reconstruct to good values of missing mass, etc. At $P_{SOS} = 0.29$ GeV/c, the $\beta_{tof} = 0$ events are not eliminated by the cut used in the analysis. Although the $\beta_{tof} = 0$ events also include protons, it is clear from Figure 3.5 that the acceptance for protons is small (about 6% of the total counts). Hence, of the $\approx$ 6% of the counts for which no β_{tof} is found, about 6% of those are protons, making a net 0.36% contamination. Furthermore, at this low momentum, all protons in the acceptance are random coincidences, so that the 0.36% contamination is eliminated in the random subtraction. At $P_{SOS} = 1.0$ GeV/c, real coincident protons are in the acceptance and could bias the random subtraction, so the $\beta_{tof} = 0$ events are discarded. These events must also be accounted for the determination of the β cut efficiency at $P_{SOS} = 1.0$ GeV/c.

At $P_{SOS} = 1.0$ GeV/c the $\beta_{tof} - \beta_p$ cut efficiency can be examined using π^- data since at this momentum, any hadronic interactions in the scintillators can be assumed to be charge symmetric. Electrons are eliminated using the gas Čerenkov cut and the efficiency is simply the number of events that pass the $\beta_{tof} - \beta_p$ cut divided by the total number of events. The same method can be employed for the π^- data at $P_{SOS} = 0.29$ GeV/c, but at this low momentum, the nuclear interactions are not charge symmetric due to the Δ resonance. Thus, even though the excluded region in $\beta_{tof} - \beta_p$ space is small, one can not assume that the efficiency is the same. However, the π^+ efficiency can be tested directly by using the energy deposited in one layer of the scintillators to get a pure π^+ sample.[4] It turns out, though that the extracted π^+ efficiency is identical (within uncertainties) to the π^- efficiency.

At each momentum setting, the cut efficiency is largely constant within the statistical uncertainties of the efficiency calculation. Hence, one efficiency is used at each momentum setting. The random uncertainty in the efficiency is taken from the scatter of the efficiencies for each run about the mean. The cut efficiencies are summarized in Table 3.2.

---

[4]This can not be done at $P_{SOS} = 1.0$ GeV/c as the energy deposited by pions and protons is quite similar.

P_{SOS} (GeV/c)	$\beta_{tof} - \beta_p$ cut	Efficiency (%)
0.29	(> -0.55) OR $(\beta_{tof} = 0)$	99.83±0.40
1.0	> -0.1	95.95±0.47

TABLE 3.2. $\beta_{tof} - \beta_p$ cut efficiency. At $P_{SOS} = 0.29$ GeV/c, the $\beta_{tof} = 0$ events are retained while at $P_{SOS} = 1.0$ GeV/c they are eliminated (as discussed in the text).

3.3.3. Tracking Cuts

After particle type identification, cuts on reconstructed quantities at the target are used to further refine the data sample. Loose cuts are placed on the spectrometer in-plane and out-of-plane angles (y'_{tar} and x'_{tar}) to reduce the number of events that are initially outside the spectrometer acceptance, but due to multiple scattering in the magnets or shielding make it to the detectors in the hut. Cuts are also placed on the reconstructed fractional momentum (δ) to restrict the accepted events to the momentum bite for which the reconstruction matrix elements are known to be good. The general tracking cuts used in this analysis are summarized in Table 3.3.

While the nominal acceptable region in HMS δ is $\pm 8\%$, further cuts are used to better match the accepted energy loss, ω $(= E_{beam} - E_e)$, between ϵ points. At each W setting, the high ϵ point has a larger ω coverage than the low ϵ point for the same HMS δ cut. Hence, the $W = 1.15$ GeV, high ϵ point is restricted to $-2\% < \delta_{HMS} < 8\%$ and the $W = 1.6$ GeV, high ϵ point to $|\delta_{HMS}| < 2\%$.

The uncertainty in the extracted cross section from these cuts is best discussed in terms of the overall acceptance, which is generally taken to be on the

HMS	SOS
$\lvert x'_{tar}\rvert < 0.080$ rad	$\lvert x'_{tar}\rvert < 0.050$ rad
$\lvert y'_{tar}\rvert < 0.045$ rad	$\lvert y'_{tar}\rvert < 0.065$ rad
$\lvert\delta\rvert < 8\%$	$-15\% < \delta < 20\%$

TABLE 3.3. Cuts on reconstructed spectrometer quantities used in the analysis. These cuts denote the maximum acceptable region for this analysis. Further cuts are placed on HMS δ, depending on kinematic setting, as discussed in the text.

order of 2%. This will be further discussed in Section 4.8. The random uncertainty in the tracking cuts can be further explored by varying the cuts and examining the variation of the cross section. This will be discussed in Section 5.5.

3.3.4. Random Coincidence Subtraction

Once the appropriate particle type has been selected and cuts on reconstructed spectrometer quantities have eliminated bad events, the random $e - \pi$ coincidences must be removed from the data sample. This analysis uses the so-called HMS coincidence time, in which the start is given by an HMS pretrigger and the stop is given by the SOS pretrigger. The raw, or uncorrected coincidence time is refined by correcting for the time difference due to the particle trajectory deviation from the central ray of the spectrometer and the velocity of the particle. These so-called pathlength corrections enable us to resolve the 2 ns beam structure of the accelerator. A sample coincidence time spectrum, before and after application of the pathlength corrections is shown in Figure 3.6. A description of the pathlength correction determination can be found in Ref. [34].

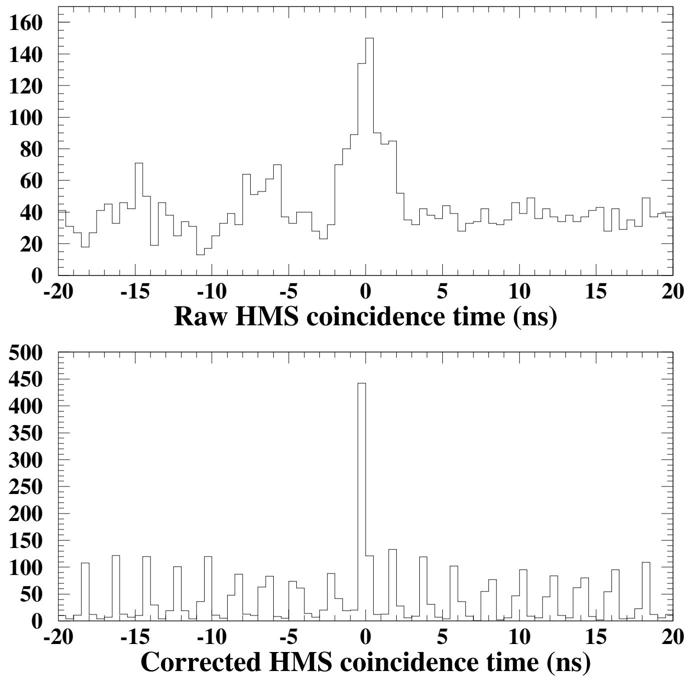

FIGURE 3.6. Raw and pathlength corrected HMS coincidence time. The real coincidence peak is clearly evident in both plots at $t = 0$ ns. In the bottom plot one can see the 2 ns structure of the electron beam.

The implementation of the random subtraction method is slightly different for the $P_{SOS} = 0.29$ GeV/c data as opposed to the $P_{SOS} = 1.0$ GeV/c data, however, the general idea is the same. In particular, a cut is placed on the "real" coincidence peak of ± 1 ns and the corresponding counts and/or histograms accumulated. Then, some sample of "random" peaks is taken (6 peaks for the $P_{SOS} = 0.29$ GeV/c data and 4 peaks for the $P_{SOS} = 1.0$ GeV/c data). The random counts are then normalized by the number of peaks sampled and subtracted from the real peak data.

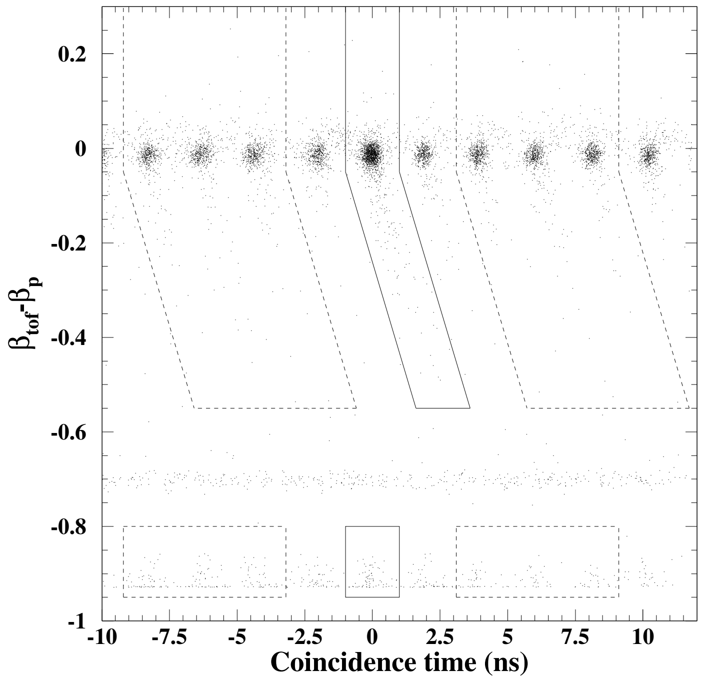

FIGURE 3.7. Real and random event coincidence time cuts at $P_{SOS} = 0.29$ GeV/c. The real event cut is shown with solid lines while the random event cut is shown with dashed lines.

The difference in the random subtraction between the two pion momentum data sets is due to correlation between β_{tof} and the corrected coincidence time, combined with the relative position of the $\beta_{tof} - \beta_p$ cut. The $P_{SOS} = 0.29$ GeV/c coincidence time cut is shown in Figure 3.7. In this case, the low $\beta_{tof} - \beta_p$ tail is correlated with coincidence time, so it is necessary to implement a two-dimensional cut as shown. Note that the events with $\beta_{tof} = 0$ (located at $\beta_{tof} - \beta_p \approx -1$) are also included in the random subtraction as discussed in Section 3.3.2. The "real" sample is enclosed by solid lines and the "random" sample by dashed lines. Note also the cluster of events at $\beta_{tof} - \beta_p \approx 0.05$ and *coincidence time* ≈ -1 ns. These events are pions that decay into muons close to the target. The coincidence time cut is chosen deliberately to reduce the number of these events that make it into the data sample. These muons are included in the simulation of the experiment and will be discussed further in Section 4.5.

The coincidence time cut for $P_{SOS} = 1.0$ GeV/c is shown in Figure 3.8. In this case, a correlated $\beta_{tof} - \beta_p$ is not used due to the necessity to have a tight time of flight cut to eliminate protons. Also, only 4 random peaks are used for the subtraction. This is to ensure that the randoms are not contaminated by in-time coincident protons (at *coincidence time* $= +9$ ns in the figure). Any random protons that "feed-through" the time of flight cut are of no concern as they are uncorrelated in time and will subtract away. However, any in-time protons that feed through the cut will bias the random sample resulting in an incorrect subtraction. $\beta_{tof} = 0$ events are also excluded for this reason.

3.3.5. Target Can Background Subtraction

The final stage in the accumulation of good events is the subtraction of events coming from the aluminum target can that holds the cryogenic target material. This is accomplished using the so-called "dummy" target - two slabs of aluminum placed at $z = \pm 2$ cm. The dummy target is 7.32 times thicker[5] than the nominal target cell wall, reducing the amount of beam time necessary for the accumulation of these background data.

[5]The dummy is actually 7.55 times thicker by length, but the aluminum used in the dummy target has only 97% the density of the aluminum used in the target cells, so $7.55 \times 0.97 = 7.32$.

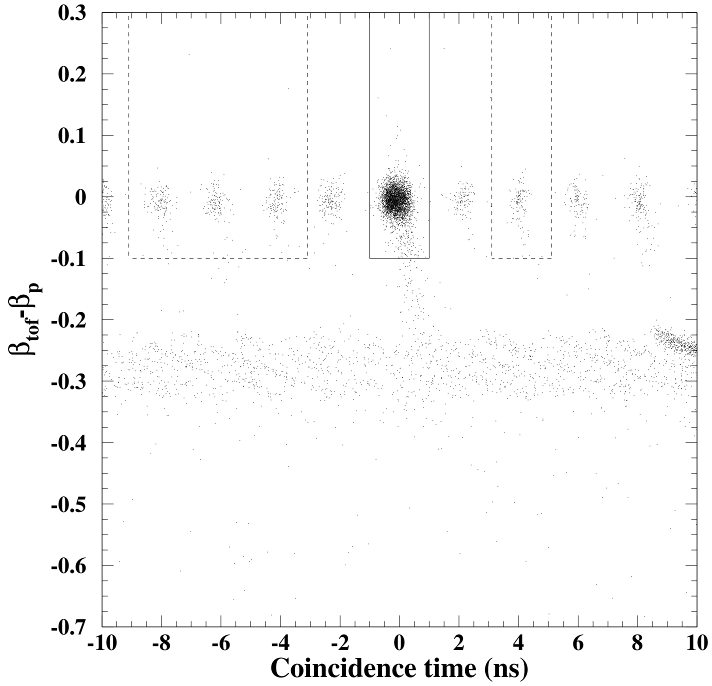

FIGURE 3.8. Real and random event coincidence time cuts at $P_{SOS} = 1.0$ GeV/c. The real event cut is shown with solid lines while the random event cut is shown with dashed lines. Real coincident protons can be seen at +9 ns. The $\beta_{tof} - \beta_p$ correlation with coincidence time for the protons arises from the fact that the pathlength corrections are done assuming the particle of interest is a pion.

The dummy data are analyzed in the same fashion as the data from the cryotargets. Identical cuts are used and random coincidences are subtracted in the same fashion. Finally, efficiency corrected and charge normalized yields are subtracted from the real data (accounting for the factor of 7.3 thickness difference between the dummy target and aluminum walls). In the case that histograms are being created for comparison to the Monte Carlo, spectra from the dummy target are created in the variable of interest (missing mass, Q^2, etc.) and subtracted bin by bin from from the cryotarget spectra.

In most cases, the estimated target can contribution to the measured yield is quite small, on the order of 2-3%. The uncertainty in the ratio of the thickness of the dummy relative to the target can (3.44%) then contributes a negligible uncertainty to the total yield. Even in the case of π^- production from the helium-3 target, where the can contribution is $\approx$ 10%, the net contribution to the uncertainty is $\approx$ 0.3%. Furthermore, this uncertainty will be largely correlated between ϵ settings (since the fractional contribution from the target can is fairly constant), hence the contribution to the separated cross sections quite small.

3.4. Corrections to the Data

In addition to applying the various cuts and background subtractions described above, the data must also be corrected for any inefficiencies in which good events may be lost. Some of these, the $\beta_{tof} - \beta_p$ cut efficiency and Čerenkov cut efficiencies, have already been discussed in Sections 3.3.1 and 3.3.2. Other corrections include things like data acquisition dead times, track finding efficiencies, and absorption of pions in the spectrometer. All efficiencies, where applicable, are applied to each run when creating histograms for Monte Carlo comparison or simply accumulating charge normalized counts.

3.4.1. Trigger (3/4) Efficiency

The trigger efficiency, although often assumed to be essentially perfect in Hall C experiments, is perhaps one of the most crucial quantities in an experiment of this nature. In both the HMS and SOS, the scintillators play a key role in determining a trigger, as discussed in Section 2.6. In the SOS, the trigger requires 3 of the 4 scintillator planes to fire. In the HMS, the electron trigger is a bit more complicated, but the 3-of-4 requirement is also quite important. Hence, any determination of the overall trigger efficiency must begin with the scintillator efficiency.

3.4.1.1. 3/4 Efficiency

Given the efficiency of each scintillator plane, the probability to have 3 of the 4 planes respond to a given event (the 3/4 efficiency) can be calculated,

$$\begin{aligned} P_{3/4} = {} & P_1 P_2 P_3 P_4 + P_1 P_2 P_3 (1 - P_4) + P_1 P_2 (1 - P_3) P_4 \\ & + P_1 (1 - P_2) P_3 P_4 + (1 - P_1) P_2 P_3 P_4 \,, \end{aligned} \tag{3.5}$$

where P_n represents the efficiency of the nth plane. At high momentum (where multiple scattering is small), the plane efficiency can be calculated by projecting the fitted track to each plane and testing to see if the scintillator paddle that intersects the track has fired. This is essentially the default calculation used in the replay ENGINE. While this method works well at high momentum, at lower momentum, multiple scattering causes the true particle trajectory through the scintillators to deviate from that of the fitted track. For this experiment, the "tracking based" efficiency calculation can only really be used for the one or two planes of scintillators closest to the drift chambers.

In this analysis, the absolute 3/4 efficiency is determined by examining a subset of runs and applying a non-tracking based algorithm which requires hits in the other three planes to determine whether an event should have given a signal in the fourth. Requiring signals in the other three planes ensures that a valid trigger would be formed whether the fourth plane fires or not. Hence, one has an unbiased sample with which to measure the efficiency of that plane. Particle identification signals are also used to ensure that the trigger efficiency is calculated for the particle of interest. For example, the last plane of scintillators in the SOS will tend to show a lower efficiency for pions than electrons. This is due to pion absorption or hadronic scattering which reduces the probability that a pion will give a signal in the last plane.[6] The non-tracking based 3/4 efficiency calculation is checked using a run at each kinematic setting (4) for each target (3) and pion polarity. The tracking based 3/4 efficiency calculations are used to verify that the hodoscopes are behaving consistently over time. The scatter in the efficiencies measured from the sample runs at each kinematic setting is used to parameterize the uncertainty in the 3/4 efficiency.

An additional complication arises from the fact that throughout the running of E91003, one photomultiplier in each spectrometer was giving no signal at the trigger level (one in the HMS 1X plane and one in the SOS 2Y plane). Although there are tubes on both sides of each paddle, the trigger requires signals from both. Hence, one dead PMT effectively makes the whole paddle dead at the trigger level. This means that every particle passing through that paddle requires a 3/3 trigger in the other three planes. In the worst case, this reduces the 3/4 efficiency for those events to $\approx 95\%$. Despite this problem however, the overall 3/4 efficiencies (averaged over the spectrometer acceptance) are still quite high. In the HMS, the 3/4 efficiency is 0.997 ± 0.001 independent of momentum

---

[6] Pion absorption in the spectrometer is addressed in Section 3.4.7. A correction is applied for absorption, but this is distinct from the 3/4 efficiency as discussed here. The absorption correction is applied only for those events that had no *chance* to give a trigger, i.e. do not make it to the third layer of scintillators. However, the 3/4 efficiency corrects for those pions that may reach the third layer, but pass through without giving a signal in that layer. Hence, the probability to give a signal in the fourth layer must also be included in the 3/4 calculation, even if that lack of signal comes from absorption.

setting. In the SOS, the 3/4 efficiency is 0.987 ± 0.002 at $P_{SOS} = 0.29$ GeV/c and 0.996 ± 0.002 at $P_{SOS} = 1.0$ GeV/c.

3.4.1.2. SOS Trigger Efficiency

Since the SOS trigger merely requires the 3/4 scintillator signal with no additional particle identification, the SOS trigger efficiency is given by the 3/4 efficiency. In this case, one may be concerned that the particles passing through the "dead" paddle in the SOS 2Y plane may influence the physics distributions since the 3/4 efficiency may be up to about 5% lower in that one region. However, since the 2Y plane is in the non-dispersive direction, the y-position at that plane is not highly correlated with any physics variables of interest. Furthermore, Monte Carlo tests in which events striking the bad paddle are weighted with the lower efficiency (as opposed to an overall efficiency applied to the data) indicate a difference in the extracted cross section of less than 0.2% in the worst case (for the low momentum pion data). Therefore, it is sufficient to apply a global correction to the data rather than specifically accounting for events that pass through the bad paddle. The SOS trigger efficiency is assigned the values for the 3/4 efficiency given above; 0.987 ± 0.002 at $P_{SOS} = 0.29$ GeV/c and 0.996 ± 0.002 at $P_{SOS} = 1.0$ GeV/c.

3.4.1.3. HMS Trigger Efficiency

In the HMS, the inefficiency caused at the trigger level by the one dead paddle is mostly compensated for by the alternate legs in the trigger. The HMS will give a trigger if either the ELLO or ELHI condition is satisfied (see Section 2.6). ELLO requires a signal from the Čerenkov as well as 2/3 of the following; the 3/4 scintillator signal, the STOF (which requires at least one scintillator plane each in the front and back), or the PRLO signal (low threshold on the first layer of the calorimeter). The ELHI leg of the trigger also requires the 3/4 signal, as well as the PRHI signal (high threshold on the first layer of the calorimeter) and the SHLO signal (low threshold on the total calorimeter signal).

Assume we have particles that do *not* hit the dead scintillator. In this case the 3/4 efficiency is ≈ 1 (greater than 0.9995). STOF is automatically satisfied for events that satisfy the 3/4 condition and a trigger will be formed if either the gas Čerenkov fires, or the remaining signals in ELHI are present. The Čerenkov is 99.7% efficient and the AND of PRHI (81.3% to 97.50% efficient) and SHLO (65.2% to 98.9% efficient) is present 53% of the time at low momentum and 96% of the time at high momentum. Thus, the overall trigger efficiency is ≈ 0.9985 at low momentum and ≈ 1.0 at high momentum.

For particles incident on the dead scintillator, the 3/4 efficiency drops to 0.967. Particles that satisfy the 3/4 condition then have a trigger efficiency of 0.9656 at low momentum and 0.967 at high momentum.

For those events that do not satisfy the 3/4 condition, a trigger can still proceed via the ELLO leg. In this case, one requires the STOF signal (a 0.966 probability for those events that do not satisfy 3/4), the PRLO signal (0.994 or greater), and the gas Čerenkov (0.997). Therefore, we recover about 95.75% of the events that do not give a 3/4 signal, giving an overall trigger efficiency for these worst case events of ≈ 0.997 at low momentum and ≈ 0.9985 at high momentum.

The above result indicates that the trigger efficiency variation at the dead scintillator paddle is only about 0.15%. Therefore, it is quite safe to assign one correction over the whole acceptance without fear of having distorted shapes in any physics variables due to local trigger efficiency changes. The overall HMS trigger efficiency at low momentum is limited by the efficiency of the calorimeter signals, while at high momentum it is effectively one. Hence, the HMS trigger efficiency is assumed to be 0.999 ± 0.001.[7]

3.4.2. Computer and Electronic Dead Time

Since electronic modules and computers require some finite time to process an event, one must correct for events that are lost or not recorded during this processing time. In general, dead times can be divided into two categories - non-extendible (or non-paralyzable) and extendible (paralyzable) [35]. In the non-extendible case, the module in question ignores new inputs while processing an event. So-called extendible modules will accept additional input while processing the first event, and extend the output generated accordingly.

Given a mean event rate R, the probability to find n counts in a time t is,

$$P(n) = \frac{(Rt)^n e^{-Rt}}{n!} \,, \tag{3.6}$$

and the mean number of counts in that time is just Rt. If an event causes a given element to be busy or "dead" for a time τ, the number of counts missed will be $R\tau$. Furthermore, in the non-extendible case, the time that the output is busy will not be extended so that the ratio of measured counts to the true number of counts (the so-called live time) is just,

$$(Live\ time)_{non-extendable} = \frac{1}{1 + R\tau} \,. \tag{3.7}$$

This is the case applicable the Hall C data acquisition system, the source of computer dead time. In this case, the Trigger Supervisor sends a "TS-BUSY" signal

[7]A subset of runs was accidentally taken with the STOF signal removed from the trigger, making the ELLO leg basically 3/4 and PRLO. In this case, though, the trigger efficiency is still 0.989. The affected runs are corrected for this additional inefficiency, with no additional uncertainty included.

to the 8LM while processing a trigger. The 8LM then suppresses all output until the Trigger Supervisor is ready for another event.

Experimentally, the computer dead time is directly measured by scalers that record the number of triggers and pretriggers. Since pretriggers are generated for each particle, and triggers are only read out for those events for which the Trigger Supervisor is not busy, the computer live time is,

$$Computer\ L.T. = \frac{N_{trigger}}{N_{pretrigger}} \ . \tag{3.8}$$

The triggers and pretriggers are recorded in both the HMS and SOS scalers, however the SOS scalers are used for the correction due to some occasional erratic behavior in the HMS pretrigger scaler. Figure 3.9 shows the experimentally measured computer live time compared to the live time as calculated using Equation 3.7. The effective gate width of $\tau = 579.4\ \mu$s has been fit using data for which $Computer\ L.T. > 0.6$. The effective τ shown on the plot represents the mean time to process an event - since HMS and SOS singles may be processed slightly faster than coincidence events, small deviations may arise from changing singles rates relative to coincidence rates. Furthermore, at high rates, the live time becomes extremely sensitive to things besides the Trigger Supervisor processing time, such as network traffic and read-out computer load. In fact, during some of these runs, it had been noted in the logbook that the data "stuttered in" at times, the readout scalers freezing for a few seconds and then counting again. The data is corrected using the measured, not the theoretical dead time.

The measurement of the computer live time for these high rate runs can be tested by looking at the run-to-run yields. The triangle points in Figure 3.9 were all taken at the same kinematics with the same target, but the measured computer live times range from 0.383 to 0.457. If the computer live time is being measured correctly, then the charge normalized, live time corrected yield should

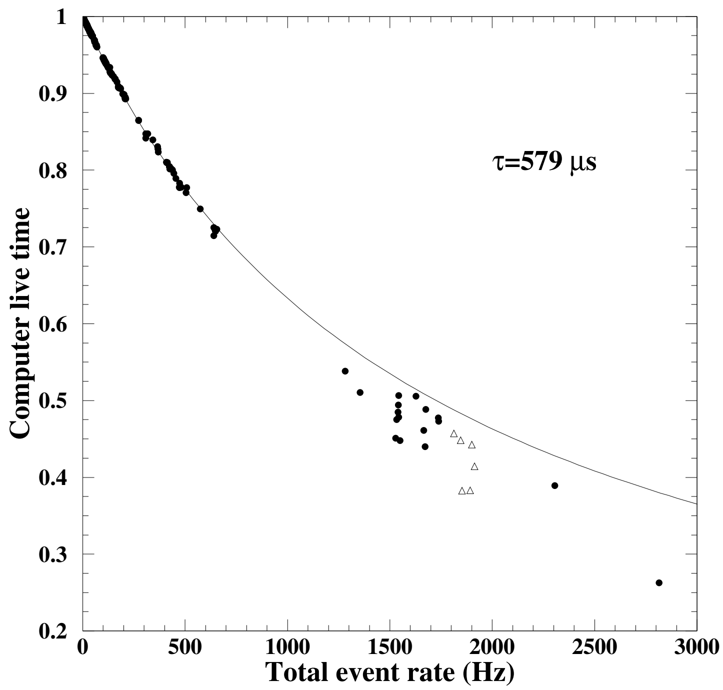

FIGURE 3.9. Measured computer live time as a function of total event rate into the Trigger Supervisor. The curve is from Equation 3.7 with $\tau = 579.4$ μs. Deviations from the curve at high rate are likely due to network traffic and load on the computer that transfers the data to disk.

be independent of live time. Figure 3.10, in which the corrected yield is plotted as a function of computer dead time ($1 - Computer\ L.T.$), shows that this is indeed the case.

The uncertainty in the computer live time measurement is estimated by the deviation of the measured value from the value calculated from the total rate (excluding the extremely large dead time region where spurious effects are large). The resulting uncertainty is 0.1%.

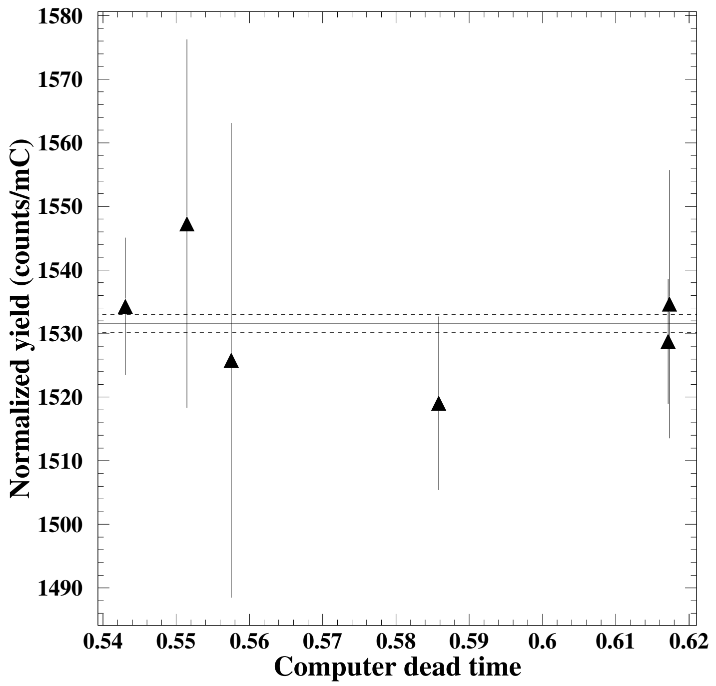

FIGURE 3.10. Run-to-run efficiency corrected yields for runs taken at the same kinematics, but with large variations in dead time. Error bars show statistical uncertainties only. The dead time correction varies by about 20%, but the yields agree to better than 2%. The solid and dashed horizontal lines denote the mean yield and its statistical uncertainty.

While the computer dead time can be calculated as a non-extendible source of dead time, it is not exactly clear how to treat the electronic dead time. Electronic dead time occurs when logic or discriminating modules in the trigger are busy and can not process new events. Some of these modules are paralyzable and some are not, so it is not clear which kind of dead time is appropriate. It will be shown however, that in this particular case, it is not crucial that we make the distinction.

In the extendible case, a module will output a pulse for every event that comes in. Hence, for a module that puts out a 30 ns pulse, the arrival of a second signal 10 ns after the first will result in a total pulse length of 40 ns. Thus, only events that arrive a time τ later than the previous event (even if that event is NOT the one that has caused the module to be busy) will be recorded. The distribution of the time between events is,

$$P(t) = Re^{-Rt} . \tag{3.9}$$

The probability that $t > \tau$ then gives the live time,

$$(Live\,time)_{extendable} = P(t > \tau) = \int_{\tau}^{\infty} Re^{-Rt} dt = e^{-R\tau} . \tag{3.10}$$

Here, the effective gate width is quite small ($\approx$ 50 ns), so that it is always true that $R\tau << 1$. In that case, expanding both Equations 3.7 and 3.10 to first order in $R\tau$ yields,

$$(Live\,time)_{extendable} \approx (Live\,time)_{non-extendable} \approx 1 - R\tau . \tag{3.11}$$

Hence, it is not important whether we treat the electronic dead time as an extendible or non-extendible source.

Unlike the computer dead time, the electronic dead time is not directly measurable and must be inferred. This is done using the so-called EL30, EL60, EL90, and EL120 scalers. These are simply modules that take the original pretrigger signal and copy it into gates of varying length (i.e. 30 ns, 60 ns, etc.). Using knowledge of these gate widths and the width of the limiting gate in the pretrigger and assuming $R\tau << 1$ so that Equation 3.11 is valid, one can extrapolate to zero gate width and calculate the true number of events. For example, if the limiting gate width is 30 ns, then the "true" number of counts is,

$$N_{true} = N_{measured} + \left(\frac{N_{EL60} - N_{EL120}}{60\text{ns}} \right) 30\text{ns}. \tag{3.12}$$

And in fact, when the trigger was designed, it had been assumed that the limiting gate width was 30 ns as that was the width of the "pretrigger" output. However, it turns out that a module earlier in the trigger logic (the scintillator discriminators), which has a gate width of ≈50 ns, is the true limiting width in the trigger system (see Ref. [36] for a discussion of how this was determined). For a 50 ns gate width, the number of true events as extrapolated from the EL* scalers is,

$$N_{true} = N_{measured} + \frac{5}{6}\left(N_{EL60} - N_{EL120}\right) \ . \tag{3.13}$$

The electronic dead time is calculated in the HMS and SOS separately using the second extrapolation, and the resulting correction is applied on a run by run basis.

The electronic live time as calculated in the SOS and HMS is shown in Figure 3.11. The rate dependence for each is fit to the approximate form given in Equation 3.11. The uncertainty in the correction is estimated from the deviation of the measured value of τ from the expected value of 50 ns (this deviation may not only be coming from the fact that we have estimated the limiting gate width a bit wrong, but from the EL60, etc. scalers not being set in exact increments of 30 ns). This gives an uncertainty of 10% of the size of the correction, or a maximum combined (HMS+SOS) uncertainty of $\approx 0.3\%$ (i.e. 10% of 3%).

3.4.3. Coincidence Blocking

The use of the coincidence time between the HMS and SOS to identify good coincident events at the interaction vertex has already been described in Section 3.3.4. However, in some cases the coincidence time TDC may receive spurious non-coincident events close enough in time to the coincidence[8] event to

[8] In this context, a coincidence is defined as any event, be it a real or random coincidence, that has overlapping pretrigger gates from the HMS and SOS, and hence is defined as a coincidence pretrigger at the 8LM.

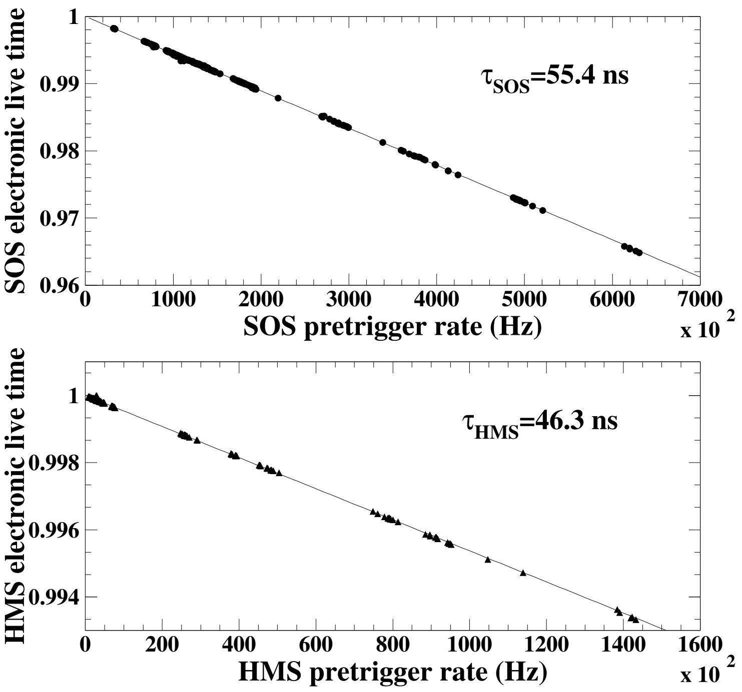

FIGURE 3.11. Electronic live time as a function of pretrigger rate in the SOS and HMS. Each is fit to the approximate form for the live time given in Equation 3.11. Due to the higher particle rate, only the SOS is a significant source of electronic dead time.

interfere with the proper measurement of the coincidence time. These so-called "coincidence blocking" events result in values of the measured coincidence time outside the main timing window (in this case, the sum of the HMS and SOS pretrigger gate widths: 40 ns + 20 ns = 60 ns) causing these events to be lost due to the coincidence time cut.

A raw coincidence timing spectrum is shown in Figure 3.12 and illustrates the effect of the coincidence blocking events. A "normal" coincidence event is started at the TDC by a delayed HMS signal (ANDed with the long

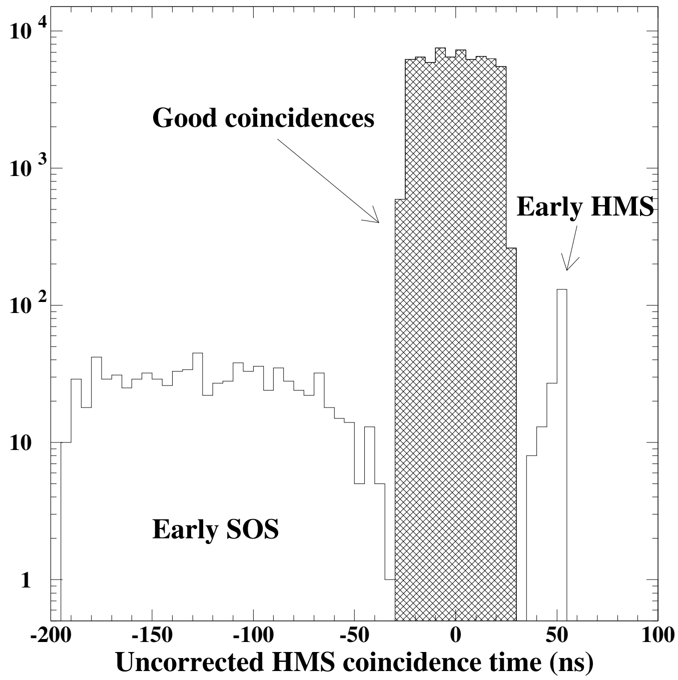

FIGURE 3.12. Raw HMS coincidence time spectrum showing coincidence blocking events. The main coincidence window is shown in the shaded region, while the regions to the left and right are from early singles events in the SOS and HMS respectively.

coincidence trigger signal coming from the trigger supervisor) and stopped by the SOS. The resulting 60 ns coincidence window is shown in the shaded region around *coincidence time* = 0 ns. The events to the left of the main coincidence window are caused by SOS singles triggers that come before the coincidence SOS event and stop the TDC prematurely.[9] Events to the right of the main window are caused by HMS singles events that arrive before the coincidence HMS event, causing an

[9]This may seem strange in that a prior event is stopping a TDC started by the event that comes after. However, this is possible due to the long gate output by the Trigger

early start at the TDC and hence a larger value of the measured coincidence time (and all other TDC values).

The above descriptions are, of course, rather simplified versions of what really transpires - a more complete discussion is presented in Ref. [36]. The important point here is to realize that the number of blocked coincidences will be directly related to the event rate in each spectrometer. In fact, one can parameterize the effect in terms of a kind of dead time and fit the fraction of blocked events to a correction of the form given by Equation 3.11. Such a fit is shown in Figure 3.13. The "measured correction" is simply given by

$$Coinblock = \frac{N_{block}}{N_{total}}, \tag{3.14}$$

where N_{block} refers the number of "early SOS" or "early HMS" events (as taken from the actual coincidence time spectrum) and N_{total} is the total number of events, regardless of measured coincidence time. The effective gate width of the correction is fit for the "early SOS" and "early HMS" events independently. The correction used in the analysis is from this fit, and is given by,

$$Coinblock = (1 - R_{SOS}\,\tau_{SOS})(1 - R_{HMS}\,\tau_{HMS})\,, \tag{3.15}$$

where $R_{SOS}(R_{HMS})$ is the event rate in the SOS (HMS) as measured by the pretrigger rate and the values of τ_{SOS} and τ_{HMS} are from the fits shown. The uncertainty in the correction is parameterized in terms of the deviation between the measured value as given by Equation 3.14 and the calculated value as given by Equation 3.15. The total uncertainty in the coincidence blocking correction (HMS and SOS combined) is 0.1%.

Supervisor upon receiving a coincidence trigger, combined with the retimed pretriggers used to ensure proper ADC/TDC readout.

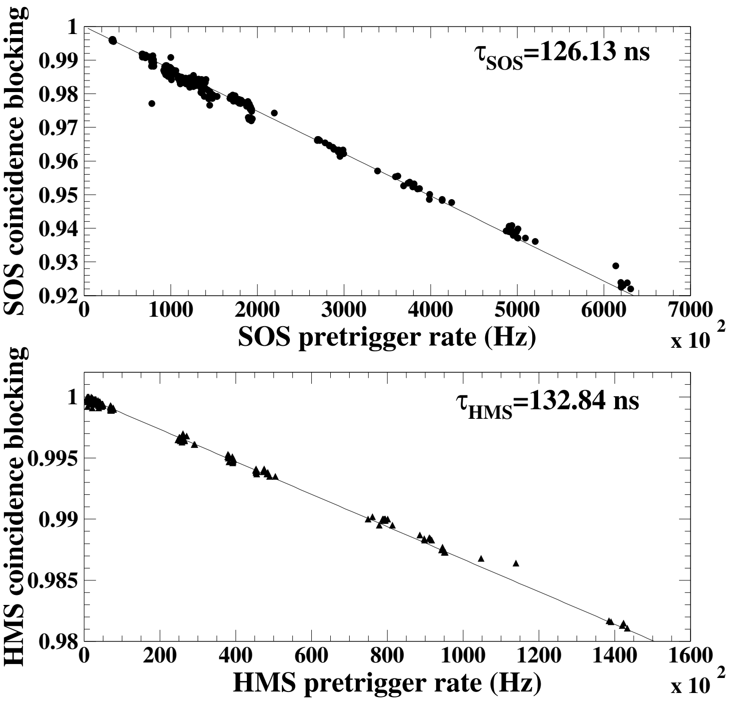

FIGURE 3.13. Measured coincidence blocking correction due to SOS and HMS singles as a function of rate. Lines are fits of the form $1 - R\tau$ with the value of τ noted on the plot.

3.4.4. Tracking Efficiency and Multiple Tracks

Failure to find a track for a given event can arise from either failure of the tracking algorithm or drift chamber inefficiency. The efficiency for finding a track is calculated by choosing events that should have passed through the drift chambers and determining the number of those events for which a track is found. The scintillators are used to define events that should have passed through the chambers, requiring hits on particular paddles that define a fiducial area.

While the above is sufficient to determine the tracking efficiency averaged over all particle types accepted by the spectrometer, it is necessary to further constrain the tests such that the tracking efficiency is calculated only for the particle of interest. This is especially important for the low momentum π^+ data. In this case, many slow protons (with very low tracking efficiencies) are also accepted, thus potentially biasing any calculation of the tracking efficiency that does not discriminate between particle types. Cuts on time-of-flight and energy deposition in the scintillators[10] are used in the SOS to select pions when calculating the tracking efficiency. In the HMS, no discernible difference is found when selecting electrons only (as opposed to electrons and pions), so no particle identification is used in the HMS tracking efficiency calculation. The resulting efficiencies in both spectrometers are rather high, typically $\approx 96-97\%$ in both, with some dependence on rate.

Examination of the events that fail to track reveals that typically about 25% of those events come from having too many "hits" in the drift chambers. The tracking algorithm allows a maximum of 15 hits per chamber in the HMS and 25 hits per chamber in the SOS. These values are chosen so as to give a reasonably high tracking efficiency while optimizing processing time, since events with more hits take longer to evaluate. At low SOS momentum, the number of events that cause too many hits in the drift chambers rises to about 50% of the events not tracked. The remaining untracked events fail merely because the tracking algorithm fails to find a track, or there are not enough hits to satisfy the

[10]Note that these cuts are stricter than those used in the analysis. In this case it is important to have a pure pion sample, even at the expense of throwing some pions out. In the normal analysis, any contaminating protons are eliminated by the random subtraction.

requirements of the tracking routine (hits on at least 5 planes in each chamber). The one-event display, combined with particle identification information for the untracked events reveals that these events look like valid events (as opposed to particle showers from scraping in the magnetic elements) and should be accounted for in the data analysis (see Figure 3.14). A scale uncertainty of 1.5% (based on the method of the tracking efficiency calculation) with a random uncertainty of 0.5% (based on variation of the tracking efficiency with rate) is assigned to the tracking efficiency correction.

At high rates, there is a non-negligible probability that more than one particle will traverse the drift chambers within the $\approx$ 200 ns TDC window ($\pm$ 100 ns around the trigger). However, the engine will pick only one of these tracks and, furthermore, this track may not be the one associated with the particle that gave the initial trigger. There are two distinct cases of interest here. In the first, a random single may traverse the drift chambers before a coincidence. In the second, a coincidence traverses the drift chambers before a single.[11]

In the case in which the single comes first, the single may give a valid trigger. If the single trigger is read out by the data acquisition, the lost coincidence will be accounted for in the computer dead time. If the single trigger is not read out (because it has been prescaled away), it will "block" the coincidence time of the good coincidence and the lost event will be taken care of in the coincidence blocking correction (see Section 3.4.3). If the single does not give a trigger (e.g. a slow proton as described in Section 2.6.2), the later coincidence event will give a good trigger and be read out. However, the single will still give hits in the drift

---

[11]The issue of two coincidences arriving within 200 ns of each other is not considered due to the extremely low coincidence rate relative to the singles rate.

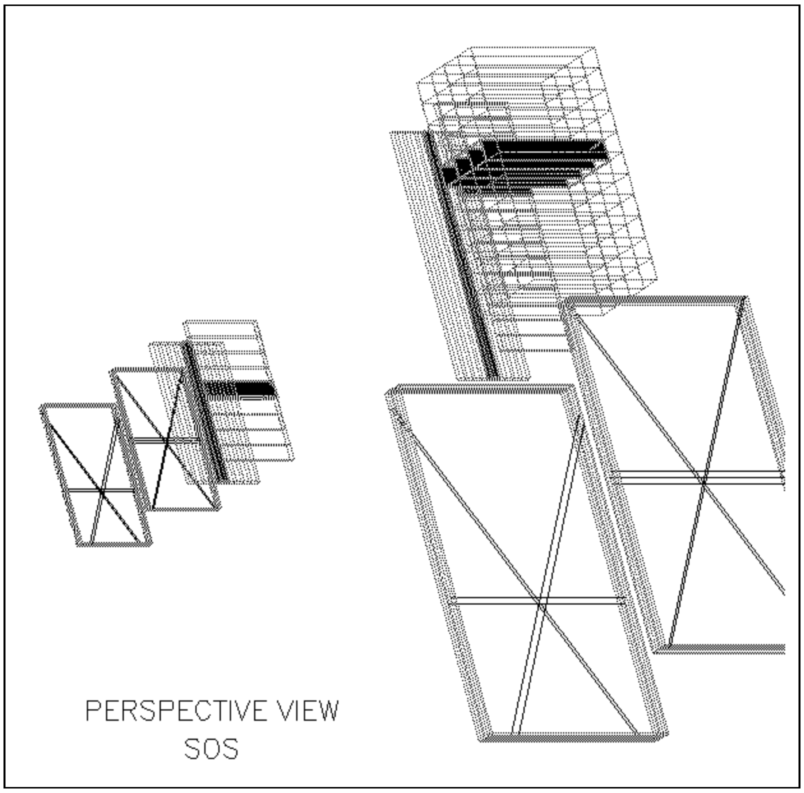

FIGURE 3.14. One event display for a pion trigger in the SOS that failed to track. Intersecting lines in the drift chambers (first two planes in detector stack and in blow-up view) denote “hit” wires. This is clearly an event that should have been tracked but was not due to failure in the tracking algorithm.

chambers and there is a chance the wrong track will be selected and associated with the coincidence time of the good event.

In the case in which a coincidence comes first and a single comes later, the hits from the later single may also cause the wrong track to be associated with the coincidence time from the original trigger. In this case, there are no other effects that may cause the coincidence to be lost that may be accounted for in other corrections. Therefore, all cases of a single arriving less than 100 ns after the coincidence must be considered in any correction made for selection of the wrong track.

At negative polarity, almost every single that passes through the drift chambers gives a valid trigger. This is also true at positive polarity at higher momentum. Therefore, we only need consider those events for which the coincidence comes before the single. The probability to lose a “good” event due to the two track problem is then reduced by about a factor of two. In the case of low momentum, positive polarity particles entering the spectrometer, about half the rate in the drift chambers comes from slow particles (protons) that give no trigger signal. In this case, then, all the events for which the single arrives after the coincidence and half the events for which the single arrives before the coincidence must be included. Hence, about 3/4 of the total number of “2 track” events can contribute to any potential track misidentification at low momentum positive polarity.

The two-track problem is helped by the fact that the track closer in time to the trigger is likely to have the correct drift distance and hence a better χ^2 than the later (or prior) track, and therefore be chosen as the good track. Examining the one-event display and choosing events where it is clear from the drift chamber hit patterns that there are two good (distinct) candidate tracks, one can examine the hit pattern in the scintillators to choose which track should be associated with the other detector signals. It turns out that about 90% of the time, the tracking algorithm chooses the correct track.

So far, we have not addressed the fact that, in the discussion about tracking efficiency above, it was noted that a significant fraction of the events for which a track is not found come from having too may hits in the drift chambers. At this point, it should be clear that a number of these events with too many drift chamber hits could potentially be events with more than one particle passing through the chambers. Therefore, we could be double-correcting for those events for which two particles pass through the chambers, but also cause there to be too many hits. Looking at a sample of these events with the one event display, we see that for negative polarity and high momentum positive polarity settings, about 5% of the expected rate of "2 track" events result in too many hits in the drift chambers. At low momentum, positive polarity, this fraction rises to about 25%. Thus, the total rate of "2 track" events contributing to track misidentification should be reduced by the number that cause too many hits in the chambers, since these are already corrected for in the tracking efficiency.

Finally, we can calculate the fraction of good events that will be lost in terms of the particle rate through the drift chambers (R - estimated using the rate in the plane of hodoscopes closest to the chambers) as follows,

$$P_{wrong\,track} = 0.1 \times C_{before/after} \times C_{too\,many} \times R \times \tau_{DC}, \tag{3.16}$$

where τ_{DC} is the effective amount of time for which the drift chambers will accept hits ($\approx$ 200 ns) and $C_{before/after}$ is the correction for the fact that some (or all) of the lost events in which the "extra" track comes before the track associated with the trigger are already taken into account in dead time and coincidence blocking corrections ($C_{before/after} = 0.5$ at negative polarity and/or high momentum and 0.75 at low momentum and positive polarity). $C_{too\,many}$ is the correction for the fact that some "2 track" events cause too many hits in the drift chambers, causing them not to be tracked at all, which is taken care of in the tracking efficiency calculation ($C_{too\,many}$=0.95 at negative polarity and high momentum positive polarity and 0.75 at low momentum positive polarity). The factor of 0.1 accounts for the fact that, given two tracks, the tracking algorithm will select the right track 90% of the time.

$P_{wrong\,track}$ is typically less than 0.1% at all settings in the HMS. In the SOS, $P_{wrong\,track}$ ranges from 0.1% to 0.7% at $P_\pi = 1.0$ GeV/c and from 0.1%

to 0.6% at $P_\pi = 0.29$ GeV/c. The uncertainty in this correction comes from the fraction of the time the tracking algorithm picks the correct track, 0.9 ± 0.05, and the effective drift chamber gate width. While the TDC cut is known, the hits for a single track have a range of TDC values, so $\tau_{DC} = 200 \pm 50$ ns. Since the correction is only significant in the SOS, and the rates at different ϵ settings are rather similar, the uncertainty in the correction is largely scale ($\approx 0.3\%$ in the worst case) with negligible amplification between ϵ settings.

3.4.5. SOS Čerenkov Signal Blocking

Another correction similar in nature to the "2 track" correction discussed above is the SOS Čerenkov signal blocking. As discussed in Section 3.3.2, the SOS gas Čerenkov is used to separate negatively charged pions from electrons. The window during which the gas Čerenkov ADC is read out is about 140 ns long. Signals associated with the trigger show up at about 55 ns, hence if a particle passes through the gas Čerenkov within about 85 ns after the first particle, some fraction of the signal caused by the second particle will also be read out and associated with the initial trigger. This means that if an electron passes through the detector less than 85 ns after a pion, there will be some Čerenkov signal associated with that pion and the event discarded due to the cut used in the analysis.

A sample spectrum of the SOS Čerenkov TDC is shown in Figure 3.15 for events in which the SOS Čerenkov produced a minimum of 2 photoelectrons (the nominal electron cut). The prominent peak in the center corresponds to the case where there are no early or late "extra" electrons for the event. The broad background to the left and right of the peak comes from electrons (not associated with the original trigger) that pass through the gas Čerenkov detector volume

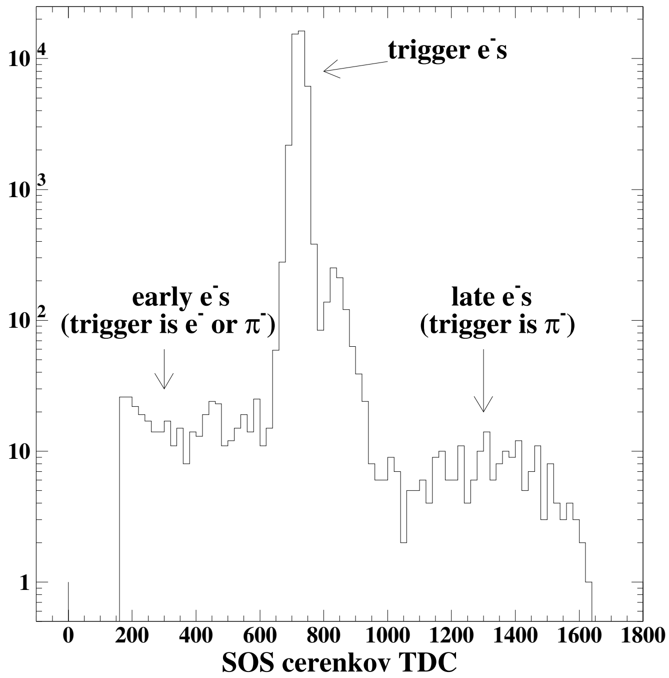

FIGURE 3.15. SOS Čerenkov TDC spectrum for events identified as electrons by the Čerenkov ADC. The peak corresponds to the signal from electrons that cause the trigger, while the backgrounds to the left and right come from earlier and later electrons, respectively. The scale is 10 TDC channels/ns.

before and after (respectively) the original "trigger" electron. In the case where we are concerned about electrons contaminating the coincidence pion signal, only the region to the right is of concern as any early single electrons will cause the coincidence time to be "blocked" as described in Section 3.4.3.

The number of pions lost to these "Čerenkov blocking" electrons can be calculated from the raw electron rate and the effective Čerenkov TDC width (≈ 85 ns). The SOS Čerenkov blocking is then,

$$SOS\ \check{C}\ Block = 1 - P_e R_{scin} \tau_{\check{C}}\ , \tag{3.17}$$

where $\tau_{\check{C}}$ is 85 ns, R_{scin} is the raw particle rate through the Čerenkov detector (as determined using the scintillator signals), and P_e is the fraction of those events that are electrons. The electron fraction can be determined from looking at the singles triggers, which provide an unbiased sample of the particles entering the spectrometer (as opposed to the coincidences which are biased in favor of pions). Fortunately, the electron fraction does not depend strongly on current, but only on kinematic setting (i.e. beam energy and spectrometer angle and momentum) and target. Hence, it is sufficient to determine the electron fraction from a small sample of runs at each setting. The electron fraction and size of the correction at each kinematic setting and each target for representative runs is shown in Table 3.4. It is important to note that the correction can be large (up to 4-5%) and is quite different at the different ϵ settings. This is quite important in that failure to account for this effect can dramatically affect the separation of the longitudinal and transverse cross sections.

The SOS Čerenkov blocking correction can be checked by making use of the fact that all "coincidence" electrons entering the SOS are random coincidences, hence they should subtract away if not removed by the SOS Čerenkov cut.[12] Therefore, the size of the blocking correction should correspond to the difference in random subtracted, real pion coincidences with and without the Čerenkov cut. The

[12]One may wonder why we bother to separate the pions and electrons at all if the random electrons just subtract away. At some settings, the increase in the number of random coincidences that comes from not cutting away the electrons increases the statistical uncertainty an unacceptably large amount. Even in those cases where the increase in statistical uncertainty is comparable to the uncertainty in the blocking correction, one must keep in mind that we are also sensitive to distributions in this analysis. Some of these distributions have low statistics tails in which the loss of statistical precision is much greater than for the integrated counts alone. Therefore, to maximize our ability to analyze the data distributions, it is preferable to cut away the random electrons.

W (GeV)	ϵ	Target	P_{e^-}	e$^-$ Rate (kHz)	SOS Č-block (%)
1.15	0.437	D	0.648	123.2	1.05
		He	0.790	140.3	1.19
	0.861	D	0.074	7.1	0.06
		He	0.123	4.1	0.04
1.60	0.490	D	0.873	554.4	4.71
		He	0.892	452.6	3.85
	0.894	D	0.103	18.8	0.16
		He	0.126	12.0	0.10

TABLE 3.4. SOS Čerenkov blocking effect at each kinematic setting for each (relevant) target. Note that the correction is quite different at each ϵ setting, significantly affecting the extraction of the longitudinal and transverse cross sections. The blocking effect shown here is for a particular representative run at each setting/target.

Čerenkov blocking effect is largest for the $W = 1.6$, low ϵ, deuterium data. In this case, the mean electron rate is 536.2 kHz and the expected correction is 4.56%. The difference in random subtracted yields (with and without Čerenkov cut) at this setting is $4.48 \pm 0.15\%$, in good agreement with the expected value.

The uncertainty in the SOS Čerenkov blocking correction mainly comes from the size of the Čerenkov timing window. Depending on the time of the original trigger, the Čerenkov TDC has some range of values up to which it will accumulate the ADC signals. Also, the shape of the signal going to the ADC will determine what fraction of the signal must be included in the ADC gate, introducing some small variation in the effective gate width. Looking at the TDC distributions for a variety of runs and kinematics, the TDC window is taken to be 85 ± 5 ns. This corresponds to an uncertainty in the worst case of about 0.3%. Since the rates are so different at each ϵ setting, this uncertainty propagates directly into the longitudinal and transverse separations with little cancellation (although there will be some cancellation in the separated target ratios).

3.4.6. Helium-3 Pressure Correction

During the running of E91003, the helium-3 target cell developed a small leak. Fortunately, the loss of material was slow enough that the target was still usable. However, because of the leak, the pressure of the material in the target changed over time. Since the helium-3 target was a high pressure target, this had definite and measurable effects on the target density.

Fortunately, the pressure of the helium-3 target material is incorporated in the stream of data acquired during runs. Using the average pressure as measured during the run (the pressure did not change a significant amount over the course of a single run), the data is normalized run-by-run to a common helium-3 target density at a pressure of 130 psi (the actual pressure of the target ranged from 122 to 140 psi). The pressure dependence is interpolated from data tables, which give the absolute density to a precision of 1% [37] . The pressure gauge used to monitor the pressure in the target cell is good to 1%, and since $d\rho/\rho \approx 0.4(dp/p)$, the relative density is monitored to a precision of 0.4%.

The effect of the helium-3 target pressure correction is shown in Figure 3.16. Here, charge normalized SOS pretriggers (including corrections for target heating effects) from the $W = 1.15$ GeV, low ϵ, π^- running is plotted as a function of target pressure. Although the target density changed by more than 2% over the course of this running, the pressure correction calculated as described above removes the dependence on target pressure.

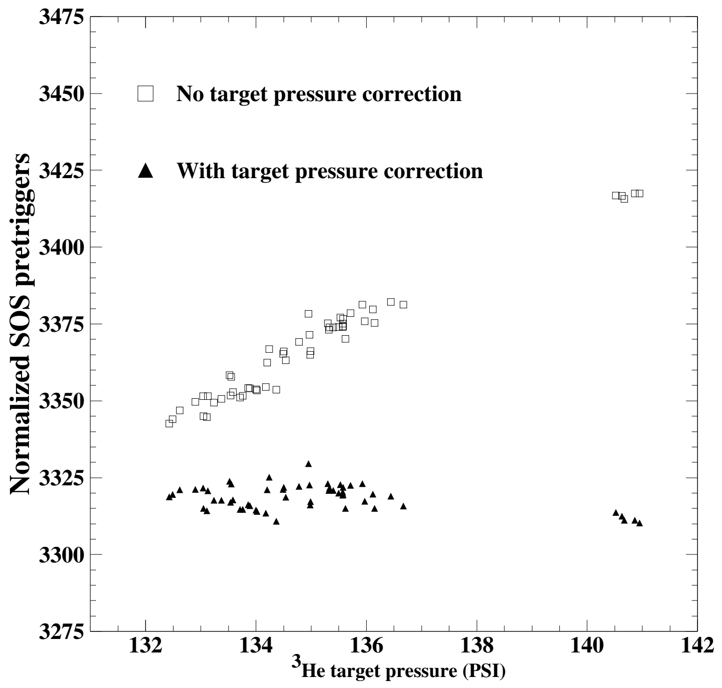

FIGURE 3.16. Charge normalized SOS pretriggers as a function of helium-3 target pressure. Points are from the $W = 1.15$ GeV, low ϵ, π^- data. Squares are uncorrected data while triangles include the pressure correction described in the text (i.e. normalized to the target density at a pressure of 130 psi).

3.4.7. Pion Absorption in the SOS

One of the larger corrections is that for pion absorption in the materials that the pion traverses on its way to the SOS and inside the SOS detector hut itself. Pions may interact hadronically resulting in no pion in the final state in the case of true absorption, or in very large angle scattering such that the pion fails to remain in the spectrometer acceptance. It will be seen that the overall uncertainty in this correction is rather large, however, since we are primarily interested in ratios of cross sections, the uncertainty largely cancels.

The fraction, T, of pions that do not interact (hadronically) on the way to and through the SOS can be expressed,

$$T = e^{-\sum \lambda_i t_i} , \tag{3.18}$$

where t_i is the thickness of the ith material and λ_i is the interaction length of that material. The interaction length is given by,

$$\lambda = \rho N_A \frac{\sigma_A}{A} , \tag{3.19}$$

with ρ the material density, N_A is Avogadro's number, A is the atomic mass and σ_A is the relevant π-A cross section. Hence, given the appropriate cross sections and materials properties, the pion transmission can be calculated.

The large uncertainty in this calculation is the choice of which π-A cross section is the most appropriate; the total cross section (all hadronic interactions), the "true" absorption cross section (no pions in the final state), or the reaction cross section (all hadronic interactions excluding elastic scattering). The true absorption cross section, being a subset of the total and reaction cross sections, is the smallest of the three alternatives and gives an upper limit to the transmission calculation. On the other hand, the total cross section, which encompasses all hadronic interactions, can serve as a lower limit. Certainly, one would expect that since the elastic cross section is peaked in the forward direction, a large number of elastic events would still give a good trigger. Furthermore, even pions that scatter inelastically may still give a valid trigger. Hence, the transmission is calculated using the reaction cross section (= absorption + inelastic) which is roughly the mean of the total and absorption cross sections. The uncertainty is then taken from the transmission as calculated using the two limiting cases of absorption and total cross sections.

Pion kinetic energy (MeV)	π^+		π^-	
	σ_0 (mb)	q	σ_0 (mb)	q
85	26.03	0.948	(32.49)	(0.858)
125	84.47	0.659	103.9	0.587
165	117.3	0.560	142.3	0.491
205	117.4	0.534	(140.4)	(0.475)
245	101.9	0.545	(120.1)	(0.491)
315	69.58	0.608	(79.86)	(0.560)
584	42.5	0.699	43.8	0.699
712	44.7	0.689	46.1	0.688
870	47.9	0.679	49.4	0.677
1228	46.5	0.683	46.5	0.689
1447	45.2	0.688	44.7	0.696
1865	39.6	0.704	38.8	0.712

TABLE 3.5. Parameterization constants for A dependence of π-A reaction cross section. The cross section is fit to the form $\sigma_A = \sigma_0 A^q$. Numbers in parentheses are not fit from actual data, but interpolated from π^-/π^+ ratios at other energies.

For large A materials ($A > 4$), the A-dependence of the π-A cross section is calculated using a parameterization of the form,

$$\sigma_A = \sigma_0 A^q \ , \tag{3.20}$$

with σ_0 and q fit from experimental data. For $P_\pi < 430$ MeV/c, absorption, reaction, and total cross section data from Ref. [38] are fit. For $P_\pi > 430$ MeV/c, reaction cross section data from Ref. [39] are fit. The total and absorption cross sections are estimated by extrapolating the low energy data to higher energy, using the energy dependence of the reaction cross sections as a guide.

A table of σ_0 and q vs. pion energy is used to interpolate the cross section used for each material (see Table 3.5). For example, given a pion with kinetic energy $T_\pi = 600$ MeV passing through some material, the A-dependent cross section is calculated at $T_\pi = 584$ and 712 MeV using Equation 3.20 and Table 3.5, and the cross section at $T_\pi = 600$ MeV interpolated from those two values. The interaction length is then calculated from Equation 3.19.

For the special case of $A \leq 3$ (i.e., the cryogenic targets), the implementation is less straightforward. The A dependence as given by Equation 3.20 breaks down, and one should use actual data where possible. For hydrogen and deuterium, total cross section data is available in Ref. [40]. Unfortunately, data breaking down the cross section into its component parts is not in abundance, so the approximation that the reaction cross section is approximately half the total cross section is used. This approximation is quite good for large A materials and even holds experimentally in helium-4 [41]. There is even less experimental data for helium-3, however, calculations [42] consistent with elastic scattering data indicate that one can well estimate the $\pi-^3$He total cross section by 1.5 times the $\pi-^2$H cross section. Fortunately, in all cases, the transmission through the target is quite large ($> 98.5\%$), so even a rather large uncertainty in these estimates is tolerable. The random uncertainty between targets (relevant for the ratios) is estimated by comparing the transmission through each target as calculated using the total cross sections (a worst case scenario) and is found to be $\approx 1\%$ for $P_\pi = 0.29$ GeV/c and $\approx 0.5\%$ for $P_\pi = 1.0$ GeV/c.

One expects the ϵ dependence of the correction at each P_π to be quite small since the π-A cross section depends only on the pion momentum. Tests indicate that this is indeed the case and that the correction for pion absorption varies by less than 0.1% as a function of ϵ setting. The dependence on pion polarity (relevant for deuterium π^-/π^+ ratios) is also found to be rather small. At low P_π the difference in the transmission based on the models used in the analysis is $\approx 0.4\%$ and the

P_π	Transmission	δ_{target}	$\delta_{polarity}$	δ_{xsec}
(GeV/c)	%			
0.29	≈90	1.0	0.4	5.8
1.0	≈95	0.4	0.0	3.5

TABLE 3.6. Uncertainties in pion absorption correction. δ_{xsec} refers to the uncertainty coming from choice of π-A cross section, (total,reaction, or true absorption) - this uncertainty is not random in the L-T separation and cancels in the target ratios. δ_{target} refers to the uncertainty between the targets (hydrogen, deuterium, and helium-3) and $\delta_{polarity}$ is the uncertainty between pion polarity (π^- vs. π^+).

uncertainty is taken to be the size of the difference. At high P_π, the difference is estimated to be less than 0.1% and no uncertainty is assigned.

The size of the corrections and relevant uncertainties are summarized in Table 3.6. The transmission is calculated using the list of materials given in Table 4.1. The pion is considered to be detected if it makes it through 25% of the third layer of scintillators (far enough to give a valid 3/4 trigger). The pion absorption is accounted for in the Monte Carlo event-by-event. Hence, the variation of the π-A cross section with the pion momentum (across the SOS δ acceptance) is taken into account. Also, one can include the fact that muons coming from pions that decay in flight will not interact hadronically, and hence will not be absorbed.

4. MONTE CARLO OF THE EXPERIMENT

4.1. Overview

SIMC, the standard Hall C Monte Carlo, is based on the SIMULATE code written for SLAC experiment NE18 [43, 44]. The main structure has been retained, substituting the Hall C coordinate system and spectrometer Monte Carlos. Unlike some Monte Carlos, SIMC does not simulate detailed detector response. Rather it is used more in the sense of an aperture checking simulation. In general, SIMC works as follows. For a given event, initial quantities such as position at the target and kinematic quantities such as electron scattering angle are generated. The initial kinematic generation limits are set by the user, generally larger than the physical acceptance of the spectrometers. Checks are made as to whether a given event is kinematically possible and the event is radiated and propagated through the target, checking for energy loss and multiple scattering. Events are then sent to the single arm Monte Carlos. These Monte Carlos simulate the magnetic optics of the Hall C spectrometers and the event trajectories are calculated as they travel through the magnets into the spectrometer huts. Inside the huts, the events are checked to see if they strike the relevant detectors necessary to give a valid trigger. Since the detector response is not simulated, all inefficiencies are corrected for in the data (aside from the pion absorption correction described in Section 3.4.7). Successful event trajectories are smeared inside the huts and tracks fit. Finally, for each successful event, a weight is calculated which consists of a model cross section modified by a radiative correction weight, an event generation weight, and a Jacobian that accounts for the fact that the event is generated in spectrometer coordinates instead of physics coordinates.

It is worth noting that while SIMC does not attempt to simulate detailed detector response, great care is taken to ensure that all kinematic and phase space quantities are handled in a realistic manner. For example, the rastering of the electron beam, as well as the energy spread and transverse size of the beam are all accounted for. Effects such as multiple scattering, ionization energy loss and finite resolution in track fitting are also included.

While the original NE18 Monte Carlo was used exclusively for $(e, e'p)$ type reactions, SIMC has been modified to handle meson electroproduction as well. Previous experiments have successfully used SIMC to model kaon electroproduction [45, 36], and Ref. [27] has used SIMC for the analysis of pion electroproduction data.

4.2. Pion Electroproduction

Experiment E91003 uses SIMC to model pion electroproduction in hydrogen, deuterium and helium-3. While the implementation is rather straightforward for production from hydrogen, the situation is a bit more complicated for production from the nuclear targets. In the $(e, e'p)$ case, where the aim is often the extraction of the nuclear structure itself, one generally iterates the spectral functions until good agreement is found between the data and the Monte Carlo distributions. In the case of pion electroproduction, the nuclear structure itself is of secondary interest. In this case, the production is assumed to be quasifree, i.e. the pion is produced from a non-interacting proton (or neutron in the case of π^- production) with some initial momentum coming from the Fermi motion in the nucleus. While this procedure sounds straightforward, there are many ambiguities and often "quasifree" is taken to mean different things by different people. The next section will focus on these issues and describe the event generation method used in SIMC.

4.2.1. Event Generation

In the case of pion electroproduction from hydrogen, the cross section is five-fold, so five quantities must be generated. In SIMC, the variables of choice are the spectrometer in-plane and out-of-plane angles for both the electron and pion arms, as well as the final electron energy. All of these quantities are generated with a flat distribution with the limits taken to be larger than the spectrometer acceptance (with some slop added to account for multiple scattering and energy loss) so as to ensure that the available phase space is filled. With these five variables specified, the kinematics are totally determined and the pion momentum is calculated.

In the case of pion production from a nuclear target (deuterium or helium-3) the situation is more complicated. There is an extra degree of freedom in that the differential cross section is now six-fold, and the final pion momentum is not specified by the above five variables. However, one can assume quasifree production from one of the nucleons in the nucleus. In SIMC this is implemented using a momentum space wave function for the "struck" nucleon. The deuterium wave function is based on a Bonn potential calculation [45] while the wave function for helium-3 is based on a Fadeev calculation [46]. The nucleon momentum is generated according to the momentum distribution while the direction is generated uniformly in $\cos\theta$ and ϕ.

Since the struck nucleon is bound in a nucleus, the energy of the struck nucleon is not specified by its momentum, i.e.,

$$E_N^2 - p_N^2 \neq m_N^2 \, . \tag{4.1}$$

Hence, some off-shell prescription must be chosen to fully determine the kinematics. In SIMC, the philosophy has been taken that, since the "spectator" nucleon (or nucleons) is not an active participant in the reaction, there is no mechanism by which to knock it on-shell. Therefore, the spectator is taken as on-shell in the initial state, and the energy of the off-shell, struck nucleon is then given by the requirement that the total momentum of the nucleus is zero, and the total energy is the mass of the nucleus, M_A. In the case of the deuteron, then, the energy of the struck nucleon is

$$E_{struck} = M_D - \sqrt{m_{spectator}^2 + p_{Fermi}^2}\,, \tag{4.2}$$

where M_D is the deuteron mass, $m_{spectator}$ is the on-shell spectator nucleon mass, and p_{Fermi} is the momentum of the struck and spectator nucleons.

In the case of helium-3, the off-shell prescription is more complicated. Not only is there the momentum of the struck nucleon, but the two spectators can have some relative momentum between them. To address this issue, a simple model spectral function is used. A spectral function describes the probability to find a nucleon in a nucleus with some momentum and energy. Typically, this is described in terms of the so-called missing momentum, P_m, and missing energy, E_m. In this case, P_m is simply what we have called p_{Fermi}, while E_m is the difference between the invariant mass of the spectator nucleons + (on-shell) struck nucleon mass from the target nucleus mass,

$$E_m = M_{2spec} + M_{struck} - M_{3He}\,. \tag{4.3}$$

In our case, we use E_m from the spectral function to determine the invariant mass of the 2-spectator system. Then the energy of the struck nucleon is given by,

$$E_{struck} = M_{3He} - \sqrt{M_{2spec}^2 + p_{Fermi}^2}\,. \tag{4.4}$$

The spectral function used is a factorized (we assume the E_m and P_m distributions are independent) approximation of a calculation [47] fit to ${}^3\mathrm{He}(e, e'p)$ data [48].

Both the helium-3 and deuterium off-shell prescriptions give good starting points in describing the experimental data. As will be discussed in Chapter 5 however, some additional modification via the application of nucleon-nucleon final state interactions is necessary to fully describe the process accurately.

4.2.2. Model and Jacobian

Once the generated variables have been thrown and the pion momentum determined as described above, the five fold cross section must be calculated. As described in Chapter 1, most models of pion electroproduction are written as the product of the virtual photon flux (Γ) and the center of mass two-fold $\gamma^* N \to \pi N'$ cross section. For production from hydrogen, implementation of the model is straightforward, and one need only calculate the Jacobian that takes one from the γ^*-N center of mass to the lab frame. Since the boost to the center of mass frame is along the virtual photon three momentum, $\mathbf{q}$, this Jacobian is not difficult to calculate.

For the nuclear targets, where it is assumed that the production is from a nucleon that is now moving, things are more difficult. First, one must deal with the issue that, in any cross section calculation, the first factor is the relative collinear velocity between the projectile and the target,

$$d\sigma \sim \frac{1}{|\mathbf{v_{projectile}} - \mathbf{v_{target}}|} \ldots \tag{4.5}$$

For an electron impinging on a stationary target, this just gives a factor of E_e/p_e. In the quasifree model, the nucleon moves. Furthermore, this motion is not necessarily collinear with the impinging electron. Therefore, the usual cross section expression must be corrected by the factor $[1 - \mathbf{p_{Fermi}} \cdot \mathbf{p_e}/(E_{struck}p_e)]$, where the fact that $E_e \approx p_e$ for relativistic electrons has been used to simplify the expression.

Finally, one must now calculate the transformation that takes one from the center of mass to the lab. Since the nucleon momentum is not collinear with the virtual photon momentum, the boost is not necessarily collinear with either $\mathbf{q}$ or the nucleon momentum. The Jacobian of the cross section transformation is quite complicated, and a derivation is given in Appendix B. Note that often, it is useful to ignore any components of $\mathbf{p_{Fermi}}$ transverse to $\mathbf{q}$ when calculating these transformations, and this is a good approximation for $q >> p_{Fermi}$. However, for E91003 kinematics, $|\mathbf{q}| \approx \mathbf{0.8} - \mathbf{1.3}$ GeV/c, while some significant fraction of the deuterium and helium-3 wave functions contribute at $|\mathbf{p_{Fermi}}| > \mathbf{0.1}$ GeV/c. The resulting quasifree model cross section is given by,

$$\frac{d^5\sigma}{d\Omega_e dE_e d\Omega_\pi} = J(\Omega^* \to \Omega^{lab}) \left[1 - \frac{\mathbf{p_{Fermi}} \cdot \mathbf{p_e}}{E_{struck}p_e}\right] \Gamma \frac{d\sigma}{d\Omega^*_\pi}\,, \tag{4.6}$$

where all quantities used in the model (W, θ_{cm}, ϕ_{cm}) are calculated in a manner consistent with the kinematics used in the event generation so that the center of mass cross section is truly evaluated in the frame where the total momentum is zero.

It is important to note that because of the iteration procedure used to analyze the data, the method used to extend the elementary model cross section to quasifree scattering has little or no impact on the extraction of the experimental cross sections (except to make the analysis more efficient), but it does come into play in the calculation of the so-called "quasifree correction". This correction will be described in more detail in Chapter 6.

4.3. Spectrometer Models

After the vertex quantities for each particle have been generated, they are sent to the single arm Monte Carlos where they are transported through the magnetic elements using a COSY INFINITY [32] model. In the case of the SOS, the COSY model of the dipoles was generated using field map data taken prior to assembly of the SOS. The SOS quadrupole was assumed to be a standard, simple quadrupole for the model. In the case of the HMS, the COSY model was adjusted so that it agreed with optics data taken during the first part of E91003.

In Chapter 3 the correlation between $hsxpfp$ and missing mass was discussed. It was discovered in the course of the analysis that this effect likely came about from a field offset in Q3 (probably due to some small offset in the set current). Although a momentum dependent correction in the $< hsxpfp|\delta >$ matrix element was fit to correct for the effect, it is clear that such a simple correction is not quite adequate at lower momentum. Rather than try to further correct the data, the Q3 offset is simulated in the HMS Monte Carlo. One can parameterize the size of the offset by looking at the Q3 current read-back divided by the central momentum. If there is no offset, the ratio should be constant as a function of P_{HMS}. This ratio is shown in Figure 4.1. A modification to the Q3 field is implemented in the Monte Carlo based on the I_{Q3}/P_{HMS} curve. Note that the curve is normalized to 1.0 at $P_{HMS} = 0.55$ GeV/c - this is because the optics data used to match the COSY model to the data was taken at approximately that central momentum. The Q3 offset effect is implemented in the Monte Carlo by adjusting the particle momentum by the appropriate amount just prior to traversing Q3, and then returning the particle to its nominal momentum just after exiting Q3. This solution, while perhaps not ideal, is much simpler than creating a momentum dependent COSY model for Q3 and describes the data adequately. The $hsxpfp$-missing mass

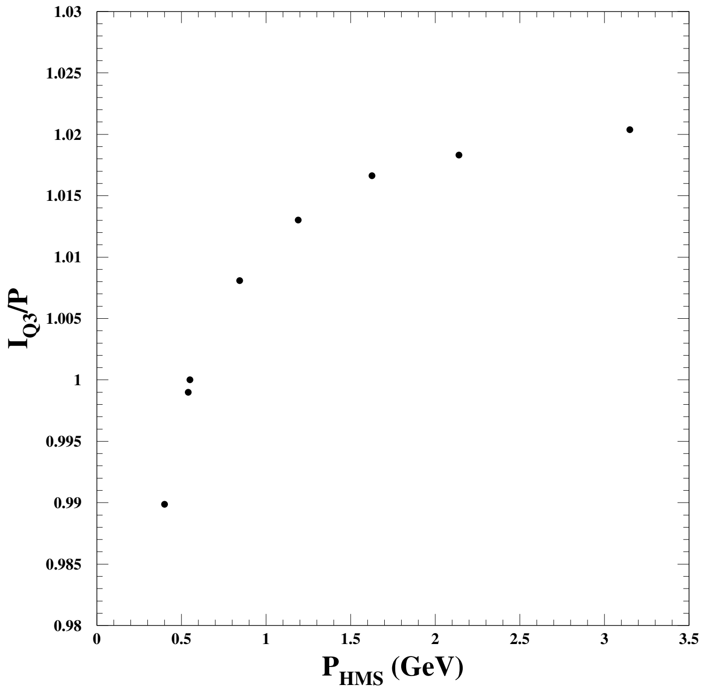

FIGURE 4.1. I_{Q3}/P_{HMS} normalized to 1.0 at $P_{HMS} = 0.55$ GeV/c. Ideally, the ratio should be constant as a function of HMS central momentum. A modification to the HMS Q3 field as used in the HMS single arm Monte Carlo was determined from these points.

correlation effect as simulated with the Q3 offset in SIMC is compared to the effect in the data in Figure 4.2 for $P_{HMS} = 0.54$ GeV/c and $P_{HMS} = 2.14$ GeV/c. Both the simulated and actual data are then corrected by the ad-hoc $< hsxpfp|\delta >$ momentum dependent matrix element discussed in Chapter 3.

In both the HMS and SOS, the matrix elements are sequential. This means that the particle is transported in a step-like manner. For example, in the HMS, one might transport the electron from the target to the entrance of the first quadrupole, from there to the middle of the first quadrupole and so on. This is in contrast to

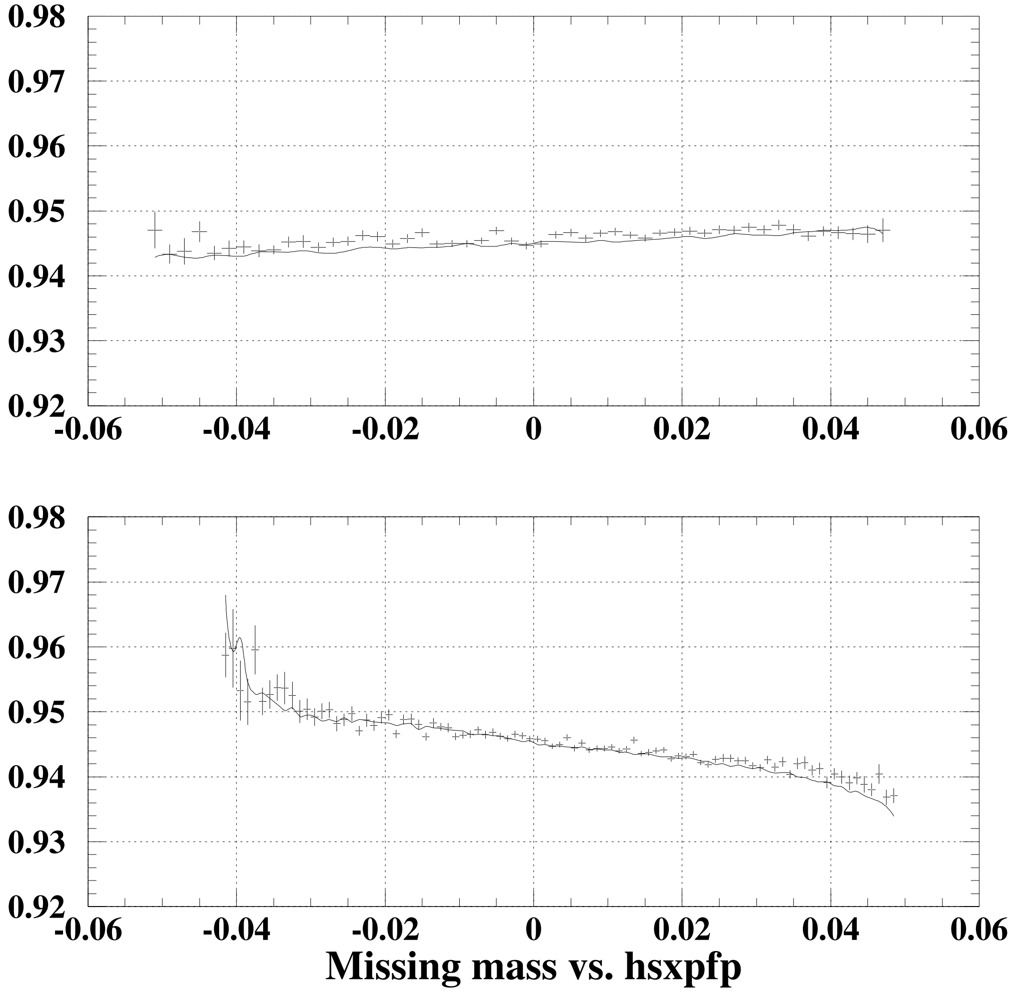

FIGURE 4.2. Correlation between reconstructed neutron mass (missing mass) and $hsxpfp$. The solid line is the effect in SIMC when modifying the Q3 effective field while the crosses are experimental data. The top plot is for $P_{HMS} = 0.54$ GeV/c while the bottom is for $P_{HMS} = 2.14$ GeV/c.

the simpler implementation of COSY in which the steps are always from the target, i.e., from the pivot to the Q1 entrance, from the pivot to the middle of Q1, etc. The sequential nature of the forward matrix elements are important in that they enable SIMC to model pion decay.

4.4. Passage Through Materials

4.4.1. Multiple Scattering

To better match the resolution of the data, it is necessary to simulate the effect of Coulomb multiple scattering in the target and spectrometers. SIMC uses a parameterization of a Molière scattering calculation [40]. The new scattering angle of the particle after it traverses a certain material (or combination of materials) is given by,

$$\theta^{new}_{(x,y)} = \theta_{(x,y)} + g\,\theta_{rms}\ , \tag{4.7}$$

where $\theta_{(x,y)}$ denotes the scattering angle in one of the two directions transverse to the particle direction of motion, g is a randomly selected Gaussian distributed number, and θ_{rms} is the width of the multiple scattering distribution. θ_{rms} is given by,

$$\theta_{rms} = \frac{13.6}{\beta p}\sqrt{t}\,[1 + 0.038\ln t]\ , \tag{4.8}$$

where t is the thickness of the material in radiation lengths, β is the particle spped, and p is the particle momentum in MeV. The materials used in the multiple scattering calculations are shown in Table 4.1

The parameterization of θ_{rms} given above has been shown to agree with calculations of Molière scattering to 11% (or better) for all Z and $\beta = 1$ particles.

Object	Material	Thickness (cm)	Density (g/cm^3)	X_0 (g/cm^2)	Radiation Lengths(%)
Target windows	Al	2(0.013)	2.70	24.01	0.292
Targets	Liquid H	4.0	0.0733	61.28	0.478
	Liquid D	4.0	0.167	122.6	0.545
	Helium-3	4.0	0.0769	64.77	0.474
Scattering chamber window	Al	0.0406	2.70	24.01	0.456
Chamber-HMS gap	air	15	0.00121	36.66	0.050
HMS entrance window	kevlar	0.0381	0.74	55.2	0.0511
	mylar	0.0127	1.39	39.95	0.0443
HMS exit window	kevlar	0.0381	0.74	55.2	0.0511
	mylar	0.0127	1.39	39.95	0.0443
Dipole-DC gap	air	35	0.00121	36.66	0.1155
HMS DC windows	mylar	4(0.0025)	1.39	39.95	0.0178
HMS DC gas	Ar/ethane	12(1.8)	0.00154	27.38	0.121
HMS DC sense wires	W	12(5.89x10^{-6})	19.3	6.76	0.020
HMS DC field wires	Be/Cu	36(0.00018)	5.40	38.88	0.090
HMS S1X	polystyrene	1.067	1.03	43.8	2.51
HMS S1Y	polystyrene	1.067	1.03	43.8	2.51
HMS Č windows	Al	2(0.102)	2.70	24.01	2.28
HMS Č gas	C_4F_10	135	0.0246	23.7	1.40
HMS Č mirror	SiO_2				0.5
HMS S2X	polystyrene	1.067	1.03	43.8	2.51
HMS S2Y	polystyrene	1.067	1.03	43.8	2.51
Air gaps from DC to S2y	air	239	0.00121	36.66	0.789
Scattering chamber window	Al	0.0406	2.70	24.01	0.456
Chamber-SOS gap	air	15	0.00121	36.66	0.050
SOS entrance window	kevlar	0.0127	0.74	55.2	0.017
	mylar	0.0076	1.39	39.95	0.026
SOS exit window	kevlar	0.0381	0.74	55.2	0.051
	mylar	0.0127	1.39	39.95	0.044
Dipole-DC gap	air	15	0.00121	36.66	0.050
SOS DC cathode foil	mylar	14(0.00127)	1.39	39.95	0.062
SOS DC sense wires	W	12(35.4x10^{-6})	19.3	6.76	0.121
SOS DC gas	Ar/ethane	12(0.617)	0.00154	25.72	0.044
SOS S1X	polystyrene	1.040	1.03	43.8	2.44
SOS S1Y	polystyrene	1.098	1.03	43.8	2.58
SOS Č windows	Al	2(0.05)	2.70	24.01	1.12
SOS Č gas	Freon-12	100	0.0051	23.7	2.152
SOS Č mirror	SiO_2	2.0			0.05
SOS S2X	polystyrene	1.040	1.03	43.8	2.44
SOS S2Y	polystyrene	1.098	1.03	43.8	2.58
Air gaps from DC to S2y	air	174	0.00121	36.66	0.574

TABLE 4.1. Materials seen by particles as they pass through the target and spectrometers. The first group is common to both the scattered electron and the electroproduced pion. The second group is relevant to particles in the HMS (electron) and the third group lists materials seen by particles entering the SOS (pions). This list is used in Monte Carlo calculations of multiple scattering and in estimating pion absorption in the SOS (see Section 3.4.7).

Note that this is not the same as saying that the parameterization agrees with experimentally measured multiple scattering distributions. However, tests indicate that changing the width of the distribution by as much as a factor of two has negligible impact on the number of events accepted by the Monte Carlo. For the purposes of this analysis, slight deviations in resolution between experimental and simulated distributions are acceptable.

Multiple scattering is applied to the both the incoming and outgoing electrons, as well as the pion. The effect of the incoming electron multiple scattering is modeled by applying a correlated modification to the outgoing electron and pion. This simplifies the calculation of the relevant scattering angles needed for the input physics model, but should have the same effect on the overall resolution.

4.4.2. Ionization Energy Loss

As the incident and scattered electron and the pion travel through the thick cryogenic target and target can, they lose energy to the ionization of atoms within the materials. While the mean energy loss is typically parameterized using the well-known Bethe-Bloch equation (see Ref. [40] for details), it is known that the energy loss follows a Landau distribution. Rather than simply use the mean energy loss for each event, SIMC calculates a Landau distributed energy loss. The energy loss distribution is easily characterized in terms of the most probable energy loss, E_{prob}, and the width of the distribution, ξ.

The most probable energy loss for a relativistic particle traversing a (thin) layer of material is given by [49],

$$E_{prob} = K\frac{Zt}{A\beta^2}\left[\ln\frac{m_e}{I^2} + 2\ln\frac{P}{M} + \ln\frac{KZt}{A\beta^2} - \delta - U + 1.06\right] , \qquad (4.9)$$

where $K = 0.15354$ MeV cm^2/g, t is the material thickness in g/cm^2, M and P are the mass and the momentum of the incident particle, and β is the velocity of the particle in units of c. Z and A refer to the atomic number and mass of the material. In the case of a mixed material, the effective Z and A are calculated weighted by the relative abundance in the mixture. I is the mean ionization energy of the material, δ is the so-called density effect correction, and U is the correction term for non-participation of the higher shell electrons at low energies of the incident particle. Calculation of I, δ, and U is more fully explained in Refs. [49] and [50].

Given the most probable energy loss, the true energy loss can be calculated using some randomly Landau distributed number λ,

$$\lambda = \frac{E_{lost} - E_{prob}}{\xi} , \tag{4.10}$$

where $\xi = KtZ/A\beta^2$. [1]To generate the Landau distributed λ, we start with an approximation[2] to the true Landau distribution, $f(\lambda)$,

$$f(\lambda) \approx \frac{1}{2\pi} e^{-(\lambda + e^{-\lambda})/2} . \tag{4.11}$$

Then, making use of the fact that,

$$\int_{-\infty}^{+\infty} e^{-(\lambda + e^{-\lambda})/2} \, d\lambda = 2 \int_{0}^{+\infty} e^{-x^2/2} \, dx , \tag{4.12}$$

(where the substitution $x = e^{-\lambda/2}$ has been made) it is sufficient to generate a (positive) Gaussian distributed x. Then λ is given by $-2\ln(x)$.

SIMC calculates the energy loss of the incident electron as it passes through the aluminum can of the cryogenic target as well as the target itself. For the

[1]What follows is based on a function developed by S. Lebedev for the Phenix Collaboration at Brookhaven National Laboratory [51].

[2]This approximation gets the shape and width generally right, but tends to somewhat underestimate the high energy loss tail.

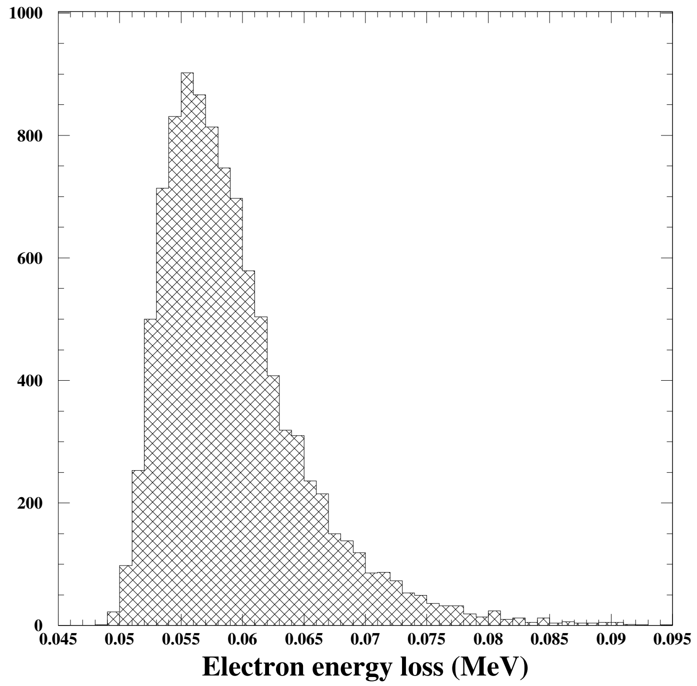

FIGURE 4.3. Simulated ionization energy loss spectrum. The distribution of the energy loss of the incident electron as it passes through the front of the aluminum can of the cryogenic target is shown.

scattered electron and produced pion, the energy loss due to passage through the remaining part of the target, the target can, and the scattering chamber and spectrometer windows is calculated. A simulated energy loss spectrum using the above method is shown in Figure 4.3. Consistent with the analysis of the data, the simulated incident and scattered electron energies as well as the pion energy are corrected by the most probable value of the ionization energy loss during event reconstruction. Technically, it is more correct to use the average energy loss, however, the difference (in absolute terms) between the most probable and average energy loss for a typical event is a small fraction of 1 MeV, negligible compared to the experimental resolution.

4.5. Pion Decay

As mentioned in Section 4.3, the use of sequential forward matrix elements in the single-arm Monte Carlos allows for the simulation of the decay of pions in flight. The primary charged pion decay mode is $\pi^{\pm} \rightarrow \mu^{\pm}\nu_{\mu}$ ($\approx$ 99.99%) and at E91003 kinematics, the fraction of pions that decay in flight is quite large. Approximately 44% (16%) at $P_{\pi} = 0.29$ (1.0) GeV/c of pions produced at the target decay before reaching the third layer of scintillators in the SOS (the minimum number needed to give a trigger).

The issue at hand is twofold. First, we must correct for the number of events lost when the pion decays and the resulting muon is not within the acceptance of the SOS. Second, we must understand those events for which the pion decays in flight and the resulting muon gives a trigger. The first correction is relatively easy to determine given the distance particles travel on their way through the spectrometer. The second issue is more subtle in that tracks from the muons distort the distributions of reconstructed variables.

Ideally, one would like to eliminate all muon tracks from the data sample and use a single correction factor to account for the number of pion decays. However, since the muon mass (0.105 GeV) is quite close to the pion mass (0.139 GeV), it is not possible to uniquely identify and separate the muons from the pions, either using time-of-flight or some kind of calorimetry.[3] Hence, SIMC is used to simulate

---

[3]In theory, it would be possible to place a thick absorber in the SOS detector hut that would eliminate most of the pions due to hadronic interactions. However, at these

pion decay and is used not only to account for the number of events lost, but to model the muon tracks that come from these decays.

In brief, the process is simulated as follows. For each "step" (where a step is defined as the distance the particle travels between apertures in the single arm Monte Carlo - for example, the first step is from the target to the entrance collimator, about 126 cm in the SOS) in the pion trajectory the pion is checked to see if it has decayed somewhere in that step. The probability that the pion would have decayed in a distance of length Z is,

$$P = 1 - e^{-Z/(\beta\gamma c\tau)} , \tag{4.13}$$

where $c\tau = 780.45$ cm is the characteristic decay length in the pion rest frame and $\beta\gamma$ is the boost necessary to evaluate the decay in the lab frame. For the current step, a random number, R , between 0.0 and 1.0 is generated, and the "decay distance" is calculated,

$$Z_{decay} = -\beta\gamma c\tau \ln(1 - R) . \tag{4.14}$$

If Z_{decay} is less than the pathlength of the current step (including deviations from the central trajectory), then the pion is forced to decay. In the case where the step is through free-space (i.e. no magnetic fields), the decay is generated exactly at Z_{decay} and the resulting muon trajectory is used to complete the step. In the case where the decay occurs during a step in a magnetic element, the decay is modeled at the nearest point where the sequential matrix elements are evaluated. If the pion decays in the first half of the step, the decay is implemented first, and then

energies, any absorber that is thick enough to remove the majority of pions would also stop a large fraction of muons as they lose energy to ionization energy loss. Thus, one could achieve a pure muon sample, but it would be biased to muons with higher energy.

the muon is transported. If the decay occurs in the second half of the step, the pion is transported and then the decay is implemented. In the SOS, the particles are transported through the quadrupole magnet in two steps, while the transport through each dipole is in one step. Tests were done with more steps added in the dipoles and no discernible difference in accepted decay fraction or the resulting distributions were found.

Figure 4.4 shows the (simulated) "decay distance" (i.e. the distance the pion travels from the target before decaying) of pions that decay into muons but still give a valid trigger in the SOS. Pions that decay close to the target have a higher chance of being accepted than those that decay within the magnetic elements. The SOS is designed to accept events coming from the target, so it seems reasonable that the closer to the target a particle decays, the better the chance that it will be accepted. On the other hand, a particle that decays just before or within the magnets is likely to have a trajectory that would not appear to be coming from the target if extrapolated backwards, hence reducing the likelihood that the optics would be conducive to guiding the decay muon to the detector hut. Note that pions that decay after ≈ 780 cm are beyond the drift chambers, so these events will still have good tracking information. In general, not many events should be lost once the pion makes it to the detector hut since the decay muons tend to be emitted in the forward direction. For standard analysis cuts, the decay fraction of the total accepted yield is about 17.5% for the $P_\pi = 0.29$ GeV/c data and about 8.3% for the $P_\pi = 1.0$ GeV/c data. However, if one excludes events that decay beyond the drift chambers (and thus have the tracks from the original pion) from that fraction, the contribution drops to about 3.5% in both cases.

While it is not possible to totally separate muon events from pion events experimentally, there are certain situations in which one can enhance the muon

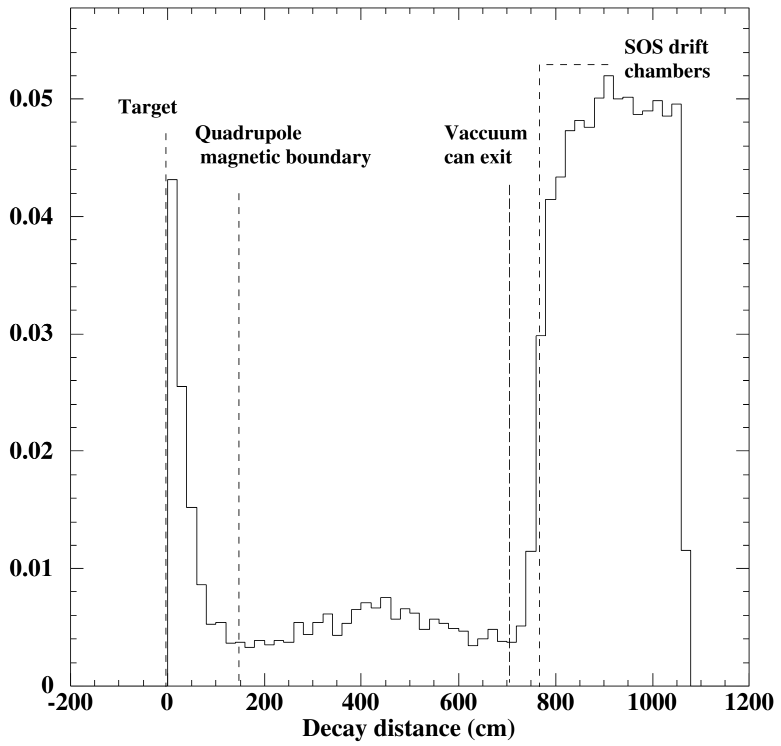

FIGURE 4.4. Simulated decay distance spectrum. Pions that decay into muons that still give a valid 3/4 trigger are shown. Pions that decay within the magnetic elements are less likely to be accepted than those that decay near the target or in the detector hut.

sample and hence test the SIMC model of pion decay. At the E91003 low momentum setting, muons coming from pions that decay near the target pivot ("prompt" decays) have a mean time of flight about 1 ns faster than the pions. This effect is apparent in the path-length corrected coincidence time. Figure 4.5 shows an experimental coincidence time spectrum. A small bump next to the real coincidences can be seen - these are the prompt decay muons coming from (mostly) real coincidences. Most of these events are cut out in the standard analysis by the ± 1 ns coincidence time cut. However, by adjusting the coincidence time cut to

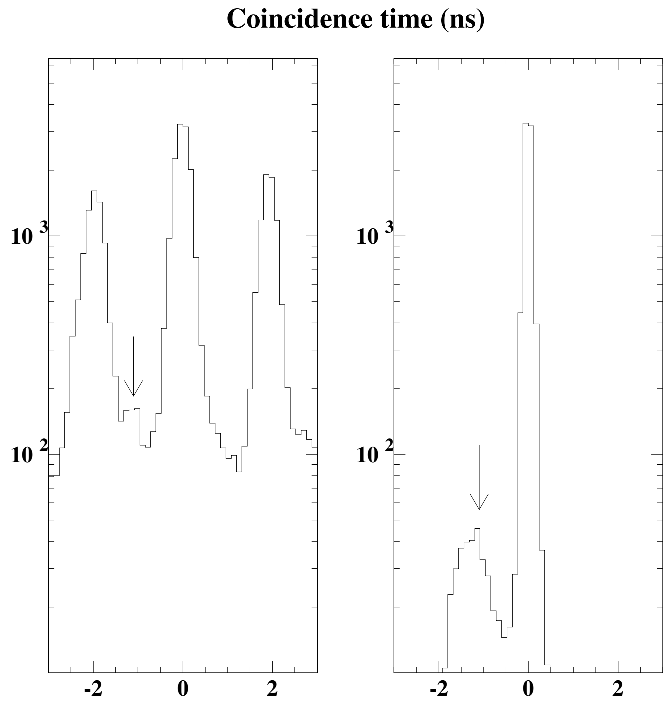

FIGURE 4.5. Coincidence time spectrum for low momentum pion data. The plot on the left is data (not random subtracted) and the plot on the right is Monte Carlo. A small bump at coincidence time < 0.0 (between the real coincidence peak and the random peak at $t = -2$ ns in the data plot) can be seen in both the data and the simulation. These events are from pions decaying into muons close to the target.

include the random peak immediately to the left of the real peak, and performing the appropriate random subtraction, one can get an estimate of the muon yield from the prompt decays by comparing to the "1 peak" subtracted yields. The ratios of 2-peak to 1-peak coincidence time cut yields are shown in Table 4.2 for both ϵ settings and all targets for the low pion momentum data set. These numbers are compared to the ratio of SIMC yields for the same coincidence time cuts. The

ϵ	Target	DATA $\frac{2-peak}{1-peak}$	SIMC $\frac{2-peak}{1-peak}$	Difference (DATA-SIMC)
0.437	H	1.032 $\pm$ 0.008	1.028	0.004 $\pm$ 0.008
	D(π^+)	1.033 $\pm$ 0.017	1.036	-0.003 $\pm$ 0.017
	D(π^-)	1.023 $\pm$ 0.021	1.032	-0.009 $\pm$ 0.021
	3He(π^-)	1.044 $\pm$ 0.025	1.038	0.006 $\pm$ 0.025
	Mean	1.032 $\pm$ 0.007	1.034	-0.002 $\pm$ 0.007
0.861	H	1.046 $\pm$ 0.008	1.030	0.016 $\pm$ 0.008
	D(π^+)	1.036 $\pm$ 0.016	1.037	-0.001 $\pm$ 0.016
	D(π^-)	1.020 $\pm$ 0.015	1.032	-0.012 $\pm$ 0.015
	3He(π^-)	1.052 $\pm$ 0.020	1.036	0.016 $\pm$ 0.020
	Mean	1.041 $\pm$ 0.006	1.034	0.007 $\pm$ 0.006

TABLE 4.2. Data to SIMC comparison of yields from promptly decaying pions. The "2-peak" and "1-peak" yields are as described in the text. Data uncertainties are statistical only.

overall agreement is very good, demonstrating the quality of the simulation of the $\pi^\pm \to \mu^\pm \nu_\mu$ process.

The comparison of the simulated prompt-decay muons to those measured in the data indicates that the muon tracks that are accepted in the SOS are well understood. Unfortunately, there is no definitive way to test our understanding of the absolute number of events that are lost to pion decay. However, the absolute number lost should depend mainly on the central momentum of the SOS and the distribution in SOS δ since the decay probability depends directly on the pion momentum. Since the pion momentum distributions are very similar at both epsilon settings and between the targets (for both the low and high P_π data), the pion decay fraction should be constant at a given P_π. Therefore, a random uncertainty of 0.5% between epsilon settings and targets and an overall scale uncertainty of 2.0% is assigned to the simulation of the in-flight pion decay.

4.6. Collimator Punch-Through

Despite the fact that the entrance collimators of the HMS and SOS are quite thick and are very effective at stopping electrons, the same is not the case for hadrons. In particular, some fraction of pions impinging on the SOS collimator are able to pass through, undergoing only multiple scattering and ionization energy loss. While a significant fraction of these punch-through events are not accepted, those that scatter into the acceptance are a non-negligible contribution to the total yield. This hadron punch-through effect has been encountered in an earlier experiment in Hall C [29]. In that case, protons punched through the HMS collimator, scattering into the HMS acceptance. Those proton collimator punch through events left long tails in HMS $ytar$, beyond the extent of the true target length. Hence, the proton punch-through events could be sampled at large HMS $ytar$ and subtracted in the analysis of the data. For E91003, such an approach is not possible for two reasons. First, the SOS $ytar$ acceptance is not uniform enough to allow for the sampling of events in one region of $ytar$ to represent the yield in another. Second, many of the pion decay events ended up with unusual values of $ytar$. Thus any attempt to use the same subtraction method would subtract some unknown fraction of the decayed pions.

To account for these collimator punch-through events, the process is simulated in the SOS single arm Monte Carlo. In previous versions of the Monte Carlo, tracks that hit either the front or back of the entrance collimator were stopped and the event counted as a failure. However, for E91003 the simulation was modified such that events that hit the collimator are stepped through. At each step the simulation tests for the probability that the pion interacts hadronically with the collimator material and allows the pion to undergo multiple scattering and ionization energy loss, using the same algorithms as described in Sections 4.4.1

and 4.4.2.[4] Pions that interact hadronically are assumed to stop in the collimator. The hadronic interaction probability is given by the parameterization of the π-A reaction cross section described in Section 3.4.7. As described in that section, the reaction cross section was chosen as a compromise between the absorption cross section and the total cross section.

For the low pion momentum data ($P_\pi = 0.29$ GeV/c), the number of pions that pass through the collimator is quite low for those pions that start out with $P_\pi = 0.29$ GeV/c $\pm 20\%$ (i.e. events within the SOS momentum acceptance). Most of these pions are either stopped, or knocked out of the SOS acceptance by the $\approx$ 140 MeV lost in passing through the collimator. However, pions with $P = 0.4$ GeV/c or greater can end up within the SOS momentum acceptance and are increasingly accepted. Because these events are highly correlated with the final electron energy, most of these events are removed by the ω ($E_{beam} - E_e$) phase space matching cut discussed in Section 3.3.3. With the standard cuts used in the analysis, the pion punch-through contribution to the total yield is estimated to be $\approx 2.4\%$ at the high ϵ point and essentially zero at the low ϵ point.

The collimator punch-through events are not as well correlated with the scattered electron energy at $P_\pi = 1.0$ GeV/c, so the events can not be removed with a simple cut on the electron energy. However, since the pions passing through the collimator lose so much energy, the reconstruction of the mass of the recoiling nucleon will no longer give the correct, physical value. The collimator punch-through events show up in the long tail of the missing mass distribution (see

[4] The Landau distributed random number generator used in the simulation of energy loss in the collimator was actually the RANLAN subroutine from the CERNLIB [52] software package. This subroutine does a better job with the high energy loss tail. Getting the tail right is quite important in describing the energy loss of a particle that loses a significant fraction of its initial momentum to ionization energy loss.

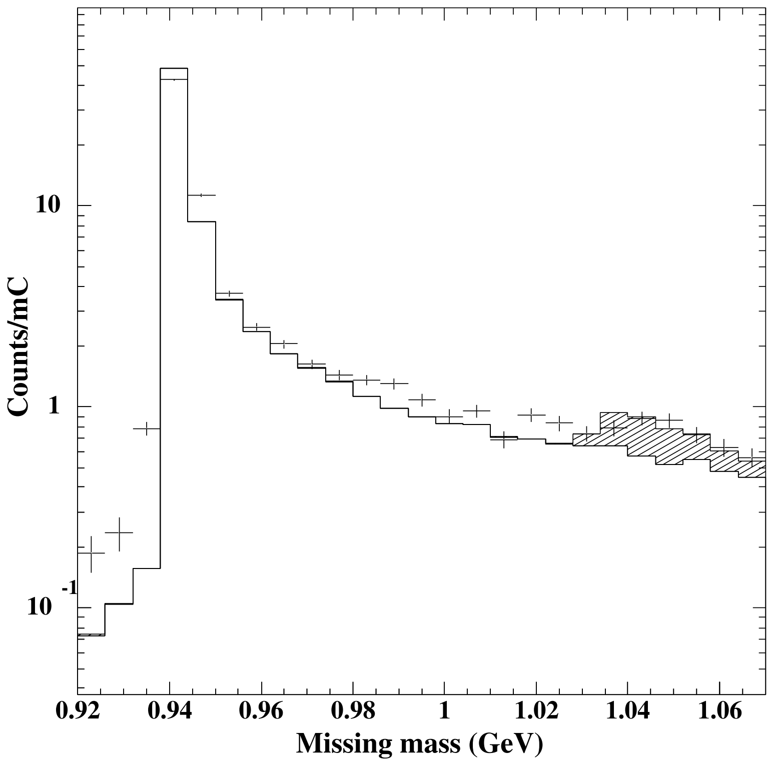

FIGURE 4.6. Simulation of SOS collimator punch-through. The solid curve is SIMC with no punch-through events while the hatched area shows the effect of including pions that pass through the SOS collimator in the simulation. Both are compared to experimental data (crosses). Punch-through events show up at higher missing mass due to the pion energy lost in passing through the collimator. Note that the simulation with pion punch-through is normalized to have the same number of counts as the data.

Figure 4.6). If we are concerned only with the hydrogen cross section, then by placing the appropriate cut on the missing mass distribution, the punch-through events would be removed. We are also concerned with extracting the nuclear cross sections, though, and in particular wish to compare them to the hydrogen cross section. In extracting the nuclear cross sections, one wishes to keep as much of the tail of the missing mass distribution as possible to maximize the acceptance of the "quasifree" distribution. Hence, it is desirable to use a loose missing mass cut, even in hydrogen, to minimize systematic uncertainties in the target comparisons. Even so, the fractional contribution is estimated to be small, $\approx 2.0\%$ for hydrogen, 1.3% for deuterium, and 0.5% for helium-3. The difference between targets can be attributed to the Fermi motion pushing some of the punch-through events beyond the missing mass cut. There is estimated to be $< 0.3\%$ variation between epsilon settings for each target.

A 0.25% random uncertainty between ϵ settings and a 0.5% random uncertainty between targets is assigned for both the high and low P_π kinematics. Based on tests using the total, reaction, and absorption cross sections, an overall 1.0% scale uncertainty is assigned for the simulation of the collimator punch-through events.

4.7. Radiative Corrections

Proper implementation of so-called radiative corrections, in which the incoming or outgoing electron or hadron emits a real or virtual photon, is one of the most important steps in analyzing electron scattering data. There are basically two philosophies in this matter. The first involves calculating a correction factor (as a function of either missing mass or missing energy) at some mean Q^2 and W and applying that correction factor to the experimental spectrum. This method is adequate for small acceptance spectrometers in which the Q^2 and W range is small. However, for the rather large acceptances of most modern spectrometers, this method is not always adequate. Its main failing is that it does not address the fact that the un-radiated cross section may vary quite significantly over the experimental acceptance. Rather, a more correct approach is to simulate the effects of radiation in a Monte Carlo of the experiment and iterate the input model of the fundamental physics process of interest. This is more thoroughly discussed in Ref. [53].

This analysis uses the second approach described above. The radiative corrections formalism is based on the work of Mo and Tsai [54, 55], originally derived for inclusive electron scattering but modified for use in coincidence experiments. Details of the implementation are well described in Refs. [43], [44], and [56]. The original formulation of the radiative corrections procedure used in SIMC was for $(e, e'p)$ reactions. To extend the formalism to pion electroproduction, two methods were tested. In the first, the "target" particle is taken to be a virtual pion. In the second, the final pion is treated as an off-shell proton. The difference between the two approaches is less than 1.0% (less than the systematic uncertainty as will be discussed later) - the second is used in this analysis.

Radiative effects in electron scattering can be separated into two categories. The most straightforward to deal with are the so-called external corrections in which one of the particles (incoming electron, outgoing electron, or outgoing pion) radiates a real photon due to interactions with the fields of nuclei other than the target. Since the particles radiate at some distance from the primary interaction vertex, the amplitudes add incoherently and one does not have to worry about interference effects. More complicated to handle are the internal effects. In the so-called soft, or first order processes, either the incoming or outgoing electron or hadron radiates in the field of the target nucleon. In this case, the amplitudes must be added coherently resulting in interference terms that must be included in the calculation (see Figure 4.7). Second order (or hard) internal corrections that involve vacuum polarization or particle self-energy diagrams (Figure 4.8) are also

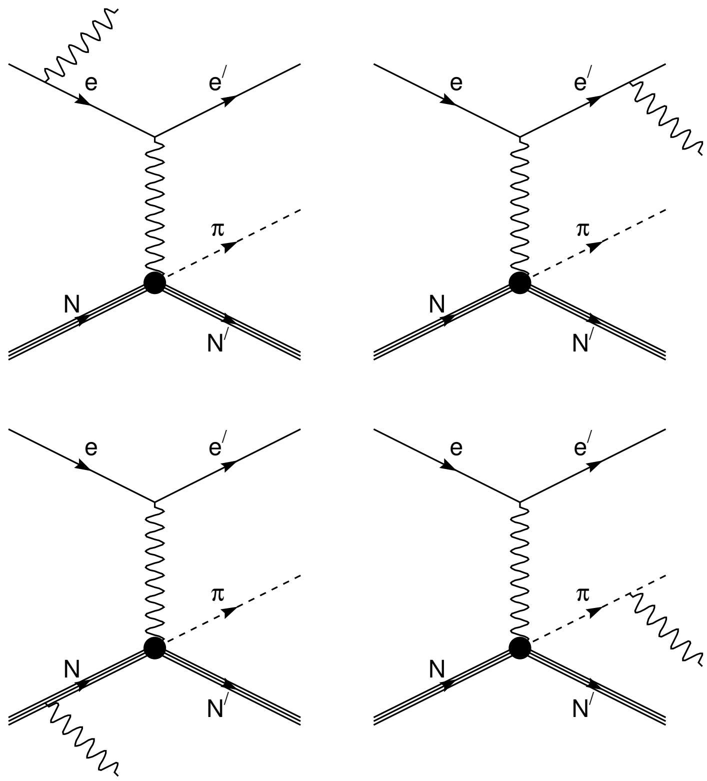

FIGURE 4.7. Feynman diagrams for internal, soft radiative corrections.

included, in particular those processes that cancel infrared divergent terms from the first order corrections are retained.

The radiative corrections formulae used in SIMC hinge on two major approximations. The first of these is the extended peaking approximation. In the extended peaking approximation, the Bremsstrahlung radiation at the one photon level is taken to be along the radiating particle direction, i.e. along the incoming electron, outgoing electron, or outgoing pion momentum. The term "extended" arises from the fact that the total radiated strength is preserved by splitting the

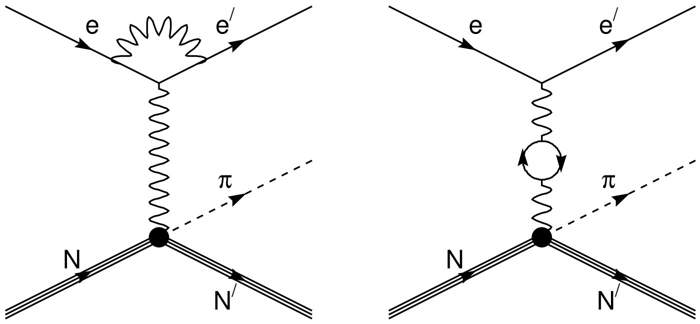

FIGURE 4.8. Internal, hard processes included in the radiative corrections.

non-peaked part of the angular distribution between the incoming and outgoing electrons. The second assumption used in SIMC radiative corrections is the soft photon approximation. This requires that the radiated photon energy is small relative to the energies of the incident and scattered particles. The soft photon approximation allows the factorization of the fundamental amplitude (the one photon exchange diagram) from the radiative processes.

The pion electroproduction cross section, including the probability to radiate photons (from internal and external processes) of total energy $E_{\gamma e}$, $E_{\gamma e'}$, and $E_{\gamma\pi}$ along the directions of the incoming electron, outgoing electron, and outgoing pion respectively, can be written,

$$\frac{d\sigma}{d\Omega_e dE_e d\Omega_\pi dE_{\gamma e} dE_{\gamma e'} dE_{\gamma\pi}} = \frac{d\sigma}{d\Omega_e dE_e d\Omega_\pi} R_{corr} \,, \tag{4.15}$$

where $\frac{d\sigma}{d\Omega_e dE_e d\Omega_\pi}$ is the one photon exchange cross section. R_{corr} is the radiative correction factor and is given by,

$$R_{corr} = (1 - \delta_{hard}) R_{soft} \overline{\Phi}_e^{ext} \overline{\Phi}_{e'}^{ext} \,. \tag{4.16}$$

The internal hard corrections are given by,

$$\delta_{hard} = \underbrace{\frac{2\alpha}{\pi}\left[1 - \frac{3}{4}\ln\left(\frac{Q^2}{m_e^2}\right)\right]}_{\delta_{e\,vertex}} + \underbrace{\frac{2\alpha}{\pi}\left[\frac{5}{9} - \frac{1}{3}\ln\left(\frac{Q^2}{m_e^2}\right)\right]}_{\delta_{e\,vacuum}}, \tag{4.17}$$

where the IR divergent terms in the two-photon exchange and nucleon self energy terms that cancel the IR divergent terms in the first order soft internal corrections have already been eliminated. The soft correction factor includes both internal and external corrections and can be written

$$\begin{aligned} R_{soft} &= \frac{1}{\Gamma(1+bt_e)} \frac{bt_e + \lambda_e}{E_e^{bt_e}(\sqrt{E_e E_{e'}})^{\lambda_e}} \frac{1}{E_{\gamma e}^{1-\lambda_e - bt_e}} \\ &\times \frac{1}{\Gamma(1+bt_{e'})} \frac{bt_{e'} + \lambda_{e'}}{E_{e'}^{bt_{e'}}(\sqrt{E_e E_{e'}})^{\lambda_{e'}}} \frac{1}{E_{\gamma e'}^{1-\lambda_{e'} - bt_{e'}}} \\ &\times \frac{\lambda_\pi}{(\sqrt{m_p E_\pi})^{\lambda_\pi}} \frac{1}{E_{\gamma\pi}^{1-\lambda_\pi}} \\ &= R^e_{soft} R^{e'}_{soft} R^\pi_{soft} \,. \end{aligned} \tag{4.18}$$

In the third line, the m_p comes from the fact that the initial hadron is assumed to be a proton, while the final pion is treated like an off-shell proton with energy E_π. The bt factors come from the external corrections, b is a parameter depending on the material traversed while t is the thickness of that material in radiation lengths. Note that the external corrections due to the pion are ignored as they are suppressed by a factor of $\approx \left(\frac{m_e}{m_\pi}\right)^2 \approx 10^{-5}$. The λ's come from the internal corrections and are given by,

$$\lambda_e = \frac{\alpha}{\pi}\left[\ln\left(\frac{4\mathbf{p_e^2}}{m_e^2}\right) - 1 + 2\ln\left(\frac{|\mathbf{p_e}|}{|\mathbf{p_{e'}}|}\right) + \ln\left(\frac{1-\cos(\theta_e)}{2}\right)\right] \tag{4.19}$$

$$\lambda_{e'} = \frac{\alpha}{\pi}\left[\ln\left(\frac{4\mathbf{p_{e'}^2}}{m_e^2}\right) - 1 + 2\ln\left(\frac{|\mathbf{p_e}|}{|\mathbf{p_{e'}}|}\right) + \ln\left(\frac{1-\cos(\theta_e)}{2}\right)\right] \tag{4.20}$$

$$\lambda_\pi = \frac{\alpha}{\pi}\left[\ln\left(\frac{E_\pi + |\mathbf{p}_\pi|}{E_\pi - |\mathbf{p}_\pi|}\right) - 2\right]. \tag{4.21}$$

The $\ln\left(\frac{|\mathbf{p_e}|}{|\mathbf{p_{e'}}|}\right)$ and $\ln\left(\frac{1-\cos(\theta_e)}{2}\right)$ terms in λ_e and $\lambda_{e'}$ represent the non-peaked strength that we split between the incoming and outgoing electrons in this "extended" peaking approximation. The final factors in the radiative correction scheme are the $\overline{\Phi}^{ext}$ which are a correction to the external radiation at high photon energies. For the prescription used here, the correction is given by,

$$\overline{\Phi}_i^{ext} = 1 - \frac{bt_i}{bt_i + \lambda_i}\frac{E_{\gamma i}}{E_i}, \tag{4.22}$$

where $i = e, e'$.

The simulation of radiation in SIMC works as follows. The radiated photon energy in each arm is generated according to a (normalizable) function of the form,

$$GenShape = \frac{gE^{g-1}}{E^g_{max} - E^g_{min}} \tag{4.23}$$

where E^g_{min} and E^g_{min} are the generated photon energy limits. E^g_{max} must be set at least as large as the maximum energy a particular particle can lose and still be accepted. The factor g is just $\lambda + bt$ for the arm of interest. Once the radiated photon energy is generated, the appropriate particle energy is adjusted. For the case in which the incoming electron radiates, the new kinematics are checked to ensure that the pion can still be produced - if not the event fails.

Finally, the weight for the event must be calculated. In this case, we want the probability for a particle to lose some amount of energy between E_{min} and E_{max} (the same limits used in the generating function) due to radiation. This just comes from the factors in equation 4.16. The hard correction and external $\overline{\Phi}^{ext}$ are calculated as described above. The soft correction is integrated from E_{min} to E_{max} giving a factor for each particle of the form

$$W^i_{soft} = \int_{E_{min}}^{E_{max}} R^i_{soft}(E)dE = \frac{R^i_{soft}}{g^i}\left(E^{g^i}_{max} - E^{g^i}_{min}\right), \tag{4.24}$$

where $i = e, e', \pi$. The total weight due to the soft correction is then the product of all three. The total radiated weight is finally,

$$W_{RAD} = (1 - \delta_{hard})W^e_{soft}W^{e'}_{soft}W^{\pi}_{soft}\overline{\Phi}^{ext}_e\overline{\Phi}^{ext}_{e'}. \tag{4.25}$$

The above prescription has been verified to work well for elastic scattering (see Refs. [57, 58]) and the overall uncertainty in the procedure (for $(e, e'p)$ reactions) is taken to be on the order of 2%. There will be additional uncertainty in this case due to the extension of the prescription to pion electroproduction. Taking the difference between the two prescriptions discussed earlier (pion = off-shell proton and target proton = off-shell pion), an extra 1% uncertainty (combined in quadrature) is assigned to the overall correction (leading to a total uncertainty of 2.23%).

The uncertainty in the radiative corrections will tend to cancel between ϵ points in the L-T separation as well as between targets since the same procedure is always used. The question, then, is what random uncertainty do we assign in the L-T separation and target ratios? This question can be partially addressed by looking at the radiative tail in the $\mathrm{H}(e, e'\pi^+)$ process. Table 4.3 shows the ratio of integrated data counts to integrated SIMC counts as a function of missing mass cut.[5] At each missing mass cut, the variation of the data to SIMC ratio with ϵ is quite small. Based on the results of Table 4.3 a random uncertainty of 0.5% between ϵ points is assigned.

The question of the variation with target is a bit trickier. The Fermi momentum of the nucleon in the nucleus makes it difficult to separate radiative effects from the large Fermi momentum tail. However, a previous experiment using a virtually identical radiative corrections procedure for $(e, e'p)$ reactions on deuterium found no discernible discrepancy between the simulated and actual radiative tail of the missing energy (E_m) spectrum [43], giving one confidence that the procedure

[5]The model used in these ratios has been iterated as described in Section 5.4.2 to match the Monte Carlo to the data. The results shown do not depend on which model is used in the initial input.

k_π (GeV/c)	M_x cut (GeV)	ϵ_1 DATA/SIMC	ϵ_2 DATA/SIMC
0.20	0.92-1.07	1.0	1.0
	0.92-1.02	0.9949	0.9965
	0.92-0.98	0.9860	0.9925
0.47	0.92-1.02	1.0	1.0
	0.92-1.00	0.9999	1.0003
	0.92-0.98	1.0021	0.9975

TABLE 4.3. Data to SIMC comparison as a function of missing mass (M_x) cut. The ratio of data to SIMC counts is normalized to 1.0 for the largest M_x cut. Note that the maximum missing mass is smaller for the high k_π data. This is due to the relatively small ω acceptance at these settings.

translates well to weakly bound nuclei. Hence, a relatively small 1% random uncertainty between targets is assigned for the radiative corrections procedure.

4.8. Elastic Scattering

The efficacy of SIMC has been verified many times using the well known elastic cross section [27, 29, 57]. SIMC can simulate both single arm H(e,e') and coincidence H$(e,e'p)$ elastic scattering. In this case, the scattered electron angles (in plane and out of plane) are generated and all other quantities calculated. All the effects described above (radiation, multiple scattering, energy loss) are applied and the single arm Monte Carlos used to check for acceptance and reconstruct the event. The model cross section used is,

$$\frac{d^2\sigma}{d\Omega_e} = \frac{\alpha^2 \cos^2\frac{\theta}{2}}{4E^2 \sin^4\frac{\theta}{2}} \frac{E'}{E} \Big(\frac{G_{E_p}^2 + \tau G_{M_p}^2}{1+\tau} + 2\tau G_{M_p}^2 \tan^2\frac{\theta}{2} \Big) \,, \tag{4.26}$$

where θ and E refer to the scattered electron angle and energy. The electric and magnetic form factors were calculated using a parameterization to the world's data by P.E. Bosted [59],

$$G_{E_p}(Q^2) = \frac{1}{1 + 0.62Q + 0.68Q^2 + 2.80Q^3 + 0.83Q^4}, \tag{4.27}$$

$$\frac{G_{M_p}(Q^2)}{\mu_p} = \frac{1}{1 + 0.35Q + 2.44Q^2 + 0.50Q^3 + 1.04Q^4 + 0.34Q^5}. \tag{4.28}$$

During E91003, elastic data were taken at two beam energies (0.845 GeV and 1.645 GeV) although coincidence data were only taken at the lower beam energy. The one pass elastic data consisted of a series of runs in which the settings of the electron spectrometer (the HMS in this case) were changed such that the elastically scattered electrons occupied different regions of HMS δ. These so-called δ-scans were done in two different ways. First, the HMS was maintained at constant central momentum ($P_{HMS} = 0.537$ GeV/c) but the angle was changed (from 79.97° to 58.24°) such that the elastic peak scanned HMS δ from -12% to +12%. The second scan involved keeping the HMS at constant angle ($\theta_{HMS} = 79.97°$) while changing the HMS central momentum ($P_{HMS} = 0.440 - 0.537$ GeV/c) to scan the elastic peak over the same δ range. In each case the recoiling protons were detected simultaneously in the SOS.

In order to compare the data and Monte Carlo, the data are corrected for all the usual dead times and efficiencies (computer dead time, electronic dead time, particle identification efficiency, etc.). Nominal cuts in the reconstructed spectrometer variables are applied (the HMS δ cut is larger than usual since the δ scan went beyond the nominal "good acceptance" region). Loose cuts are also placed on the missing energy to ensure that the data sample is from truly elastic events.

One additional correction that has to be applied to the data is the absorption of protons in the SOS. The recoiling proton can undergo hadronic interactions (both elastic and inelastic) in the target and spectrometer thus reducing the number of protons counted. The correction for proton absorption is determined experimentally by the following method. First, cuts are placed on electron variables such that a proton is kinematically constrained to be within the hadron arm acceptance. The ratio of efficiency corrected coincidences to electron events (coincident or electron only) is then the proton transmission,

$$T_{proton} = \frac{N_{coins}}{N_{coins} + N_{e^- only}} . \tag{4.29}$$

More details on the method can be found in Ref. [60]. This method was employed for a sample of six runs from the δ scan data. The measured proton transmission is 0.954 $\pm$ 0.005. This compares well with the measurement from Ref. [60] of 0.951 $\pm$ 0.005. A calculation using the mean of the proton total cross section and the proton inelastic cross section gives 0.943, in good agreement with the measured values.

One further complication that arises in analyzing the elastic data is that no empty target data was taken, making it impossible to subtract the target cell wall background from the experimental yields. In general, the cell wall yield is not large, but still contributes at least a few percent to the total yield. An estimate of this background is made by simulating quasielastic scattering from aluminum (using a simple one-particle momentum distribution for the struck proton). The magnitude of the aluminum contribution is fixed by fitting the simulated aluminum + hydrogen yield to the experimentally measured W distribution. The aluminum background contributes most significantly relative to the elastic hydrogen spectrum in the super-elastic region and the radiative tail. The spectrum is fit for 0.89 GeV $< W <$ 1.05 GeV although the data is analyzed using tighter cuts (0.92 GeV $< W <$ 0.98 GeV). For the coincidence data, the aluminum background is estimated to be $\approx 3\%$ with a slight δ dependence while for the electron only data, the background is estimated to be $\approx 5\%$. The uncertainty on this estimate is assigned to be half the size of the correction.

Results for the one pass HMS δ scan are shown in Figure 4.9. The data has been analyzed using the scattered electrons only (top) and the coincidence events (bottom). The overall systematic uncertainty is rather large ($\approx 3\%$) mostly due to the uncertainty in estimating the dummy contribution. Since SIMC has been well tested in the past and Ref. [27] has shown good agreement for the overall normalization with the new HMS100 tune, the normalization uncertainty assigned to the actual data is smaller (on the order of 2%). Figure 4.9 shows that, in general, the acceptance in HMS δ is well understood. Within the nominal "good" acceptance region of $\pm 8\%$, the H(e, e') data agree within the point-to-point uncertainties (dashed line in the figure) and only one data point for the H$(e, e'p)$ data disagrees (at about +7.5%). This last point was taken at $P_{HMS} = 0.440$ GeV/c and raises concerns that perhaps the HMS acceptance at low momentum is not well understood, however the H(e, e') data indicate that this is not the case. Even assuming that for $P_{HMS} < 0.5$ GeV/c, the acceptance is on average 2% low for $\delta > 5$, the net effect on the analysis of the pion electroproduction data is minimal.[6] It is also worth noting that the spurious point has a significant fraction (about 30%) of its counts at $\delta > 8\%$.

The one pass elastic data, while not convincing in and of itself that the overall normalization is well understood, is consistent with past analyses. However,

---

[6]Only one setting involved putting the HMS at $P_{HMS} < 0.5$ GeV/c. However, the shape of the distributions in HMS δ is such that at most 10% of the total counts are at $\delta > 5\%$ which leads to an overall discrepancy in total counts of 0.2%.

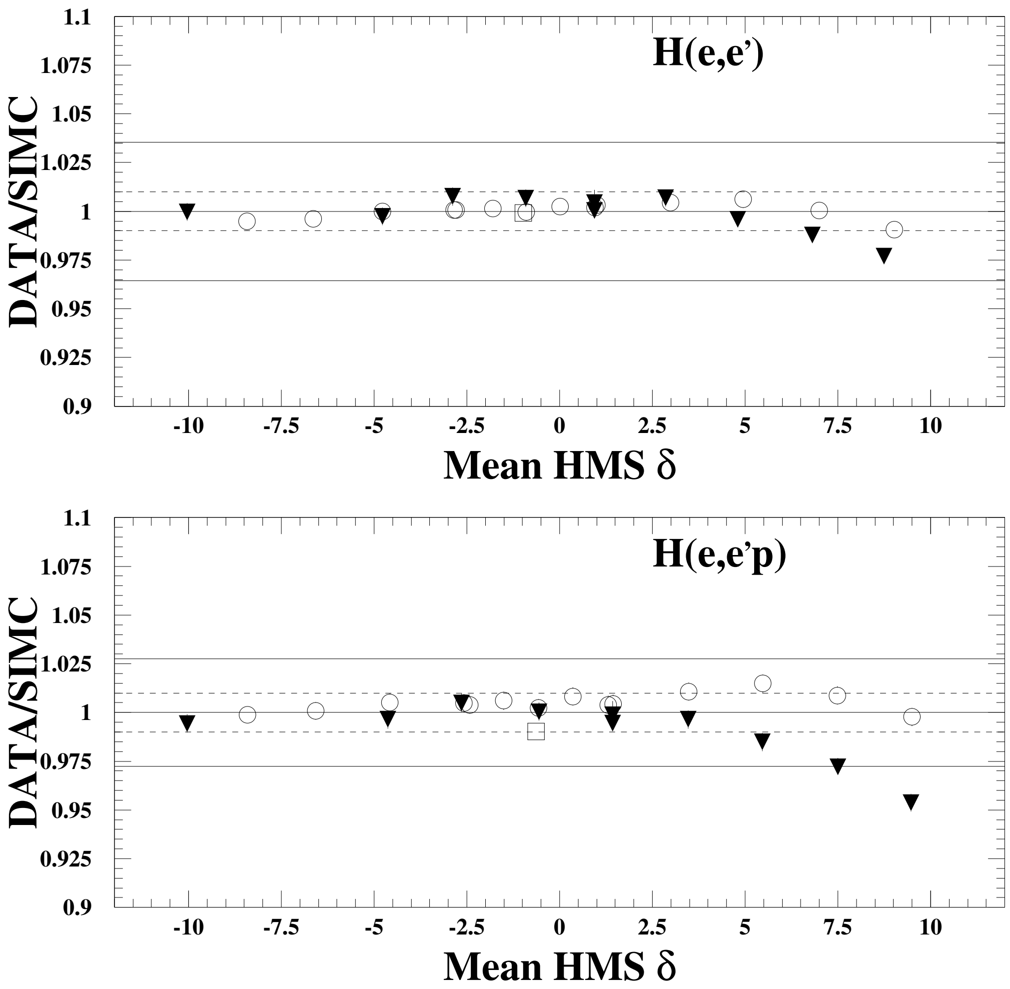

FIGURE 4.9. Ratio of data to Monte Carlo yields for one pass elastic data. The top plot is analyzed in terms of electron yields only while the bottom plot shows coincidence yields. Error bars on the points are statistical only. The dashed lines represent random errors between the points shown, while the solid lines show the overall systematic uncertainty. Open circles were taken with $P_{HMS} = 0.537$ GeV/c and $\theta_{HMS} = 58.24° - 79.97°$. Triangles were taken at $P_{HMS} = 0.440 - 0.537$ GeV/c and $\theta_{HMS} = 79.97°$. The open square was a calibration run taken just previous to, but not as part of, the HMS δ scan.

the significance of this data (and perhaps more relevant for E91003 where absolute normalization is not of critical importance) is that it demonstrates that the acceptance is well understood not only at the central δ but over the nominal good acceptance range of the HMS ($\pm 8\%$). Some information is also gained regarding the SOS acceptance in that the "changing angle" δ-scan also moved the elastic peak in SOS δ. Furthermore, the SOS had to be moved to larger angle for larger HMS δ, thus implicitly testing the understanding of the SOS extended target acceptance. Results for the two pass elastic are not shown here. For that data, runs were only taken at the central δ. It was verified that SIMC reproduced the data within the (rather large) systematic uncertainties, but more convincing evidence that the absolute normalization is reproduced is to be found in the references previously mentioned.

5. EXPERIMENTAL CROSS SECTION EXTRACTION

5.1. Overview

The extraction of the experimental cross section relies to a large extent on the Hall C Monte Carlo (SIMC). The Monte Carlo starts with a model of the "true" cross section and applies various effects such as radiative corrections, spectrometer acceptance, and pion decay. Assuming all such experimental effects are simulated appropriately, the experimental cross section can be extracted by modifying the input model cross section until agreement between the data and Monte Carlo is achieved.

If the cross section model input to the Monte Carlo accurately reproduces the dependence on all kinematic variables (ω, Q^2, etc.) then the experimental cross section is simply given by,

$$\sigma^{exp} = \frac{Y_{DATA}}{Y_{SIMC}} \times \sigma^{model} , \tag{5.1}$$

where Y_{DATA} is the charge normalized, efficiency corrected experimental yield integrated over the acceptance and Y_{SIMC} is the SIMC yield (for the same charge) resulting from the input model cross section, σ^{model}. Here, the role of the model cross section is twofold. It gives the appropriate cross section weighting of the acceptance as well as taking care of bin centering corrections to the experimental cross section.

The fact that both the data and Monte Carlo cover some range in the kinematic variables that determine the cross section complicates the extraction of the experimental cross section. One approach is to extract the experimental cross section averaged over the acceptance by calculating the average of the input model in Equation 5.1. In this case it is necessary to quote not only the mean values of the relevant kinematics, but also their range. This method has the advantage of reducing the sensitivity of the final answer on the detailed shape of the input model cross section as it is mainly used to determine the acceptance. It has the disadvantage of reducing the interpretability of the absolute cross sections. Since E91003 is mostly concerned with cross section ratios, it may appear that this is the method of choice. However, in an L-T separation, it is often the case that the range of the kinematic variables of interest within the experimental acceptance is quite different at the forward and backward electron kinematics (high and low ϵ). If one takes the full acceptance in both cases, one is then averaging over two different regions at each ϵ, and the meaning of the separated cross sections, σ_L and σ_T, becomes unclear. For example, in the extraction of σ_L, one would have to quote an average value since one has taken average forward and backward lab cross sections. However, then it is unclear over what kinematic range one has averaged σ_L. One solution is to match the range over the kinematic variables with simple cuts so that the average is over the same region. Unfortunately, this results in an unacceptable loss in statistics for E91003.

The approach taken in this analysis is to evaluate the cross section at some particular point in the acceptance, or "bin-center" the data. This allows us to keep the full statistics at each ϵ point[1] and results in cross sections that are easy to interpret. The down side of this approach is that one is much more sensitive to the detailed structure of the model across the acceptance. For that reason, an iteration procedure is used to match the kinematic dependencies of the Monte Carlo to the data. Although the procedure used in this analysis is not extremely

---

[1]In point of fact, some data is discarded by the ω range matching cut at the high ϵ points. However, the loss of statistical precision due to the phase space matching in this one variable is acceptable.

sophisticated, it works quite well as can be seen in the agreement of the final cross sections extracted from very different starting models.

5.2. Monte Carlo Equivalent Yield

The first step in comparing the data to Monte Carlo in order to extract the cross section is to calculate the proper SIMC yield. Since the data yield is expressed in counts per mC, the Monte Carlo is normalized to 1 mC of charge. The Monte Carlo luminosity is then given by,

$$\mathcal{L} = \left(\frac{1 \times 10^{-3}\,C}{1.602 \times 10^{-19}\,C/electron}\right)\left(\frac{\rho t N_A}{M}\right) , \tag{5.2}$$

where ρ is the target density in g/cm^3, t is the target thickness in cm, N_A is Avogadro's number and M is the target mass in amu. Then, in the general case, the SIMC yield can be expressed,

$$Y_{SIMC} = \mathcal{L} \int_V \left(\frac{d^6\sigma}{d\Omega_e dE_e d\Omega_\pi dP_\pi}\right)^{model} A(V)R(V)J(\Omega \rightarrow \mathbf{X}')d\mathbf{X}'_e dE_e d\mathbf{X}'_\pi dP_\pi \, , \tag{5.3}$$

where A is the coincidence acceptance function, R is the radiative correction factor, $d\mathbf{X}' = dx'dy'$ is the differential solid angle in spectrometer coordinates, and J is the Jacobian that transforms the model cross section from "physics" coordinates to the spectrometer coordinates (used for event generation). The Jacobian is given by,

$$J(\Omega \rightarrow \mathbf{X}') = \frac{1}{(1 + (y'_e)^2 + (x'_e)^2)^{3/2}(1 + (y'_\pi)^2 + (x'_\pi)^2)^{3/2}} \, . \tag{5.4}$$

Note that the acceptance function, in this context, is assumed to incorporate many of the features described in Chapter 4 such as energy loss, pion decay, collimator punch-through, etc. Including $A(V)$ and $R(V)$ in the simulation means that we extract the "true" cross section, undistorted by radiative effects and those effects included in the acceptance function. However, any effect not explicitly included in the simulation (as something distinct from the input model) such as π-N final state interactions is not corrected for in the cross section extraction.

In the case of pion electroproduction from hydrogen, the pion momentum is totally determined by the electron quantities and pion direction, so the integration over P_π becomes a δ-function, and the six-fold model cross section reduces to a five-fold cross section. The SIMC yield is then,

$$Y_{SIMC} = \mathcal{L} \int_V \left(\frac{d^5\sigma}{d\Omega_e dE_e d\Omega_\pi} \right)^{model} A(V) R(V) J(\Omega \rightarrow \mathbf{X}') d\mathbf{X}'_e dE_e d\mathbf{X}'_\pi \,. \quad (5.5)$$

Note that even though the integral is over electron variables and pion angles only, the acceptance correction A and radiative corrections R still take into account the pion momentum. In practical terms, the differential elements reflect the quantities that are generated in the Monte Carlo evaluation of the integral.

In electroproduction from deuterium and helium-3, the e-N cross section is calculated as described in Section 4.2.2 and convolved with the struck nucleon momentum space wave function (in the quasifree picture). The SIMC yield is then,

$$Y_{SIMC} = \mathcal{L} \int_V \left(\frac{d^5\sigma}{d\Omega_e dE_e d\Omega_\pi} \right)^{model} A(V) R(V) J(\Omega \rightarrow \mathbf{X}') \rho(\mathbf{p}_F) d\mathbf{p}_F d\mathbf{X}'_e dE_e d\mathbf{X}'_\pi \,, \quad (5.6)$$

where $\mathbf{p}_F$ is the (Fermi) momentum of the struck nucleon and $\rho = |\Phi(\mathbf{p}_F)|^2$, the magnitude squared of the momentum space wave function. Comparing Equations 5.3 and 5.6, we can make the equivalence,

$$\frac{d^6\sigma}{d\Omega_e dE_e d\Omega_\pi dP_\pi} = \frac{d}{dP_\pi} \int \frac{d^5\sigma}{d\Omega_e dE_e d\Omega_\pi} \rho(\mathbf{p}_F) d\mathbf{p}_F \,. \quad (5.7)$$

Note that since ρ is a normalized distribution, the integral on the right hand side is just the 5-fold cross section averaged over the nucleon wave function.

5.3. Cross Section Calculation

5.3.1. General Method

The extraction of the experimental hydrogen cross section is facilitated by the realization that Equation 5.5 can be expressed,

$$\begin{aligned} Y_{SIMC} = \mathcal{L} \left(\frac{d^5\sigma}{d\Omega_e dE_e d\Omega_\pi} \right)^{model}_{(\omega_0, Q_0^2, \theta_0)} \\ \times \int_V F(\omega, Q^2, \theta_{pq}, \phi_{pq}) A(V) R(V) J(\Omega \to \mathbf{X}') d\mathbf{X}'_e dE_e d\mathbf{X}'_\pi \ , \end{aligned} \tag{5.8}$$

where $\left(\frac{d^5\sigma}{d\Omega_e dE_e d\Omega_\pi} \right)^{model}_{(\omega_0, Q_0^2, \theta_0)}$ is the model cross section evaluated at some point $(\omega_0,\, Q_0^2,\, \theta_0)$ near the center of the acceptance, and $F(\omega, Q^2, \theta_{pq}, \phi_{pq})$ describes the behavior of the model across the acceptance relative to the central cross section. Note that the ϕ_{pq} dependence has been removed from the central cross section. Since the virtual photon cross section can be expressed,

$$\frac{d\sigma}{d\Omega} = A + B\cos\phi_{pq} + C\cos 2\phi_{pq} \ , \tag{5.9}$$

this is the equivalent of saying that we trust our model to appropriately describe the B and C terms and allow us to extract A at a particular point in phase space. This approach is justified for three reasons. First, the B and C terms are expected to be roughly proportional to $\sin\theta_{cm}$, which in parallel kinematics is small over most of the acceptance. Also, the iteration procedure (to be described in Section 5.4.2) fits any residual ϕ_{pq} dependence. Finally, we restrict the θ_{pq} acceptance such that we have complete ϕ_{pq} coverage so that the B and C terms should average to zero.[2]

[2]Strictly speaking, the interference terms only average to zero at the cross the section level. At the raw counts level (not corrected for acceptance), the terms do not necessarily average to zero. The key is that if the Monte Carlo accurately reproduces the data, we already know the B and C terms and there is no point in determining the full ϕ_{pq} dependent cross section and subtracting those terms away.

If the input model is perfect, then experimental and simulated yields should be identical. In this analysis, we assume (and later, force) the model to accurately describe the kinematic dependence across the acceptance, but not necessarily have the correct scale. Thus, we scale the model cross section by the measured yield,

$$\left(\frac{d^5\sigma}{d\Omega_e dE_e d\Omega_\pi}\right)^{exp}_{(\omega_0,Q_0^2,\theta_0)} = \frac{Y_{DATA}}{Y_{SIMC}} \times \left(\frac{d^5\sigma}{d\Omega_e dE_e d\Omega_\pi}\right)^{model}_{(\omega_0,Q_0^2,\theta_0)} . \tag{5.10}$$

The subscript $(\omega_0, Q_0^2, \theta_0)$ on the experimental cross section indicates that, by evaluating the model at a particular point in the acceptance, we are extracting the experimental cross section at that point. For both the low and high recoil data, the cross sections are evaluated at $Q^2 = 0.4$ (GeV/c)^2 and $\theta_{pq} = 0.03$ radians[3] (1.72 degrees) in the lab. The low recoil data is evaluated at $\omega = 1.108$ GeV (which corresponds to $W = 1.6$ GeV for the free nucleon) while the high recoil data is given at $\omega = 0.449$ GeV ($W = 1.15$ GeV).

Extraction of the experimental cross sections for deuterium and helium-3 is similar to that for hydrogen, but a bit more complicated. The important thing to keep in mind here is that we are interested more in the cross section integrated over the extra degree of freedom (P_π) than in the shape of the cross section differential in P_π. In analogy with Equation 5.10, consider the experimental cross section in the ith P_π bin,

$$\left(\frac{d^6\sigma}{d\Omega_e dE_e d\Omega_\pi dP_\pi}\right)^{exp}_{(\omega_0,Q_0^2,\theta_0),i} = \left(\frac{Y_{DATA}}{Y_{SIMC}}\right)_i \times \left(\frac{d^6\sigma}{d\Omega_e dE_e d\Omega_\pi dP_\pi}\right)^{model}_{(\omega_0,Q_0^2,\theta_0),i} , \tag{5.11}$$

---

[3]Ideally, we would like to evaluate the cross section at $\theta_{pq} = 0$. However, at zero angle, there is no phase space available and no data to constrain the iteration procedure (to be described in Section 5.4.2) at that point. Hence, it was decided to scale the data to a non-zero angle that represents the central value for the settings with the smallest θ_{pq} acceptance.

where in this case the model cross section is evaluated at the center of the ith P_π bin. What we really want to measure is the cross section integrated over P_π, which would be given by,

$$\left(\int \frac{d^6\sigma}{d\Omega_e dE_e d\Omega_\pi dP_\pi} dP_\pi\right)^{exp}_{(\omega_0,Q_0^2,\theta_0)} = \sum_i \left(\frac{Y_{DATA}}{Y_{SIMC}}\right)_i \times \left(\frac{d^6\sigma}{d\Omega_e dE_e d\Omega_\pi dP_\pi}\right)^{model}_{(\omega_0,Q_0^2,\theta_0),i} \times \Delta P_\pi \,. \tag{5.12}$$

However, assuming that the model in the Monte Carlo accurately reproduces the data in every P_π bin, the ratio of data and SIMC yields would be 1 (or at least a constant if the model reproduces the shape appropriately). Then, the integrated experimental cross section can be calculated,

$$\left(\int \frac{d^6\sigma}{d\Omega_e dE_e d\Omega_\pi dP_\pi} dP_\pi\right)^{exp}_{(\omega_0,Q_0^2,\theta_0)} = \frac{Y_{DATA}}{Y_{SIMC}} \times \int \left(\frac{d^6\sigma}{d\Omega_e dE_e d\Omega_\pi dP_\pi}\right)^{model}_{(\omega_0,Q_0^2,\theta_0)} dP_\pi. \tag{5.13}$$

The experimental cross sections are extracted using Equations 5.10 and 5.13. In both cases, the "central" cross section is calculated using the same model as is used in the full Monte Carlo.

5.3.2. Calculation of the Model Cross Section

Determination of the experimental cross section requires the calculation of the input model at the kinematic point of interest. In the case of electroproduction from hydrogen this is straightforward. Given a particular ω, Q^2, and θ_{pq} (at a particular beam energy), the γ^*-N virtual photon cross section is directly parameterized. However, in the case of deuterium and helium-3, the calculation is complicated by the extension of the model to quasifree scattering (as described in Section 4.2.2). In this case, we must make the connection between the quasifree calculation integrated over the nucleon momentum space wave function, and the six-fold cross section, differential in P_π.

To calculate the central cross section, all extraneous processes in SIMC such as radiation, multiple scattering, and energy loss are turned off. The single arm spectrometer acceptance models are also turned off (this is the equivalent of setting $A(V) = R(V) = 1$ in Equations 5.5 and 5.6). This means that we are, in essence, just using the event generation parts of SIMC. The "spectrometer" kinematics in the electron arm are set such that the central values correspond to Q_0^2 and ω_0 (where we wish to evaluate the cross section), with the generation volume set to be a point in angle and momentum. The pion arm is set such that the central angle lies along the direction of the momentum transfer, $\mathbf{q}$ and the angular generation volume is set to correspond to θ_0, the angle relative to $\mathbf{q}$ at which we wish to evaluate the central cross section. In the case of hydrogen, the kinematics are totally determined, so the model gives a single value.[4] For the nuclear targets, we make use of Equation 5.7 and the central cross section is given by,

$$\left(\int \frac{d^6\sigma}{d\Omega_e dE_e d\Omega_\pi dP_\pi} dP_\pi \right)^{central} = \sum_i \frac{\Delta \langle \sigma^5_{model} \rangle_i}{\Delta P_\pi} \times \Delta P_\pi \tag{5.14}$$

where $\Delta \langle \sigma^5_{model} \rangle_i$ is the 5-fold cross section averaged over the nucleon wave function in the ith P_π bin. Note that in this calculation of the central cross section, the integration must be over the same P_π range as is used in the accumulation of charge corrected counts, Y_{DATA}.

[4]At non-zero θ_{pq}, the ϕ_{pq} degree of freedom remains, but any ϕ_{pq} dependent terms are eliminated by the integration over azimuthal angle.

5.4. Data and Monte Carlo Matching

It is clear that the extraction of the experimental cross section depends heavily on the cross section model and how well it describes the data across the experimental acceptance. Previous pion electroproduction data serves to constrain current models, and these models do a fairly good job of describing our data. However, since L-T separated data is rare, it is not too surprising that the models are inadequate in some areas. Therefore, it is necessary to alter the input cross section model until agreement with the data is achieved. To that end, an iteration procedure is used, fitting corrections to reasonable starting models until the extracted cross section converges. Furthermore, to improve the quasifree description of pion electroproduction from the nuclear targets, a simple description of nucleon-nucleon final state interactions is added to the model.

5.4.1. NN Final State Interactions

The starting point for our simulation of pion electroproduction is the fundamental virtual photon - nucleon cross section ($\gamma^* N \rightarrow \pi N'$), with modeling of experimental (resolution, acceptance) and extraneous physics (radiative corrections, pion decay) effects handled in the Monte Carlo. In the hydrogen case, the cross section model is straightforward to implement. Production from deuterium and helium-3 is treated as quasifree scattering in which the pion is produced from a nucleon that is no longer stationary, but has some momentum, p_F. This approximation ignores the fact that, in the final state, the recoiling nucleons may interact with one another, either through the nucleon-nucleon force or through the Pauli Exclusion Principle. As will be seen in Section 5.4.2, an iteration procedure is used to match the data to the Monte Carlo, so one may hope that this procedure corrects for any of the aforementioned shortcomings of the quasifree approximation. However, as the iteration procedure itself is rather simple, it behooves us to make the starting model as good as reasonably possible. To that end, we attempt to improve the quasifree model to also include some of the more apparent effects of NN final state interactions. The effect of such interactions can be seen in Figure 5.1.

While it is non-trivial to account for the NN final state interactions in an exact and quantitative manner, it is relatively straightforward to include some of the general features of these interactions. The relevant point here is that at low relative momentum between the nucleons, k_{rel}, the NN force is non-negligible leading to an enhancement of the pion electroproduction cross section. This attractive force leads to distortions in the shape of the missing mass distributions, as k_{rel} and missing mass are totally correlated (at least in the case of electroproduction from deuterium).

The prescription followed in this analysis is the Jost function formalism in which it is assumed that the primary interaction (pion electroproduction) factorizes from the secondary interaction (the NN force) [61]. In this case, the electroproduction cross section is modified by the inverse of the magnitude squared of the Jost function,

$$\sigma_{\pi}^{NN\ \mathrm{FSI}} = \frac{1}{|J_l(k_{rel})|^2}\sigma_{\pi}\ , \tag{5.15}$$

where the $J_l(k_{rel})$ is the Jost function for the lth partial wave - generally the first non-vanishing partial wave. Given a potential V that represents the interaction that describes the final state interaction (in this case the NN potential), it can be shown that [62],

$$\lim_{r\to 0}\frac{|\psi_l(k_{rel},r)|^2}{|\psi_l^{(0)}(k_{rel},r)|^2} = \frac{1}{|J_l(k_{rel})|^2}\ , \tag{5.16}$$

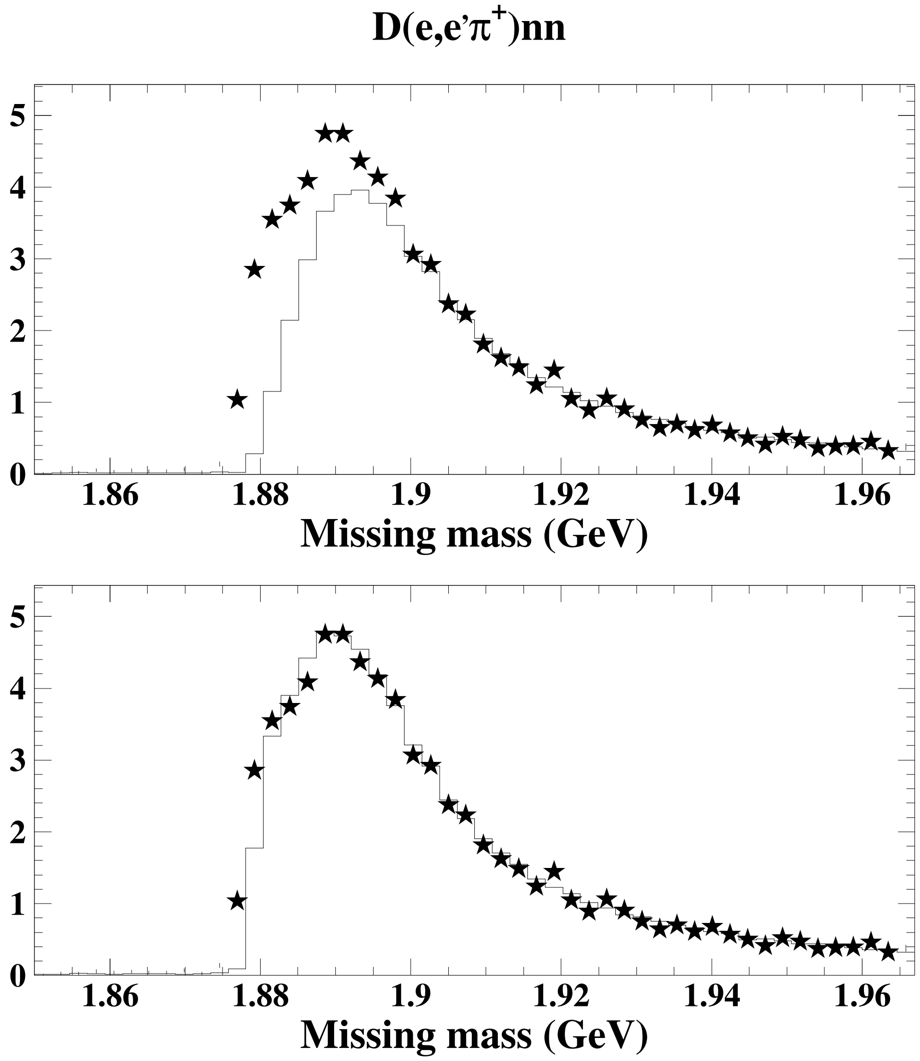

FIGURE 5.1. Missing mass distribution for π^+ production from deuterium. The stars are experimental data while the solid curve is Monte Carlo with pure quasifree production only (top) and including a correction for NN final state interactions (bottom). The Monte Carlo has been normalized to agree with the data at high missing mass. The NN final state interaction creates an enhancement (relative to pure quasifree production) at low missing mass.

where $\psi_l(k_{rel}, r)$ is the l wave solution to the Schroedinger equation for that potential, and $\psi_l^{(0)}(k_{rel}, r)$ is the solution when $V = 0$. This form for the correction factor is convenient in that as the potential goes to zero (or equivalently, as k_{rel} becomes large), the correction becomes 1.

In this case, we are mostly interested in the $^1S_0$ NN interaction (other partial waves contribute, but this is the most significant). This interaction is often described in terms of an effective range potential. The s-wave Jost function for such a potential can be written [62],

$$J(k_{rel}) = \frac{k_{rel} - i\beta}{k_{rel} - i\alpha}\,, \tag{5.17}$$

where α and β can be determined from the scattering length (a) and effective range (r_e) of the potential,

$$\frac{1}{2} r_e(\alpha - \beta) = 1 \tag{5.18}$$

$$\frac{1}{2} r_e \alpha\beta = -\frac{1}{a}\,. \tag{5.19}$$

The above form of the Jost function is calculated and applied in the Monte Carlo. The scattering length and effective range for proton-proton scattering is used in the case of π^- production (where the recoiling system is two or three protons). In the case of π^+ production (where the recoiling system is two neutrons for deuterium or two neutrons + one proton for helium-3), the values for a and r_e are taken from neutron-neutron data (radiative pion capture and neutron-deuteron breakup). For pion electroproduction from the deuteron, the relative momentum between the final state nucleons is totally determined once the pion kinematics are specified, and the Jost function can immediately be calculated. The helium-3 case is a bit more complicated, and some simplifying assumptions must be made to estimate k_{rel} and hence the final state interaction correction. Here, we assume that the two spectator particles are recoiling together with little or no relative momentum between them. This is consistent with the trial spectral function we use in the event generation scheme in that the missing energy distribution is biased to low E_m. Then, the relative momentum between the recoiling struck nucleon and *one* of the spectators is calculated using half the total momentum of the recoiling pair.

Implementation of the NN final state interactions in helium-3 is further complicated by the fact that there are two spectator nucleons instead of one. The ground state helium-3 wave function is basically a diproton in the ${}^1S_0$ state with an unpaired neutron. Because of this, when a π^- is produced off the neutron, the resulting recoiling proton is Pauli blocked from interacting (in the s-wave) with one of the protons in the spectator diproton. Hence, NN final state interactions should not play a significant role in π^- production from helium-3. In the case of π^+ production, there are three possible final states: ^{3}H, Dn, and pnn. Only in the last two are NN final state interactions possible. Here, the recoiling neutron is not Pauli blocked from interacting with either spectator. In the same way that the proton-deuteron cross section is roughly the pp + pn cross section, we assume that the strength of the final state interaction is roughly double that of the single spectator case. This leads to the ansatz that the inverse of the Jost function, $J_l^{-1}(k_{rel})$, is doubled and that appropriate correction is four times as large ($2^2 \times |J_l(k_{rel})|^{-2}$) in the two spectator case.

While the NN final state interaction correction procedure described above is easy to understand and implement, it has the disadvantage that it presents a rather simplified picture of the processes involved. In particular, the Jost function for the effective range potential (Equation 5.17) is incorrect when one wishes to properly account for Coulombic effects (as in the proton-proton final state). It is possible to properly include Coulomb modifications to the Jost function, but it is not a simple calculation. Rather, we recognize that the form in Equation 5.17

may have some shortcomings and introduce an altered form of the correction given in Equation 5.15. We introduce an arbitrary scaling factor for the part of the correction that deviates from unity and the correction then becomes,

$$\sigma_{\pi}^{NN\ \mathrm{FSI}} = \left[1 + \delta \times \left(\frac{1}{|J_l(k_{rel})|^2} - 1\right)\right] \sigma_{\pi}. \tag{5.20}$$

This form of the correction also approaches 1 as k_{rel} gets large. However, the parameter δ gives us a handle on how quickly (or slowly) the correction dies off. Note that for $\delta = 1$, the original form of the correction is recovered.

In practice, we extract the appropriate value of δ by fitting to the $W = 1.6$ GeV, high ϵ data. This data is chosen because the kinematic spread at the γ^*-N vertex is small, and the high ϵ models are constrained by real data. The extracted values of δ are given in Table 5.1. Note that the deuterium π^+ value is very close to 1 (i.e. little modification to the Jost function is necessary), giving one confidence in the overall procedure. The deviation of the deuterium π^- value from 1 is likely due to the improper inclusion of Coulombic effects as discussed above. The helium-3 π^- value is consistent with zero, which affirms the idea that NN FSI should be suppressed in the three proton final state. Note that the helium-3 π^+ value is not fit due to the difficulties in subtracting away the radiative tail of the ^{3}H final state that lies beneath the Dn and pnn final states. However, tests using the "doubling of the inverse Jost function" procedure described above show similar agreement for the deuterium and helium-3 π^+ final states for the same value of δ.

As a test of the systematic effects of the NN FSI correction, the experimental cross sections are extracted three ways. First, we use Equation 5.20 and the appropriate value of δ given in Table 5.1. Second, we fit the parameter δ for each model prior to iteration. Finally, we allow the iteration procedure to extract the experimental cross section with no correction for NN FSI. All three of these

Target	Polarity	δ
Deuterium	π^+	0.891
	π^-	0.437
Helium-3	π^-	0.0
	π^+	0.891[a]

[a]In this case, the value of the inverse Jost function has been doubled to account for possible interactions between either of the two spectators.

TABLE 5.1. NN final state interaction parameter, δ, fit to $W = 1.6$ GeV, high ϵ data. The fact that $\delta \approx 1$ for the deuterium π^+ data indicates that the overall method works well. The deviation from one in the deuterium π^- case results from the fact that we do not properly account for Coulomb repulsion (between the final state protons) in the simple Jost function formalism.

methods are used for all targets - except in the case of π^- production from helium-3 where the good value of δ is the same as the "no FSI" case.

In general, the extracted cross sections can vary on the order of 1% depending on which prescription is used. However, it is important to note that the effect is mostly constant for a given target (i.e. not ϵ dependent) so the assigned uncertainty of 1% is assumed not to propagate randomly in the L-T separation.

5.4.2. Iteration of the Model Cross Section

The Monte Carlo model cross section is iterated using a stand-alone FORTRAN program. This program makes use of HBOOK [63] routines to take care of histogramming the data and SIMC quantities and uses the MINUIT [64] optimization package to fit corrections to the model. The corrected model is given by,

$$\sigma_\pi^{it} = C(\omega, Q^2, \theta_{pq}, \phi_{pq}, P_\pi)\sigma_\pi^{model}\,, \tag{5.21}$$

where $C(\omega, Q^2, \theta_{pq}, \phi_{pq}, P_\pi)$ is the correction function and σ_π^{model} denotes the original model cross section (be it the hydrogen cross section or the deuterium/helium-3 cross section modified by the NN FSI prescription). The total correction function is approximated by,

$$C(\omega, Q^2, \theta_{pq}, \phi_{pq}, P_\pi) = O(\omega)K(Q^2)T(\theta_{pq})F(\phi_{pq})P(P_\pi)\,, \tag{5.22}$$

where it is assumed that the total correction can be factorized into independent 1-dimensional correction functions. The iteration scheme fits corrections to 1-dimensional distributions in ω, Q^2, θ_{pq}, ϕ_{pq}, and P_π (for the nuclear targets) in that sequence. One such cycle through each variable in considered one "iteration." At each step, the "experimental" cross section is calculated. The iteration has converged when this quantity stops changing with each successive cycle. In general it takes only 5-10 iterations for the model to converge, however the routine runs for 20 iterations to ensure there is no slow drift.

The iteration of the model cross section relies on two main assumptions. First, we assume the starting model largely corrects for any gross behaviors of the cross section across the acceptance. A good example of this is the $\approx Q^{-4}$ behavior of the Mott cross section. Second, we assume that we can tweak the existing model with small corrections and that these corrections largely factorize in the variables of interest. Hence, we can fit a separate correction to the model in ω, Q^2, etc. Clearly, one should not expect that the actual cross section will factorize in this fashion. We take the point of view that these corrections are a small perturbation on the original input model, and hence our factorized correction can be viewed as a product of truncated Taylor expansions in ω, Q^2, etc.

The iteration procedure itself can be broken down into three major steps: 1) histogramming 2) correction fitting and 3) cross section calculation. The following sections will examine each of these steps in more detail.

5.4.2.1. Creating the histograms

One dimensional histograms are created and filled for the data and Monte Carlo in the variables in which we wish to iterate. For pion electroproduction from hydrogen, these variables are ω ($=E_{beam} - E_e$), Q^2, θ_{pq}, and ϕ_{pq}.[5] In the case of deuterium and helium-3, the cross section contains an extra degree of freedom, so an extra variable (P_π) is added to the iteration scheme. It is important to note that since we have assumed that our corrections to the model will factorize in each variable, we sum over all the other variables when making the one-dimensional histograms. For example, the ω histogram contains contributions from all Q^2 in the acceptance - no effort is made to make each bin in ω sample some narrow region in Q^2, although the ranges in the data and Monte Carlo are identical.

Once the histograms have been created, we take ratios of the data and Monte Carlo distributions to look for deviations between the two. Since we already know that the data and Monte Carlo resolutions are not perfectly matched, it is necessary to restrict the histograms of the variables in which we will be iterating to regions where the acceptance is not changing rapidly, or where there is not a low number of counts. In general, the histograms are restricted such that the number of counts in a given bin is not less than ≈ 0.25 of the largest number of counts per bin in the acceptance. Also, regions where the number of counts is changing very rapidly are avoided. This is illustrated in Figure 5.2.

---

[5]Note that in the electroproduction models, W and θ_{cm}, as opposed to ω and θ_{pq}, are the relevant inputs. However, since these quantities are calculated in the γ^*-N center of mass frame, which cannot be reconstructed for a given event in the case of production from deuterium and helium-3, it was decided to use a set of variables that are analogous to the "physics" variables, but are more clearly interpretable experimentally.

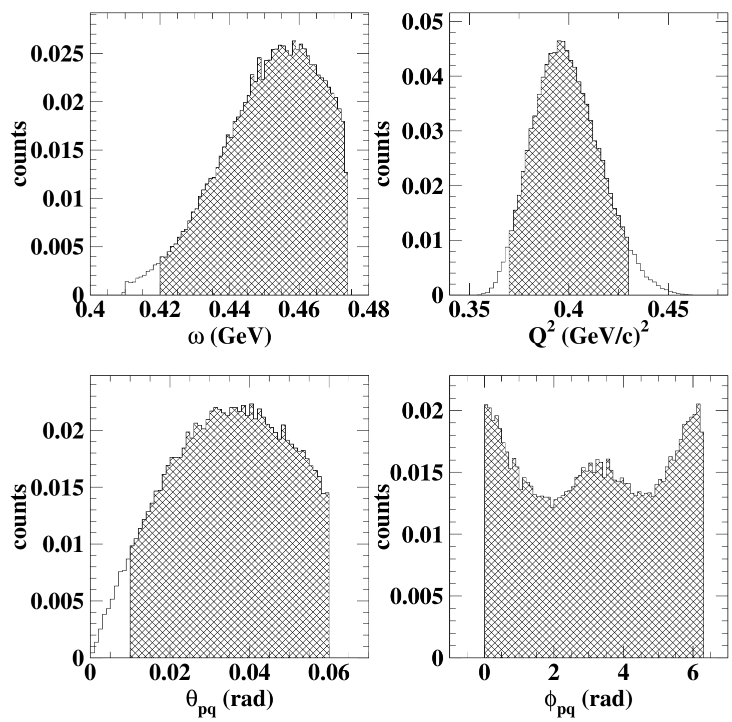

FIGURE 5.2. Regions of experimental acceptance included in the iteration procedure for $W = 1.15$ GeV, $\epsilon = 0.437$ data. Unfilled regions denote data excluded from the "iteration" histograms. Regions of low relative counts and rapidly varying acceptance are avoided. Note that these cuts apply to the iteration only - cross sections are extracted using the full data set.

Note that although we restrict the region over which we fit the correction functions to the input model, we use the "full" distributions to extract the cross sections. This goes along with our philosophy of letting the spectrometers set the accepted region as much as possible. In regions excluded from the correction fitting, we merely use the value of the correction at the nearest point at which it is fit, i.e. a constant correction beyond the fit region. Since the regions excluded from the fits generally have lower numbers of counts, the difference between assuming a constant correction, and extrapolating the correction beyond the region of the fit is minimal (generally much less than the statistical precision of the measurement).

5.4.2.2. Fitting the correction function

Once the histograms have been filled, the histogram ratios are created. If the model description of the dependence on a particular variable is accurate, the ratio should be flat. Any deviation from flat is fit with some smooth function. This function becomes the correction and is applied to the model. It is important to point out that although the correction function is fit using "experimental" distributions (i.e. distributions that include radiation, multiple scattering, etc.) the correction is applied to the model cross section in terms of the vertex variables.

The correction functions fit to the data/SIMC ratios are,

$$O(\omega) = a_0 + a_1\omega \,, \tag{5.23}$$

$$K(Q^2) = b_0 + b_1 Q^2 \,, \tag{5.24}$$

$$T(\theta_{pq}) = c_0 + c_1\theta_{pq} \,, \tag{5.25}$$

$$F(\phi_{pq}) = d_0 + d_1\cos(\phi_{pq}) + d_2\cos(2\phi_{pq}) \,, \tag{5.26}$$

$$P(P_\pi) = e_0 + e_1 P_\pi + e_2 P_\pi^2 \,. \tag{5.27}$$

The total correction is then,

$$C(\omega, Q^2, \theta_{pq}, \phi_{pq}, P_\pi) = O(\omega)\, K(Q^2)\, T(\theta_{pq})\, F(\phi_{pq})\, P(P_\pi) \,, \tag{5.28}$$

and the iterated model cross section is,

$$\sigma_\pi^{it} = C(\omega, Q^2, \theta_{pq}, \phi_{pq}, P_\pi)\, \sigma_\pi^{model}. \tag{5.29}$$

Once the correction function for a particular variable has been fit, the SIMC histograms are re-filled with the new (iterated) model weighting, and the next variable is fit. The fitting sequence is ω, Q^2, θ_{pq}, ϕ_{pq}, and finally, if we are dealing with a nuclear target, P_π. Note that in each subsequent iteration of a given variable, the correction function is fit to the data/SIMC ratio multiplied by the correction function from the previous iteration. For example, consider the nth cycle through the iteration process. The new function fit to ω is,

$$O_n(\omega) = \frac{Y_{DATA}}{Y_{SIMC}}(\omega_{exp})\, O_{n-1}(\omega)\,, \tag{5.30}$$

where ω_{exp} denotes the reconstructed value of ω as opposed to the value at the vertex, which is not directly available experimentally. The Monte Carlo histograms are reweighted using this new function of ω, but the functions of the other variables still carry over from the previous iteration and the correction is given by,

$$C(\omega, Q^2, \theta_{pq}, \phi_{pq}) = O_n(\omega)K_{n-1}(Q^2)T_{n-1}(\theta_{pq})F_{n-1}(\phi_{pq})\,. \tag{5.31}$$

Proceeding to the next variable in the sequence, the ratio of the reweighted histograms in Q^2 is calculated, and the correction fit,

$$K_n(Q^2) = \frac{Y_{DATA}}{Y_{SIMC}}(Q^2_{exp})\, K_{n-1}(Q^2)\,. \tag{5.32}$$

Again, the Monte Carlo histograms are reweighted using the new correction in Q^2,

$$C(\omega, Q^2, \theta_{pq}, \phi_{pq}) = O_n(\omega)K_n(Q^2)T_{n-1}(\theta_{pq})F_{n-1}(\phi_{pq})\,. \tag{5.33}$$

The procedure progresses in this manner through all the fit variables and then begins again. The sequence in which the variables are fit turns out to have little or no impact on the extracted cross sections. The effect of the iteration can be seen in Figures 5.3-5.6. In this case the starting model describes the data well so that small corrections are adequate to match the Monte Carlo to the data.

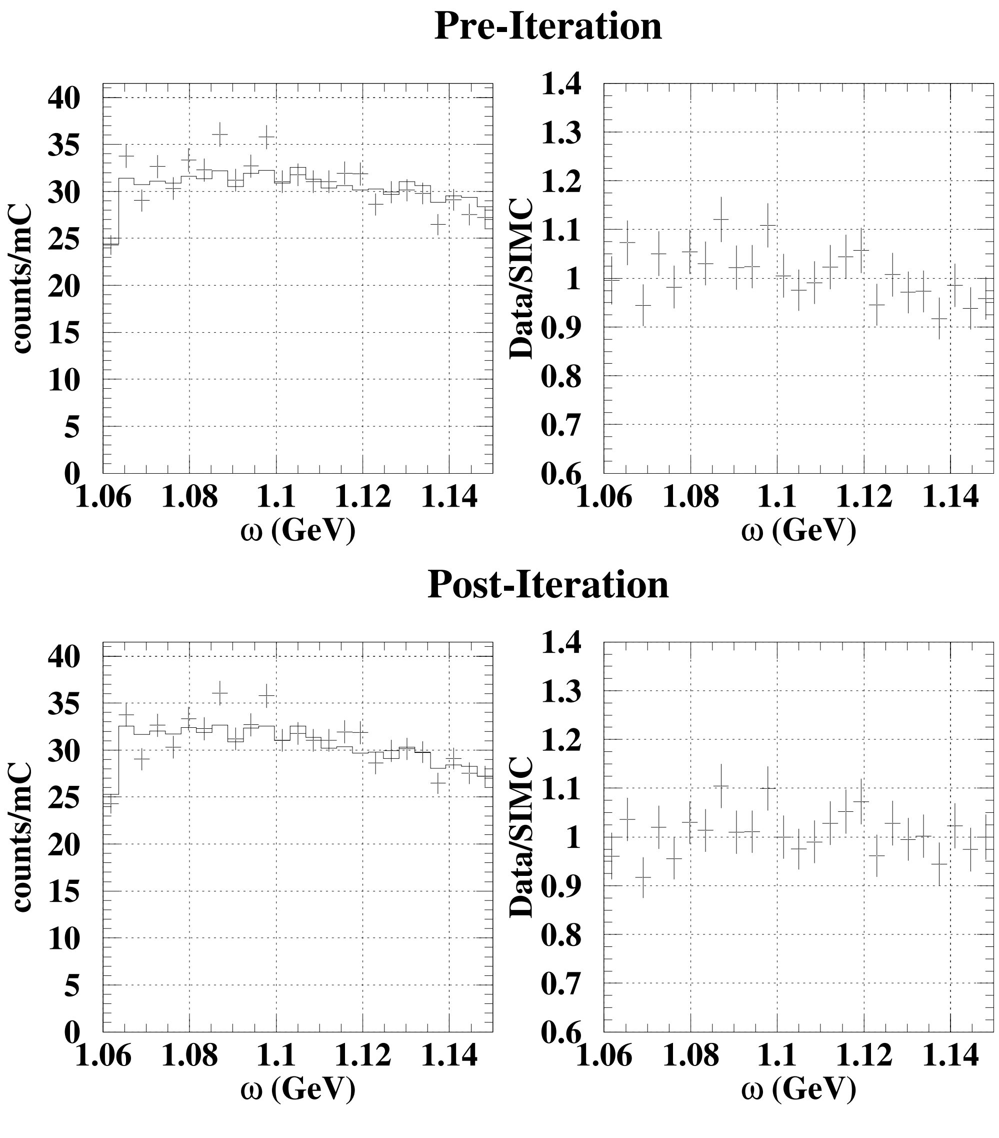

FIGURE 5.3. Effect of iteration scheme on ω for $W = 1.6$ GeV, $\epsilon = 0.89$ hydrogen data. Plots on the left are data (crosses) and SIMC (solid line) charge normalized counts before (top) and after (bottom) iteration. Plots on the right are the ratios of the two histograms on the left. All error bars are statistical only.

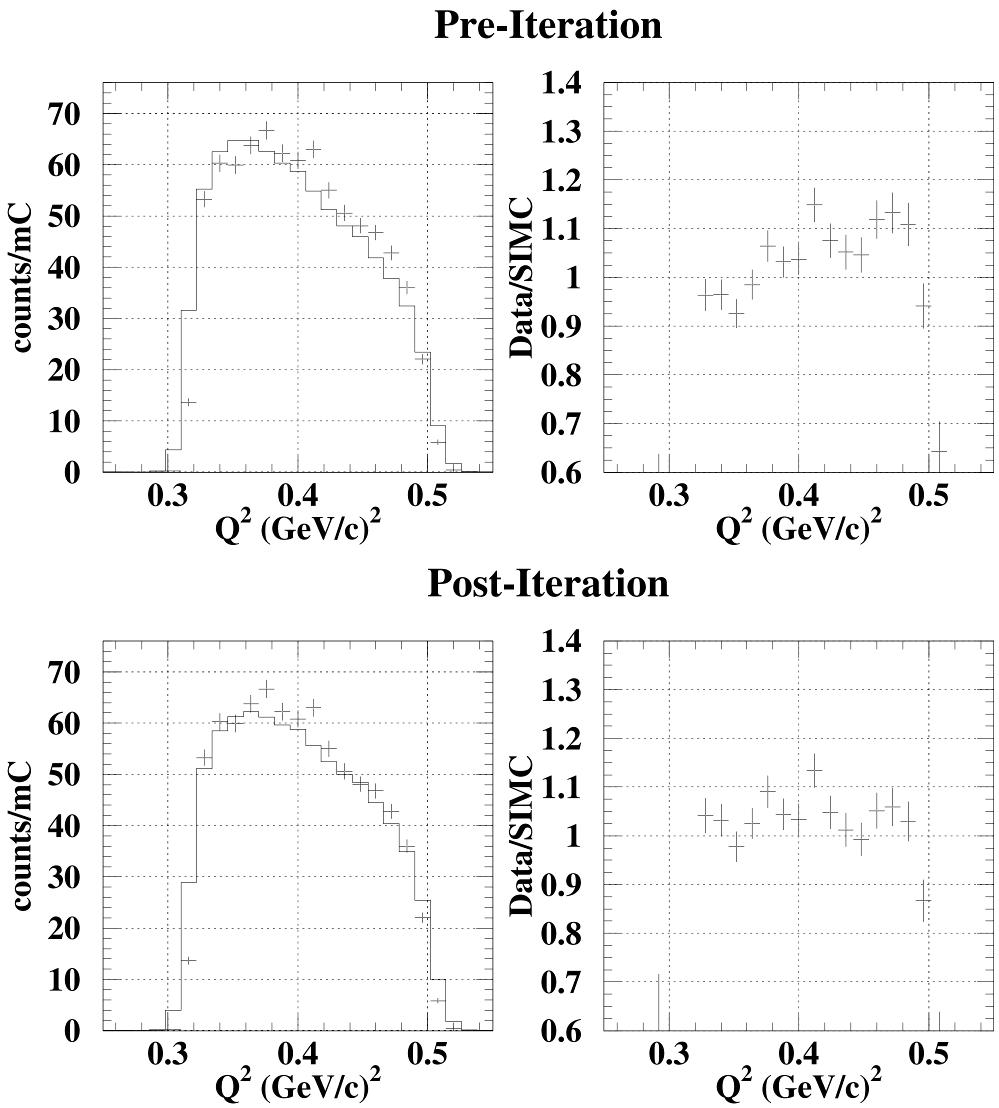

FIGURE 5.4. Effect of iteration scheme on Q^2 for $W = 1.6$ GeV, $\epsilon = 0.89$ hydrogen data. Since the Monte Carlo is normalized to counts, the resolution mismatch between data and SIMC causes the ratio to be greater than 1 in some regions. For our purposes, this is acceptable and it is important only that the ratio be flat in the region of slowly varying acceptance.

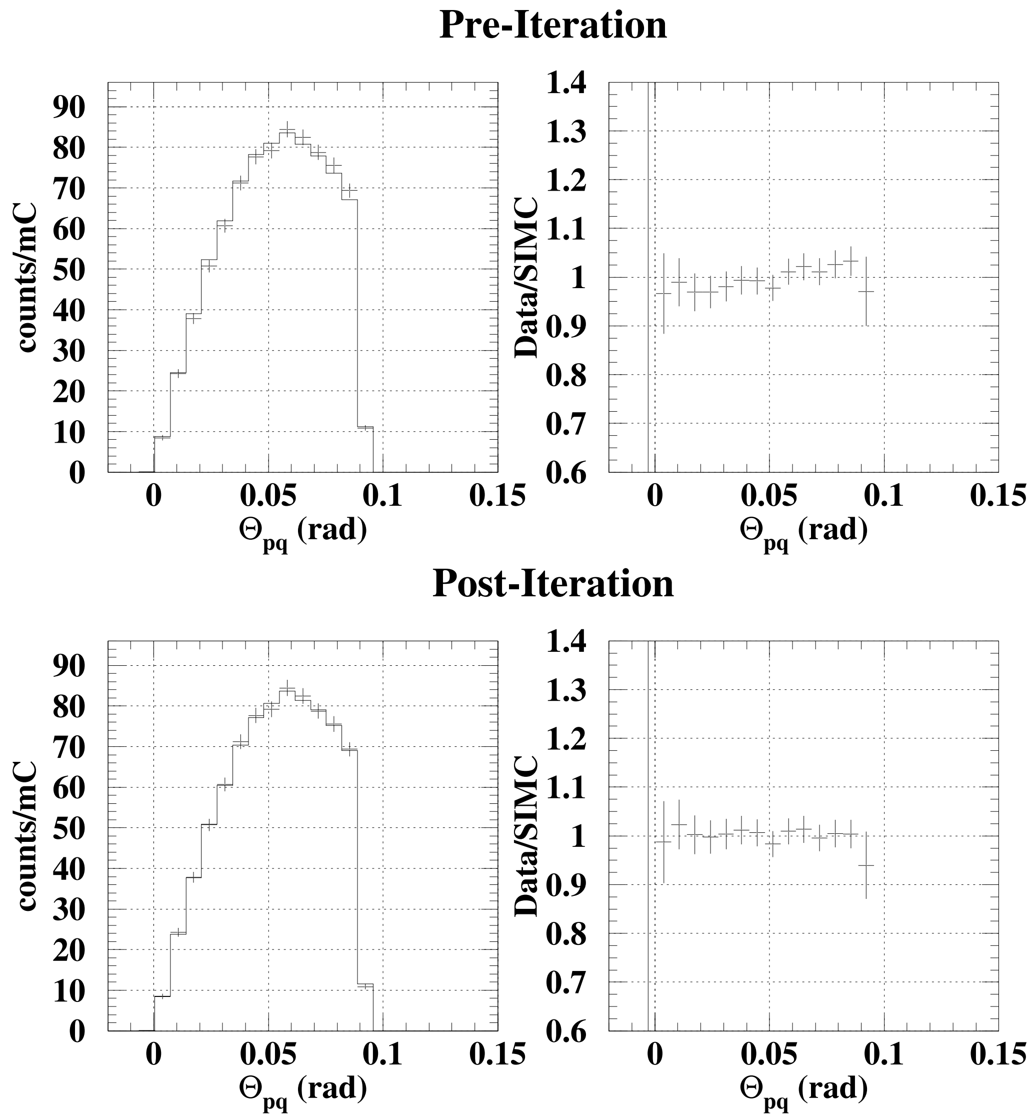

FIGURE 5.5. Effect of iteration scheme on θ_{pq} for $W = 1.6$ GeV, $\epsilon = 0.89$ hydrogen data.

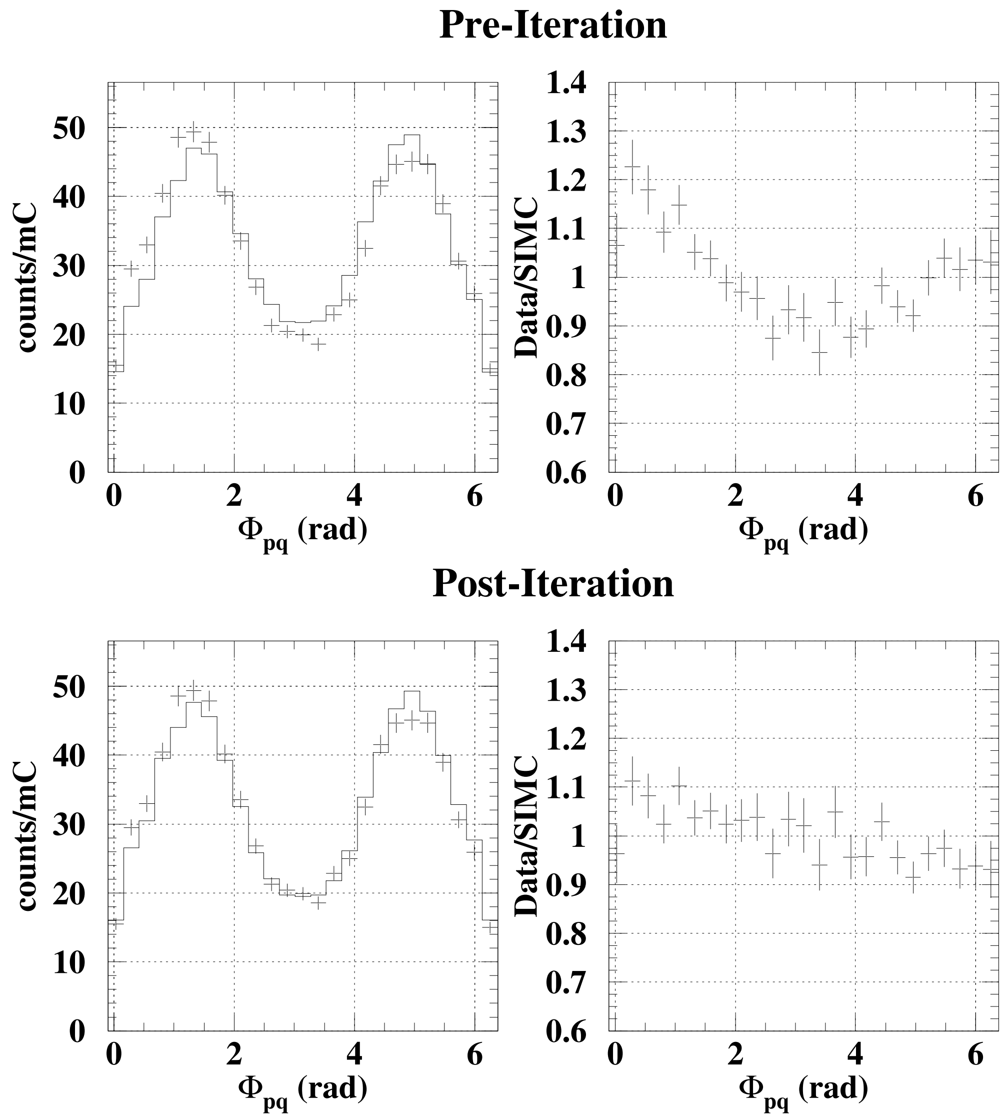

FIGURE 5.6. Effect of iteration scheme on ϕ_{pq} for $W = 1.6$ GeV, $\epsilon = 0.89$ hydrogen data.

5.4.2.3. Cross Section Calculation

At each step in the iteration process, the experimental cross section is re-calculated. Since the experimental cross section is $\sigma^{exp} = \sigma^{model} Y_{DATA}/Y_{SIMC}$, this basically entails determining the new SIMC yield after the model has been tweaked, as well as re-evaluation of the central, model cross section. Using Equation 5.29, the new central cross section (for hydrogen) is,

$$\sigma^{it}_{central} = C(\omega_0, Q^2_0, \theta_0, \phi_{pq})\, \sigma^{model}_{central}\,, \tag{5.34}$$

where the correction function is evaluated at the central kinematics. Note that the ϕ_{pq} dependence is retained in the above expression. Although the ϕ_{pq} dependent terms do not contribute, we must retain the overall scale term from $F(\phi_{pq})$, d_1. In the case of electroproduction from the nuclear targets, the new central cross section is,

$$\sigma^{it}_{central} = \int_{P_{min}}^{P_{max}} C(\omega_0, Q^2_0, \theta_0, \phi_{pq}, P_\pi)\, \frac{d\langle\sigma^{model}_{central}\rangle}{dP_\pi} dP_\pi\,. \tag{5.35}$$

5.4.2.4. $^3He(e, e'\pi^+)$ Cross Section Extraction

The above description of the iteration procedure applies to almost all of the data taken during E91003 in that the pion electroproduction process can usually be described in terms of free or quasifree production (with some refinements). Positively charged pion production from helium-3 however is a special case. Here, we have not only the quasifree production mechanism, but also a coherent channel in which the final state is a bound system, ^{3}H. A comparison of the helium-3 spectra at $W = 1.6$ GeV for π^+ and π^- production is shown in Figure 5.7. Clearly present in the π^+ spectrum is the ^{3}H coherent final state in addition to the Dn

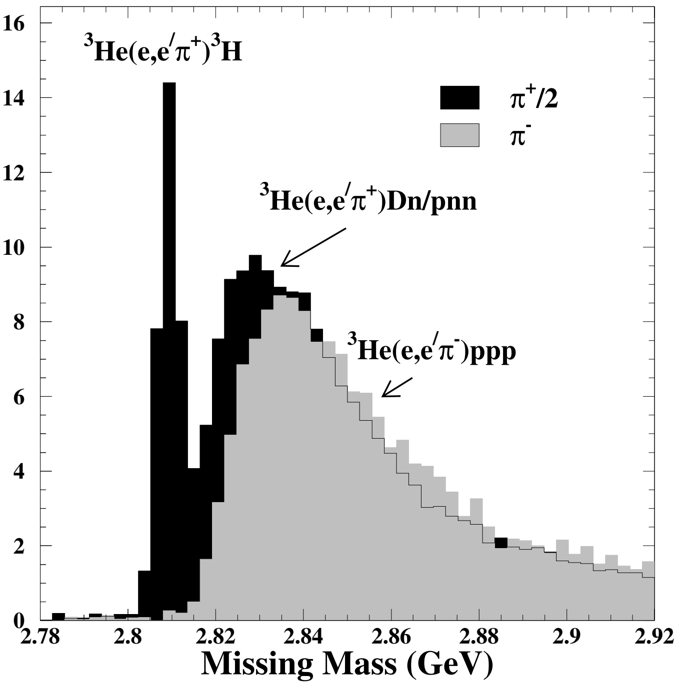

FIGURE 5.7. Helium-3 π^+ and π^- spectra for $W = 1.6$ GeV, high ϵ data. The π^+ yield has been divided by 2 for comparison with the π^- data.

and *pnn* continuum states. To extract the total cross section integrated over all these final states, the ^{3}H and Dn/pnn contributions are modeled separately in the Monte Carlo.[6] Then, the input model is iterated in the same fashion as described above, except in this case the relative strength of the ^{3}H final state is also fit during each iteration cycle. A missing mass spectrum showing the data compared to the Monte Carlo (after a single iteration to find the relative strength of the ^{3}H peak)

[6]The trial spectral function (see Section 4.2.1) is assumed to model the strength of the deuterium final state relative to the *pn* final state appropriately so that we need not treat them separately.

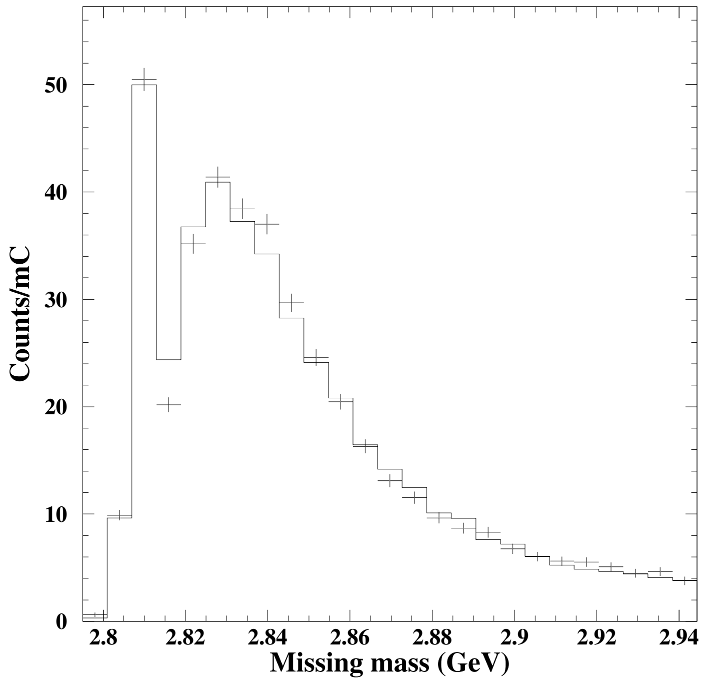

FIGURE 5.8. Missing mass spectrum for ^{3}He$(e, e'\pi^+)$ at $W = 1.6$ GeV compared to Monte Carlo. Crosses are the data and the solid curve is the Monte Carlo simulation. The relative strength of the ^{3}H peak has been fit as described in the text.

is shown in Figure 5.8. The Monte Carlo also includes corrections for final state interactions between the recoiling neutron and the spectator pn system.

At $W = 1.15$ GeV the ^{3}H final state is not in the acceptance because of the limited P_π/missing mass coverage. Despite this, it is possible that events produced from the ^{3}He$(e, e'\pi^+)^3$H process may radiate into the raw missing mass spectrum. We ignore this process for two reasons. First, our lower effective missing mass cut at $M_x = 2.845$ GeV is approximately 35 MeV above the position of the ^{3}H peak - the radiative tail should be quite small at that point. Second, calculations [65] indicate that the $^3\mathrm{He}(e,e'\pi^+)^3\mathrm{H}$ cross section should be suppressed relative to the $\mathrm{H}(e,e'\pi^+)n$ cross section by a factor approximately proportional to the square of the helium-3 form factor, F^2. At these kinematics, $F^2 \approx 0.0425$, hence the likely contamination in our missing mass region is on the order of 10% of $F^2/2$, or 0.2%. Therefore, we extract the cross sections at this point including only the Dn/pnn final states in the iteration scheme.

5.4.2.5. Input Model Dependence and Iteration Procedure Uncertainty

The initial input model used in the above described iteration procedure is the MAID model [66] developed by Drechsel *et al.* This model is constrained by existing pion electroproduction and photoproduction data and is applicable across the full kinematic range of this experiment. Four forms of this model are used in the analysis; 1) the original formulation that matches most closely the description in Ref. [66], 2) the new MAID 2000 formulation that has an improved unitarization procedure, 3) the original MAID model with the longitudinal to transverse ratio adjusted to agree with the first pass analysis results from our data, and 4) the same L-T adjustment to the MAID 2000 model. Since our data does not seem to prefer any one of these variations over the other (at least over our limited acceptance), the final result is taken to be the mean of these four variations of the model.

The model dependence of the iteration procedure is estimated using the variation of the extracted cross section with the four versions of MAID described above. Additionally, one more "reasonable" starting model is used to check the procedure. The additional model for the $W = 1.15$ GeV data is a multipole analysis by von Gehlen [67] (valid up to $W \approx 1.35$ GeV) while for the $W = 1.6$ GeV data, a parameterization of pion electroproduction data taken at $W = 2.2$ GeV [68] is used. Use of the latter may seem inappropriate due to the fact that, even at $W = 1.6$ GeV, we are still in the resonance region. However, at that W, we are above most of the prominent resonances (the $\Delta(1232)$ and $S_{11}(1535)$ for example) and examination of the data reveals no strong W dependence over the limited region of our acceptance.

As a further test, the cross section is also extracted using a "flat" model in which only the virtual photon flux (Γ) is used as the starting model in the iteration process. This last test is a kind of worst case scenario. Our iteration procedure is based on the assumption that the starting model only needs small corrections - in the case of the "flat" model, it is clear that there is no reason to expect the starting model to well describe the data. This can be seen in Figure 5.9 where the post-iteration correction ($C(\omega, Q^2, \theta_{pq}, \phi_{pq}, P_\pi)$ as defined in Equation 5.28) is shown for the MAID and flat starting models. In the former case, the correction is peaked at ≈ 1 and has a (symmetric) spread of about 9% (rms). On the other hand, the correction to the flat starting model is not quite centered at 1, with a spread of $\approx 14\%$ (rms). It is worth noting that in the MAID case, almost all events have a correction of less than 20% while in the flat case, a significant number of events require corrections of more than 20%.

As an example of the model dependence of the experimental cross section, consider the $W = 1.15$ GeV helium, π^+ data. In this case, the variation in the extracted cross section amongst the four forms of MAID is 0.42% at low ϵ and 0.19% at high ϵ. The extracted cross section using the multipole analysis of von Gehlen yields a cross section 0.49% (0.30%) different from the mean of the four MAID forms at low (high) ϵ. Even the flat model, which is clearly a poor candidate for a good starting model for the iteration, gives an iterated result within 1.65% (0.23%) at low (high) ϵ of the average MAID value.

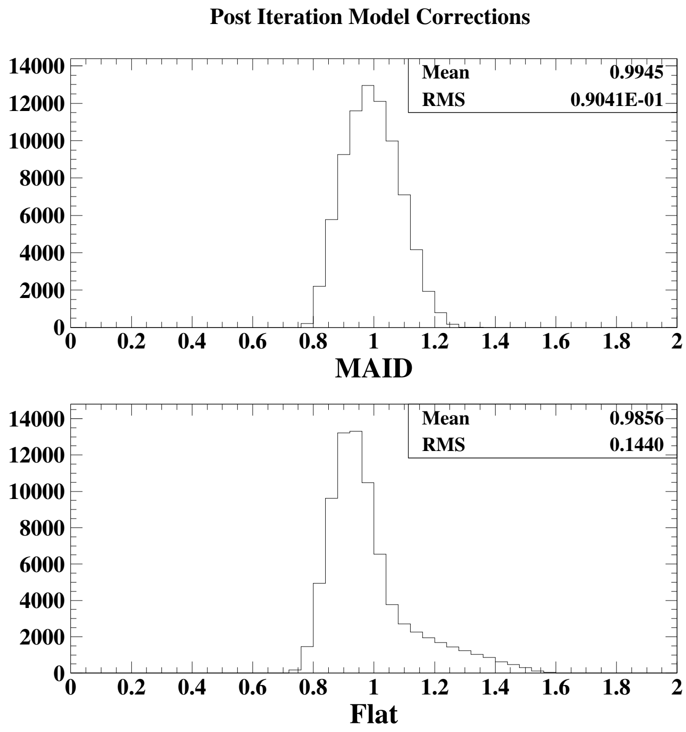

FIGURE 5.9. Distribution over the event population of the iterated correction function, $C(\omega, Q^2, \theta_{pq}, \phi_{pq}, P_\pi)$, for MAID and flat input models. The large spread in the size of the correction (0.8-1.6) for the flat case indicates that it is not a good choice as a starting model for the iteration procedure.

The results of such an examination of the model dependence, averaged over all targets, are shown in Table 5.2. Clearly, the cross sections extracted using the flat starting model deviate most strongly from the nominal "good" value. However, considering that we do not expect the iteration procedure to deal well with poor starting models, the agreement is surprisingly good. While it is possible that the model dependence of the extracted cross section is somewhat correlated between ϵ settings and targets, precise determination of which part of the corresponding uncertainty is random and which part is correlated is a challenging prospect. However, since other systematic uncertainties render these relatively insignificant, we conservatively assign a totally uncorrelated uncertainty of 0.4% for all targets and kinematic settings, based on the deviation amongst the reasonable starting models.

Model	$W = 1.15$ GeV		$W = 1.6$ GeV	
	$\epsilon = 0.437$	$\epsilon = 0.861$	$\epsilon = 0.490$	$\epsilon = 0.894$
MAID	0.37%	0.38%	0.17%	0.23%
von Gehlen	0.55%	0.14%	-	-
Brauel param.	-	-	0.29%	0.40%
Flat	2.50%	0.82%	2.34%	1.28%

TABLE 5.2. Input model dependence of experimental cross sections extracted using the iteration procedure. The mean of the values extracted using the four forms of MAID described in the text is taken to be the "good" value. The MAID row denotes the standard deviation among the four, while the remaining rows denote the deviation from the average MAID value using those models. The value at each kinematic setting is averaged over all targets.

As a further test, the iteration procedure was carried out varying the cuts used on the spectrometer quantities (δ, x'_{tar}, and y'_{tar}) in each arm. While this is partially a test on our understanding of the spectrometer acceptances, it also tests the stability of the iteration procedure. Table 5.3 shows the variation of the extracted hydrogen cross sections when the spectrometer cuts have been varied $\approx 10-20\%$. The variations shown are the average of increasing and decreasing the cut. In the case of the $W = 1.15$ GeV, HMS δ cut variation, the change in the cross section may be amplified a bit due to the fact the cut is explicitly chosen so as to eliminate as many collimator punch-through events as possible (see Section 4.6). Nonetheless, the variation of the extracted cross section is fairly

Cut (variation)	$W = 1.15$ GeV		$W = 1.6$ GeV		Average
	$\epsilon = 0.44$	$\epsilon = 0.86$	$\epsilon = 0.49$	$\epsilon = 0.89$	
HMS δ (nom$\pm$1%)[a]	0.77%	0.55%	0.60%	0.34%	0.57%
HMS x'_{tar} (nom$\pm$1.5 mrad)	0.41%	0.08%	0.42%	0.05%	0.24%
HMS y'_{tar} (nom$\pm$1 mrad)	0.17%	0.01%	0.06%	0.02%	0.18%
SOS δ (nom$\pm$2%)	1.06%	0.20%	0.04%	0.06%	0.34%
SOS x'_{tar} (nom$\pm$1 mrad)	0.05%	0.05%	0.10%	0.14%	0.24%
SOS y'_{tar} (nom$\pm$1.5 mrad)	0.15%	0.07%	0.11%	0.15%	0.12%
Quadrature Sum					0.78%

[a]Cut variation for full δ range ($\pm$8%). In the case of smaller δ cuts to match ω acceptance, the same fractional (rather than absolute) variation is used.

TABLE 5.3. Change in extracted cross section with variation of spectrometer cuts. Deviations shown are for hydrogen cross sections only and denote the mean of the effect of increasing and decreasing the cuts by the indicated amount.

small. The quadrature sum of the mean variation for each quantity is 0.78%. Assuming a point to point uncertainty of 0.5% for the acceptance, we assign a 0.6% ($= [(0.78\%)^2 - (0.5\%)^2]^{1/2}$) random uncertainty for the iteration procedure.

5.5. Error Analysis

A number of the systematic uncertainties in this analysis have already been discussed in previous sections. Tables 5.4 and 5.5 list these uncertainties and the sections in which they were discussed.

One class of uncertainties that has not yet been discussed are the errors arising from incorrect values of kinematic quantities: namely, beam energy and central spectrometer angles and momenta. These uncertainties are estimated using a pion

Quantity	Correction Size (%)	Random (%)	Random b/t targets (%)	Scale (%)	Discussed in Section
Particle ID					
SOS Č π ID	0.07 (.29 GeV)	0.02	-	-	3.3.2
	0.46 (1 GeV)	0.05	-	-	"
SOS β	0.17 (.29 GeV)	0.40	-	-	"
efficiency	4.05 (1 GeV)	0.47	-	-	"
HMS Č e^- ID	0.14	0.14	-	-	3.3.1
Normalization					
Charge	-	0.5	-	1.0	2.2.3
Target thickness:					
19K H	-	0.68	-	-	2.3
18K H	-	-	0.89	-	"
D2	-	-	0.83	-	"
He3	-	-	1.24	-	"
Corrections					
SOS Trigger Efficiency	1.3 (.29 GeV)	0.2	-	-	3.4.1
	0.4 (1 GeV)	0.2	-	-	"
HMS Trigger Efficiency	0.1	0.1	-	-	"
Computer dead time	0-60	0.1	-	-	3.4.2
Coincidence blocking	0-8	0.1	-	-	3.4.3
Tracking efficiency	0-5	0.5	-	1.5	3.4.4
^{3}He pressure	0-2	0.4	-	-	3.4.6
Pion absorption	$\approx$ 10(.29 GeV)	-	1.0(0.4pol)	5.8	3.4.7
	$\approx$ 5(1 GeV)	-	0.4(0pol)	3.5	"
Kinematics[a]					
E_{beam}	-	0.28-0.56	-	-	
θ_e	-	0.37-1.43	-	-	
E_e	-	0.11-0.5	-	-	
θ_π	-	0.1-0.23	-	-	
P_π	-	-	-	0.1-0.47	
Monte Carlo					
Pion Decay	-	0.5	-	2.0	4.5
Collimator Punch Through	-	0.25	0.5	1.0	4.6
Radiative Corrections	-	0.5	1.0	2.2	4.7
Acceptance	-	0.5	-	2.0	4.8 and 5.4.2.5
Iteration Procedure	-	0.6	-	-	5.4.2.5
Model Dependence	-	0.5	-	-	"
NN FSI	-	-	1.0	1.0	5.4.1

[a] Kinematic uncertainties listed in the random column will partially cancel in the separated ratios as discussed in the text.

TABLE 5.4. Summary of random and scale type uncertainties. The uncertainties in the table refer to the uncertainty in the final cross section due to the uncertainty in that quantity. Random uncertainties must be included at each ϵ when extracting the separated cross sections, σ_L and σ_T. Scale uncertainties apply directly to the separated cross sections. Quantities in the "Random b/t target" column are scale for a given target, but not between targets.

Quantity	Size of Correction	Uncertainty in Correction	Discussed in Section
Efficiencies and corrections			
Dummy subtraction	2.4-8%	3.44% of dummy fraction	3.3.5
Electronic dead time	0-3.5%	10% of elec d.t.(each)	3.4.2
multiple tracks	0-0.5%	25.61% of correction	3.4.4
SOS Č blocking	0-5%	5.88% of correction	3.4.5
Target heating			
19K H	2.9%/100μA	0.43%/100μA	Appendix A
18K H	2.7%/100μA	0.33%/100μA	"
18K H (small raster)	5.4%/100μA	0.67%/100μA	"
D	1.15%/100μA	0.31%/100μA	"
D (small raster)	2.3%/100μA	0.63%/100μA	"
He	5.68%/100μA	1.11%/100μA	"

TABLE 5.5. Rate/current dependent uncertainties. The uncertainty in these corrections is related to incident particle rate and/or beam current. Whether these errors propagate as random or scale depends on the difference in running conditions between ϵ points.

electroproduction model (MAID) and varying each quantity (one at a time) by its corresponding uncertainty (0.1% for the beam energy and momenta and 1 mrad for the spectrometer central angles). The resulting difference in the calculated cross section from the value at the nominal "good" kinematics is taken as the uncertainty in the cross section due to the uncertainty in that quantity. In general, the uncertainty due to kinematic variations is less than 1%, except for the variation due to the central electron scattering angle for the high ϵ settings which gives an uncertainty in the cross section of $\approx$ 1.4%.

In performing an L-T separation, it is important to keep track of two types of errors. The first, random errors, propagate randomly between ϵ settings and must be included at each ϵ point when extracting the longitudinal and transverse cross sections. Examples of random errors are simple counting statistics, kinematic uncertainties (i.e. the beam energy between the different ϵ settings), and certain detector efficiencies. The second type of errors, scale errors, are the same at each ϵ setting so propagate directly into the separated cross sections. Examples of scale errors include the uncertainty in the pion absorption correction and overall target thickness (not including modifications due to beam heating). Since scale errors are the same for the longitudinal and transverse pieces, they cancel in the longitudinal to transverse ratio, R. For this reason, R is sometimes better known than the separated cross sections themselves. Often, uncertainties in a given quantity are a mixture of random and scale type errors. For example, we assign an overall 2.2% uncertainty to the radiative corrections procedure, but acknowledge that some part of that uncertainty may be random between ϵ settings (0.5%).

Some types of uncertainty are proportional to incident particle rates or beam currents, and hence are not clearly identifiable as either random or scale. An example of this is the target heating correction, the uncertainty of which is directly proportional to the incident beam current. If the beam current were identical between ϵ settings, then the uncertainty in the correction is totally scale and propagates directly into the separated cross sections. However, this is rarely the case, and any random components must be accounted for. In this analysis, the effect of uncertainties of this nature are estimated as follows: the unseparated cross sections are varied simultaneously by the 1 σ value of the uncertainty of the rate/current dependent correction (for the average rate/current at a given measurement) and the effect on the separated cross section determined. For example, given an uncertainty, $\delta(I)$, that is a function of beam current, the uncertainty on the longitudinal cross section is calculated,

$$\delta\sigma_L = \frac{\sigma_1(1+\delta_1(I_1)) - \sigma_2(1+\delta_2(I_2))}{\epsilon_1 - \epsilon_2} - \frac{\sigma_1 - \sigma_2}{\epsilon_1 - \epsilon_2}\,. \tag{5.36}$$

Other examples of this kind of uncertainty include the electronic dead time, the multiple track correction, and the SOS Čerenkov blocking correction. The uncertainties in the separated cross sections from these quantities are estimated as in Equation 5.36.

The propagation of errors becomes a bit more complicated in the extraction of the longitudinal (and transverse) ratios between targets. In addition to random errors between ϵ settings, there are some errors that propagate directly into the separated cross sections, but are random between targets. An example of this is the target thickness, the uncertainty of which is constant between ϵ settings, but not between targets. Another class of uncertainty comes into play when data for two targets at a given ϵ setting was acquired at the same period in time. In a case such as this, the uncertainty in kinematic quantities would cancel if we were measuring the unseparated cross section ratio between targets. In the case of separated ratios, the uncertainty should still partially cancel. Consider the uncertainty due to the beam energy, δ_E, for the $W = 1.15$ GeV, high ϵ hydrogen and deuterium data (which were taken at the same period in time). Then, the uncertainty in the longitudinal cross section ratio is estimated,

$$\delta\left(\frac{\sigma_D}{\sigma_H}\right)_{Longitudinal} = \frac{\sigma_1^D(1+\delta_E)-\sigma_2^D}{\sigma_1^H(1+\delta_E)-\sigma_2^H} - \frac{\sigma_1^D-\sigma_2^D}{\sigma_1^H-\sigma_2^H}\,, \tag{5.37}$$

where we have ignored any contribution to the uncertainty in the value of ϵ from the beam energy (this is negligible in most cases). The uncertainty in the separated ratios due to the scattered electron energy and angle, and scattered pion angle is also calculated in this fashion. Finally, the rate dependent uncertainties are also calculated in this fashion, except in this case all four cross sections are varied by their 1 σ uncertainties *simultaneously.*

6. RESULTS AND DISCUSSION

6.1. Overview

Although the primary aim of E91003 is to extract separated longitudinal cross section ratios, the absolute cross sections are of much interest in their own right. In the following sections, we will present both the unseparated and separated absolute cross sections for each target, followed by the target ratios.

In order to more easily interpret our results, we focus on the target ratios in which quasifree pion production is the dominant mechanism. In particular, this means that in the helium-3 case we focus on π^- production and compare that to π^- production from deuterium. In the case of π^+ production from helium-3, we are faced with the complication of the bound ^{3}H state in addition to the continuum pnn and Dn final states. Also, it is known that absorption effects are quite large at low pion momentum in this case. These absorption effects are much smaller for $T = 1$ pairs, i.e. in the case of π^- production from helium-3 where the spectator pair consists of two protons.

Of primary interest here are the longitudinal cross section ratios. As noted in Chapter 1, the longitudinal cross section is sensitive to the pole process in which one can view the pion electroproduction process as the knockout of a virtual pion. In that picture, the cross section can be viewed as the probability to have the virtual photon interact with the pion (described in terms of the pion form factor $F_\pi(Q^2)$) times the probability for the nucleon(s) to emit a virtual pion (described in terms of the πNN form factor $g_{\pi NN}(t)$). Any effects from the presence of a pion excess would result in a perceived increase in $g_{\pi NN}$ and hence an enhancement of the pole process.

6.2. Definition of Cross Sections

Recall from Section 1.2 that the lab cross section for hydrogen can be written,

$$\frac{d^5\sigma}{d\Omega_e dE_e d\Omega_\pi} = \Gamma \frac{d\sigma}{d\Omega_\pi}\,, \tag{6.1}$$

where Γ is the virtual photon flux given by,

$$\Gamma = \frac{\alpha}{2\pi^2}\frac{E'_e}{E_e}\frac{1}{Q^2}\frac{1}{1-\epsilon}K_{eq}\,. \tag{6.2}$$

K_{eq} is the equivalent photon energy, given in the Hand convention by,

$$K_{eq} = \frac{W^2 - M^2}{2M}\,, \tag{6.3}$$

with M the target mass and W the total energy in the virtual photon - nucleus center of mass. $d\sigma/d\Omega_\pi$, the virtual photon cross section, can be further broken down into contributions from transverse and longitudinal photons as well as interference terms,

$$\frac{d\sigma}{d\Omega_\pi} = \frac{d\sigma_T}{d\Omega_\pi} + \epsilon\frac{d\sigma_L}{d\Omega_\pi} + \sqrt{2\epsilon(1+\epsilon)}\frac{d\sigma_{LT}}{d\Omega_\pi}\cos\phi + \epsilon\frac{d\sigma_{TT}}{d\Omega_\pi}\cos 2\phi\,. \tag{6.4}$$

In parallel kinematics, the ϕ dependent terms are small and in our case are averaged to zero by integrating over ϕ.

Equation 6.1 holds for pion electroproduction from hydrogen, but in the case of production from deuterium and helium-3, there is an extra degree of freedom and the lab cross section has a 6-fold kinematic dependence instead of a 5-fold dependence. In this case, the lab cross section can still be broken into a virtual photon cross section times the virtual photon flux,

$$\frac{d^6\sigma}{d\Omega_e dE_e d\Omega_\pi dP_\pi} = \Gamma \frac{d\sigma}{d\Omega_\pi dP_\pi}\,. \tag{6.5}$$

The nuclear virtual photon cross section can be broken down in the same way as the hydrogen cross section into longitudinal, transverse, and interference terms,

$$\frac{d\sigma}{d\Omega_\pi dP_\pi} = \frac{d\sigma_T}{d\Omega_\pi dP_\pi} + \epsilon\frac{d\sigma_L}{d\Omega_\pi dP_\pi} + \sqrt{2\epsilon(1+\epsilon)}\frac{d\sigma_{LT}}{d\Omega_\pi dP_\pi}\cos\phi + \epsilon\frac{d\sigma_{TT}}{d\Omega_\pi dP_\pi}\cos 2\phi\,. \tag{6.6}$$

Since we wish to compare the nuclear cross sections to the free proton, we integrate the nuclear cross sections over P_π.[1] The experimental acceptance is limited, so our integrated nuclear cross sections only sample a portion of the full P_π spectrum and will depend on the limits used. Thus, one should keep in mind throughout this chapter that most of the time the integrated nuclear cross sections are really

$$\frac{d\sigma^A}{d\Omega_\pi} = \int_{Pmin}^{Pmax} \frac{d\sigma}{d\Omega_\pi dP_\pi}\, dP_\pi\,. \tag{6.7}$$

It is common practice to express the virtual photon cross section in the virtual photon - target center of mass frame. However, in our case, this is not especially convenient in that the center of mass frame is different for each target. Since we are interested in target comparisons, the virtual photon cross sections given in most of the results that follow are in the laboratory frame where the target is at rest.

6.3. Unseparated Cross Sections

The unseparated cross sections are shown in Table 6.1. The deuterium and helium-3 cross sections have been integrated over P_π to obtain the 5-fold lab

---

[1] One could consider the hydrogen cross sections to also have been integrated over P_π with the P_π dependence given by a δ function.

Target	ϵ	ΔP_π (GeV/c)	$\int_{\Delta P_\pi} d^6\sigma dP_\pi$ (μb/GeV/sr^2)	$\sigma_T + \epsilon\sigma_L$ (μb/sr)	$\frac{\delta\sigma}{\sigma}_{stat}$ (%)	$\frac{\delta\sigma}{\sigma}^{ran}_{sys}$ (%)	$\frac{\delta\sigma}{\sigma}^{scale}_{sys}$ (%)
$W = 1.15$ GeV, $k_\pi = 0.469$ GeV/c							
H	0.437	-	3.12×10^{-3}	17.22	1.4	1.8	7.1
H	0.861	-	2.86×10^{-2}	25.03	1.4	2.3	7.1
D(π^+)	0.437	0.248-0.350	2.18×10^{-3}	8.27	2.3	1.7	7.2
D(π^+)	0.861	0.248-0.350	2.02×10^{-2}	12.19	2.2	2.1	7.2
D(π^-)	0.437	0.248-0.350	1.66×10^{-3}	6.32	2.4	1.7	7.2
D(π^-)	0.861	0.248-0.350	1.87×10^{-2}	11.28	2.0	2.1	7.2
^{3}He(π^-)	0.437	0.248-0.350	1.27×10^{-3}	4.53	3.1	1.8	7.2
^{3}He(π^-)	0.861	0.248-0.350	1.39×10^{-2}	7.61	2.7	2.2	7.2
^{3}He(π^+)	0.437	0.248-0.350	3.52×10^{-3}	12.14	3.0	1.9	7.2
^{3}He(π^+)	0.861	0.248-0.350	3.15×10^{-2}	17.21	1.9	2.3	7.2
$W = 1.60$ GeV, $k_\pi = 0.203$ GeV/c							
H	0.490	-	2.34×10^{-2}	44.23	0.8	1.7	5.4
H	0.894	-	2.99×10^{-1}	58.18	0.8	2.2	5.4
D(π^+)	0.490	>0.936	2.11×10^{-2}	35.62	0.9	1.7	5.5
D(π^+)	0.894	>0.936	2.66×10^{-1}	46.32	0.6	2.3	5.5
D(π^-)	0.490	>0.936	1.81×10^{-2}	30.59	0.9	1.8	5.5
D(π^-)	0.894	>0.936	2.73×10^{-1}	47.46	0.7	2.2	5.5
^{3}He(π^-)	0.490	>0.943	1.37×10^{-2}	22.40	1.2	1.9	5.6
^{3}He(π^-)	0.894	>0.943	1.87×10^{-1}	31.40	0.9	2.3	5.6
^{3}He(π^+)	0.490	>0.943	3.71×10^{-2}	60.38	1.1	1.9	5.6
^{3}He(π^+)	0.894	>0.943	4.74×10^{-1}	79.75	0.8	2.3	5.6

TABLE 6.1. Unseparated cross sections for the $(e, e'\pi)$ process. Results are presented *in the lab frame.* $d^6\sigma$ denotes $\frac{d^6\sigma}{d\Omega_e dE_e d\Omega_\pi dP_\pi}$. Cross sections from deuterium and helium-3 are integrated over P_π, the limits given in the table. Virtual photon cross sections $(\sigma_T + \epsilon\sigma_L)$ are extracted by dividing the lab cross sections by the virtual photon flux (Γ) as defined in Equation 6.2. The uncertainties are listed in three parts. The first set of uncertainties are statistical and the second set are random systematic uncertainties - both of these must be included at each ϵ when extracting the separated cross sections. The third set of uncertainties are the scale systematic uncertainties that propagate directly into the separated cross sections. All results are at $Q^2 = 0.4$ (GeV/c)^2 and $\theta_{pq}^{lab} = 1.72$ degrees.

cross section. The virtual photon cross sections are then calculated by dividing the lab cross sections by the virtual photon flux, Γ (defined in Equation 6.2). At $W = 1.15$ GeV the range of integration is from $P_\pi = 0.248$ GeV/c to 0.350 GeV/c (this corresponds to a missing mass range of $M_x = 1.901 - 1.971$ GeV for deuterium and $M_x = 2.849 - 2.926$ GeV for helium-3). At $W = 1.6$, the P_π acceptance is from ≈ 0.85 to 1.15 GeV/c, however the integration is limited by the missing mass cut (at about 10 MeV below 2 pion threshold) which limits the integration of the central cross section to the region where $P_\pi > 0.935$ (0.943) GeV/c in deuterium (helium-3).

It should be noted that at $W = 1.15$ GeV, the acceptance of the P_π distributions from the nuclear targets is not complete. Figure 6.1 compares the P_π acceptance for the low and high W deuterium data. Because of this limited acceptance, the direct cross section comparison between targets is not very meaningful. This will be discussed further in Section 6.5.

As a check on the extraction of the experimental cross sections, it is useful to compare the E91003 data to previous results. While L-T separated cross sections are not common, there exists a good deal of unseparated cross section data. For the most part, this data has been taken at higher ϵ where the rates are higher.

Figure 6.2 shows E91003 high ϵ hydrogen cross sections compared to previous data. Note that the cross sections are given as the γ^*-p cross sections in the center of mass, different from our usual convention. The low W E91003 cross section has been scaled in ϵ from 0.86 to 0.90 using the separated (experimental) longitudinal and transverse cross sections and has been scaled from $Q^2 = 0.4$ (GeV/c)^2 to 0.3 (GeV/c)^2 and from $\theta^*_{pq} = 3.7$ degrees to 5.0 degrees using the MAID model. Similarly, the higher W E91003 data has been scaled from $\epsilon = 0.89$, $\theta^*_{pq} = 3.6$ degrees to $\epsilon = 0.93$, $\theta^*_{pq} = 0$ degrees. The previous low W data was taken at the

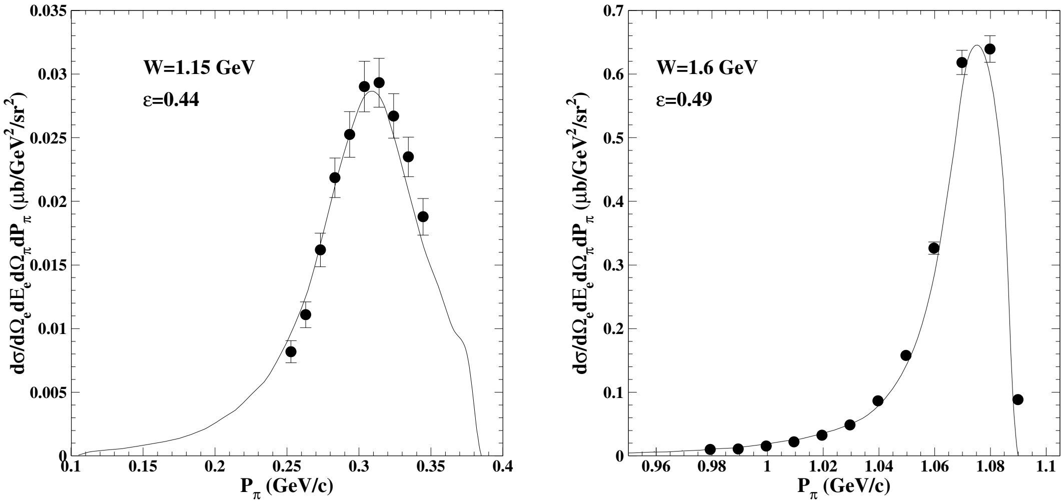

FIGURE 6.1. P_π acceptance for low and high W deuterium data. Points are data with statistical uncertainties only. Curves are our quasifree calculations using the MAID 2000 model modified to include the effects of NN final state interactions (NN FSI are the source of the small "bump" at high P_π in the curve on the left). The curves have been arbitrarily normalized to agree with the data.

2.5 GeV Bonn synchrotron in 1978 [69], while the high W data was taken at the Daresbury Nuclear Physics Laboratory 4 GeV electron beam in 1973 [70]. Both the Bonn and Daresbury data sets show statistical errors only. The systematic uncertainty of the Bonn data is $\approx 5\%$ while the Daresbury data systematic error is $\approx 10\%$. The E91003 data shows combined statistical and systematic uncertainties. The E91003 data agrees very well with these older data sets.

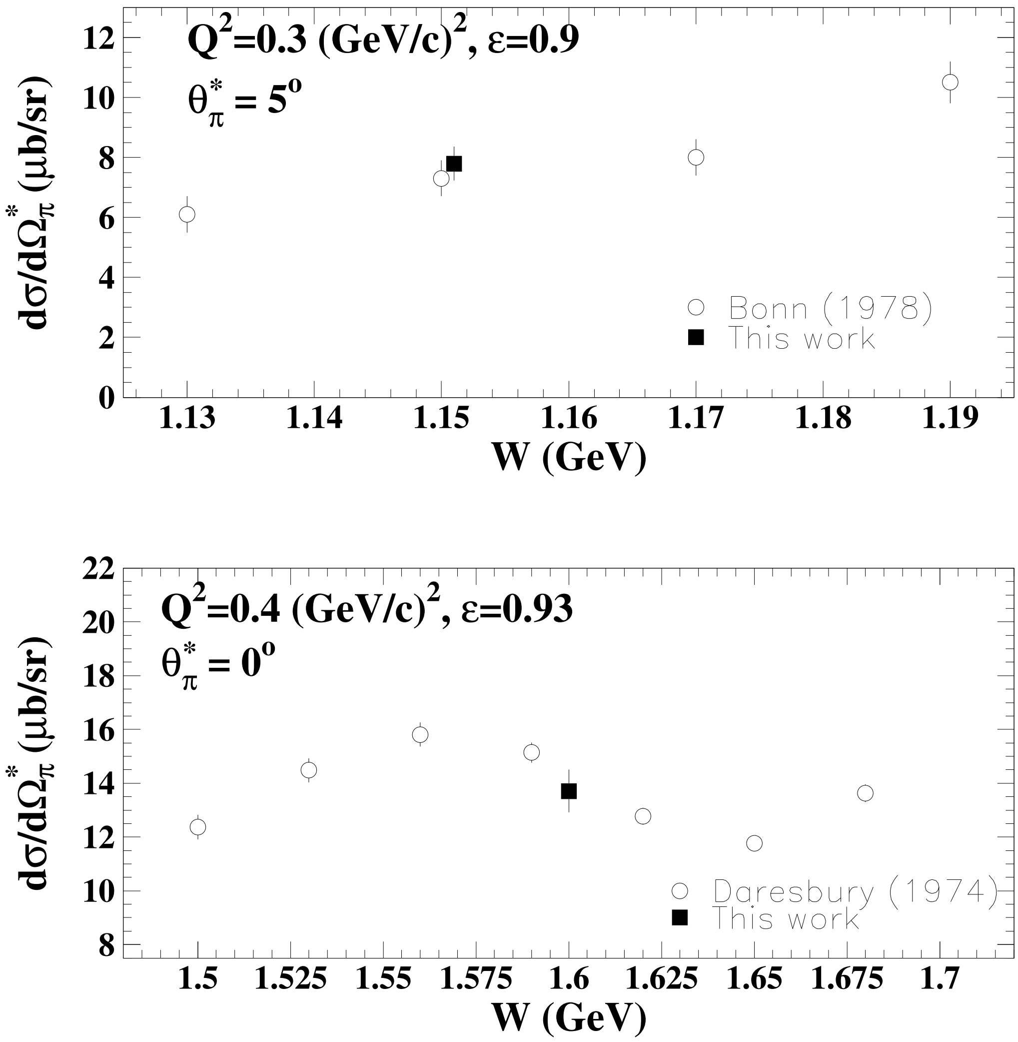

FIGURE 6.2. Unseparated high ϵ hydrogen cross sections from E91003 compared to previous data. The E91003 data has been scaled in Q^2 and θ_π^* using MAID, and scaled in ϵ using the extracted separated cross section information. Errors on previous data are statistical only. The systematic uncertainty on the lower W Bonn data (top plot) is on the order of 5%, while the higher W Daresbury data (bottom) systematic error is 10%.

6.4. Separated Cross Sections

Recalling that the virtual photon cross section (for hydrogen) can be written,

$$\frac{d\sigma}{d\Omega_\pi} = \frac{d\sigma_T}{d\Omega_\pi} + \epsilon \frac{d\sigma_L}{d\Omega_\pi} , \tag{6.8}$$

where the ϕ dependent interference terms have been set to zero, it is clear that the longitudinal and transverse pieces of the cross section can be extracted by varying ϵ and fitting a line - the longitudinal cross section being the slope and the transverse piece the y-intercept. In our case, there are only two ϵ points, so the separated cross sections are,

$$\frac{d\sigma_L}{d\Omega_\pi} = \frac{\sigma_1 - \sigma_2}{\epsilon_1 - \epsilon_2} \tag{6.9}$$

$$\frac{d\sigma_T}{d\Omega_\pi} = \frac{\epsilon_1\sigma_2 - \epsilon_2\sigma_1}{\epsilon_1 - \epsilon_2} . \tag{6.10}$$

For the nuclear cross sections we have,

$$\int_{Pmin}^{Pmax} \frac{d\sigma}{d\Omega_\pi dP_\pi} dP_\pi = \int_{Pmin}^{Pmax} \frac{d\sigma_T}{d\Omega_\pi dP_\pi} dP_\pi + \epsilon \int_{Pmin}^{Pmax} \frac{d\sigma_L}{d\Omega_\pi dP_\pi} dP_\pi . \tag{6.11}$$

In this case, we can extract the P_π integrated longitudinal and transverse cross sections by sampling the P_π integrated virtual photon cross sections at two values of ϵ.

The separated cross sections, σ_T and σ_L, are given in Table 6.2 along with statistical and total systematic uncertainties. For completeness, R, the ratio of σ_L to σ_T, is also included. Again, the cross sections from deuterium and helium-3 are integrated over the P_π acceptance of the experiment (these limits are given in Table 6.1) and all cross sections are in the lab (target at rest) frame.

While not the main focus of this experiment, the separated nucleon cross sections alone are of significant interest. As noted in Section 6.3 there is a good

Target	$\sigma_L = \int_{\Delta P_\pi} d^2\sigma_L \, dP_\pi$ (μb/sr)	$\sigma_T = \int_{\Delta P_\pi} d^2\sigma_T \, dP_\pi$ (μb/sr)	$R = \frac{\sigma_L}{\sigma_T}$
$W = 1.15$ GeV, $k_\pi = 0.467$ GeV/c			
H	$18.40 \pm 1.01 \pm 2.24$	$9.18 \pm 0.62 \pm 1.24$	2.00 ± 0.30
D(π^+)	$9.23 \pm 0.77 \pm 1.22$	$4.24 \pm 0.47 \pm 0.68$	2.18 ± 0.39
D(π^-)	$11.68 \pm 0.65 \pm 1.23$	$1.22 \pm 0.39 \pm 0.51$	9.57 ± 4.04
^{3}He(π^-)	$7.27 \pm 0.59 \pm 0.90$	$1.36 \pm 0.36 \pm 0.44$	5.36 ± 1.76
^{3}He(π^+)	$11.96 \pm 1.15 \pm 1.78$	$6.91 \pm 0.81 \pm 1.12$	1.73 ± 0.34
$W = 1.60$ GeV, $k_\pi = 0.203$ GeV/c			
H	$34.57 \pm 1.41 \pm 4.38$	$27.29 \pm 0.96 \pm 2.89$	1.27 ± 0.19
D(π^+)	$26.50 \pm 1.02 \pm 3.53$	$22.63 \pm 0.76 \pm 2.37$	1.17 ± 0.18
D(π^-)	$41.80 \pm 1.08 \pm 3.86$	$10.10 \pm 0.73 \pm 1.97$	4.14 ± 0.83
^{3}He(π^-)	$22.32 \pm 1.00 \pm 2.56$	$11.46 \pm 0.70 \pm 1.55$	1.95 ± 0.24
^{3}He(π^+)	$48.01 \pm 2.20 \pm 6.18$	$36.85 \pm 1.59 \pm 4.13$	1.30 ± 0.20

TABLE 6.2. Longitudinal and transverse separated cross sections. $d^2\sigma_{L(T)}$ denotes $\frac{d\sigma_{L(T)}}{d\Omega_\pi dP_\pi}$. Errors on the cross sections are statistical and total systematic while the errors on R are total. Cross sections are given in the lab frame and those from nuclear targets have been integrated over the experimental P_π acceptance.

deal of unseparated cross section data, but fewer experiments were able to separate the longitudinal and transverse components of the pion electroproduction cross sections. Furthermore, in some cases the longitudinal piece was extracted using one ϵ setting and calculating the transverse component. The E91003 data set will serve to further constrain existing models of the pion electroproduction cross section.

As an illustration, we compare our separated hydrogen cross sections to the MAID model. While MAID does a good job in general of reproducing our high ϵ cross sections, the lack of L-T constraining data becomes apparent in the comparison of separated cross sections. The comparison is shown in Figures 6.3 and 6.4. In this case, we have transformed our hydrogen cross sections to the γ^*-N

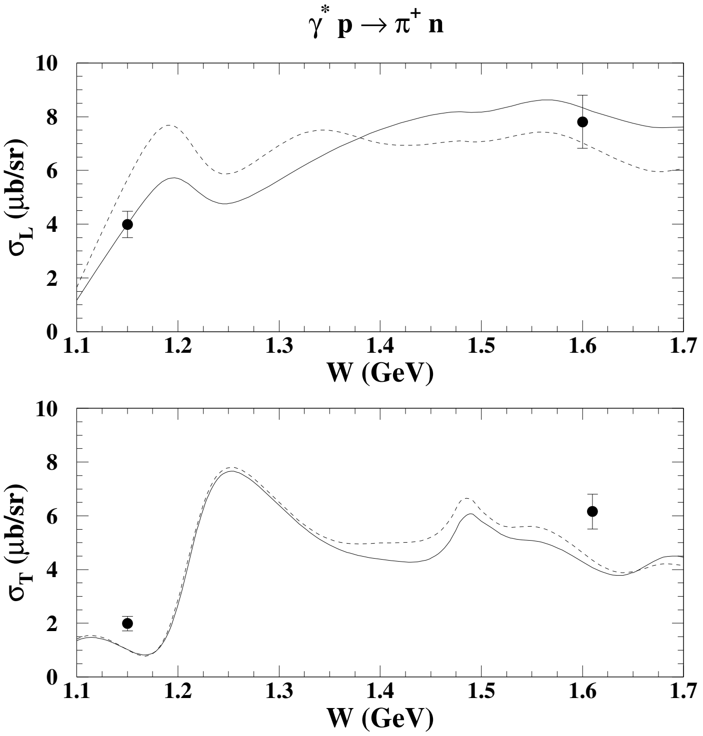

FIGURE 6.3. $\gamma^* p \to \pi^+ n$ separated cross sections compared to MAID calculations. Cross sections are given in the γ^*-N center of mass at $Q^2 = 0.4$ (GeV/c)^2 and $\theta^*_\pi \approx 3.6$ degrees. The solid curve is the original MAID model, while the dashed curve is the MAID 2000 model which has an improved uniterization procedure.

center of mass for more ready comparison. Note that "neutron" separated cross sections are also presented. These values are extracted experimentally via the ratio method where,

$$\sigma_n = \sigma_D(\pi^-) \times \frac{\sigma_p(\pi^+)}{\sigma_D(\pi^+)} \, . \tag{6.12}$$

The reasoning here is that one gets the "neutron" cross section via the bound neutron in deuterium while correcting for the binding effects by evaluating the π^+ proton to deuteron ratio. While the validity of this approximation may be

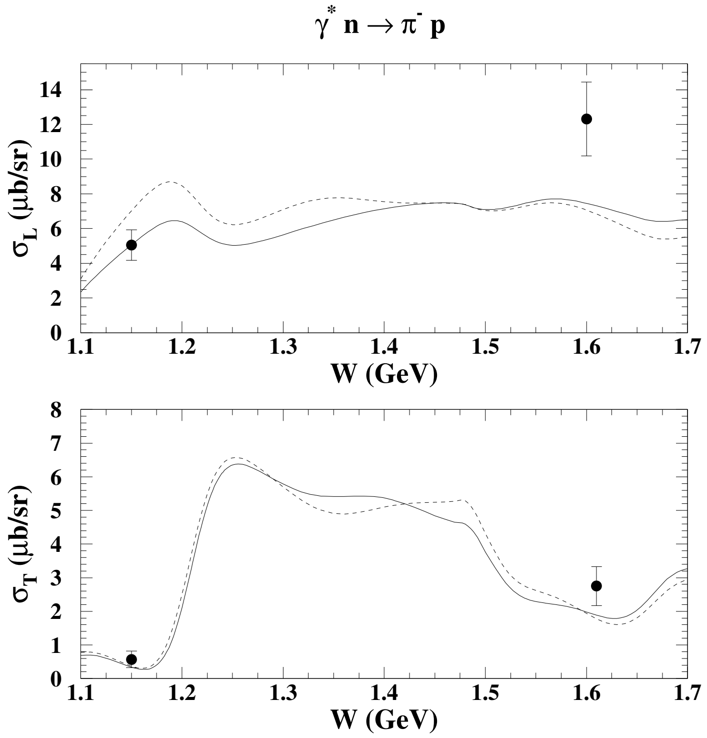

FIGURE 6.4. $\gamma^* n \to \pi^- p$ separated cross sections compared to MAID calculations. Kinematics are the same as Figure 6.3. The solid curve is the original MAID model, while the dashed curve is the MAID 2000 model.

questioned, it is at least consistent with previous extractions of the γ^*-n cross section, so is useful for comparing to this model.

Although there is clear room for improvement, MAID compares well overall with the separated cross sections. The transverse cross sections are systematically underpredicted in both the π^+ and π^- case. This is likely due to the uncertainty involved in extrapolating multipoles appropriate to photoproduction to non-zero Q^2. The original MAID model seems to do a bit better than MAID 2000 (the updated model with an improved unitarization procedure) in describing the longitudinal cross sections, however, both fail to agree with the $W = 1.6$ GeV, π^- point. This is not surprising when one considers that, in the absence of isoscalar backgrounds, one expects the longitudinal π^+/π^- ratio to approach 1 as the 4-momentum transfer to the nucleon, t, gets small ($t \approx -0.04$ GeV^2 for this point). Without data to constrain the model, it is quite reasonable to assume that the longitudinal π^- cross section is similar to the π^+ cross section at these kinematics. It should also be noted that our unseparated π^-/π^+ ratio at high ϵ is consistent with previous data (taken at $Q^2 \approx 0.5$ (GeV/c)^2) [71], giving us confidence that we are not making some systematic mistake in comparing the π^- and π^+ data.

6.5. Separated Cross Section Ratios

Our investigation of the separated cross section ratios (in particular the longitudinal ratio) is motivated by the desire to look for mass dependent effects that arise from sources *other than* those coming from known processes such final state interactions and the Fermi motion of the bound nucleon. Even neglecting those effects, however, there is an issue in the definition of the separated cross sections that complicates the interpretation of the separated ratios. Consider the hypothetical case in which the quasifree integrated deuterium lab cross section is exactly equal to the hydrogen cross section at both ϵ settings. In that case, it is clear that there is no nucleus dependence in the cross sections. However, because of the way in which the virtual photon cross section is defined (see Equations 6.1 to 6.3), the extracted deuterium longitudinal and transverse cross sections will differ from those in hydrogen. The problem arises in the target mass dependent term in the definition of the equivalent photon energy, $K_{eq} = (W^2 - M^2)/2M$. For that reason, we define the "reduced" virtual photon cross section which is simply,

$$\sigma_{REDUCED} = \frac{d\sigma}{d\Omega_\pi} K_{eq} \; , \tag{6.13}$$

which can be broken down piece by piece into the reduced longitudinal and transverse pieces. With the above definition, equal lab cross sections between targets will result in equal "reduced" cross sections and hence equal separated cross sections. We emphasize that the typical definition of the virtual photon cross section is rather arbitrary[2] and we are not skewing the physics in any way. When there is any confusion, it is simplest to consider the separated ratios in the context of the 5-fold lab cross sections.

6.5.1. Results

The (reduced) separated cross section ratios are given in Table 6.3. The helium-3, π^+ quantities have been divided by an extra factor of 2.0 to account for the two protons in the helium-3 nucleus. Note again that all cross sections are evaluated in the lab frame at $Q^2 = 0.4$ (GeV/c)^2 and $\theta_{pq} = 1.72$ degrees. Statistical errors are listed along with the total uncertainty (systematic and statistical combined in quadrature).

As measured, the above separated ratios are difficult to interpret. At both low and high W (high and low k_π, respectively), there is some fraction of the quasifree cross section that is not sampled, either due to the limited experimental

[2]In fact, K_{eq} can be defined such that there are no mass dependent terms to begin with (e.g. the Gilman convention) thus avoiding the above redefinition. The Hand convention is used in this work, though, as it is the most common convention to be found in the literature.

Ratio	R_L	δR_L^{stat}	δR_L^{tot}	R_T	δR_T^{stat}	δR_T^{tot}
$W = 1.15$ GeV, $k_\pi = 0.469$ GeV/c						
D/H(π^+)	0.73	0.07	0.10	0.67	0.09	0.12
^{3}He/D(π^-)	0.69	0.07	0.09	1.23	0.51	0.61
D(π^-/π^+)	1.27	0.13	0.16	0.29	0.10	0.12
^{3}He/H(π+)	0.52	0.06	0.09	0.60	0.08	0.11
$W = 1.60$ GeV, $k_\pi = 0.203$ GeV/c						
D/H(π^+)	0.86	0.05	0.12	0.93	0.05	0.10
^{3}He/D(π^-)	0.55	0.03	0.07	1.17	0.11	0.24
D(π^-/π^+)	1.58	0.07	0.19	0.45	0.04	0.08
^{3}He/H(π+)	0.81	0.05	0.13	0.78	0.04	0.11

TABLE 6.3. Longitudinal and transverse separated (reduced) cross section ratios. Statistical and total uncertainties are listed. Cross sections have been evaluated in the lab frame and those from nuclear targets have been integrated over the experimental P_π acceptance. Note that the helium-3 π^+ cross sections have been divided by 2 to account for the fact that a positively charged pion can be produced from either proton in the nucleus.

acceptance (at low W) or the necessity to cut out the 2-pion background (at high W). To best interpret this data, one would ideally like to compare our integrated cross sections to detailed nuclear calculations that include all known effects such as a realistic nuclear wave function, antisymmetrization of the final state wave functions, NN final state interactions, etc. Deviations would then be clearly interpretable as signs of new physics (e.g. the pion excess). However, one can also attempt to interpret this data in a more rudimentary fashion. In the next two sections, two approaches to understanding the above ratios will be presented. In the first, we simply attempt to extrapolate our measured nuclear cross sections to full P_π coverage. Second, we compare our limited acceptance ratios to a simple calculation integrated over the same P_π region.

6.5.2. Acceptance Extrapolation

As a first step in interpreting our separated cross section ratios, it is useful to attempt to extrapolate the measured nuclear cross sections to full P_π acceptance. In the case of the $W = 1.6$ GeV data, this extrapolation can be done with little uncertainty due to the large fraction of the P_π distribution sampled (see Figure 6.1). On the other hand, the relatively small fraction of the P_π distribution sampled at $W = 1.15$ GeV results in significantly larger uncertainties.

In this section, we discuss the extrapolation of the longitudinal cross sections only - the resulting uncertainty in any such extrapolation of the transverse piece results in ratios with such large uncertainties that they may be considered effectively non-measurements (especially for the low W data where the nearby Δ resonance can distort the simple quasifree shape). The extrapolation is done using two models. First, we simply take our quasifree extension of the pion electroproduction model (including NN FSI effects) and estimate the fraction of the longitudinal cross section distribution measured. Second, we use the modified version of this model after it has undergone the iteration procedure described in Section 5.4.2. In general, these two methods yield very similar results. Further checks are done on the iterated version of the model by allowing the P_π correction to be extended beyond the "fit" region and by fitting the NN FSI parameter, δ (see Section 5.4.1), at each setting. The results obtained via these last two tests are used to parameterize the uncertainty in the extrapolation procedure.

Figure 6.5 shows the $W = 1.15$ GeV longitudinal cross section for pion production from each nuclear target as a function of P_π. The two curves shown on the figure correspond to the iterated version of the cross section model (as used in the iteration procedure) and the un-iterated version of the model. The iterated model and un-iterated model yield approximately the same correction in

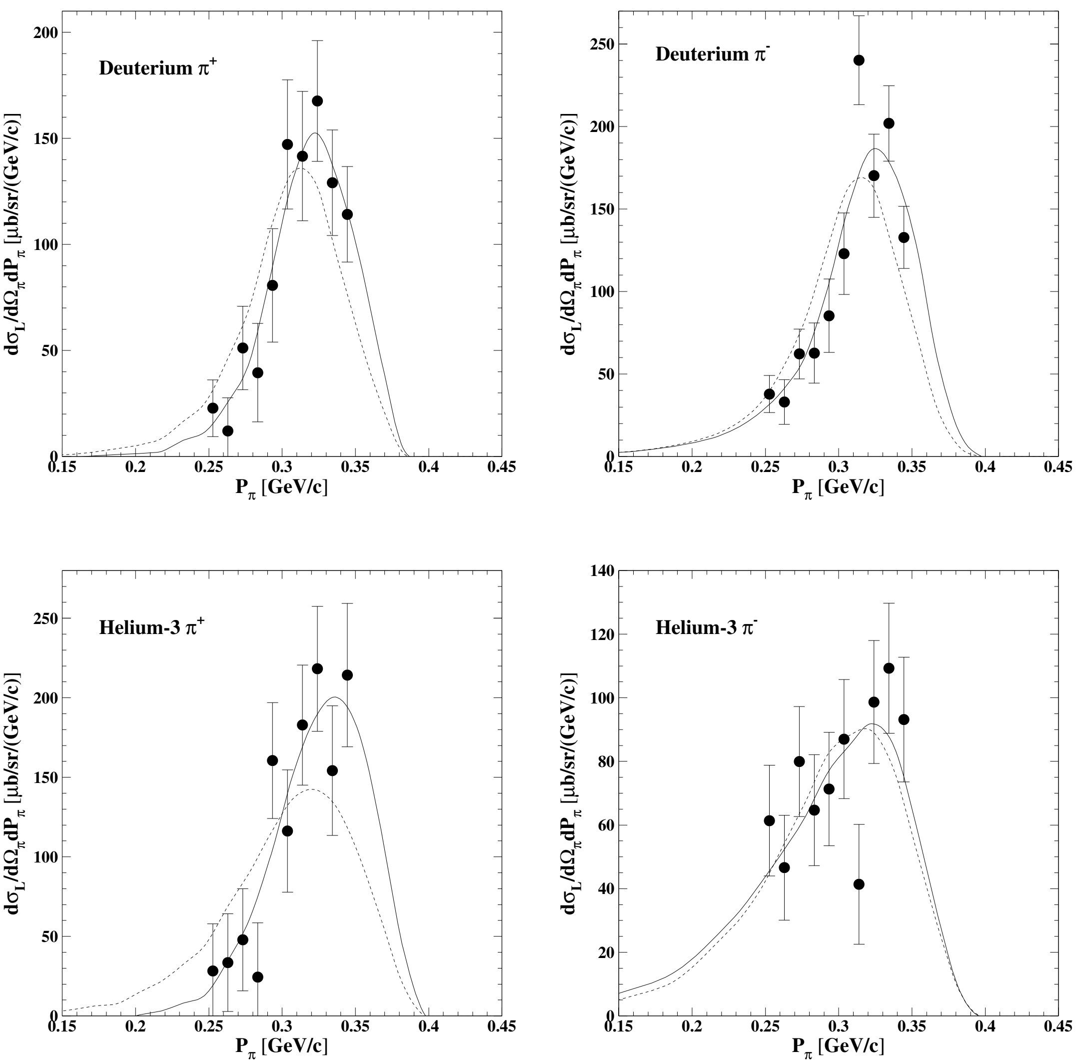

FIGURE 6.5. Longitudinal cross section P_π spectra compared to two versions of the Monte Carlo input cross section model for $W = 1.15$ GeV data. Uncertainties on the data are statistical only. The solid curve is the iterated version of the quasifree, NN-FSI modified MAID model, while the dashed curve is the un-iterated version. These curves are used to estimate the fraction of the longitudinal cross section distribution measured.

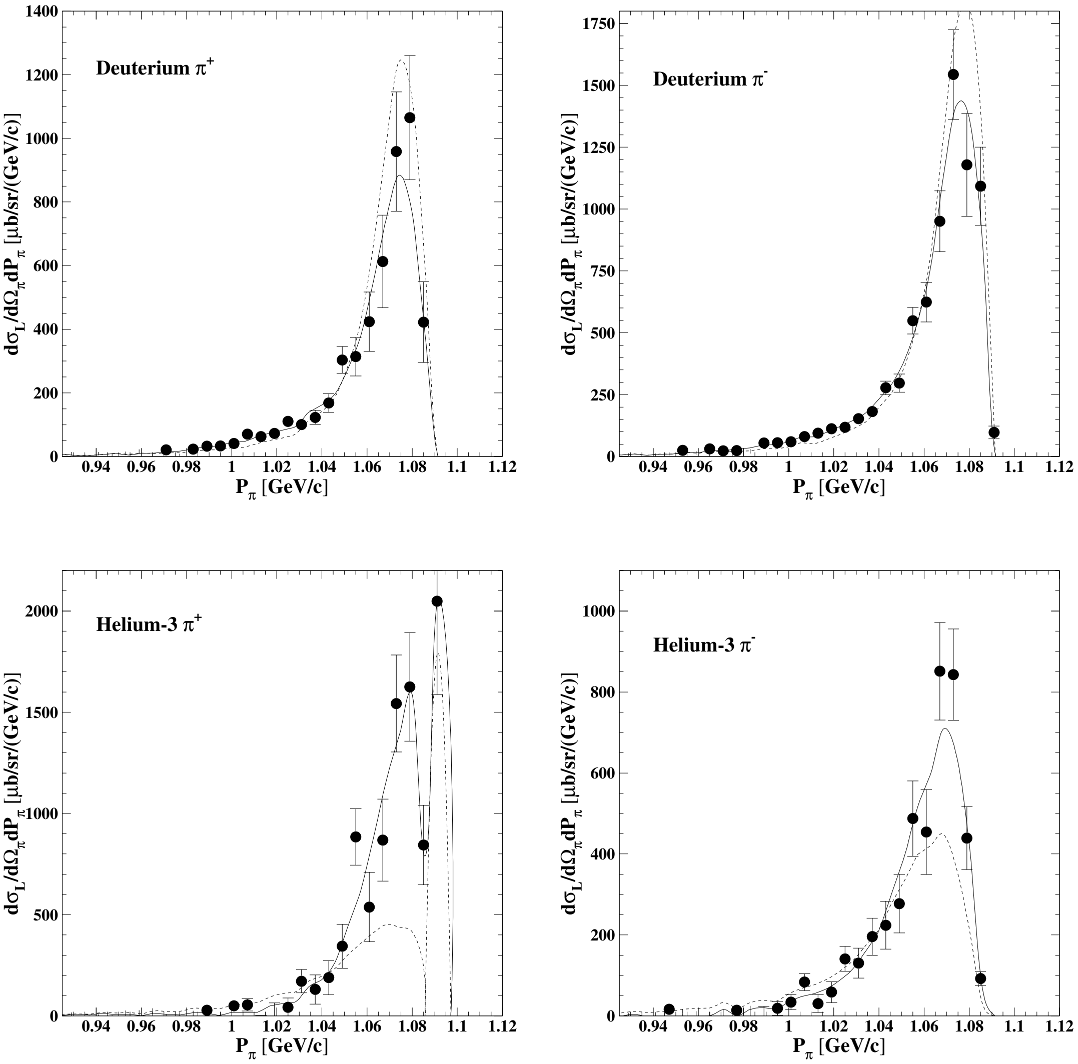

FIGURE 6.6. Longitudinal cross section P_π spectra compared to two versions of the Monte Carlo input cross section model for $W = 1.6$ GeV data. Uncertainties on the data are statistical only. The solid curve is the iterated version of the quasifree, NN-FSI modified MAID model, while the dashed curve is the un-iterated version. These curves are used to estimate the fraction of the longitudinal cross section distribution measured.

W (GeV)	k_π (GeV/c)	Target (polarity)	Longitudinal P_π acceptance (%)
1.60	0.20	D(π^+)	99.0 $\pm$ 1.0
1.60	0.20	D(π^-)	99.0 $\pm$ 1.0
1.60	0.20	^{3}He(π^+)	98.5 $\pm$ 1.0
1.60	0.20	^{3}He(π^-)	97.5 $\pm$ 1.5
1.15	0.47	D(π^+)	83.5 $\pm$ 7.1
1.15	0.47	D(π^-)	79.5 $\pm$ 6.8
1.15	0.47	^{3}He(π^+)	74.0 $\pm$ 7.4
1.15	0.47	^{3}He(π^-)	70.0 $\pm$ 7.0

TABLE 6.4. Estimated fraction of the longitudinal P_π distribution within the E91003 experimental acceptance.

most cases. Note that in the helium-3 π^+ case, we have modeled only the quasifree piece of the cross section and have ignored the coherent channel. As discussed in Section 5.4.2.4, we expect this contribution to be on the order of a few percent - we make no attempt to account for this contribution. Figure 6.6 shows similar spectra for the $W = 1.6$ GeV longitudinal cross sections. The estimated fractions of the longitudinal P_π distributions measured are given in Table 6.4. The corrections (and their associated uncertainties) are significantly larger for the $W = 1.15$ GeV data.

Applying the acceptance corrections from Table 6.4, one can now make a reasonable comparison between the integrated nuclear cross sections and the free nucleon. The P_π acceptance-fraction corrected longitudinal ratios (per contributing nucleon) are shown in Figure 6.7. Note that none of the ratios have been corrected for final state interactions between the outgoing pion and the spectator nucleon(s). In the deuterium and π^- helium-3 case these should be relatively small, but the in the π^+ helium-3 case (at high k_π) these effects can grow to 20-40%.

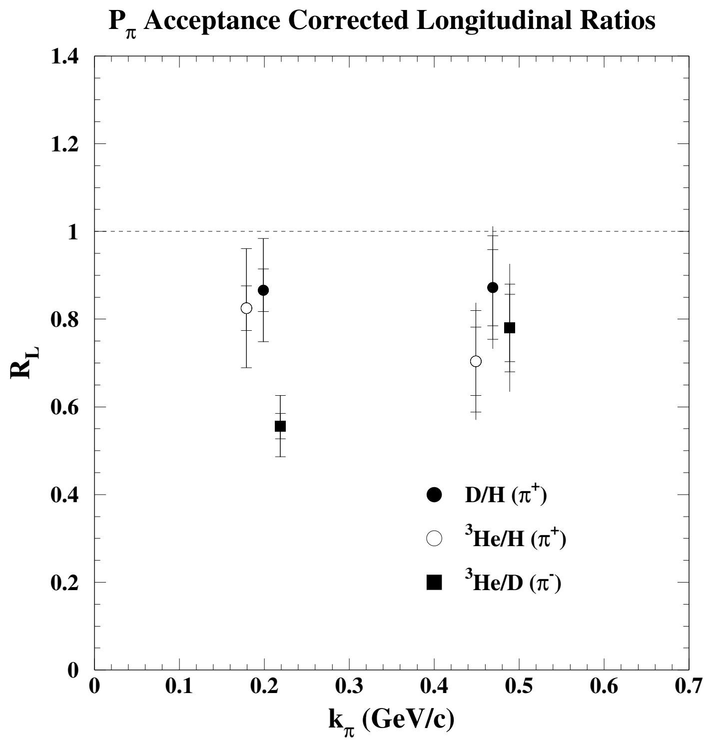

FIGURE 6.7. P_π acceptance corrected longitudinal cross section ratios. Inner error bars are statistical, middle errors are statistical+systematic, and the outer errors include the uncertainties from the P_π acceptance extrapolation. In most cases, pion-nucleon final interaction effects are estimated to be on the order of 5% or less. In the case of the helium-3, high k_π π^+ data however, these effects are estimated to be much larger (20-40%). The ^{3}He/H and ^{3}He/D ratios have been shifted in k_π for ease of viewing.

It is somewhat surprising that at high k_π, the longitudinal ratios all are less than 1. This is in marked contrast to the expectation of some sign of a pion enhancement, and hence a longitudinal ratio greater than one. However, one must keep in mind that at the high value of k_π, the total center of mass energy W is 1.15 GeV, close to the pion production threshold of 1.08 GeV. It is probable that some regions of the momentum space wave functions can not contribute to pion electroproduction due to too low values of the γ^*-N energy. An estimate using the momentum space wave functions in the Monte Carlo (along with our off-shell prescriptions, etc.) indicates that about 10% of the wave function is excluded in the deuteron and about 20% in helium-3 (ignoring ^{3}H contributions in the π^+ case). On the other hand, the low recoil data taken at higher W (=1.6 GeV) do not suffer from threshold effects in the nuclear wave functions. We estimate that about 99-99.5% of the nucleon momentum distributions in deuterium and helium-3 can contribute to the quasifree pion electroproduction process.

The P_π acceptance corrected ratios can also be suppressed due to final state interactions between the outgoing pion and spectator nucleon(s). In the case of pion production from deuterium, these effects should be on the order of [72],

$$P^{\pi N} = \frac{\sigma_{\pi N}}{4\pi \langle r_{pn}^2 \rangle} , \tag{6.14}$$

where $\sigma_{\pi N}$ is the total pion-nucleon cross section and $\langle r_{pn}^2 \rangle$ is the mean of the square of the separation between the struck nucleon and the spectator nucleon ($\approx$ 4 fm in the deuteron). For the high recoil data ($P_\pi = 0.290$ GeV/c), $\sigma_{\pi N} \approx 7$ fm so the effect should be on the order of 3.5%. At low recoil ($P_\pi = 1.0$ GeV/c), $\sigma_{\pi N} \approx 6$ fm so the effect should be about 3%. In the case of pion production from helium-3, one can have significant effects from pion absorption on the spectator NN pair. In a factorization approximation, the effect can be estimated by [73],

$$P^{\pi NN} = \left[1 - \frac{P_\pi^2}{4\pi}\sigma_{tot}^{abs}\right]^2 , \tag{6.15}$$

where σ_{tot}^{abs} is the total absorption cross section on the spectator NN pair (pn in the π^+ case or pp in the π^- case). For the pn spectator pair, σ_{tot}^{abs} is taken from experimental π^+D $\rightarrow pp$ data, while for the pp pair, σ_{tot}^{abs} is inferred from ^{3}He(π^-, np) data. At low recoil, the effect is estimated to be less than 2% for both π^+ and π^- data. At high recoil, the π^- correction is small (3-4%), but the π^+ effect is $\approx$ 33%. It should be noted that this is a rough estimate intended only to indicate the magnitude of the effect - a more precise determination would likely require a full distorted wave calculation.

In Table 6.5 and Figure 6.8, we show the acceptance corrected ratios with our estimates of the fractional contribution of the nucleon momentum distribution. We also correct the high recoil helium-3 π^+ data for the pion absorption effect described above. Pion absorption and final state interaction effects should be less than 5% for all other ratios. With these additional corrections, the ratios at high k_π are more consistent with unity.

Ratio	k_π (GeV/c)	P_π Acceptance Corrected Ratio	Momentum Dist. Fraction	Corrected Ratio
D/H(π^+)	0.203	0.866 ± 0.118	0.994	0.871 ± 0.119
^{3}He/D(π^-)	0.203	0.556 ± 0.071	0.990/0.994	0.558 ± 0.071
^{3}He/H(π^+)	0.203	0.810 ± 0.133	0.993	0.831 ± 0.137
D/H(π^+)	0.469	0.872 ± 0.139	0.90	0.969 ± 0.154
^{3}He/D(π^-)	0.469	0.780 ± 0.146	0.80/0.90	0.878 ± 0.164
^{3}He/H(π^+)	0.469	0.647 ± 0.126	0.80	1.170 ± 0.222[a]

[a]Corrected by an additional factor of 1.33 to account for effects from π^+ absorption on the spectator pn pair.

TABLE 6.5. P_π acceptance corrected (longitudinal) ratios with estimated fraction of nucleon momentum distribution that can kinematically contribute to the integrated cross sections. Final state interactions between the pion and spectator nucleon(s) are included in the corrected ratio only for the high recoil, helium-3 π^+ data. For all other ratios, the effect should be less than 5%. Uncertainties are on the data and acceptance extrapolation procedure. No extra uncertainty due to the estimate of the momentum distribution fraction (or the π-N FSI correction) has been assigned.

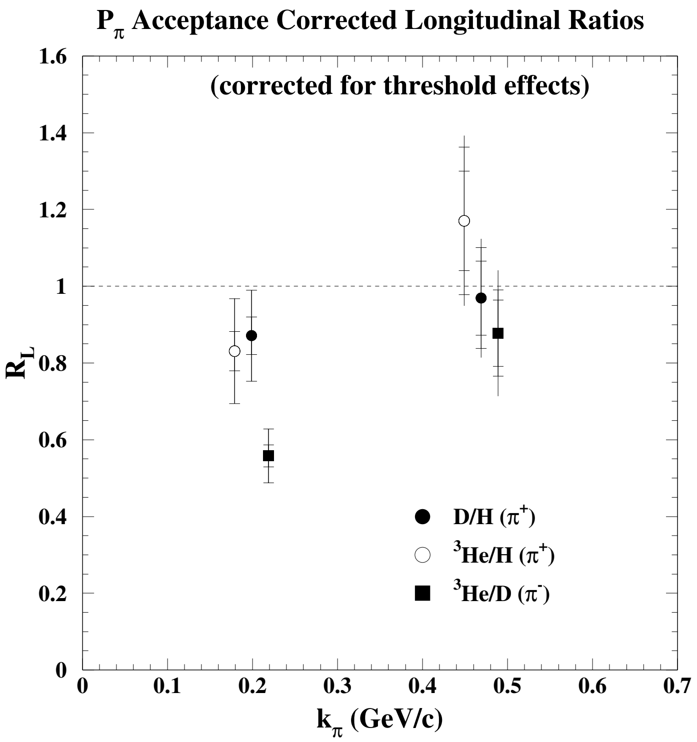

FIGURE 6.8. P_π acceptance corrected longitudinal ratios with additional corrections for the fraction of the nucleon momentum distribution that can kinematically contribute to the integrated cross sections. The high k_π helium-3 π^+ point has been corrected by an additional factor of 1.33 to account for absorption of the pion on the spectator pn pair. No additional uncertainty has been assigned for these extra corrections.

The acceptance corrected ratios represent the *experimental* quantity most directly sensitive to nuclear modifications to the longitudinal cross section. Unfortunately, a deviation from 1 is not an unambiguous sign of these nuclear effects. Likewise, apparent agreement with 1 is not necessarily a sign of their absence. One must ask the question, do we expect some modification to the integrated cross section just due to the fact that we are now producing the pion from a moving nucleon (in the quasifree picture) rather than a stationary nucleon? Such a modification of the longitudinal cross section must be understood if one hopes to make any claims about seeing evidence for the enhancement of the virtual pion field in nuclei. Furthermore, any attempt to understand such quasifree modifications will be model dependent. As will be shown in the next section, however, one can make a reasonable attempt at taking these effects into account.

6.5.3. Comparison with Quasifree Calculation

Rather than extrapolating the data to the region of the P_π distribution that was not measured experimentally, we can compare our results directly to a calculation that samples the same limited region of P_π. In fact, this second approach has certain advantages. The acceptance corrected ratios presented in Section 6.5.2 suffer from the fact that they fail to address the issue of potential Fermi smearing of the bound nucleon cross section. One would like to account for kinematic variations of the γ^*-N cross section as one integrates over the nucleon momentum distribution. Clearly, the Fermi motion of the bound nucleon will result in values of W, θ_{pq}, etc. in the γ^*-N center of mass that deviate from the values obtained with a stationary, free nucleon. A cartoon of this is shown in Figure 6.9. In light of these kinematic effects, it is clear that even in the case of 100% acceptance of the quasifree P_π distribution, the integrated cross section may not equal that of the hydrogen cross section.

The situation is further complicated by the fact that the total energy in the virtual photon - nucleon center of mass, W, is below pion production threshold for some regions of the nucleon momentum distribution. This issue is especially important for the $W = 1.15$ GeV data, which is not far from the $W = 1.08$ GeV pion production threshold.

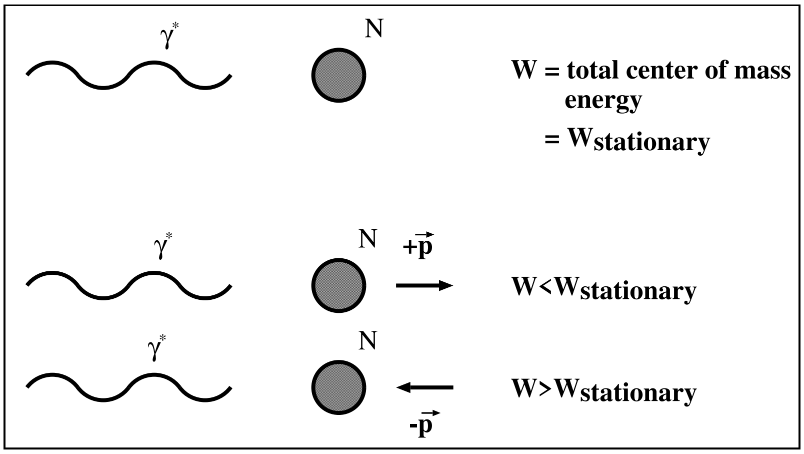

FIGURE 6.9. Cartoon of the modification of the γ^*-N center of mass energy (W) due to the Fermi motion of the bound nucleon.

In light of these issues, it is useful to try to calculate a baseline that accounts for the kinematic variations and threshold effects. Making use of the Monte Carlo apparatus that has already been developed for the cross section extraction, we can perform a simple calculation of the integrated longitudinal cross section from the nuclear targets in which the only nuclear effect we include is the motion of the "struck" nucleon. This simple calculation we call the "quasifree correction" because it accounts only for the quasifree nature of the electroproduction process. The experimental ratios compared to the quasifree calculation give us some insight into the non-trivial nuclear effects in longitudinal pion electroproduction. Furthermore, the quasifree calculation is integrated only over the region of P_π in the experimental acceptance so that we are making the most direct comparison possible between the actual data and this calculation.

The quasifree corrected ratio is defined as the experimental ratio divided by the quasifree calculated ratio. Take as an example the deuterium to hydrogen longitudinal ratio. The experimental ratio is,

$$R_L^{exp} = \left(\int_{Pmin}^{Pmax} \frac{d\sigma_L^D}{d\Omega_\pi dP\pi}\right) / \frac{d\sigma_L^H}{d\Omega_\pi} \,. \tag{6.16}$$

Similarly, the quasifree calculated ratio is,

$$R_L^{quasifree} = \left(\int_{Pmin}^{Pmax} \left[\frac{d\sigma_L^D}{d\Omega_\pi dP\pi}\right]^{model}\right) / \left[\frac{d\sigma_L^H}{d\Omega_\pi}\right]^{model} \,, \tag{6.17}$$

where *model* denotes the fact that we are using a model cross section whose only nuclear effect is the Fermi motion of the bound nucleon. It should be emphasized that the limits of integration, $Pmin$ and $Pmax$, on both the quasifree calculation and the data are set by the experimental acceptance (listed in Table 6.1). With the experimental and quasifree ratios defined, the quasifree corrected ratio is then,

$$R_{corrected} = \frac{R_L^{exp}}{R_L^{quasifree}} \,. \tag{6.18}$$

The quasifree correction is calculated using the MAID/MAID 2000 models as well as a third model appropriate to the kinematics (the same models as discussed in Section 5.4.2.5). The correction is taken as the average of the three models. Also, these results are compared to the raw fraction of the momentum space wave function that contributes to the pion electroproduction process within our P_π limits. The difference between the model calculations and pure wave function fraction is taken as the uncertainty. The calculated quasifree ratios are shown in Table 6.6.

Note that in the case of the low k_π (high W) helium-3 π^+ data, we compute the quasifree correction only for the Dn/pnn continuum final states. Recall that at these kinematics, the coherent ^{3}H final state contributes significantly to the cross section integrated over final states. It is inappropriate to model this coherent contribution in a quasifree picture, so we restrict the comparison to the final states in which a simple spectator/quasifree picture makes sense. Of course, since we calculate the quasifree ratio for the continuum states only, we must compare that to the same region in the data. Previously, we have discussed only the extraction of the experimental cross section integrated for all final states, however, we can extract the ^{3}He$(e,e'\pi^+)^3$H and ^{3}He$(e,e'\pi^+)$Dn/pnn cross sections separately. This is described in Section 6.6.2. On the other hand, at high k_π (low W), the ^{3}H contribution is expected to contribute only a few percent to the total integrated cross section (as discussed in Section 5.4.2.4). Thus, one can picture the process as dominantly quasifree.

Ratio	k_π (GeV/c)	Quasifree Ratio ($R^{quasifree}$) Longitudinal	Transverse
D/H(π^+)	0.20	0.952 ± 0.026	1.037 ± 0.064
^{3}He/D(π^-)	0.20	0.951 ± 0.020	1.062 ± 0.090
^{3}He/H(π^+)	0.20	0.918 ± 0.053	1.047 ± 0.110
D/H(π^+)	0.47	0.670 ± 0.042	0.776 ± 0.064
^{3}He/D(π^-)	0.47	0.696 ± 0.037	0.761 ± 0.072
^{3}He/H(π^+)	0.47	0.485 ± 0.049	0.584 ± 0.072

TABLE 6.6. Calculated quasifree ratios for longitudinal and transverse cross sections. Note that the calculations of the cross sections from the nuclear targets are integrated over the same region of P_π as sampled in the experiment (see Table 6.1 for the P_π limits). The ^{3}He, π^+ calculations involve the continuum Dn/pnn final states only. At high k_π (low W), the coherent ^{3}H contribution is expected to be quite small, so the process can be viewed as dominantly quasifree. However, at low k_π (high W), the coherent contribution is large so we must extract the Dn/pnn contribution only from the data to compare to the calculation.

The quasifree corrected longitudinal and transverse ratios are shown in Figures 6.10 and 6.11 as a function of the struck virtual pion momentum, k_π. At low k_π (the $W = 1.6$ GeV data) there is a clear suppression of the helium-3 longitudinal cross section with respect to deuterium and hydrogen while the deuterium to hydrogen ratio also sees a small suppression, but is consistent with 1 within the uncertainty. On the other hand, at the higher k_π, there is no evidence for any deviation from 1 in the longitudinal ratios. One must keep in mind that final state interactions between the positive pion and spectator nucleons in the $^3\mathrm{He}(e, e'\pi^+)$ channel can be quite large (20-40%), so that apparent value of ≈ 1.05 is better interpreted as an $\approx 40\%$ enhancement. Aside from the low k_π, ^{3}He/H ratio, which is clearly suppressed, the transverse ratios also show little evidence for any target dependence within the uncertainties of the measurement (with the same caveat regarding the high k_π helium-3 π^+ data). It should be emphasized that these points are not purely experimental data, but involve our interpretation via the quasifree correction.

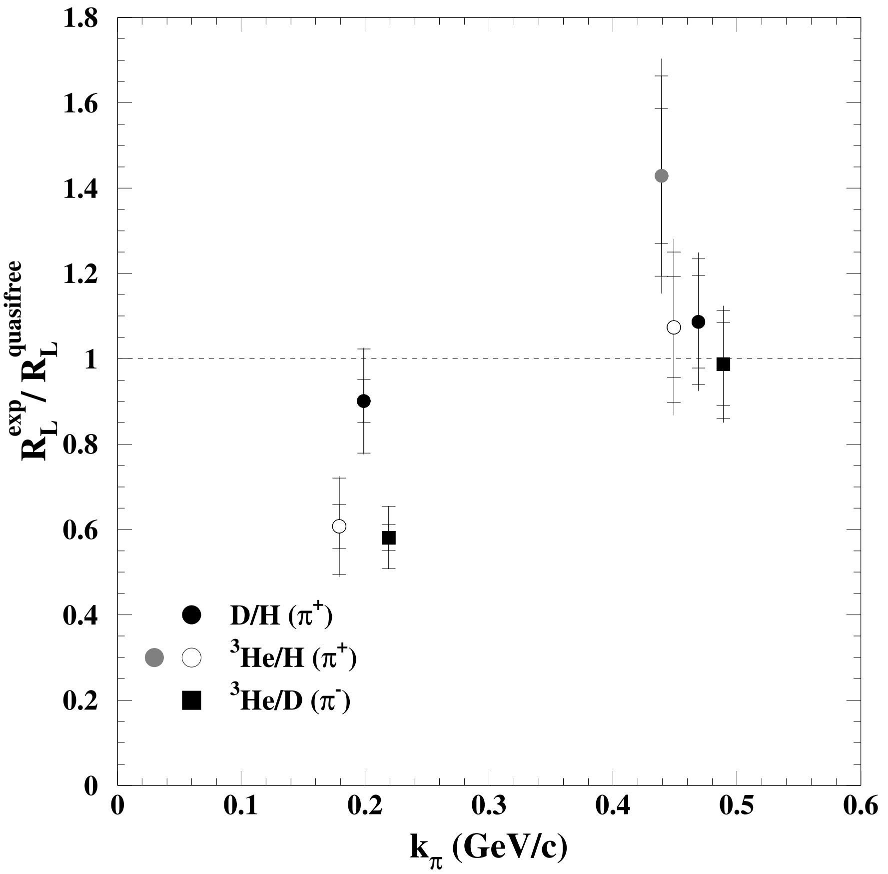

FIGURE 6.10. Quasifree corrected longitudinal cross section ratios. Inner error bars are statistical uncertainties, middle error bars denote statistical+systematic experimental uncertainties, and outer include the uncertainty due to the calculation of the quasifree correction. The ^{3}He π^+ data and calculation includes contributions from the continuum Dn/pnn final states only. The π^+ ^{3}He/H point at high k_π is shown corrected by a factor of 1.33 for pion absorption on the spectator pn pair (gray circle, see Section 6.5.2) and with no absorption correction (open circle).

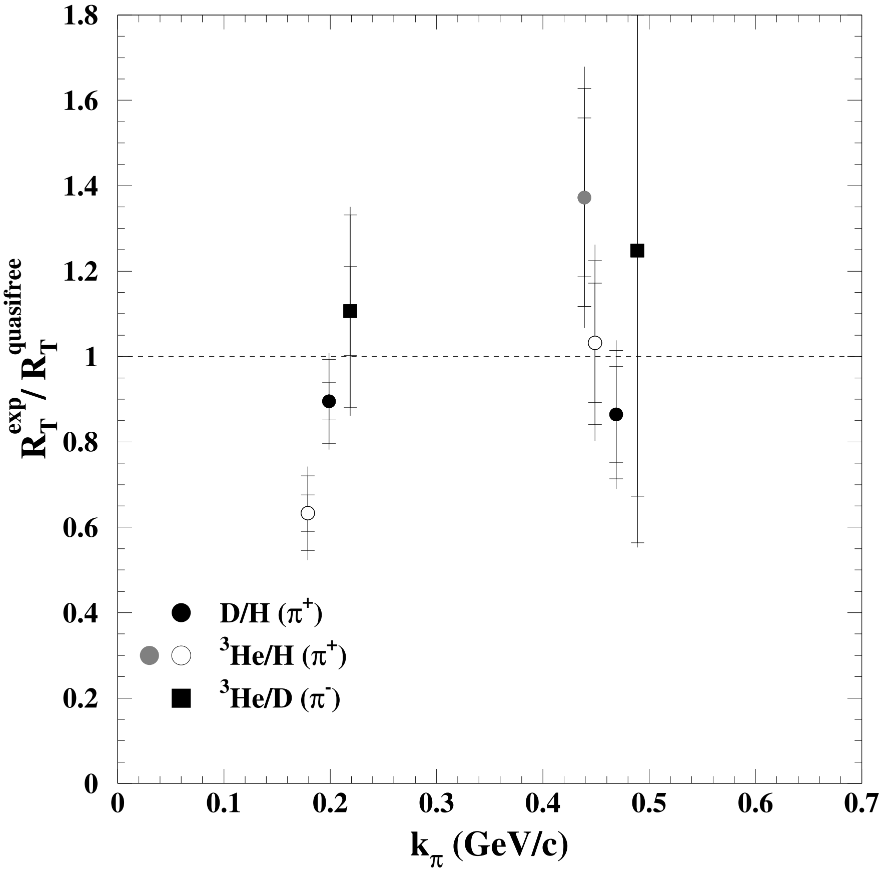

FIGURE 6.11. Quasifree corrected transverse cross section ratios. Inner error bars are statistical uncertainties, middle error bars denote statistical+systematic experimental uncertainties, and outer include the uncertainty due to the calculation of the quasifree correction. The ^{3}He π^+ data and calculation includes contributions from the continuum Dn/pnn final states only. The π^+ ^{3}He/H point at high k_π is shown corrected by a factor of 1.33 for pion absorption on the spectator pn pair (gray circle, see Section 6.5.2) and with no absorption correction (open circle)

6.6. Other Results

6.6.1. π^-/π^+ *Ratio and Pole Dominance*

Throughout this work, it has been asserted that to the extent that the pole process dominates, the longitudinal cross section is sensitive to the nuclear pion field of the free proton and light nuclei used in this experiment. At this point, we attempt to address whether it is indeed the case for our data.

The ratio of longitudinal π^- to π^+ production from deuterium can be used to test if the pole term does indeed dominate. The pole process proceeds only through isovector photons, while other terms contributing to the longitudinal cross section can proceed through both isoscalar and isovector photons. In terms of isovector and isoscalar amplitudes (A_v and A_s), the ratio of longitudinal cross sections can be written [27],

$$\frac{\sigma(\gamma^* n \to \pi^- p)}{\sigma(\gamma^* p \to \pi^+ n)} = \frac{|A_v - A_s|^2}{|A_v + A_s|^2} \,. \tag{6.19}$$

Provided that the relative phase does not conspire to mask the contribution of the isoscalar terms, a ratio of unity would indicate a lack of isoscalar backgrounds and give one some confidence that the pole process is indeed the dominant contribution to the longitudinal cross section. The kinematics for E91003 were chosen so as to attempt to satisfy the above condition. However, analysis of the longitudinal π^- to π^+ ratios indicate that there are non-negligible isoscalar backgrounds (see Table 6.3 and Figure 6.12). Although the ratios are on the order of 1.0, it is unclear how the deviation from unity maps to the size of the contributions from the isoscalar backgrounds. For the $W = 1.15$ GeV data, theory can provide some guidance and calculations indicate that the pole term alone gives about 50% of the total

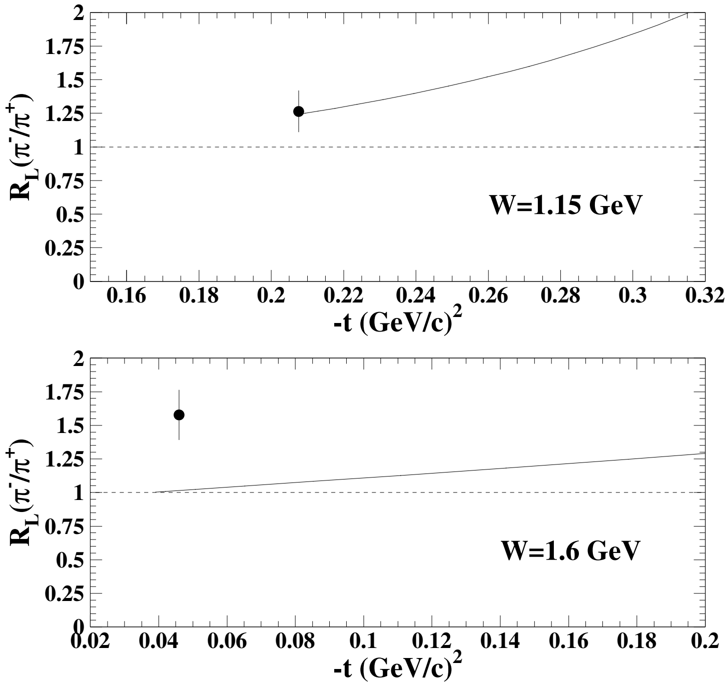

FIGURE 6.12. Longitudinal π^-/π^+ ratios. Errors on data points are statistics+systematic. Curves are from the MAID 2000 model. Note that these ratios do not include corrections for the fact that we may be sampling more of the longitudinal π^+ cross section at $W = 1.15$ GeV as indicated by the acceptance corrections in Table 6.4 (although this effect should not be larger than a few percent).

longitudinal cross section [74]. Unfortunately, the theory is less helpful for the $W = 1.6$ GeV data, making the interpretation of the data more difficult.

In the most optimistic scenario, we can assume the isovector and isoscalar amplitudes to be real (or at least have the same phase), in which case we find,

$$\frac{A_S}{A_V} = \frac{1-\sqrt{R}}{1+\sqrt{R}}\,, \tag{6.20}$$

where R is the longitudinal π^-/π^+ratio defined in Equation 6.19. Then, for the $W = 1.15$ GeV data, we have $A_S/A_V = -0.059$ and for $W = 1.6$ GeV,

$A_S/A_V = -0.113$. These numbers can serve as a lower limit on the isoscalar backgrounds, although they may certainly be larger.

6.6.2. Separation of Final States in ^{3}He$(e, e'\pi^+)$

As noted in Section 5.4.2.4, there is the bound ^{3}H final state in addition to the quasifree pnn and Dn final states available in positive pion electroproduction from helium-3. At the $k_\pi = 0.47$ GeV/c kinematics ($W = 1.15$ GeV), this final state is not within the experimental acceptance and is expected to have a small contribution to the total integrated cross section. However, at the $k_\pi = 0.2$ GeV/c kinematics ($W = 1.6$ GeV), the coherent channel is within the acceptance and is a significant fraction of the P_π integrated cross section. In general, the emphasis in this work has been on the cross section integrated over final states (bound and continuum states). It is of some interest, though, to examine the coherent and quasifree pieces independently.

While the experimental missing mass resolution is good enough to pick out the ^{3}H final state, it is not quite sufficient to totally separate it from the Dn and pnn continuum states. However, as will be shown, we can separately extract the ^{3}He$(e, e'\pi^+)^3$H and ^{3}He$(e, e'\pi^+)$Dn/pnn cross sections with reasonable precision with some aid from the Monte Carlo to estimate the backgrounds

A missing mass cut at $M_x = 2.815$ GeV is implemented to separate the triton final state from the Dn and pnn continuum. Background from the continuum final states that may leak into this cut is estimated by fitting Monte Carlo missing mass distributions for the ^{3}H, Dn, and pnn final states up to a missing mass of 2.84 GeV. This is shown in Figure 6.13. The contribution to the ^{3}H yield from these backgrounds is estimated to be 4-8%. In general, the shape of the

Dn/pnn background below $M_x = 2.815$ GeV is driven by the nucleon-nucleon final state interactions. To estimate the uncertainty in the extracted ^{3}H cross sections due to the modeling of the Dn/pnn background, the background is calculated using our nominal final state interaction prescription and assuming no nucleon-nucleon interaction. The difference between the two results is about 3%, but largely independent of epsilon setting. Hence we assign a scale uncertainty of 3% and a random uncertainty of 1% between epsilon settings for this background contribution to ^{3}H yield.

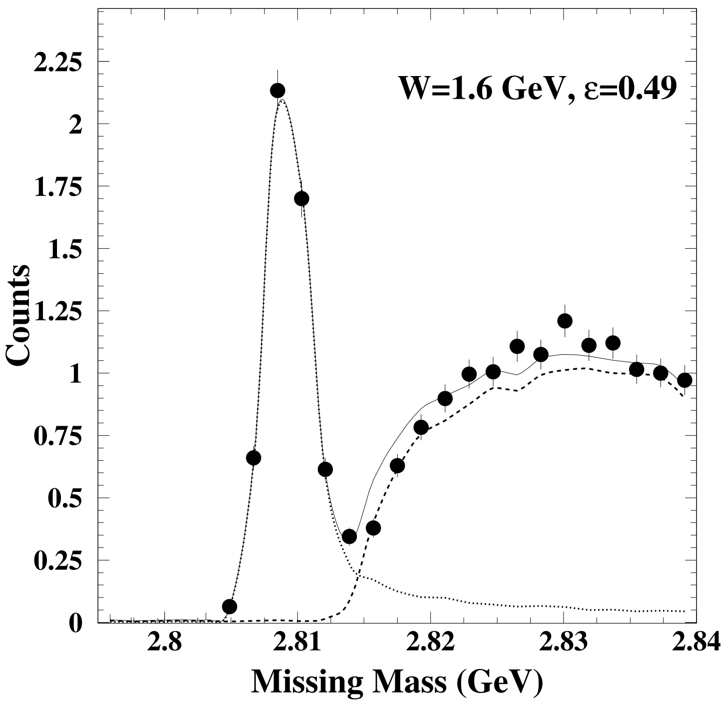

FIGURE 6.13. Data and SIMC missing mass distributions for $^3\mathrm{He}(e, e'\pi^+)$. The solid curve is the total simulation while the dotted and dashed curves are the simulation of the ^{3}H and Dn/pnn final states respectively. The latter is used to estimate the Dn/pnn background to the ^{3}H final state for $M_x < 2.815$ GeV.

A further complication arises from the extremely tight missing mass cut. Although the resolution is matched fairly well between the data and Monte Carlo, SIMC does not perfectly model some of the non-Gaussian resolution broadening seen in the data. In general, this is not an issue in the analysis because we cut far out in the tail of the missing mass distributions. However, in this case, we are forced to use a tight missing mass cut close to the peak to separate the coherent channel from the continuum states. This means that in comparing the data yields to the SIMC yields, we may overestimate the expected number of Monte Carlo counts and hence underestimate the extracted cross section. However, we can correct for this lack of resolution matching via comparison with the hydrogen data. Applying the same tight cut to the hydrogen data and comparing to the result with a wider cut in which resolution effects should be minimal, we can estimate a correction to the ^{3}H data. This correction is about 1.5-1.9% with the random uncertainty taken to be half the size of the correction.

The $^3\mathrm{He}(e, e'\pi^+)^3\mathrm{H}$ cross section is extracted by iterating the input pion electroproduction model (where in this case the input model includes the Dn/pnn background in addition to the ^{3}H final state) in our usual fashion (see Section 5.4.2) and then correcting for the resolution effects described above. Furthermore, since we have already obtained the $^3\mathrm{He}(e, e'\pi^+)$ cross sections integrated over all final states (at least up to a few MeV below two pion threshold), the Dn/pnn cross sections can be trivially obtained by subtracting the ^{3}H cross sections from the integrated cross sections. The unseparated cross sections are shown in Table 6.7 and the separated cross sections are given in Table 6.8.

While comparing the quasifree piece of the helium-3 cross section to that from hydrogen requires either the P_π extrapolation described in Section 6.5.2 or some kind of calculation as in Section 6.5.3, it is straightforward to compare the

Final State	ϵ	ΔP_π (GeV/c)	$\int_{\Delta P_\pi} d^6\sigma dP_\pi$ (μb/GeV/sr^2)	$\sigma_T + \epsilon\sigma_L$ (μb/sr)	$\frac{\delta\sigma}{\sigma}_{stat}$ (%)	$\frac{\delta\sigma}{\sigma}^{ran}_{sys}$ (%)	$\frac{\delta\sigma}{\sigma}^{scale}_{sys}$ (%)
All	0.490	>0.943	3.71×10^{-2}	60.38	1.1	1.9	5.6
All	0.894	>0.943	4.74×10^{-1}	79.75	0.8	2.3	5.6
^{3}H	0.490	-	7.89×10^{-3}	12.85	2.5	2.3	6.3
^{3}H	0.894	-	1.12×10^{-1}	18.81	1.9	2.6	6.3
Dn/pnn	0.490	>0.943	2.92×10^{-2}	47.53	1.5	1.9	5.6
Dn/pnn	0.894	>0.943	3.62×10^{-1}	60.94	1.2	2.4	5.6

TABLE 6.7. Unseparated cross sections for the ^{3}He$(e, e'\pi^+)$ process. The cross sections integrated over final states as well as the final-state specific cross sections for the ^{3}H and P_π integrated Dn/pnn final states are given.

coherent ^{3}H cross sections to hydrogen. We roughly expect the size of ^{3}H cross section relative to the H cross section to go as the helium-3 form factor squared times a phase space factor [65]. At these kinematics, the form factor squared is ≈ 0.45 while the phase space factor is 0.95, yielding a net ratio of 0.425. The ratios of the unseparated cross sections are shown in Table 6.9. Note that the ratios have not been adjusted for the fact that there are two protons in helium-3 so that the ratio quoted is the true cross section ratio and not the ratio of the cross section per contributing nucleon. Our results seem consistent with the notion that the suppression is dominated by the helium-3 form factor.

It is also interesting to compare the separated ^{3}H and H cross sections. Defining the "reduced" separated cross sections as in Section 6.5 we find that the longitudinal ratio is $R_L = 0.50 \pm 0.08$ and the transverse ratio is $R_T = 0.24 \pm 0.06$. In other words, the longitudinal and transverse pieces of the cross section are not suppressed in the same manner. An in-depth calculation of this effect would be very interesting to see if it can be reproduced by known nuclear processes.

Final State	$\sigma_L = \int_{\Delta P_\pi} d^2\sigma_L \, dP_\pi$ (μb/sr)	$\sigma_T = \int_{\Delta P_\pi} d^2\sigma_T \, dP_\pi$ (μb/sr)	$R = \frac{\sigma_L}{\sigma_T}$
All	$48.01 \pm 2.20 \pm 6.18$	$36.85 \pm 1.59 \pm 4.13$	1.30 ± 0.20
^{3}H	$14.77 \pm 1.17 \pm 2.05$	$5.61 \pm 0.82 \pm 1.25$	2.63 ± 0.65
Dn/pnn	$33.23 \pm 2.49 \pm 5.18$	$31.24 \pm 1.79 \pm 3.63$	1.06 ± 0.19

TABLE 6.8. Longitudinal and transverse separated cross sections for $^3\mathrm{He}(e, e'\pi^+)$. Cross sections integrated over final states as well as the separate coherent ^{3}H and continuum Dn/pnn contributions are shown. $d^2\sigma_{L(T)}$ denotes $\frac{d\sigma_{L(T)}}{d\Omega_\pi dP_\pi}$. Uncertainties on the cross sections are statistical and total systematic. R, the ratio of σ_L to σ_T is also given. The kinematics correspond to our high W data, $W = 1.6$ GeV, $Q^2 = 0.4$ (GeV/c)^2 and $\theta_{pq} = 1.72$ degrees.

ϵ	$\sigma^5_{lab}(^3\mathrm{H})$ (μb/sr^2/GeV)	$\sigma^5_{lab}(\mathrm{H})$ (μb/sr^2/GeV)	$\sigma(^3\mathrm{H})/\sigma(\mathrm{H})$
0.490	$(7.89 \pm 0.27) \times 10^{-3}$	$(2.34 \pm 0.04) \times 10^{-2}$	0.34 ± 0.01
0.894	$(1.11 \pm 0.04) \times 10^{-1}$	$(2.99 \pm 0.07) \times 10^{-1}$	0.37 ± 0.02

TABLE 6.9. Unseparated cross section ratios for ^{3}H and H. Uncertainties on the cross sections include only the pieces that propagate randomly. There is an additional 1.99% uncertainty that comes from the relative normalization between targets.

6.7. Discussion of Results

In light of the results presented in Section 6.5, what, if anything, can be said about nuclear pions and the predicted enhancement of the nuclear pion field? Recall that according to pion excess calculations, one expects to see a suppression at low k_π and an enhancement at high k_π. The real issue at hand is how do these pion excess calculations translate to the cross sections we measure?

The simplest approach is to assume that the longitudinal cross section is proportional to the "number" of virtual pions. Given the number density in the free nucleon, $n(k_\pi)$, and the pion excess per nucleon in the bound nuclear system, $\delta n(k_\pi)$, the longitudinal ratio would be,

$$\frac{\sigma_L^A}{\sigma_L^H} = \frac{n(k_\pi) + \delta n(k_\pi)}{n(k_\pi)} \,. \tag{6.21}$$

There are of course problems with the above assumption. First, as shown in Section 6.6.1, there are significant isoscalar backgrounds in the longitudinal cross sections which indicates that we are sensitive to other processes besides the pole process, i.e. we are not just scattering from virtual pions. Furthermore, the above equation assumes that we have sampled all virtual pion energy (ω_π) for a given virtual pion momentum (k_π) and that we sample at a fixed k_π. Rather, due to the constraint of detecting the final on-shell pion in parallel kinematics (at fixed θ_{pq}) in order to separate out the longitudinal piece, we sample a fixed (ω_π, k_π) in the case of hydrogen and integrate over a contour in (ω_π, k_π) space for the nuclear targets. Nonetheless, the above simple formula will give a sense of the size of the effects one could most optimistically expect.

Calculations of the pion fields of nuclei tend to focus on the pion excess, subtracting away the contribution from the free nucleon. This latter quantity in itself is of significant interest and not a theoretically well determined quantity. However, to usefully extract a value for the expected ratios, we must make some estimate. A useful starting point is a simple field theory model outlined in Ref. [75]. The expression for the probability to find a pion with momentum k_π is given by,

$$n(k_\pi) = \frac{3}{\pi}\frac{f^2}{4\pi}\frac{k_\pi^4}{\omega_\pi^3}\left|G_{\pi NN}(k_\pi)\right|^2 \,, \tag{6.22}$$

where $\omega_\pi = \sqrt{k_\pi^2 + m_\pi^2}$, $G_{\pi NN}$ is the πNN vertex form factor, and f is the fundamental πNN coupling (given by low energy π-N scattering, $f^2/4\pi \approx 0.08$).

k_π	$n(k_\pi)$	$\delta n(k_\pi)$ (GeV^{-1})		
(GeV/c)	(GeV^{-1})	D	^{3}He	^{4}He
0.20	0.392	-0.004	-0.056	-0.120
0.47	1.005	0.063	0.135	0.242

TABLE 6.10. Estimated pion density $n(k_\pi)$ in the nucleon and the pion excess density $\delta n(k_\pi)$ in deuterium, helium-3 and helium-4 at E91003 kinematics. $n(k_\pi)$ is calculated as described in the text, and $\delta n(k_\pi)$ is from Ref. [2] (see Figure 1.1).

Typically, $G_{\pi NN}$ is expressed in a monopole form in terms of Λ, the phenomenological πNN cut-off factor,

$$G_{\pi NN}(k_\pi) = \frac{1}{1 + k_\pi^2/\Lambda^2} \, . \tag{6.23}$$

There is some disagreement regarding the value of Λ, but it is generally taken to be between 0.5-1.3 GeV. Alternatively, $G_{\pi NN}$ is sometimes expressed,

$$G_{\pi NN}(k_\pi) = \frac{(\Lambda^2 - m_\pi^2)^2}{(\Lambda^2 + k_\pi^2)^2} \, . \tag{6.24}$$

Friman *et al* [2] use this second form and, as we will compare $n(k_\pi)$ to their pion excess calculations, we also use this form and take their value of $\Lambda = 1.38$ GeV. Values of $n(k_\pi)$ along with the pion excess calculations from Ref. [2] for our kinematics and targets (as well as ^{4}He) are shown in Table 6.10. The ratios implied by the values in Table 6.10 are shown in Table 6.11.

From Table 6.11, we see that the fractional enhancement in deuterium and helium-3 at $k_\pi = 0.47$ GeV/c is about 6% and 13% respectively. On the other hand, the fractional suppression at $k_\pi = 0.20$ GeV/c is 2% for deuterium and 14% for helium-3 (relative to the free nucleon).

Within uncertainties, the quasifree corrected deuterium ratios agree with these estimates (D/H $= 0.90 \pm 0.12$ at low k_π and D/H $= 1.09 \pm 0.16$ at high k_π),

k_π (GeV/c)	D/H	^{3}He/H	^{3}He/D	^{4}He/H
0.20	0.99	0.86	0.87	0.69
0.47	1.06	1.13	1.07	1.24

TABLE 6.11. Ratio of pion number density in nuclei to the free nucleon (or deuterium) for E91003 kinematics. These ratios are simply $R = (n(k_\pi)+\delta n(k_\pi))/n(k_\pi)$ from Table 6.10.

although the errors are large enough that both points are consistent with 1. The high recoil helium-3 π^+ data, once corrected for the large pion absorption effects, yields a ratio of $\approx 1.43 \pm 0.28$ which is consistent with the prediction, but also not totally inconsistent with 1 given the errors.

One the other hand, the helium-3 π^- and π^+ quasifree corrected ratios at low k_π are suppressed quite a bit more than the above expectation (^{3}He/D(π^-) = 0.58 ± 0.07 and ^{3}He/H(π^+) = 0.61 ± 0.12). However, these numbers can not be directly compared to our simple pion excess estimate. First, recall that the quasifree corrected ratio for the low k_π helium-3 π^+ data involves only the continuum Dn/pnn final states and ignores the contribution from the coherent ^{3}H final state.[3] Hence, it is not surprising that the π^+ and π^- (which has only the ppp final state available) quasifree corrected ratios are suppressed by roughly the same amount. The pion excess, though, is calculated by summing over all final nuclear states (bound and unbound) and all charge states. Therefore, to compare to the pion excess calculation, we need to include the contribution from the coherent ^{3}H

[3]Strictly speaking, this is also true for the high k_π data, but we expect the coherent contribution to be much smaller there.

final state from the π^+ data and take the isospin average over pion final states $(= \frac{2}{3}\,\pi^+ + \frac{1}{3}\,\pi^-)$.

In the case of the Dn/pnn final states, the quasifree calculation corrects for the finite P_π coverage, possible wave function threshold effects, and smearing of the γ^*-N cross section. The first two effects should require no correction in the ^{3}H case, so it is sufficient to estimate the correction due to smearing of the γ^*-N cross section. Here, we make the assumption that the ^{3}H smearing correction is small (in the Dn/pnn case it is about 2.5%), or at least insignificant relative to the experimental uncertainties. Therefore, combining the ^{3}H/H ratio extracted in Section 6.6.2 with the Dn/pnn quasifree corrected result, we get an estimate of the nuclear dependence of the total ^{3}He$(e, e'\pi^+)$ cross section coming from sources other than the Fermi motion of the "struck" nucleon (in our simple spectator picture). The resulting combined ^{3}H and Dn/pnn ratio is ^{3}He/H $= 0.86 \pm 0.12$. This implies a ^{3}He/D(π^+) ratio of 0.95 ± 0.18, which can be combined with the π^- value to give ^{3}He/D$(\pi^+ + \pi^-) = 0.83 \pm 0.12$, in agreement with our simple estimate of 0.88.

The main conclusion that we reach from this exercise is that, given that the experimental uncertainties are on the order of the expected effect and that the ratios are for the most part consistent with unity, we can not rule out the predicted pion excess nor conclude that there is no modification of the pion field in nuclei. While the uncertainties are too large to detect an effect in deuterium or helium-3, slightly heavier nuclei may yield a larger signal. Table 6.10 shows the predicted pion excess for helium-4. In this case, the fractional excess is $\approx 28\%$ at $k_\pi = 0.47$ GeV/c while the suppression is about 30% at $k_\pi = 0.20$ GeV/c. One may argue that even heavier nuclei should be probed, however helium-4 holds out the best hope for a sizable effect in a nucleus for which microscopic calculations are feasible.

6.8. Conclusions

Experiment E91003 measured charged pion electroproduction from hydrogen, deuterium, and helium-3. 5-fold lab cross sections were obtained for hydrogen and the 6-fold cross sections from deuterium and helium-3 were integrated over the resulting pion momentum, P_π. Rosenbluth separations were performed to extract the longitudinal cross sections by measuring the lab cross sections at two values of the virtual photon polarization, ϵ. These longitudinal cross sections from different nuclei were then compared to look for signs of mass dependent effects that may be attributable to a pion excess coming from pion exchange currents in the nucleus.

Interpretation of the data was complicated by many factors. At high k_π, where one would predict an enhancement of the longitudinal cross section, the P_π coverage was incomplete, forcing us to extrapolate the integrated cross section to lower and higher P_π. Furthermore, the high k_π data were taken at relatively low W, meaning that parts of the nucleon wave function could not contribute to the pion electroproduction process. Finally, the kinematic variation of the longitudinal pion electroproduction cross section averaged over the nucleon wave function had to be taken into account.

Despite the above difficulties, clear signs of a suppression of the longitudinal pion electroproduction cross section were seen at $k_\pi \approx 200$ MeV/c. Furthermore hints of some enhancement were seen at $k_\pi \approx 470$ MeV/c in the helium-3 to hydrogen ratio, although at about the 1 σ level. Interpretation of these effects are hampered by the fact that it is unclear to what extent the longitudinal electroproduction process is dominated by the pole term.

In light of these results, it seems clear that an improved experiment is worth pursuing. Such an experiment could be easily accomplished by taking data at higher W ($\approx$ 1.95 GeV or higher). This would avoid the γ^*-N threshold issues, allow for more complete P_π acceptance, and reduce the effects of final state interactions between the outgoing pion and spectator nucleons. Furthermore, it is known that the longitudinal π^-/π^+ ratio is consistent with one (to about 10%) [76] indicating that the pole term dominates the longitudinal pion electroproduction cross section in this region. A survey of the longitudinal cross section from hydrogen would also be beneficial in reducing the model dependence of the correction used to account for the kinematic variation of the γ^*-N cross section in the nuclear targets. The resulting improvement in the experiment, combined with the expected doubling of the pion excess in helium-4, would significantly increase the sensitivity of such a search.

BIBLIOGRAPHY

[1] G. Bertsch, L. Frankfurt, and M. Strikman, Science **259**, 773 (1993).

[2] B. L. Friman, V. R. Pandharipande, and R. B. Wiringa, Phys. Rev. Lett. **51**, 763 (1983).

[3] J. J. Aubert *et al.*, Phys. Lett. **123B**, 275 (1983).

[4] M. Ericson and A. W. Thomas, Phys. Lett. **128B**, 112 (1983).

[5] J. D. Sullivan, Phys. Rev. **D5**, 1732 (1972).

[6] C. H. Llewellyn Smith, Phys. Lett. **128B**, 107 (1983).

[7] J. Ashman *et al.*, Z. Phys. **C57**, 211 (1993).

[8] J. Gomez *et al.*, Phys. Rev. **D49**, 4348 (1994).

[9] A. Bodek *et al.*, Phys. Rev. Lett. **50**, 1431 (1983).

[10] R. G. Arnold *et al.*, Phys. Rev. Lett. **52**, 727 (1984).

[11] J. Ashman *et al.*, Phys. Lett. **202B**, 603 (1988).

[12] T. A. Carey *et al.*, Phys. Rev. Lett. **53**, 144 (1984).

[13] L. B. Rees *et al.*, Phys. Rev. **C34**, 627 (1986).

[14] J. B. McClelland *et al.*, Phys. Rev. Lett. **69**, 582 (1992).

[15] X. Y. Chen *et al.*, Phys. Rev. **C47**, 2159 (1993).

[16] T. N. Taddeucci *et al.*, Phys. Rev. Lett. **73**, 3516 (1994).

[17] D. M. Alde *et al.*, Phys. Rev. Lett. **64**, 2479 (1990).

[18] G. E. Brown *et al.*, Nucl. Phys. **A593**, 295 (1995).

[19] V. R. Pandharipande *et al.*, Phys. Rev. **C49**, 789 (1994).

[20] D. S. Koltun, Phys. Rev. **C57**, 1210 (1998).

[21] P. Gueye, *Status of the Actual Beam Position Monitors in the Hall C Beamline*, Jefferson Lab Hall C Internal Report (unpublished).

[22] C. Yan, R. Carlini, and D. Neuffer, *Beam Energy Measurement Using the Arc Beam Line as a Spectrometer*, CEBAF-PR-93-004, 1993.

[23] C. Armstrong, *Beam Current Measurement in Hall C*, Jefferson Lab Hall C Internal Report (unpublished).

[24] G. Niculescu, *Resonant Cavities used as Beam Current Monitors*, Jefferson Lab Hall C Internal Report (unpublished).

[25] D. G. Meekins, Ph.D. thesis, The College of William and Mary in Virginia, 1999.

[26] M. Seely and K. Bailey, private communication, February 28, 2000.

[27] J. Volmer, Ph.D. thesis, Vrije Universiteit, 2000.

[28] J. R. Arrington, Ph.D. thesis, California Institute of Technology, 1998.

[29] C. S. Armstrong, Ph.D. thesis, The College of William and Mary in Virginia, 1998.

[30] M. I. Niculescu, Ph.D. thesis, Hampton University, 1999.

[31] D. Abbott *et al.*, in *Proc. of the IEEE Conference on Real-Time Computer Applications in Nuclear, Particle, and Plasma Physics*, edited by R. Fox (Michigan State University - NSCL, East Lansing, 1995), p. 147.

[32] K. Makino and M. Berz, Nucl. Instrum. Meth. **A427**, 338 (1999).

[33] K. Assamagan, D. Dutta, and P. Welch, *Hall C Matrix Element Optimization Package (CMOP)*, Jefferson Lab Hall C Internal Report (unpublished).

[34] G. Niculescu, *On Pathlengths and Corrected Coincidence Time*, Jefferson Lab Hall C Internal Report (unpublished).

[35] W. R. Leo, *Techniques for Nuclear and Particle Physics Experiments* (Springer-Verlag, Berlin, 1994), p. 122.

[36] R. M. Mohring, Ph.D. thesis, University of Maryland, 1999.

[37] R. M. Gibbons and D. I. Nathan, *Thermodynamic Data of Helium-3*, AFML-TR-67-175, 1967.

[38] D. Ashery *et al.*, Phys. Rev. **C23**, 2173 (1981).

[39] B. W. Allardyce *et al.*, Nucl. Phys. **A209**, 1 (1973).

[40] C. Caso *et al.*, Eur. Phys. J. **C3**, 1 (1998).

[41] F. Binon *et al.*, Nucl. Phys. **A298**, 499 (1978).

[42] R. Mach, M. G. Sapozhnikov, and Y. A. Shcherbakov, Czech. J. Phys. **B26**, 1248 (1976).

[43] N. C. R. Makins, Ph.D. thesis, Massachusetts Institute of Technology, 1994.

[44] T. G. O'Neill, Ph.D. thesis, California Institute of Technology, 1994.

[45] D. M. Koltenuk, Ph.D. thesis, University of Pennsylvania, 1999.

[46] T. S. H. Lee, private communication, March 3, 1998.

[47] H. Meier-Hajduk *et al.*, Nucl. Phys. **A395**, 332 (1983).

[48] E. Jans *et al.*, Nucl. Phys. **A475**, 687 (1987).

[49] L. C. L. Yuan and C. S. Wu, *Methods of Experimental Physics* (Academic Press, New York, 1961), Vol. 5A, p. 17.

[50] J. Volmer, *Calculation of Energy Losses in Hall C's Replay Engine*, Jefferson Lab Hall C Internal Report (unpublished).

[51] S. Lebedev, *utiLandau PHENIX utility*, www.phenix.bnl.gov/WWW/software/luxor/uti/mod/landau.html, 1998.

[52] CERN Program Library Short Writeups, p. G110, 1993.

[53] J. A. Templon *et al.*, Phys. Rev. **C61**, 014607 (2000).

[54] L. W. Mo and Y.-S. Tsai, Rev. Mod. Phys. **41**, 205 (1969).

[55] Y.-S. Tsai, Phys. Rev. **122**, 122 (1961).

[56] R. Ent *et al.*, *Radiative Corrections for (e,e'p) Reactions*, submitted to Phys. Rev. C., 2000.

[57] D. Dutta, Ph.D. thesis, Northwestern University, 1999.

[58] D. van Westrum, Ph.D. thesis, University of Colorado, 1998.

[59] P. E. Bosted, Phys. Rev. **C51**, 409 (1995).

[60] D. van Westrum, *Measurement and Estimate of Proton Absorption in the Hall C Spectrometers*, Jefferson Lab Hall C Internal Report (unpublished).

[61] J. R. Taylor, *Scattering Theory* (John Wiley and Sons, New York, 1972), pp. 424–432.

[62] J. Gillespie, *Final-State Interactions* (Holden-Day, San Francisco, 1964).

[63] *HBOOK - Reference Manual*, CERN Program Library Long Writeup Y250, Version 4.22, 1994.

[64] F. James, *MINUIT - Function Minimization and Error Analysis, Reference Manual*, CERN Program Library Long Writeup D506, Version 94.1, 1994.

[65] R. J. Loucks and V. R. Pandharipande, Phys. Rev. **C54**, 32 (1996).

[66] D. Drechsel *et al.*, Nucl. Phys. **A645**, 145 (1999).

[67] G. von Gehlen, Nucl. Phys. **B20**, 102 (1970).

[68] P. Brauel *et al.*, Z. Phys. **C3**, 101 (1979).

[69] H. Breuker *et al.*, Nucl. Phys. **B146**, 285 (1978).

[70] E. Evangelides *et al.*, Nucl. Phys. **B71**, 381 (1974).

[71] J. Wright *et al.*, Nucl. Phys. **B181**, 403 (1981).

[72] R. J. Loucks, V. R. Pandharipande, and R. Schiavilla, Phys. Rev. **C49**, 342 (1994).

[73] T. S. H. Lee, private communication, June 10, 1999.

[74] T. S. H. Lee, private communication, November 2, 1999.

[75] E. M. Henley and W. E. Thirring, *Elementary Quantum Field Theory* (McGraw-Hill, New York, 1962), pp. 219–231.

[76] V. Tadevosyan, *for the F_π collaboration*, private communication, May 19, 2000.

[77] K. Gustafsson, *Cryotarget Density Dependence on Beam Current*, Jefferson Lab Hall C Internal Report (unpublished).

[78] X. Li, L. E. Wright, and C. Benhold, Phys. Rev. **C45**, 2011 (1992).

APPENDICES

APPENDIX A. Target Heating Corrections

The small size of the electron beam at Jefferson Lab ($\approx$ 50-100 μm full-width at half maximum), while indicative of the small energy spread and high quality of the electron beam, can be a problem when conducting experiments with cryogenic targets. The small beam size results in a significant amount of power being deposited in the target in a very small area. This power deposition in turn results in heating (and perhaps even boiling) of the target material, and hence, density variations. This problem is somewhat alleviated by wiggling, or rastering the beam. Small magnets twenty meters upstream of the target apply fields that deflect the electron beam in the transverse direction. The field applied by the magnets is time-varying such that the electron beam does not spend too much time at any one point on the target (see Figure 2.4). During E91003, a circular raster pattern was used with an inner radius if 0.015 cm and an outer radius of 0.15 cm. Although the beam raster did reduce heating effects in the target, there was still a non-negligible heating of the target material that resulted in an effective reduction of the target thickness. It should be noted that although previous Hall C experiments had already measured target density effects in hydrogen and deuterium due to the electron beam [77], it was necessary to repeat these measurements since both the target configuration (i.e. vertical flow targets) and raster pattern (circular as opposed to the square pattern used in previous experiments) were new. Furthermore, the ^{3}He target was first commissioned during E91003, and its density change with beam current also needed to be characterized.

A.1. Luminosity Scan Runs

During the running of E91003, time was set aside for so-called "luminosity scans" to investigate the effect of beam current on target density (local target boiling). During these scans, the HMS and SOS were set at angles and momenta corresponding to the kinematics for elastic (or quasielastic in the case of $A > 1$ targets) scattering (for $E_{beam} = 1.645$ GeV, $\theta_e^{elastic} = 40.0°$, and $P_e^{elastic} = 1.167$ GeV). Then, a series of high statistics runs (typically $\approx$ 100,000 events) were taken at varying beam currents. Elastic kinematics were desirable because of the large cross section, thus giving a high rate with low background. The beam currents used for these runs ran from 10 μA to 50 μA in steps of 10 μA. Such a procedure was repeated for each target (H, D, and ^{3}He).

A.2. Analysis

The luminosity scan runs for each target were then analyzed in two ways. The first method, a scaler analysis, looked at just the raw counting rates while the second involved a tracking based analysis.

The scaler based analysis involved looking at the SOS and HMS pretrigger signals. The HMS and SOS triggers were configured for electrons for these runs, so a pretrigger generally occurred when three out four scintillator planes fired and certain particle type discriminating signals were present (see Section 2.6 for more details). One advantage of the pretrigger signal is that the inefficiencies involved are very small, and change relatively slowly as a function of incident particle rate. The only real corrections to the charge-normalized yield were the electronic dead time and the trigger (3/4) efficiency. The pretrigger signal also has the advantage that it provided some small measure of particle identification (although with poor rejection since hardware thresholds are in general set conservatively so that no electrons are lost). Efficiency corrected pretrigger yields were calculated as a function of beam current and the current dependence determined from these yields.

The tracking based analysis involved analyzing tracked events and implementing particle identification and tracking based cuts ($xptar$, $yptar$, $ytar$, δ) to confine events to the region of good spectrometer acceptance. Additional cuts were placed on the reconstructed mass (W) to exclude any inelastic events. The tracking based analysis reduces backgrounds from the target cell walls as well as ensuring that one is measuring one particular process. In addition to the electronic dead time and trigger efficiency, the tracked events were corrected for computer dead time and tracking efficiency. As with the scaler analysis, the charge normalized yield was determined for each beam current, and the resulting dependence fit. It is important to note that the HMS and SOS took data simultaneously during the luminosity scan runs. This means that we have two quasi-independent measurements from each analysis method at each current.

A further complication in the analysis of the luminosity scan runs came about due to uncertainties in the calibration of the beam current monitors. In particular, the current monitors have relatively unstable zero-offsets, typically reaching up 0.1 μA. At large currents, this is not a problem. However, at 10 μA, a 0.1 μA offset is a 1% effect. The issue, then is that since the current monitor offset effect is different at each current, the perceived current dependence of the normalized yield will be affected.

This problem was addressed in the following manner. First, calibrations were made for the beam current monitors from runs that were taken either immediately before or immediately after the luminosity scan runs. Next, the current dependence of the normalized yield was fit (a simple linear function was used) for

Target	Slope (initial) (%/100μA)	Slope ($I_{offset} = 0.1\mu A$) (%/100μA)	Slope (χ^2_ν minimized) (%/100μA)
Hydrogen	2.83	4.14	2.56
Deuterium	0.98	2.33	0.71
^{3}He	7.23	8.62	5.69

TABLE A.1. Effect of BCM zero-offset on target luminosity beam current dependence. Target thickness reduction as measured by HMS pretriggers is shown for no BCM zero-offset, a zero-offset of 0.1 μA, and the zero-offset as determined using the fitting procedure described in the text.

the HMS and SOS pretrigger signals and tracks. The mean chi-squared per degree of freedom (χ^2_ν) was determined for the four fits. Next, the BCM offset was varied, the charge recalculated, and the current dependence fit again. This was repeated until the mean χ^2_ν was minimized. The effect of varying the BCM zero-offset can be seen in Table A.1. A variation of the offset of $\approx$ 0.1 μA leads to significant variations in the extracted reduction of the target thickness at 100 μA (on the order of $\pm$ 1%). Note, however, that the final uncertainty in the correction will be minimized due to two facts: first, an arbitrary offset of 0.1 μA can be ruled out simply by noticing that the resulting current dependence is poorly described by a straight line and second, the actual correction is typically a quarter to one half the magnitude of the numbers quoted at 100 μA (typical running conditions were usually below 50 μA). The BCM offsets obtained using the above χ^2_ν minimization procedure were -0.02 μA for hydrogen and deuterium and -0.11 μA for ^{3}He.

One additional correction that had to be considered was the contribution of the target cell walls to the normalized yield. This contribution will be independent of current so will affect the extracted slope as an overall scale. Unfortunately, no data was taken on the empty or dummy targets at the kinematics of the luminosity scan runs. Thus, some reasonable estimate had to be made for the dummy contribution. These estimates were made based on data taken in 1996 under identical kinematic conditions. Also, the thickness of the target cell walls relative to the cryogenic material was taken into account. The dummy contribution to the scalers (tracks) was estimated to be 15±8% (4.5±2.4%) for the hydrogen and ^{3}He targets and 10±8% (3±2.4%) for the deuterium target. Note that the estimated contribution is smaller for the tracks. This is because one greatly reduces the background from the target cell walls when cutting on the (quasi)elastic peak.

A.3. Hydrogen Results

The results of the combined scaler and tracking based analyses for the HMS and SOS are shown in Figure A.1 The BCM offset has been modified to minimize the mean χ^2_ν of the four fits and the estimated contribution from the target cell walls has been subtracted.

During the running of the experiment, the hydrogen target was operated under two conditions. For the first part of the running (in February), the hydrogen target was operated at its nominal design temperature of 19 K. Due to technical problems, the operating temperature of the target had to be reduced to 18 K for the second part of the running (where the majority of the data was acquired). This reduction in temperature resulted in a target that was $\approx$ 1.23% more dense. It was thought that the target heating properties might also differ between the two targets. The luminosity scan runs for the hydrogen target were taken primarily at 18 K, however, a few runs were taken with the target operated at 19 K as well. The 19 K runs (adjusted for the 1.23% density difference) are plotted with the 18 K runs in Figure A.1. At 20 μA, there is no discernible difference between the

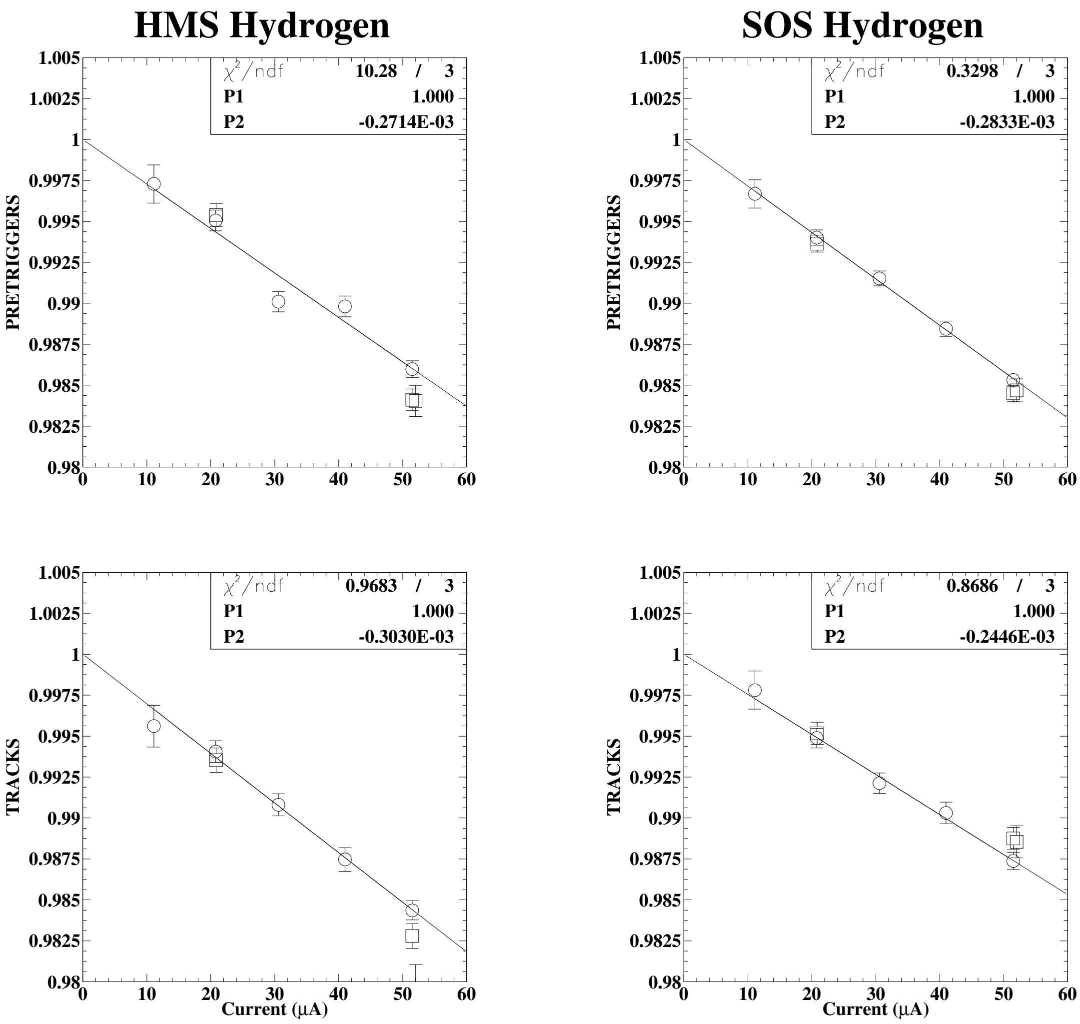

FIGURE A.1. Normalized yield as a function of beam current from hydrogen target as measured in the HMS and SOS. Data points are normalized such that the line fit to the points is equal to one at zero current. Error bars are statistical only. Circles are data from the 18 K hydrogen target while squares are from the 19 K target.

normalized yields from the 18 K and 19 K hydrogen targets. At 50 μA, the HMS 19 K points are about 0.2% lower than the 18 K points, however, the SOS points show about a 0.1% lower yield (SOS pretriggers) or a slightly larger yield (SOS tracks). The mean difference among the four points is about 0.1% lower. For this reason, the correction for the 19 K target was assigned to be 0.2% larger at 100 μA, although a slightly larger uncertainty was assigned for that correction.

A.4. Deuterium and Helium Results

The normalized yields and fits as a function of beam current for the deuterium target are shown in Figure A.2 while the helium yields are shown in Figure A.3. For the deuterium data, the same BCM offset was used as for the hydrogen case (-0.02 μA) since the deuterium runs were taken at the same time as the hydrogen runs. The small slope made it difficult to effectively minimize the mean χ^2_ν, but tests indicated that it was roughly minimized at that offset. The helium data required a larger offset of -0.11 μA. This is somewhat near the bounds of what one might consider a reasonable BCM offset. However, this is in part explained by the fact that the BCM calibration run taken close to the luminosity scan runs was difficult to analyze (the beam current drifted during the nominally "constant current" parts of the run). Thus, a mean calibration for that general period of running was used as the initial calibration.

The final correction factors for all three targets and their associated uncertainties are shown in Table A.2. The largest single contribution to the uncertainty was the BCM zero-offset optimization procedure (0.24% for hydrogen and deuterium, 1.0% for ^{3}He).

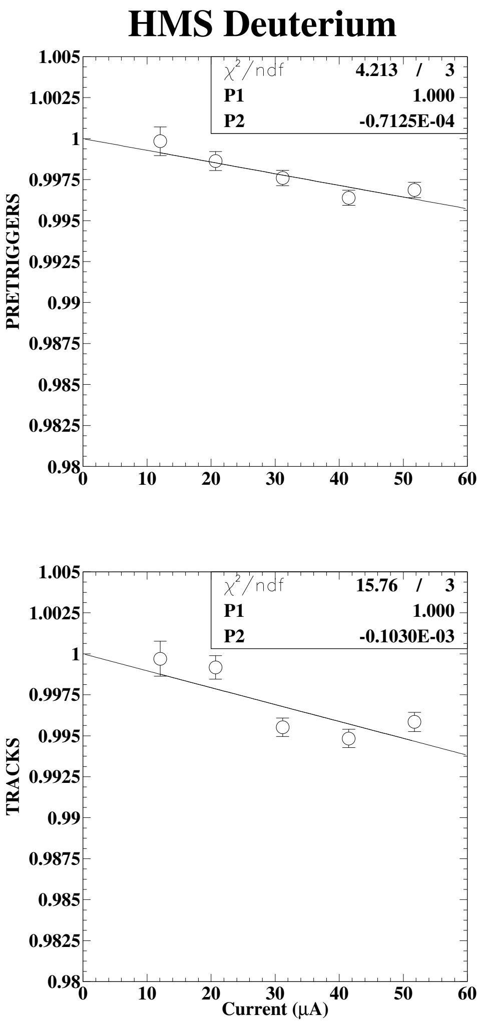

FIGURE A.2. Normalized yield as a function of beam current from deuterium target as measured in the HMS and SOS. Points are normalized as described in Figure A.1.

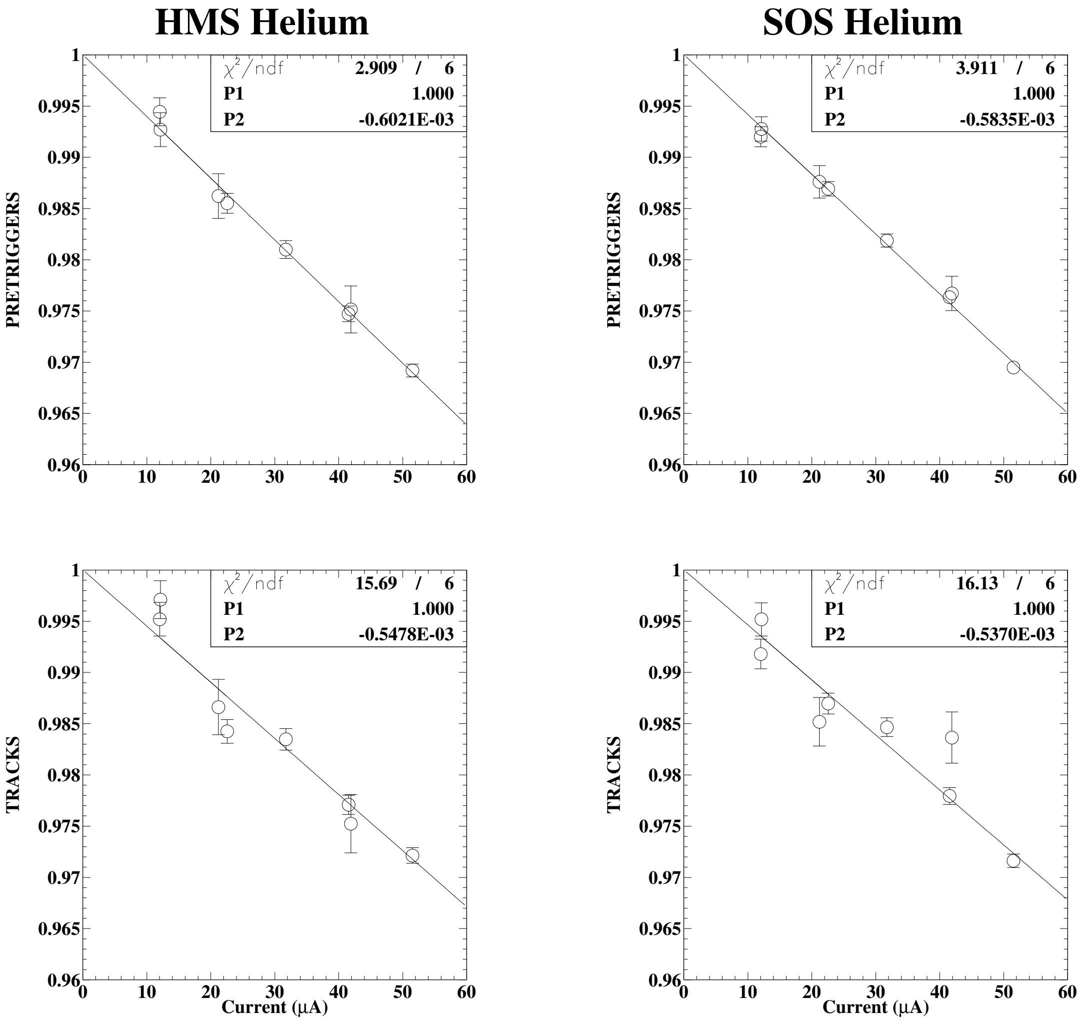

FIGURE A.3. Normalized yield as a function of beam current from helium-3 target as measured in the HMS and SOS. Points are normalized as described in A.1.

Target	Target Density Correction (%/100μA)
H (18K)	2.70 $\pm$ 0.33
H (19K)	2.90 $\pm$ 0.43
D	1.15 $\pm$ 0.31
^{3}He	5.68 $\pm$ 1.11

TABLE A.2. Target density corrections and associated uncertainties for the three cryotargets used during E91003.

A.5. Raster Size Effects

The above corrections were fit and applied for data taken with the nominal raster size (0.15 cm outer radius, 0.015 cm inner radius). Unfortunately, some small fraction of the pion production data was taken with a raster of about half the nominal radius. This came about because the raster magnets were not re-initialized after a beam energy change. The problem was discovered and corrected by the machine operators after a few hours, but the experimenters were not notified, so no measures were taken to take more data with the nominal raster size. In fact, the raster size was changed in the middle of a run as was discovered in subsequent data quality checks after the completion of the experiment (see Figure A.4).

Fortunately, all the runs affected by the raster size mistake were taken at low beam current (10 to 20 μA). Furthermore, analysis of previous luminosity scan data (for which the raster size as well as the beam current was varied) indicated little density change as a function of raster amplitude (the density changed at most linearly with raster amplitude). One can also check the effect of the small raster size by checking the runs themselves. The entire $E_{beam} = 3.245$ GeV hydrogen data set and part of the deuterium data set was taken with the smaller raster. The hydrogen

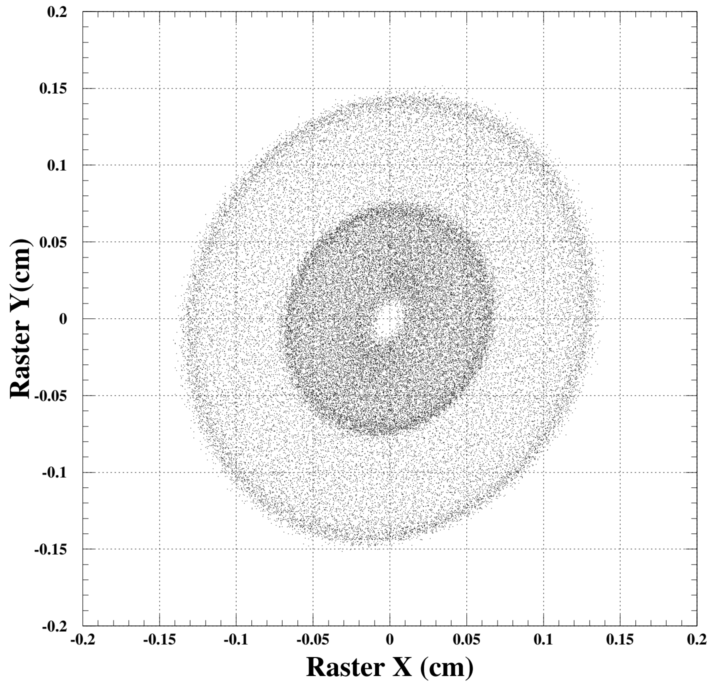

FIGURE A.4. Raster pattern during run 18483. The raster size was changed at some point during the run as can be seen from the dense cluster of points within a circle of radius 0.075 cm.

runs were taken at two different currents, 12 and 20 μA. The charge normalized pretriggers[1] for the SOS (corrected using the nominal density correction) disagree by about 0.2% for the two currents. However, by doubling the size of the correction per μA (basically, assuming the correction is inversely proportional to the raster radius) the points are in better agreement as can be seen in Figure A.5. For this subset of runs, the correction was therefore doubled, and an additional uncertainty

[1]Note that the pretriggers include coincidence events as well as un-prescaled singles. Hence, the pretriggers can be considered a distinct sample from the coincident pion electroproduction yield.

of 0.1% (added in quadrature) was assigned. The relevant correction factors were then 5.40 $\pm$ 0.67%/100μA for the hydrogen runs and 2.30 $\pm$ 0.63%/100μA for deuterium.

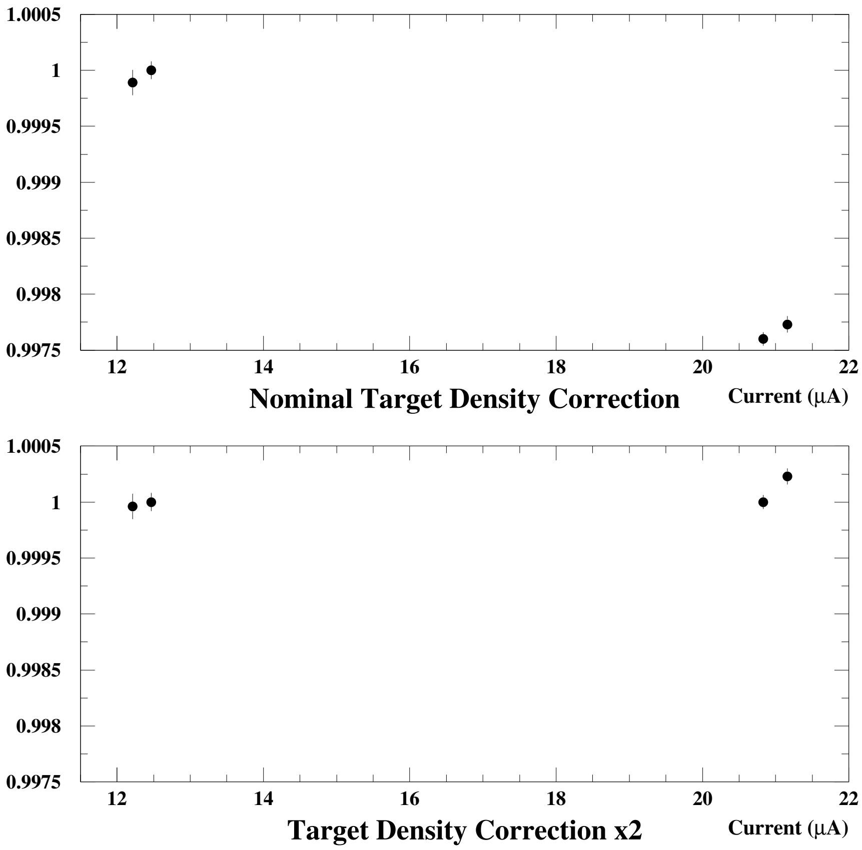

FIGURE A.5. SOS pretriggers (normalized) for E_{beam} = 3.245 GeV hydrogen data. Error bars are statistical only and are comparable to the size of the points. The first two runs were taken at 12μA and the second two at 20 μA.

APPENDIX B. The Jacobian

In calculating the cross section for a given event in SIMC, models are used that describe the virtual photon cross section in the γ^*-N center of mass, $(d\sigma/d\Omega_\pi^*)$[1] multiplied by a virtual photon flux factor (Γ). Since the generation volume in SIMC is in terms of lab variables, one must transform the virtual photon cross section to the lab in order to properly weight the event.

Rather than do the transformation $d\sigma/d\Omega_\pi^* \rightarrow d\sigma/d\Omega_\pi$ all at once, it is somewhat simpler to do it in two steps. The first step is to transform $d\sigma/d\Omega_\pi^*$ to $d\sigma/dtd\phi_{q\pi}^*$. The invariant t is written,

$$t = -Q^2 + m_\pi^2 - 2\omega E_\pi + 2p_\pi q cos\theta_{q\pi} \ , \tag{B1}$$

where all the relevant angles and momenta can be written in terms of lab or center of mass variables. In the center of mass, all energy and momenta are independent of the pion direction, $\theta_{q\pi}$, so

$$\frac{dt}{d\cos\theta_{q\pi}^*} = 2p_\pi^* q^* \ , \tag{B2}$$

and

$$\frac{d\sigma}{dtd\phi_{q\pi}^*} = \frac{d\sigma}{d\Omega^*}\frac{d\cos\theta_{q\pi}^*}{dt} = \frac{1}{2p_\pi^* q^*}\frac{d\sigma}{d\Omega^*}. \tag{B3}$$

The full transformation is then,

$$\frac{d\sigma}{d\Omega_\pi} = J(t, \phi_{q\pi}^* \rightarrow \cos\theta_{q\pi}, \phi_{q\pi})\frac{1}{2p_\pi^* q^*}\frac{d\sigma}{d\Omega_\pi^*} \ , \tag{B4}$$

where the Jacobian, J, is given by the determinant,

$$J(t, \phi_{q\pi}^* \rightarrow \cos\theta_{q\pi}, \phi_{q\pi}) = \begin{vmatrix} \frac{\partial t}{\partial\cos\theta_{q\pi}} & \frac{\partial t}{\partial\phi_{q\pi}} \\ \frac{\partial\phi_{q\pi}^*}{\partial\cos\theta_{q\pi}} & \frac{\partial\phi_{q\pi}^*}{\partial\phi_{q\pi}} \end{vmatrix} . \tag{B5}$$

[1]In this section, all variables with a "*" refer to the center of mass frame.

Before proceeding with the calculation of the above determinant, it is worth noting a couple of useful derivatives. One derivative that will appear repeatedly is $\partial p_\pi/\partial\cos\theta_{q\pi}$.

$$\frac{\partial p_\pi}{\partial\cos\theta_{q\pi}} = \tag{B6}$$
$$\frac{p_\pi p_{recoil}(\hat{\mathbf{q}}) + p_\pi^2\cos\theta_{q\pi} - p_\pi p_N \sin\theta_{qN}\frac{\cos\theta_{q\pi}}{\sin\theta_{q\pi}}F(\phi_{qN},\phi_{q\pi})}{p_\pi\sin^2\theta_{q\pi} - p_N\sin\theta_{qN}\sin\theta_{q\pi}F(\phi_{qN},\phi_{q\pi}) + E_{recoil}\frac{p_\pi}{E_\pi} - p_{recoil}(\hat{\mathbf{q}})\cos\theta q\pi},$$

where $F(\phi_{qN},\phi_{q\pi}) = \cos\phi_{q\pi}\cos\phi_{qN} + \sin\phi_{q\pi}\sin\phi_{qN}$, E_{recoil} is the energy of the recoiling nucleon ($= \omega + E_N - E_\pi$), and $p_{recoil}(\hat{\mathbf{q}})$ is the component of the recoiling nucleon momentum parallel to $\mathbf{q}$ ($= q + p_N\cos\theta_{qN} - p_\pi\cos\theta_{q\pi}$). Another useful derivative is $\partial p_\pi/\partial\phi_{q\pi}$.

$$\frac{\partial p_\pi}{\partial\phi_{q\pi}} = \tag{B7}$$
$$\frac{p_N\sin\theta_{qN}p_\pi\sin\theta_{q\pi}G(\phi_{qN},\phi_{q\pi})}{p_{recoil}(\hat{\mathbf{q}})\cos\theta_{q\pi} + p_N\sin\theta_{qN}\sin\theta_{q\pi}F(\phi_{qN},\phi_{q\pi}) - p_\pi\sin^2\theta_{q\pi} - E_{recoil}\frac{p_\pi}{E_\pi}},$$

where $G(\phi_{qN},\phi_{q\pi}) = \cos\phi_{qN}\sin\phi_{q\pi} - \sin\phi_{qN}\cos\phi_{q\pi}$.

With these two partial derivatives in hand, the derivatives of t with respect to the pion angles are relatively simple:

$$\frac{\partial t}{\partial\cos\theta_{q\pi}} = 2p_\pi q + 2(q\cos\theta_{q\pi} - \omega\frac{p_\pi}{E_\pi})\frac{\partial p_\pi}{\partial\cos\theta_{q\pi}}, \tag{B8}$$
$$\frac{\partial t}{\partial\phi_{q\pi}} = 2(q\cos\theta_{q\pi} - \omega\frac{p_\pi}{E_\pi})\frac{\partial p_\pi}{\partial\phi_{q\pi}}. \tag{B9}$$

The derivatives of $\phi^*_{q\pi}$ are somewhat involved. The first step is to describe how $\phi_{q\pi}$ is defined in the lab. First, all relevant vectors are described in the lab using what will be called the "q" coordinate system. This coordinate system is defined such that the z-axis lies along $\mathbf{q}$. Then, since $\mathbf{q}$ and $\mathbf{P_{beam}}$ describe the scattering plane, the y-axis chosen to be in the direction $\mathbf{q}\times\mathbf{P_{beam}}$, and the x-axis is $\mathbf{y}\times\mathbf{z}$. Then $\phi_{q\pi}$ is simply $\arctan\frac{p_y}{p_x}$. Typically, when the target is stationary, the boost to the center of mass is along $\mathbf{q}$, so that $\phi_{q\pi}$ is the same in the lab and the center of mass since the boost does not affect transverse components of the pion momentum. When the target is allowed to move, however, the boost is not always along $\mathbf{q}$, so $\phi^*_{q\pi}$ must be recalculated.

To calculate $\phi^*_{q\pi}$, the "q" system is defined as above in terms of $\mathbf{q}$ and $\mathbf{P_{beam}}$, but evaluated in the center of mass. For clarity, the transformation will be described. Starting with some $\mathbf{p}_\pi$ in the lab "q" system, the pion momentum must be boosted to the center of mass (from this point the π subscript will be dropped - unless specifically noted, all momenta refer to the pion). In this calculation, the explicit angular dependence of p_x $(= p\sin\theta\cos\phi)$, etc. will be be fully written out so that it is clearer how to take the partial derivatives later:

$$\begin{aligned} p^*_x &= p\sin\theta_{q\pi}\cos\phi_{q\pi} + p\frac{\gamma-1}{\beta^2}\beta_x(\beta_x\sin\theta_{q\pi}\cos\phi_{q\pi} + \beta_y\sin\theta_{q\pi}\sin\phi_{q\pi} + \beta_z\cos\theta_{q\pi}) \\ &\quad -\gamma\beta_x E\ , \qquad \text{(B10)} \\ p^*_y &= p\sin\theta_{q\pi}\sin\phi_{q\pi} + p\frac{\gamma-1}{\beta^2}\beta_y(\beta_x\sin\theta_{q\pi}\cos\phi_{q\pi} + \beta_y\sin\theta_{q\pi}\sin\phi_{q\pi} + \beta_z\cos\theta_{q\pi}) \\ &\quad -\gamma\beta_y E\ , \qquad \text{(B11)} \\ p^*_z &= p\cos\theta_{q\pi} + p\frac{\gamma-1}{\beta^2}\beta_z(\beta_x\sin\theta_{q\pi}\cos\phi_{q\pi} + \beta_y\sin\theta_{q\pi}\sin\phi_{q\pi} + \beta_z\cos\theta_{q\pi}) \\ &\quad -\gamma\beta_z E\ . \qquad \text{(B12)} \end{aligned}$$

Note that the above quantities describe the components of the center of mass momentum in terms of the lab "q" coordinate system and must be rotated to the center of mass "q" coordinate system. This rotation is totally determined by the boosted beam and q vectors (so does not depend on the pion angles):

$$p^{*'}_x = p^*_x R_{xx} + p^*_y R_{xy} + p^*_z R_{xz}\ , \qquad \text{(B13)}$$

$$p^{*'}_y = p^*_x R_{yx} + p^*_y R_{yy} + p^*_z R_{yz}\ . \qquad \text{(B14)}$$

Which completes the calculation of $\phi^*_{q\pi} = \arctan\frac{p^{*'}_y}{p^{*'}_x}$.

Now, at last the partial derivatives for the Jacobian can be calculated. First making use of the fact that $\tan\phi^*_{q\pi} = \frac{p^{*'}_y}{p^{*'}_x}$ and,

$$\frac{\partial \tan\phi^*_{q\pi}}{\partial X} = (1+\tan^2\phi^*_{q\pi})\frac{\partial\phi^*_{q\pi}}{\partial X}, \tag{B15}$$

gives,

$$\frac{\partial\phi^*_{q\pi}}{\partial X} = \frac{p^{*'}_x\frac{\partial p^{*'}_y}{\partial X} - p^{*'}_y\frac{\partial p^{*'}_x}{\partial X}}{(p^{*'}_x)^2 + (p^{*'}_y)^2}\ , \tag{B16}$$

where X is either $\cos\theta_{q\pi}$ or $\phi_{q\pi}$. So, the derivative of $\phi^*_{q\pi}$ with respect to some lab variable can be done using the above formula, with the expressions for the $p^{*'}_n$ derived above and assuming that the R_{nn} and β_n do not depend on the pion angles (which they should not because they are calculated completely from initial quantities). The expression for the derivative of $\phi^*_{q\pi}$ involves derivatives of the components of the rotated, center of mass pion momentum. These derivatives are cumbersome and will not all be given here, but an example follows. Consider the derivative of the y-component of the boosted, rotated pion momentum with respect to lab $\phi_{q\pi}$,

$$\frac{\partial p^{*'}_y}{\partial\phi_{q\pi}} = R_{yx}\frac{\partial p^*_x}{\partial\phi_{q\pi}} + R_{yy}\frac{\partial p^*_y}{\partial\phi_{q\pi}} + R_{yz}\frac{\partial p^*_z}{\partial\phi_{q\pi}}. \tag{B17}$$

The partial derivatives of the unrotated, boosted components are given by,

$$\frac{\partial p^*_x}{\partial\phi_{q\pi}} = -p\sin\theta_{q\pi}\sin\phi_{q\pi} + p\frac{\gamma-1}{\beta^2}\beta_x\sin\theta_{q\pi}(\beta_y\cos\phi_{q\pi} - \beta_x\sin\phi_{q\pi}) + \left(\frac{p^*_x+\gamma\beta_x E}{p} - \gamma\beta_x\frac{p}{E}\right)\frac{\partial p}{\partial\phi_{q\pi}}\ , \tag{B18}$$

$$\frac{\partial p^*_y}{\partial\phi_{q\pi}} = p\sin\theta_{q\pi}\cos\phi_{q\pi} + p\frac{\gamma-1}{\beta^2}\beta_y\sin\theta_{q\pi}(\beta_y\cos\phi_{q\pi} - \beta_x\sin\phi_{q\pi}) + \left(\frac{p^*_y+\gamma\beta_y E}{p} - \gamma\beta_y\frac{p}{E}\right)\frac{\partial p}{\partial\phi_{q\pi}}\ , \tag{B19}$$

$$\frac{\partial p^*_z}{\partial\phi_{q\pi}} = p\frac{\gamma-1}{\beta^2}\beta_z\sin\theta_{q\pi}(\beta_y\cos\phi_{q\pi} - \beta_x\sin\phi_{q\pi}) + \left(\frac{p^*_z+\gamma\beta_x E}{p} - \gamma\beta_z\frac{p}{E}\right)\frac{\partial p}{\partial\phi_{q\pi}}\ . \tag{B20}$$

Although the algebra involved in the center of mass to lab transformation is tedious, it is straightforward. The above formulation was checked to make sure that it reduced to the simpler "collinear boost" case. An alternative, more elegant formulation can be found in Ref. [78].

CORRECTIONS (MAY 20, 2001)

- Section 1.1, Figure 1.1 (page 2).

  This figure, like the original reference, lists the y-axis units incorrectly. The plotted quantity is a number density per unit energy, so the units should read "fm" rather than "fm^{-1}".

- Chapter 6.

  A normalization error of about 3.5% was made on the ^{3}He(π^-) $\epsilon = 0.437$, $W = 1.15$ GeV, data. The separated cross sections and cross section ratios are also affected. Corrected versions of tables and figures follow, the relevant new value in bold where appropriate.

  - Section 6.3, Table 6.1 (page 181).

Target	ϵ	ΔP_π (GeV/c)	$\int_{\Delta P_\pi} d^6\sigma dP_\pi$ (μb/GeV/sr^2)	$\sigma_T + \epsilon\sigma_L$ (μb/sr)	$\frac{\delta\sigma}{\sigma}_{stat}$ (%)	$\frac{\delta\sigma}{\sigma}^{ran}_{sys}$ (%)	$\frac{\delta\sigma}{\sigma}^{scale}_{sys}$ (%)
$W = 1.15$ GeV, $k_\pi = 0.469$ GeV/c							
H	0.437	-	3.12×10^{-3}	17.22	1.4	1.8	7.1
H	0.861	-	2.86×10^{-2}	25.03	1.4	2.3	7.1
D(π^+)	0.437	0.248-0.350	2.18×10^{-3}	8.27	2.3	1.7	7.2
D(π^+)	0.861	0.248-0.350	2.02×10^{-2}	12.19	2.2	2.1	7.2
D(π^-)	0.437	0.248-0.350	1.66×10^{-3}	6.32	2.4	1.7	7.2
D(π^-)	0.861	0.248-0.350	1.87×10^{-2}	11.28	2.0	2.1	7.2
^{3}He(π^-)	**0.437**	**0.248-0.350**	**1.27×10^{-3}**	**4.53**	**3.1**	**1.8**	**7.2**
^{3}He(π^-)	0.861	0.248-0.350	1.39×10^{-2}	7.61	2.7	2.2	7.2
^{3}He(π^+)	0.437	0.248-0.350	3.52×10^{-3}	12.14	3.0	1.9	7.2
^{3}He(π^+)	0.861	0.248-0.350	3.15×10^{-2}	17.21	1.9	2.3	7.2

  - Section 6.4, Table 6.2 (page 186).

Target	$\sigma_L = \int_{\Delta P_\pi} d^2\sigma_L\, dP_\pi$ (μb/sr)	$\sigma_T = \int_{\Delta P_\pi} d^2\sigma_T\, dP_\pi$ (μb/sr)	$R = \frac{\sigma_L}{\sigma_T}$
$W = 1.15$ GeV, $k_\pi = 0.467$ GeV/c			
H	18.40 ± 1.01 ± 2.24	9.18 ± 0.62 ± 1.24	2.00 ± 0.30
D(π^+)	9.23 ± 0.77 ± 1.22	4.24 ± 0.47 ± 0.68	2.18 ± 0.39
D(π^-)	11.68 ± 0.65 ± 1.23	1.22 ± 0.39 ± 0.51	9.57 ± 4.04
^{3}He(π^-)	**7.27 ± 0.59 ± 0.90**	**1.36 ± 0.36 ± 0.44**	**5.36 ± 1.76**
^{3}He(π^+)	11.96 ± 1.15 ± 1.78	6.91 ± 0.81 ± 1.12	1.73 ± 0.34

  - Section 6.5, Table 6.3 (page 191).

Ratio	R_L	δR_L^{stat}	δR_L^{tot}	R_T	δR_T^{stat}	δR_T^{tot}
$W = 1.15$ GeV, $k_\pi = 0.469$ GeV/c						
D/H(π^+)	0.73	0.07	0.10	0.67	0.09	0.12
^{3}He/D(π^-)	**0.69**	**0.07**	**0.09**	**1.23**	**0.51**	**0.61**
D(π^-/π^+)	1.27	0.13	0.16	0.29	0.10	0.12
^{3}He/H(π+)	0.52	0.06	0.09	0.60	0.08	0.11

– Section 6.5.2, Figures 6.7 and 6.8 (pages 196 and 199).

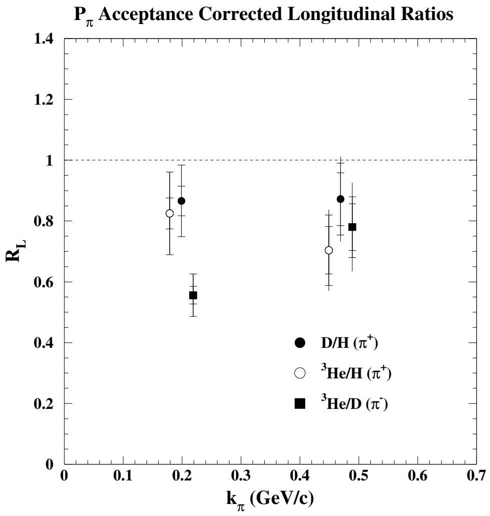

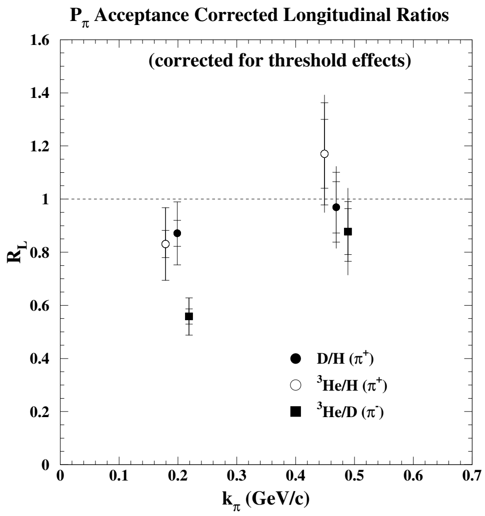

– Section 6.5.2, Table 6.5 (page 198).

Ratio	k_π (GeV/c)	P_π Acceptance Corrected Ratio	Momentum Dist. Fraction	Corrected Ratio
D/H(π^+)	0.203	0.866 ± 0.118	0.994	0.871 ± 0.119
^{3}He/D(π^-)	0.203	0.556 ± 0.071	0.990/0.994	0.558 ± 0.071
^{3}He/H(π^+)	0.203	0.810 ± 0.133	0.993	0.831 ± 0.137
D/H(π^+)	0.469	0.872 ± 0.139	0.90	0.969 ± 0.154
^{3}He/D(π^-)	**0.469**	**0.780 ± 0.146**	**0.80/0.90**	**0.878 ± 0.164**
^{3}He/H(π^+)	0.469	0.647 ± 0.126	0.80	1.170 ± 0.222

– Section 6.5.3, Figures 6.10 and 6.10 (pages 205 and 206).

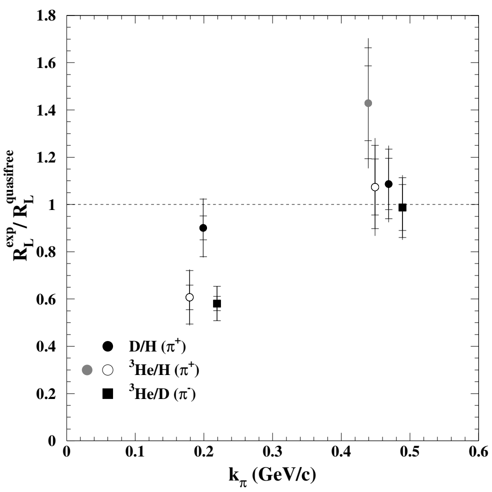

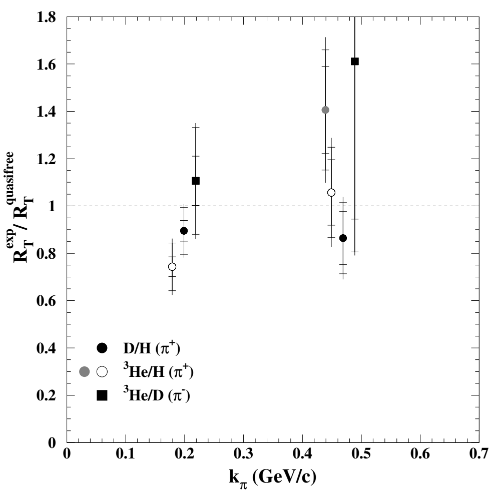

- Section 6.6.2 (page 212).

  In the original version, the form-factor was calculated using the momentum transfer as calculated for the free nucleon. Using the momentum transfer for the ^{3}He-^{3}H system increases the previous estimate by about 10%. Hence the estimated suppression factor goes from 0.39 to 0.425.

- Section 6.7 (page 214).

  To compare Equation 6.22 to the pion-excess calculations of Friman *et al* [2], it should contain a factor of m_π^{-2} for consistency. This, combined with the units confusion on Figure 1.1 led to incorrect estimates (and units) for the pion content of the nucleon, the pion excess in D, ^{3}He, and ^{4}He, as well as the resulting fractional enhancement (Table 6.10 and Table 6.11). These tables are reproduced with the correct values here. Note that all subsequent discussion should refer to these numbers, although the conclusions are the same.

  - Section 6.6.2, Table 6.10 (page 215).

k_π (GeV/c)	$n(k_\pi)$ (GeV^{-1})	$\delta n(k_\pi)$ (GeV^{-1})		
		D	^{3}He	^{4}He
0.20	0.392	-0.004	-0.056	-0.120
0.47	1.005	0.063	0.135	0.242

  - Section 6.6.2, Table 6.11 (page 216).

k_π (GeV/c)	D/H	^{3}He/H	^{3}He/D	^{4}He/H
0.20	0.99	0.86	0.87	0.69
0.47	1.06	1.13	1.07	1.24